

Leibniz Institute for Astrophysics Potsdam (AIP)  
— Milky Way and Local Volume —

---

# Chemo-Kinematic Constraints on Milky Way Models from the Spectroscopic Surveys SEGUE & RAVE

---

Dissertation  
for obtaining the academic degree  
“doctor rerum naturalium”  
(Dr. rer. nat.)  
in the scientific discipline “Astrophysics”

submitted at the  
Faculty of Mathematics and Natural Sciences  
at the Potsdam University

by

Dorothee E. Brauer

Potsdam, November 21, 2016

Published online at the  
Institutional Repository of the University of Potsdam:  
URN urn:nbn:de:kobv:517-opus4-403968  
<http://nbn-resolving.de/urn:nbn:de:kobv:517-opus4-403968>

This dissertation is a product of the collaboration between the Potsdam University and the Leibniz Institute for Astrophysics Potsdam (AIP).



**Potsdam University**

— Faculty of Mathematics and Natural Sciences, Institute for Physics and Astronomy —

Karl-Liebknecht-Str. 24-25  
14476 Potsdam OT Golm, Brandenburg  
Federal Republic of Germany



**Leibniz Institute for Astrophysics Potsdam (AIP)**

— Milky Way and Local Volume —

An der Sternwarte 16  
14482 Potsdam, Brandenburg  
Federal Republic of Germany

Thesis advisor: Prof. Dr. Matthias Steinmetz (AIP, Potsdam University)

Referees: 1<sup>st</sup> Prof. Dr. Matthias Steinmetz (AIP, Potsdam University)  
2<sup>nd</sup> Dr. Cristina Chiappini (AIP)  
3<sup>rd</sup> Prof. Dr. Timothy C. Beers (University of Notre Dame, USA)

Date of oral defence: September 8, 2017



The Milky Way is one of billions of galaxies in the universe. These galaxies turn gas into stars, producing most of the chemical elements that form the origin of all life. But it is the best spiral galaxy that allows to explore the main mechanisms involved in its evolution and formation history by unpicking the system star-by-star. That is why, based on detailed observations from Earth or the outer space, “galactic archaeologists” sift through stellar fossil records akin to archaeologists, who study human history by investigating the remnants of ancient civilisations. Thereby their goal is not only to assemble clues of past events in the galaxy’s lifetime but to decipher the current structure and building blocks of the Galaxy.

With a number of massive stellar spectroscopic Galactic surveys that were launched in the past decade elaborately scanning millions of stars far beyond the rim of the solar neighbourhood, Galactic science has progressed. The recently available spectroscopic information, which uncovers Galactic substructure of great detail and provides unprecedented insights to the chemo-dynamics of the Milky Way, let observers realise that the Galaxy is a highly complex system that does not easily unfold its exact underlying physical properties and real distribution functions. Hence, great effort is spent to unite observers with modellers. Their theoretical analytic models and numerical simulations provide necessary descriptions and predictions suited for comparison with the observations.

In the thesis at hand various approaches are taken to connect theoretical modelling of galaxy formation and evolution with observations from Galactic stellar surveys. With its focus on the chemo-kinematics of the Galactic disk this work aims for new observational constraints on the formation of the Milky Way providing also proper comparisons with the different models. These are the population synthesis model TRILEGAL based on analytical distribution functions and the hybrid MCM model that combines a  $N$ -body simulation of a Milky Way like galaxy in the cosmological framework with a semi-analytic chemical evolution model for the Milky Way. The major observational data sets in use come from two large pioneer spectroscopic surveys (Chapter 2), namely the Radial Velocity Experiment (RAVE) and the Sloan Extension for Galactic Understanding and Exploration (SEGUE). Both surveys together have observed almost a million stars in the Galaxy.

In the first approach chemo-kinematic correlations as traced by a selection of SEGUE G-dwarf stars (Chapter 3) are directly compared to predictions by the MCM model (Chapter 5). As a necessary condition for this SEGUE’s selection function and its survey volume are evaluated in detail (Chapter 5) to correct the spectroscopic observations for their survey specific selection biases. Also, based on a Bayesian method spectro-photometric distances with uncertainties below 15% are computed (Chapter 4) and used for a selection of SEGUE G-dwarfs which, in this work, are studied up to a distance of 3 kpc from the Sun.

For the second approach two synthetic versions of the SEGUE survey are generated based on the above models (Chapters 6 and 7). Thereby, to prepare the MCM version of the SEGUE survey the GALAXIA code is used as a tool to transform from the MCM model parameter space to the space of observables. Basically, the GALAXIA code is a framework for creating synthetic stellar catalogues according to any given model of the Galaxy which the user is either able to specify by a collection of analytic expressions or as an  $N$ -body realisation.

The obtained synthetic stellar catalogues are then used to create mocks best resembling the compiled sample of observed SEGUE G-dwarfs. It is shown that those mock samples are not only ideal to compare predictions from various models. They also allow validation of the models' quality and offer the opportunity to cross-check whether a certain chemo-kinematic finding is a true property of the Milky Way or a caveat of the model rather than an artefact that, in the first approach, may have been introduced by the empirical selection bias corrections.

By comparing the SEGUE G-dwarf sample and its TRILEGAL mock counterpart it was possible to improve the TRILEGAL code by constraining one of its main input parameters: the metallicity distribution function of the thick disk. Since then the improved version of TRILEGAL is the one that is officially used by the astronomical community. In this way with TRILEGAL it was possible to especially reproduce the statistical properties of the thin and thick disk as seen in the observed SEGUE sample. The MCM model on the other hand has shown to be more suitable in reproducing many chemo-kinematic correlations in the SEGUE G-dwarf sample. However, also evidence has been found that the MCM model may be missing a stellar component with the properties of the thick disk that the observations clearly show. While the SEGUE stars do indicate a thin-thick dichotomy of the stellar Galactic disk in agreement with other spectroscopic stellar studies, no sign for a distinct metal-poor disk is seen in the MCM model.

Usually stellar spectroscopic surveys are limited to a certain volume around the Sun covering different regions of the Galactic disk depending on their scientific aims and technical capabilities. This often prevents to obtain a global view on the chemo-dynamics of the Galactic disk. A suitable combination of stellar samples from independent surveys is not only useful for the verification of results that strongly rely on the surveys parameter and reduction pipelines but it also helps to complete the picture of the Milky Way.

Therefore, this thesis uses a sample of RAVE giant stars to question the chemo-kinematic constraints obtained with the SEGUE G-dwarfs. The comparison of both surveys reveals that the chemo-kinematic relations agree in disk regions where both samples show a similar number of stars. For those parts of the survey volumes where one of the surveys lacks statistics they beautifully complement each other. This demonstrates that the comparison of theoretical models on the one side, and the combined observational data gathered by multiple surveys on the other side, are key ingredients to understand and disentangle the structure and formation history of the Milky Way.

<b>Abstract</b>		<b>iii</b>
<b>1 Introduction</b>		<b>1</b>
1.1 A present-day view on the Milky Way . . . . .		2
1.1.1 The inner region: bulge and bar . . . . .		3
1.1.2 The halo . . . . .		4
1.1.3 The disk . . . . .		4
1.2 Milky Way models and simulations . . . . .		7
1.2.1 Stellar population synthesis . . . . .		9
1.2.2 The chemo-dynamical MCM model for the Milky Way . . . . .		11
1.3 Spectroscopic surveys of the Milky Way . . . . .		13
1.3.1 A first look on the counterparts RAVE and SEGUE . . . . .		14
1.4 Aims of the thesis . . . . .		16
<b>2 The RAVE and SEGUE surveys</b>		<b>19</b>
2.1 RAVE . . . . .		19
2.1.1 Target selection . . . . .		20
2.1.2 The stellar parameter pipelines in RAVE . . . . .		20
2.1.3 The RAVE chemical pipeline . . . . .		22
2.2 SEGUE . . . . .		23
2.2.1 Target selection . . . . .		24
2.2.2 The SEGUE Stellar Parameter Pipeline (SSPP) . . . . .		25
<b>3 A SEGUE G-dwarf sample</b>		<b>29</b>
3.1 Data assembly . . . . .		29
3.2 SEGUE G-dwarfs from DR9 . . . . .		30
3.2.1 Extraction of G-type stars . . . . .		32
3.2.2 Compiling a G-dwarf sample . . . . .		34
3.3 Stellar parameter systematics between DR8 and DR9 . . . . .		38
3.3.1 Calibration of $\log g$ . . . . .		40
3.4 Discussion . . . . .		40

<b>4</b>	<b>Kinematics</b>	<b>43</b>
4.1	Distances . . . . .	44
4.1.1	The method . . . . .	45
4.1.2	Special features and further add-ons . . . . .	47
4.1.3	Uncertainties . . . . .	48
4.1.4	Method validation . . . . .	48
4.1.5	Distances for SEGUE G-dwarfs . . . . .	51
4.2	Proper motions . . . . .	54
4.3	Space motions . . . . .	55
4.4	Orbits . . . . .	55
<b>5</b>	<b>Chemo-kinematic constraints from the SEGUE G-dwarf sample</b>	<b>57</b>
5.1	Accounting for selection effects and biases in the SEGUE G-dwarf sample . . . . .	58
5.1.1	Correction for the SEGUE target-type . . . . .	59
5.1.2	Correction for the SEGUE selection function . . . . .	60
5.1.3	Correction for the cut in colour-magnitude space . . . . .	65
5.1.4	Correction for the survey volume . . . . .	67
5.1.5	How do the corrections affect the MDF? . . . . .	68
5.2	Chemo-kinematic constraints from SEGUE G-dwarfs . . . . .	69
5.2.1	The $[\text{Fe}/\text{H}]-[\alpha/\text{Fe}]$ -plane . . . . .	69
5.2.2	The spatial and kinematic structure of the disk . . . . .	72
5.2.3	Variations in the MDF with radial distance from the Galactic centre . . . . .	77
5.3	Comparing the corrected SEGUE observations with model predictions . . . . .	79
5.3.1	The chemical plane . . . . .	80
5.3.2	The $[\text{Fe}/\text{H}]$ distribution . . . . .	81
5.4	Discussion . . . . .	85
<b>6</b>	<b>A TRILEGAL mock sample of SEGUE G-dwarfs</b>	<b>89</b>
6.1	Simulating the SEGUE survey with TRILEGAL . . . . .	91
6.1.1	Calculation of the input extinction . . . . .	91
6.1.2	Correction for overlap of SEGUE pointings . . . . .	92
6.2	Creation of a synthetic SEGUE G-dwarf sample . . . . .	93
6.2.1	Modification of the thick disk MDF in TRILEGAL . . . . .	94
6.2.2	Implementation of the SEGUE selection function . . . . .	95
6.2.3	Introduction of observational errors . . . . .	97
6.2.4	Definition of the final G-dwarf mock sample . . . . .	101
6.3	Comparison of the observed and the mock G-dwarf sample . . . . .	103
6.3.1	Chemo-kinematics of the SEGUE G-dwarfs as predicted by TRILEGAL . . . . .	109
6.4	Discussion . . . . .	116
<b>7</b>	<b>Modelling the SEGUE G-dwarf sample with the MCM model</b>	<b>119</b>
7.1	Creating a mock SEGUE survey with GALAXIA . . . . .	119
7.1.1	Modifications to GALAXIA . . . . .	120
7.1.2	Stellar population synthesis from an $N$ -body model . . . . .	120
7.1.3	Modelling a MCM based SEGUE G-dwarf sample . . . . .	122
7.2	Comparing the MCM, the SEGUE and the TRILEGAL G-dwarf mock sample . . . . .	122
7.2.1	Chemo-kinematics of the disk . . . . .	126
7.3	Discussion . . . . .	134

---

<b>8</b>	<b>Chemo-kinematics as seen with RAVE and SEGUE - a comparison</b>	<b>137</b>
8.1	The RAVE giants from Boeche et al. (2013a)	139
8.1.1	Spectro-photometric distances	140
8.2	Chemo-kinematic relations from RAVE and SEGUE	142
8.2.1	The metallicity distribution with galactic distance and vertical height	142
8.2.2	Vertical distribution of RAVE and SEGUE stars	147
8.2.3	Orbital families in the $e$ - $z_{\max}$ -plane	148
8.2.4	Velocity dispersions as a function of metallicity and $\alpha$ -enhancement	153
8.2.5	Discussion	156
<b>9</b>	<b>Summary and Conclusion</b>	<b>161</b>
9.1	A stellar sample of SEGUE G-dwarfs	162
9.2	Constraining models of the Galaxy	163
9.3	RAVE versus SEGUE - a unique comparison	166
9.4	Closing remarks and future prospects	167
<b>A</b>	<b>Supplement to RAVE</b>	<b>171</b>
A.1	The RAVE selection function	171
<b>B</b>	<b>Supplement to SEGUE</b>	<b>175</b>
B.1	General adjustments of the SSPP for DR9	175
B.2	Refinement of the SSPP estimators in DR9	176
B.3	The SDSS bitmask system	176
B.4	SQL query to select SEGUE G-dwarfs based on photometry	177
<b>C</b>	<b>Supplement to TRILEGAL</b>	<b>181</b>
	<b>Bibliography</b>	<b>185</b>
	<b>Acknowledgements</b>	<b>195</b>
	<b>Selbstständigkeitserklärung</b>	<b>197</b>



Throughout human history each generation has been fascinated by the strange shiny band and the multitude of twinkling dots that appear on our home planet's night sky, appealing to mankind's native curiosity and inspiring the desire to unriddle the origin of life and the reason of our existence. Since the first high crops each century has contributed with a new puzzle piece of scientific discovery to the comprehensive picture of the Universe's history. Ambition has brought us to set foot on the moon and to reach to the far edge of the solar system, sending satellites to comets and the Pluto system. Yet, for the matter beyond the outskirts of our star system today's astronomers are reliant on the pure light that reaches earth, after having travelled through the dark and mostly empty space for ages being the only source of information about the content of the Universe.

So, as our ancestors deduced the history of life on earth by examining rocks, modern astronomers act as "Galactic archaeologists". They use the properties of stars transmitted by light in order to understand the formation and evolution of Galaxies, the fundamental luminous building blocks in the  $\Lambda$ CDM Universe, because stars, like fossils on Earth, record the past in their ages, compositions, and in their kinematics.

### **Galactic archaeology**

The Milky Way and its neighbours in the local group are the ideal test-ground for investigating various theories of galaxy formation and evolution because of the exquisite detailed information that is available for these systems. Especially, our position right in the middle of the Milky Way enables us to use this Galaxy as a unique laboratory where not only individual stars can be resolved and analysed photometrically or spectroscopically with good precision and radial velocities are measurable. In particular, for the Milky Way also distances and proper motions are available to its stars which are hardly obtainable outside a few 10 kpc from the Sun. This distinguishes the Milky Way from its surrounding neighbours. Such near-field cosmology, i.e. the characterisation of stellar populations, gives insights into key processes that cannot be extracted from observations of distant galaxies, that often appear as faint and poorly resolved objects. Nonetheless, observations and surveys of distant galaxies at high redshift and long lookback times are an important and valuable complement because they provide us with snapshots of the earlier phases of galaxy formation and information on ensembles and interactions of galaxies.

Combining the chemical and kinematic information imprinted in stars of different age for stellar samples of large size, thereby covering significant portions of the Galaxy, has proven to be a very powerful method to detect signatures from the epoch of Galaxy assembly. Therewith figuring out how important mergers and accretion events are to the development of the different components of the Milky Way. The knowledge about the internal kinematics and chemistry of the Galaxy on sub-galactic scales also allows to spot the formation of clusters and substructure which reflects the nature of dark matter, indicating that Galactic archaeology provides crucial insights to test and understand the current cosmological paradigm.

At the moment one of the main challenges in the field of Galactic Archaeology is the adequate description of internal dynamical mixing mechanisms and their influence on shaping the Galaxy through time. The detailed data emerging from the suite of large Galactic stellar surveys shows clear evidence for the acting of secular evolution processes. Many studies reveal the presence of stars, e.g. super-metal-rich stars, in the solar neighbourhood with distinctively different chemistry than usual for stars born in situ from the interstellar medium in the solar annulus. The existence of those stars can not be explained by the common chemical evolution models (Chiappini 2009, and references therein), so their origin needs to be in a different location of the Galaxy. This points to efficient mechanisms that effect stellar orbits, the two main players likely being stellar heating and radial migration<sup>1</sup> (Sellwood & Binney 2002; Roškar et al. 2008b,a; Schönrich & Binney 2009b; Minchev et al. 2011). Radial heating mainly changes the eccentricity of the star and does not alter its guiding radius, while radial migration permanently changes the angular momentum of the star and thus the guiding radius of the stellar orbits, leaving the star still on a circular orbit. This allows that the migrated star shows the kinematics of the ones born in situ and the only way to recognise them as migrators is by their chemical fingerprints.

In theoretical simulations these secular evolution mechanism were recognised too, proving that radial migration is a common phenomena in the formation process of disk galaxies. Thus, one needs to act with discretion when studying the chemo-kinematics or -dynamics of the Galaxy knowing that secular evolution processes can affect classical observable constrains, such as, the age-metallicity relation, the metallicity distribution or the abundance gradients.

## 1.1 A present-day view on the Milky Way

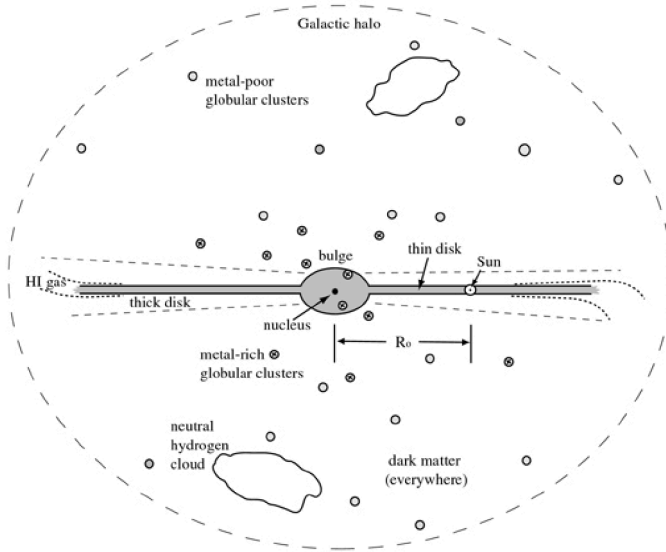
In the zoo of galaxies the Milky Way is in many ways a fairly typical spiral system because the majority of present-day stars live in late-type galaxies that resemble our Galaxy in stellar mass, size, chemical abundances, etc. within factors of a few. Commonly accepted is, that the Sun - a usual G-type dwarf star and the host star of the solar system - is located at about 8 kpc from the Galactic centre<sup>2</sup>, well embedded within a rotating disk system that harbours the majority of the Galaxy's stars, gas and dust and appears as a fuzzy, dim glowing, narrow stripe arching across earth's night sky. Conventionally, the Galaxy is decomposed into separate components: the central Bulge (Bar), the spherical Halo and the Disk, all of which differ significantly in terms of the stellar populations they hold, revealing specific and often very strong correlations between the position, velocities, chemical abundances and ages of their stars.

Figure 1.1 displays a schematic illustrating how the Milky Way is expected to look like in an edge-on view from the outside, listing its different parts. A brief but more detailed discussion on

---

<sup>1</sup>Radial migration is thought to be caused by scattering of stars at the corotation radius of transient spiral arms (Sellwood & Binney 2002), when the bar and the spiral structure's resonances overlap (Minchev & Famaey 2010) or by satellite perturbations (mergers) (Bird et al. 2012).

<sup>2</sup>Over the past four decades the actual estimate of the Sun's position has been gradually lowered from 10 kpc to values close to 8 kpc, e.g., 7.68 kpc  $\pm$  0.32 kpc (Eisenhauer et al. 2005), 8.27 kpc  $\pm$  0.29 kpc (Schönrich 2012)



**Figure 1.1:** Schematic sketch of the Milky Way in edge-on view from outside the Galaxy. Figure taken from Sparke & Gallagher (2007).

those various Galactic components, with a special focus on the disk which is main subject and of major interest to the present thesis, is given below.

### 1.1.1 The inner region: bulge and bar

The Galactic bulge is a massive and rather old spherical component dominating the Galaxy's central part interior to 3 kpc, harbouring a black hole of mass  $M_{\text{BH}} = 4 \times 10^6 M_{\odot}$ . The bulge appears as an over-density that swells up from the plane of the disk and is known to also host a bar, an important dynamical feature whose presence could be confirmed by IR photometry and radio observations of gas kinematics (Blitz & Spergel 1991; Binney et al. 1991) as well as star count studies (e.g. Saito et al. 2012). Several studies show that the gravitational influence of the central bar and its interplay with the spiral arms is the cause of various orbital resonances observed within the Galactic disk (see e.g. Dehnen 2000; Bovy & Hogg 2010; Minchev et al. 2010).

The bulge is found to have a boxy/peanut structure (Shen et al. 2010; Howard et al. 2009) with a likely origin in the disk and its instabilities forming via internal evolution (see e.g. Combes & Sanders 1981; Raha et al. 1991; Athanassoula 2005). There is also evidence for the presence of an additional spheroidal component (a classical bulge) which is believed to have formed rapidly at early times previous to the disk, via mergers or dissipational collapse processes (e.g. Ortolani et al. 1995; Zoccali et al. 2003). Hence, there are groups that even argue for the presence of a composite bulge (e.g. Babusiaux et al. 2010; Hill et al. 2011; Dékány et al. 2013). Due to this complex (geometric) structure there is no clear picture of the chemical composition, yet. While the innermost region is gas-rich and a place of active star formation, the major part of the bulge is gas-poor and contains mainly old stars which show a wide spread of metallicities. Evidently, the stellar content is a mix of more than one stellar population. Yet, it remains to be understood if the populations relate to the same structure or if they have a different origin.

Lately, several projects, such as the BRAVA (Kunder et al. 2012), ARGOS (Freeman et al. 2013) or even APOGEE (Allende Prieto et al. 2008a) survey have been looking into the heavily

dust obscured but intriguing heart of the Galaxy. Even though the field of Milky Way bulge research is currently revolutionised with the advent of photometric and spectroscopic surveys, several outstanding questions remain unresolved, e.g. the shape of the metallicity distribution function. Summarising information about the current knowledge on the bulge, including its believed formation scenarios can be found in Zoccali (2015), Gonzalez & Gadotti (2015) or Babusiaux et al. (2010).

### 1.1.2 The halo

The stellar halo of the Milky Way comprises old stars with heavy-element abundances of less than a tenth of the solar value, hosting the most metal-poor stars discovered to date (Frebel et al. 2005, 2008). The overall metallicity distribution shows a wide spread, but recent findings from photometric and spectroscopic surveys suggest that the halo consists of two broadly overlapping structural components, an inner and outer halo (Carollo et al. 2007, 2010) with different stellar populations. The inner population exhibits a flattened spatial density distribution (oblate spheroid), shows no net rotation and a peak in metallicity at  $[\text{Fe}/\text{H}] = -1.6$  dex being in good agreement with Jurić et al. (2008), Ivezić et al. (2008) and Bond et al. (2010).<sup>3</sup> The outer component has a more spherical density, a slight counter-rotation with respect to the disk and a metallicity peak at  $[\text{Fe}/\text{H}] = -2.2$  dex (based on BHB stars, Xue et al. 2008; Beers et al. 2012). Evidently, the latter is rich in substructure which points to the presence of accreted debris of tidally disrupted satellites, e.g. the Sagittarius spheroidal dwarf galaxy (Ibata et al. 1995). What fraction of the outer halo was actually accreted and how much of the debris is e.g. low in  $\alpha$ -elements (Nissen & Schuster 2010) are still questions under debate.

### 1.1.3 The disk

The disk is the Milky Way's dominant stellar component which contains about three quarters of all Galactic stars, defines the Galactic plane and appears as a highly flattened, axisymmetric structure with a flat rotation profile due to which the majority of disk stars move around the Galactic centre (GC) on nearly circular orbits with a  $v_{\text{circ}}$  of about 200 km/s to 220 km/s. The Sun surrounds the GC in roughly 250 Myrs at a speed of about  $v_{\text{circ}} = 220$  km/s. The stellar mass of the disk is estimated to be about  $5 \times 10^{10} M_{\odot}$  (see e.g. Flynn et al. 2006; McMillan 2011). As inferred from NIR star counts the outer disk reaches at least out to  $15 \text{ kpc} \pm 2 \text{ kpc}$  in radius (Ruphy et al. 1996). Also, the outer disk shows signs of a warp (Reylé et al. 2009). In analogy to other external disk galaxies the Milky Way's stellar density profile is an exponential function of radius, with a disk scale length currently assumed to be of the order 2 kpc to 3 kpc (McMillan 2011). Obscuration within the disk usually challenges the exact determination of the radial density profile. More details on current estimates of the Galaxy's structural parameters are given in Chapter 1 and Table 1.2 of Binney & Tremaine (2008). For an extensive overview on the chemical, kinematic and dynamic structure of the Galaxy's stellar disk the interested reader is also referred to Turon et al. (2008), Ivezić et al. (2012) and Rix & Bovy (2013).

---

<sup>3</sup>Conventionally, the abundance of an element  $X$  is expressed as:

$$[X/\text{H}] = \log \left( \frac{N_X}{N_{\text{H}}} \right)_{\star} - \log \left( \frac{N_X}{N_{\text{H}}} \right)_{\odot} \quad (1.1)$$

where  $N_X$  and  $N_{\text{H}}$  are the number of atoms of the element  $X$  and hydrogen in the stars atmosphere and the subscript  $\odot$  indicates the corresponding values of the Sun. Hence, a value of  $[X/\text{H}] = 0.0$  means that the star has an equal amount of  $X$  as the Sun, if  $[X/\text{H}] = -1.0$  the stars is about one tenth less rich in  $X$  than the Sun. Note that throughout this work the latter bracket notation is in use when dealing with elemental abundances.

## The disk's kinematic and chemical structure

Since Gilmore & Reid (1983), who discovered that there is variation in the stellar density profile of the Galactic disk perpendicular to the plane that can be fit by the sum of two exponential laws, the stellar disk is recognised to be a superposition of two (or even more) distinct populations of stars<sup>4</sup> with different scale heights,  $h_z$ . The latter depend on the age of the population defining its extent within the disk because older stars tend to have larger vertical scale heights as a result of stochastic processes (e.g. fluctuations in the gravitational field) related to spiral arms and giant molecular clouds. These processes are able to increase the random velocities, orbital eccentricities and inclinations of stars.

Over the past years many studies favoured a two component disk scenario. Especially high-resolution surveys of the solar neighbourhood revealed that from a chemical point of view there are two distinct populations of stars that separate in the  $[\alpha/\text{Fe}]$  vs.  $[\text{Fe}/\text{H}]$  diagram. These can be related to the existence of two kinematically different disk components, the Thin and the Thick disk<sup>5</sup>. The latter represents the older and hotter disk component ( $h_z = 900 \text{ pc} - 1000 \text{ pc}$ , Jurić et al. 2008; Veltz et al. 2008) which hosts stars mostly older than 10 Gyrs (Freeman & Bland-Hawthorn 2002) and shows a larger dispersion in all three velocity components and more inclined and eccentric orbits. Also, the entire thick disk population exhibits a rotational lag with respect to the thin disk which on the other hand contains a stellar population more confined to the galactic plane ( $h_z = 300 \text{ pc}$ ). Usually, thin disk stars are younger and on nearly circular orbits. Since there is still ongoing star formation due to the large amount of gas and dust settled in a small layer of about 100 pc from the midplane, the thin disk shows an age-sequence from around 9 Gyrs to a few millions years because newly born stars were added to the population at a fairly constant rate over the lifetime of this component. The thin disk is kinematically cold with low stellar velocity dispersion near the Sun which is far less than 220 km/s. Most important, the old and young stellar population show distinct chemical properties. Whereas the thick disk stars are poor in heavy elements (metal-poor<sup>6</sup>) but are enhanced in  $\alpha$ -elements, i.e. at a given metallicity they have a larger abundance of  $\alpha$  nuclides (O, Ca, Mg, Si, Ne, etc.) relative to iron, the thin disk stars are richer in metals (higher  $[\text{Fe}/\text{H}]$ ) and less  $\alpha$ -enhanced.

A common explanation for this distinct behaviour of the two disk components is that they were formed on different timescales. From the point of chemical evolution the thick disk's chemical composition suggests the component to have formed on short timescales (Chiappini 2009), i.e. in a short star formation event (less than 1 Gyr), when the interstellar matter (ISM) had been polluted and enriched mainly with heavier elements from core-collapse supernovae (SNII). SNII arise from gravitational collapse of massive stars ( $> 8 M_\odot$ ) with short lifetimes and produce ejecta rich in  $\alpha$ -elements. Until supernova type SNIa<sup>7</sup> exploded with a typical time delay of 1 Gyrs, releasing mostly iron, all disk stars formed by then show a distinctively higher  $[\alpha/\text{Fe}]$  ratio than today. As the galaxy aged the composition of the ISM changed: the  $[\alpha/\text{Fe}]$  ratio decreased monotonically with time while the  $[\text{Fe}/\text{H}]$  ratio increased. Observational evidence suggest that the short and turbulent thick-disk and halo formation phases were followed by a

<sup>4</sup>Actually, the discovery of different stellar populations in galaxies, as observed in M31 and two of its companions, dates back to Baade (1944) who reported that galaxies are composed of an older and metal-poor (Population I) and a younger and metal-rich population (Population II) of stars.

<sup>5</sup>Gratton et al. (2000) and Fuhrmann (1998) were among the first to discover that the spatial and kinematic behaviour of disk stars varies tremendously as a function of their chemical composition, being apparent as separate populations of stars in the chemical abundance plane.

<sup>6</sup>The thick disk's metallicity distribution function is found to extend from low  $[\text{Fe}/\text{H}]$  ( $-1.5 \text{ dex}$ ) to values above solar (e.g. Bensby et al. 2007) with a peak around  $-0.5 \text{ dex}$ .

<sup>7</sup>Thermonuclear (or SNIa) supernova which is caused by runaway nuclear burning on the surface of white dwarfs in binary systems. Their occurrence lags star formation by the order of 0.5 Gyrs to 10 Gyrs.

quiet epoch with a sudden decrease in star formation that preceded the extended formation of the thin disk, which was build in a second phase of star formation after the infall of new gas into the galaxy's system. The latter scenario is e.g. described by the two-infall model (Chiappini et al. 1997; Chiappini 2009) which proposes a double-peak in the Galactic star formation rate.

In agreement to that cosmological simulations seem to converge to a similar scenario (e.g. see Brook et al. 2004, 2012; Bird et al. 2013; Stinson et al. 2013a). They show that in the context of a cold dark matter (CDM)-based hierarchical galaxy formation a kinematically hot and geometrically thick disk forms naturally at high redshift as long as there are multiple mergers of building blocks at play. With these building blocks being gas-rich galaxies, the in-situ formation of stars than mainly takes place in the new central gas-rich disk that originates from the mergers. This creates a situation in which on short-timescales intense star formation can produce a population of  $[\alpha/\text{Fe}]$ -high disk stars that reside in a kinematically hot and geometrically thick disk. The thinner  $[\alpha/\text{Fe}]$ -low disk component is than build up later in a quiet and merger free epoch through less intense and more moderate star formation that is driven and kept alive by a continuous low-level of gas accretion.

At least on the observational side most of the presented ideas are based on very local Galactic datasets of stars. A better knowledge and much more constraining information can yet be obtained from larger stellar samples. That is exactly where the current thesis steps in by focussing on statistically significant stellar samples.

### The origin and extent of the thick disk

The origin of the thick disk is currently by far one of the most extensively discussed topics and a clear consensus is yet not reached. Even though many observational studies support a separation (chemical gap) between the thin and thick disk, recently it has been claimed that the thin-thick disk dichotomy may be mainly a result of common selection biases (Rix & Bovy 2013) rather than a sign for two distinct stellar disk components. In addition to the controversial discussion among observational astronomers theorists have developed and simulated a wealth of various scenarios that try to explain the formation of the thick disk on a chemo-dynamical level in the context of the cosmological paradigm. The four main thick disk formation scenarios under debate are:

- **heating scenario:** the thick disk formed from an pre-existing thin disk that has been dynamically heated and puffed up by a satellite merger (Villalobos & Helmi 2008).
- **accretion scenario:** the thick disk is a product of the accretion of stars belonging to disrupted satellites whose orbits reached near the galactic disk plane (Abadi et al. 2003).
- **gas-rich merger scenario:** thick disk stars are born *in situ* in an violent epoch of gas-rich mergers where gas was accreted and early star formation was induced before and after the mergers (Brook et al. 2004, 2005).
- **Radial migration scenario:** thick disks may have formed by processes that are associated with radial migration of stars (e.g. Schönrich & Binney 2009a,b).

All discussed mechanisms are able to create a thick disk but it is still not clear whether the presence of a thick disk component found in spiral galaxies is caused by one or a combination of them (see e.g. the study by Sales et al. 2009). Currently, the two main contenders remain the gas-rich merger and the radial-migration scenario, whereas the accretion and disk heating scenarios appear to be in conflict with observations (Dierickx et al. 2010; Wilson et al. 2011).

Despite the origin question the actual scale length of the thick disk is an equally intense discussed issue. Stellar disk decomposition into thinner and thicker components in external edge-on

galaxies suggest that the thin and thick disk have comparable scale length (Robin et al. 1996; Ojha 2001; Jurić et al. 2008). The same is found for the Milky Way as long as a similar morphological (structural) definition is used. However, results based on spectroscopic observations reveal that the older,  $\alpha$ -enhanced population (thick disk) is centrally concentrated and thus has a shorter scale length, while the young thin disk component is radially extended (Bensby et al. 2011; Bovy et al. 2012c; Cheng et al. 2012). According to a recent study presented in Minchev et al. (2015) these contradictory findings can be explained as follows: in galactic disks that formed inside-out, where the scale length of a stellar population increases with decreasing age, i.e. being larger for younger stars, mono-age populations of stars tend to flare towards the outskirts of the Galaxy. While their density profile is well fit with a single exponential, the total stellar density (including all ages) yet requires two exponentials for a good fit leading to thin and thick disks without any sign of flaring. As claimed by the authors the latter fact is a direct result of the flaring which allows chemically thin disk stars to reach large vertical distances in the outer disk and that at progressively larger radii with decreasing age. More important, the proposed scenario sheds light on the apparent contradictions that chemically (or age) defined thick disks are concentrated in the inner disk, but structurally thick populations as observed in edge-on galaxies and the Milky Way show a similar or even larger extend than the thinner component.

## 1.2 Milky Way models and simulations

In the era of modern computing and ever increasing computational power numerical simulations in the context of  $\Lambda$ CDM cosmology have emerged to one of the main pillars in the field of galaxy formation and evolution. Considering the extremely complex and highly non-linear galaxy formation process and the strong environmental influences that continuously emanate from accretion, interaction with satellites and merger events during a galaxy's lifetime, simulations are the only tool to follow such a complicated evolutionary history. Especially, in the past 20 years much effort has been spent in sophisticated computer simulations that now also focus on the baryonic matter content within the galaxy's systems (Navarro & Steinmetz 1997, 2000). This is because many authors gradually realised that the implementation of pure hydrodynamics alone is not sufficient to obtain realistic disk-dominated galaxies. Even if on large scales the driving force is dark matter and following its evolution suffices in order to trace, reconstruct and clarify the Universe's filamentary structure as is found in galaxy redshift surveys (e.g. Springel et al. 2006), on smaller scales physical processes other than gravity come to the fore having an essential effect on the global structure of galaxies. By now it is commonly accepted that the creation of galaxies, such as our own, requires a vivid interplay of processes like star formation and energy feedback related to supernovae, stellar winds and super massive black holes (Governato et al. 2004; Piontek & Steinmetz 2011; Springel 2012). However, for most of these small scale physics (e.g. the UV-background and reionisation, energy feedback from supernovae (Scannapieco et al. 2005, 2006) or massive stars (Aumer et al. 2013; Stinson et al. 2013b)) the current spatial resolution of the simulations is not adequate enough. Cosmological simulations need to cover huge dynamical ranges and timescales which prevents to include small scale processes in the first place. Instead, these have to be implemented in a phenomenological way known as 'subgrid' physics (Scannapieco et al. 2012) which is one of the simulation's weak points.

## Fully-self consistent simulations of the Milky Way

Recently, fully-self consistent cosmological simulations of galaxies have significantly leaped forward on its way to produce realistic disk-dominated galaxies (Governato et al. 2010; Guedes et al. 2011). An increased resolution and improved modelling of star formation and feedback puts them now to a level where the resulting simulated systems start to compete with simpler galaxy modelling approaches and observations resembling certain Milky Way features, such as the mass or the bulge fraction (Stinson et al. 2010; Martig et al. 2012). Yet, especially the introduction of chemical evolution remains an issue in many self-consistent cosmological simulations. Most of the Galaxy formation simulations by groups that attempt to include chemical evolution (Scannapieco et al. 2005; Kawata & Gibson 2003; Kobayashi 2004; Wiersma et al. 2009; Few et al. 2012, e.g.) have been able to reproduce global trends, e.g. with respect to the chemical properties of different Galactic components, but are far from matching the observed small scale properties of the Milky Way (Tissera et al. 2012).

Given that for quite some time the validity of a simulated galaxy could only be evaluated through its global structural properties, e.g. by measuring the Tully-Fisher relation or the mass-to-light ratio, the vast amount of detailed observational information from today's Galactic surveys offer the great opportunity to probe the simulations on scales where feedback processes are most important. A successful comparison of models and observations however demands the simulation of Milky Way like systems with stellar populations having statistical properties as observed in our own Galaxy. Considering that the subgrid physics, i.e. the correct handling of star formation and chemical enrichment history, still poses a challenge to most cosmological simulations alternative simpler models are needed which include the essence of the hierarchical build-up typical for cosmological simulations, but at the same time have the flexibility to “play” with the input physics relevant on small scales. One of those alternatives is the approach taken by Minchev et al. (2013) who present the creation of a new kind of chemo-dynamical model for the Milky Way that exactly suffices the above requirements of a simpler model and is further referred to as the MCM model. A detailed discussion on the MCM model and its specifications is given in Section 1.2.2.

## Models of the Milky Way

Despite numerical simulations a variety of detailed models of the Milky Way have seen first light in the last decades. The driving element for their development was the wish to create Galaxy models that could be compared to observational data in order to understand and constrain the structure of the major components of the Galaxy. According to their type the models can be divided into three categories: mass (Dehnen & Binney 1998; McMillan 2011; Irrgang et al. 2013), population synthesis (see next section below) and dynamical models (Widrow et al. 2008; Binney 2012). Common to all is their analytical nature and the fact that they have been progressively tuned (e.g. recalibrating the respective model parameters) through observational constraints.

Along with the MCM model the population synthesis models are the only ones relevant to the current thesis. They are also known as star count models and aim to specify the density and velocity distributions of the luminous matter in the Galaxy making also predictions on the spatial distribution of chemical abundances and ages. Yet, the kinematic models have a major caveat: their distribution functions and parameters happen to be set and tuned by hand. The most popular examples for this type of model are the so-called Besançon<sup>8</sup> model (Robin et al.

---

<sup>8</sup>Contrary to other population models presently available the Besançon model features a dynamical self-consistency to constrain the scale height of the disk (Bienayme et al. 1987).

2003) and the TRILEGAL code (Girardi et al. 2005) (see more details in Section 1.2.1). Latterly, kinematic models can also be produced using the newly developed numerical code framework GALAXIA by Sharma et al. (2011) and Pasetto et al. (2012) which has the additional ability to convert mass distributions, e.g., represented by the particles of a  $N$ -body simulation, to the space of observables.

### 1.2.1 Stellar population synthesis

Among the different modelling approaches mentioned above the stellar population synthesis approach represents itself as a particular special case. It acts as a bridge between observations and theoretical models providing a way to map from physical to observational space, i.e. linking the information encoded in the detected light of astronomical observations (e.g. quantities like apparant brightness, spectral energy distribution, line-of-sight velocities, etc.) to meaningful physical parameters (like e.g., mass, age, etc.), through the use of stellar evolution and atmosphere theory.

The basic scheme behind stellar population synthesis is to convert analytic or  $N$ -body descriptions of the Galaxy into synthetic catalogues of stellar objects whose observable properties, e.g. luminosity, effective temperature, surface gravity or magnitude etc., can be directly compared to those of real stars. Thereby, the models assemble the knowledge about current galaxy formation and evolution scenarios, theories of stellar evolution and formation, models of stellar atmospheres as well as dynamical constraints. A simulation of the Galaxy's stellar content based on one of these specific alternative scenarii (models) serves than not only to verify the latter, when compared to existing photometric, spectroscopic or astrometric datasets from surveys at different wavelength. It also helps, at the same time, to test the available observations to answer given questions in relation to Galactic structure and evolution.

One caveat, however, is that most of the population synthesis models describe a smooth galaxy which questions their validity because, as a known fact, the Milky Way shows inhomogeneities in its disk and halo components. Therefore, the goal can not be to create a perfect model that resembles the Galaxy at any scale, but to provide a useful tool that is able to contribute to the analysis and interpretation of today's large datasets and that supports the conceptual design of future observations. Especially, when planning new observational facilities a forecast of observable objects is of immeasurable value. In that context the two most prominent and recent examples are: (1) the analysis software of the Gaia space mission (Perryman et al. 2001) which was developed and validated using an extended version of the Besançon model (Robin et al. 2012) that is able to simulate the characteristics of all various types of objects that Gaia will observe and (2) the GALAXIA based, simulated input catalogue of targets possibly observed by the currently developed 4MOST instrument (de Jong et al. 2012). The latter catalogue being created with the purpose to optimise the final target input catalogues (and selection functions) for each of the scientific surveys that will be run in parallel during the operation period of the 4MOST instrument allowing to test the actual science capabilities of the planned instrument. Other studies used the available star count models, e.g. to constrain the Galactic warp (Reylé et al. 2009) with the help of the Besançon model, to investigate the statistical significance of a stellar stream found in the RAVE (Steinmetz et al. 2006) dataset by use of GALAXIA (Williams et al. 2011) or to disentangle true features from selection effects exploiting the predictions by TRILEGAL (see Miglio et al. 2013b; Boeche et al. 2013b).

More details on specific characteristics that apply to the majority of star count models are given below using the examples of TRILEGAL and GALAXIA.

## TRILEGAL

The TRIdimensional model of thE GALaxy (TRILEGAL<sup>9</sup>) is one of the popular Milky Way star count models which was created for simulating the stellar photometry of any line-of-sight in the Galaxy. It is a geometric model build as a superposition of a set of stellar components, including a thin and thick disk, a stellar halo and a central galactic bulge. Each of them contains a particular stellar population that is defined through the assumed phase space distribution function (DF) of its corresponding component. The DF is determined by the chosen scenario of formation and evolution and is a product of several analytic expressions that specify the spatial density profile, the initial distributions in age (star formation rate - SFR), metallicity (age-metallicity-relation - AMR) and velocity, the masses (initial mass function - IMF) and the interstellar absorption of the individual Galactic components. The final modelling of each population is than based on a library of theoretical evolutionary tracks<sup>10</sup> and the DF. In that process TRILEGAL is able to simulate the star's photometry in almost any broad band filter system using an extensive stellar spectral library (bolometric corrections). Some of the geometric parameters are well calibrated using data from wide-field surveys (mainly optical and near-IR). For example, the density profiles can be constrained through fits against deep photometric observations. Also, the velocity distributions are set to match local measurement in the solar neighbourhood. Other ingredients, e.g. the shape of the IMF or SFR, are not well constraint and still under debate. Hence, TRILEGAL offers different options for the input libraries and its further ingredients (SFR, AMR, IMF and geometry) and their parametrisation, which can be chosen and changed by the user allowing a certain freedom to define a simulation according to personal needs.

With the addition of the kinematics module the TRILEGAL code has broadened its spectrum of applications, now also being able to explore the detailed information on stellar movements that are provided by spectroscopic survey projects. Yet, spatial and kinematic distribution functions are assumed to be functions of age only as is the metallicity. The star's kinematic properties are not correlated to its chemistry. This is why the model should not be able to predict and reproduce any of the de facto observed trends between kinematic parameters and chemical abundances or kinematics and spatial distribution. Also, to date there are no metallicity gradients implemented for any of the stellar components as are observed in reality. TRILEGAL assumes a metallicity distribution function for each disk, thin and thick, which has no dependence on radius and height, so that any radial or vertical metallicity variation needs to be a result of the assumed mix of populations.

## GALAXIA

GALAXIA is a general frame-work for creating synthetic catalogues of stars according to any given model of the Galaxy or its individual components, which the user can either specify by a collection of analytical expressions or as an  $N$ -body realisation. The latter option is an important achievement with respect to models like TRILEGAL or Besançon whose smooth<sup>11</sup> relaxed stellar halo populations are inadequate to accommodate for any stellar substructure such as the known

---

<sup>9</sup>Original code description is layed out in Girardi et al. (2005) while more recently Girardi et al. (2012) gives an overview about the current status and future of the model.

<sup>10</sup>The current version 1.6 of TRILEGAL, being accessible through its web interface at <http://stev.oapd.inaf.it/cgi-bin/trilegal>, uses evolutionary tracks as described in Marigo et al. (2008); Girardi et al. (2010)

<sup>11</sup>In populations synthesis models smooth means that the different Galactic components are quite uniform in their distributions of ages and metallicities. This stands in contrast to observations and the hierarchical structure formation paradigm, which assumes that a significant fraction of the stellar halo is build up by accretion events, whose signatures, a large number of stellar streams, should be visible as substructure.

Sagittarius dwarf stream (Ibata et al. 1995). High-resolution  $N$ -body models of the halo that are simulated in a cosmological context (Bullock & Johnston 2005; Cooper et al. 2010; De Lucia & Helmi 2008), however, have the ability to make accurate predictions on the spherical component’s substructure and can also be used to test the  $\Lambda$ CDM paradigm. GALAXIA’s implemented standard model takes this into account by combining the Besançon Milky Way model for the disk components with the simulations by Bullock & Johnston (2005) for the Galaxy’s stellar halo. The details of the code and its specials can be found in Sharma et al. (2011).

The principal concept of GALAXIA, when executed in its main mode that produces discrete realisations of the Galaxy based on analytical descriptions, is similar to the one used by TRILEGAL (see details about superposition of components and individual phase space distribution function in the previous paragraph on TRILEGAL). Also the two models currently use the same set of Padova stellar atmosphere models (Marigo et al. 2008) to obtain the basic stellar parameters  $\log g$ ,  $T_{\text{eff}}$ ,  $L$  and absolute magnitudes in several filters for each mock star. There is yet a clear difference concerning the codes’ sampling schemes and their output magnitudes. TRILEGAL has the shortcoming that it generates stars at a specific location along a line of sight (i.e. the step size for radial and angular coordinates as well as distances is discretised) and returns photometry (apparent magnitudes) that is internally equipped with extinction. GALAXIA on the other hand is able to generate a continuous and smooth distribution of stars over any given volume and delivers absolute but de-reddened magnitudes. In order to still provide information on dust extinction GALAXIA incloses a mechanism that computes extinction estimates  $E(B - V)$  based on a double exponential dust disk that is fit to the extinction maps by Schlegel et al. (1998). In order to weaken the effects that arise due to the inaccuracies of the Schlegel et al. (1998) maps in regions close to the Galactic plane Sharma & Bland-Hawthorn (2013) introduce an additional correction. Note, that this correction is most interesting for stellar surveys that concentrate on lower latitudes. The two spectroscopic surveys that this thesis focuses on however do avoid the highly extinguished regions of the Galactic disk by construction.

Building up on GALAXIA’s  $N$ -body mode Tilmann Piffl further extended the framework’s abilities as part of his PhD thesis (see Section 2.3 in Piffl 2014) to enable GALAXIA to also process an entire  $N$ -body realisation of a self-consistently simulated galaxy. The few modifications that had to be done and were applied to the code are outlined in Section 2.3 of Piffl (2014) or summarised in this thesis’ Section 7.1.1. A first immediate application of this new extension is discussed in Section 3.3 of Piffl (2014) which deals with a GALAXIA simulation of the complete RAVE survey that is based solely on the new model approach proposed by Minchev et al. (2013). A similar application will be shown in this work’s Chapter 7.

## 1.2.2 The chemo-dynamical MCM model for the Milky Way

The recently developed chemo-dynamical model by Minchev et al. (2013), the MCM model, represents a new type of hybrid model for the Galaxy fusing a numerical simulation of disk galaxy formation and evolution in the cosmological context (Martig et al. 2012) with a detailed semi-analytic chemical thin-disk evolution model (Chiappini 2009) of the Milky Way. The general idea behind this approach is to avoid the known problems with chemical enrichment and star formation history currently encountered in fully self-consistent cosmological simulations. Therefore, in this hybrid model the star formation history and chemical enrichment is taken from the chemical evolution model to be subsequently assigned to the individual particles of the cosmological  $N$ -body simulation. As a result the MCM model is not fully self-consistent as is a cosmological simulation but provides at least self-consistent Galaxy dynamics. This new concept allows to especially study the role and effects of radial migration on the distribution of chemical

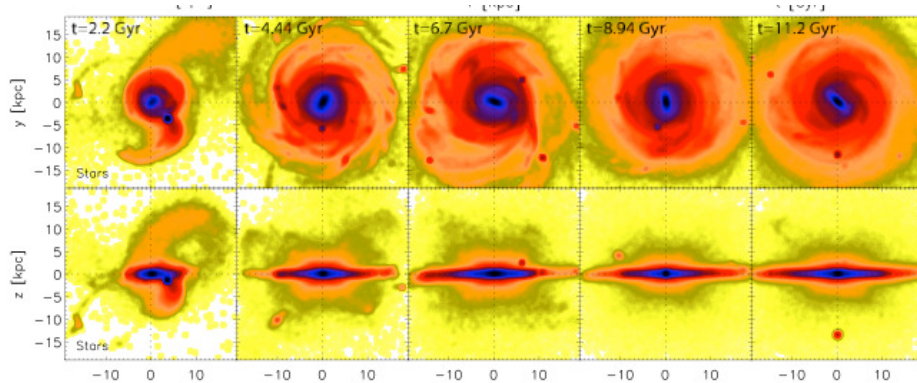


**Figure 1.2:** Face-on (*top row*) and edge-on (*bottom row*) density maps of the stellar component for the simulated barred late-type spiral galaxy which was used in the MCM model presented by Minchev et al. (2013). The galaxy has been taken from the set of 33 zoomed-in simulations by Martig et al. (2012). Shown are different timesteps. The contour spacing is logarithmic. Figure from Minchev et al. (2013).

elements in the Galaxy and hence its impact on the classical constraints, such as the metallicity distribution function, the age-metallicity-relation or the abundance gradients.

### General description of the model

The numerical cosmological simulation utilised in the model is taken from the suite of 33 zoomed-in simulations presented in Martig et al. (2012) and represents a barred late-type spiral galaxy whose properties are close to those of the Milky Way. All 33 simulations are actual re-simulations of a dark matter-only simulation of a much larger volume. The exact simulation technique and details are described in Martig et al. (2009, 2012) and references therein.

As both, the simulation and the chemical evolution model, come with its own star formation history (SFH) a simulation was chosen that provided a SFH as close as possible to the one owned by the chemical model. However, opting for the latter SFH the simulation's SFH needed adjustment as described in Section 4 of Piffi (2014) by resampling the simulated particles to match the exact SFH of the chemical evolution model. Furthermore, in order to match the Milky Way in terms of dynamics, particularly matching the size of the Galactic bar and the circular velocity at the position of the Sun,  $v_{\text{LSR}} = 220 \text{ km/s}$ , the simulation is re-scaled according to the following transformations:

$$\mathbf{r}' = \mathbf{r}/f_1 \quad (1.2)$$

$$\mathbf{v}' = \mathbf{v} \times \sqrt{f_1/f_2} \quad (1.3)$$

with  $f_1 = 1.67$  and  $f_2 = 1.38$ .

The chemical enrichment history is superimposed to the simulation by assigning a metallicity to each  $N$ -body star particle according to its birth time and place within the Galaxy following the independent predictions of the chemical evolution model which aims to recover the evolution of the interstellar medium as a function of time and radius, where  $R = \sqrt{x^2 + y^2}$ . In other words, the particle's chemistry is uniquely linked to the chemical enrichment and composition of the interstellar medium at the time and location the star particle was born. In order to account for an inside-out formation of the Galactic disk the chemical model adopts a star formation law dependent on the local gas surface density and  $R$ . Further main assumptions are an initial mass

**Table 1.1:** Overview of past, current and future spectroscopic Galactic surveys.

survey	period	sky area	# of spectra	apparent magnitude	$\sigma(v_{\text{los}})$ [km/s]	$\sigma([\text{Fe}/\text{H}])$ [dex]	char. d [kpc]
GCS	1981-2000	South	16 k	$V \approx 10$	0.5	indiv.	0.003
<b>RAVE</b>	2003-2013	South	480 k	$9 < I < 12$	2	0.2	0.5
<b>SEGUE</b>	2004-2009	North <sup>12</sup>	360 k	$14 < g < 20$	4	0.2	2
APOGEE	2011-2014	North <sup>13</sup>	150 k	$H < 13.8$	0.5	indiv.	10
Gaia-ESO <sup>14</sup>	2012-2015	South	140 k	$V < 18$	0.1 - 5	indiv.	4
Gaia-ESO <sup>15</sup>	2012-2015	South	10 k	$V < 15$	0.1 - 5	$< 0.1$	4
LAMOST	2012-2018	North	3 M	$V < 18$	10	0.2	4
GALAH	2013-2018	South	1 M	$12 < V < 14$	1	0.1	$< 15$
Gaia	2013-2018	all sky	50 M	$V < 16$	10	0.25	4

function (IMF) according to Scalo (1986) and an exponentially declining smooth gas accretion. Note that Chiappini (2009) also provides a model for the thick disk. However, in case of the chemo-dynamical MCM model the thick disk is deliberately ignored to test if the dynamical processes in the simulation alone are able to produce features like a low-metallicity thick disk component. Ideally, this thesis will provide additional constraints to the MCM model that should indicate whether a chemical thin-disk model in combination with the dynamical evolution of the simulation are sufficient in order to match the thick disk component generally seen in observations.

### 1.3 Spectroscopic surveys of the Milky Way

Over the past decade several large stellar surveys (astrometric, photometric and spectroscopic) have been designed to map the Milky Way to provide essential clues to the assembly and enrichment history of the Galaxy (see Table 1.1). By exploiting their wealth of data the common understanding on the complex kinematical and chemical structure of the Galaxy and its components (i.e., disk, halo and bulge) has already been substantially improved. In this gradual process of gaining knowledge the extensive photometric surveys 2MASS (Skrutskie et al. 2006) and SDSS (Abazajian et al. 2003), ongoing high-resolution surveys, such as, Gaia-ESO (GES, Gilmore et al. (2012)), HERMES/GALAH (Zucker et al. 2012) or APOGEE (Allende Prieto et al. 2008a) as well as the recently completed medium and low-resolution surveys RAVE (Steinmetz et al. 2006) and SEGUE (Yanny et al. 2009), which followed the Geneva-Copenhagen-Survey (Nordström et al. 2004) have and still play an important role.

For the first time kinematically unbiased, homogeneous and statistically significant stellar samples are available with known stellar parameters, chemical abundances and kinematics beyond the Hipparcos volume. All these information are especially crucial to decipher the internal processes working in the Galactic disk that are related to secular evolution. Furthermore they

<sup>12</sup> $l > 20^\circ$

<sup>13</sup> $l < 20^\circ$

<sup>14</sup>The major part of the Gaia-ESO observations are taken with the Giraffe spectrograph (R = 20 000) which is one of the two spectrographs of the FLAMES instrument at VLT's Unit Telescope 2.

<sup>15</sup>A smaller set of high resolution Gaia-ESO observations (R = 47 000) are taken with the UVES spectrograph using FLAMES.

**Table 1.2:** RAVE and SEGUE in numbers

	RAVE	SEGUE
resolution	$R = 7\,500$ (intermediate)	$R = 2\,000$ (low)
sky coverage	wide angular coverage ( $\sim 20\,000 \text{ deg}^2$ )	selected pointings ( $\sim 5\,000 \text{ deg}^2$ )
survey depth	intermediate	deep
wavelength	$8\,410 \text{ \AA} - 8\,795 \text{ \AA}$ (restricted coverage)	$3\,900 \text{ \AA} - 9\,000 \text{ \AA}$ (large coverage)
hemisphere	southern	northern
repeat observations	cadence	some
stellar parameters	$T_{\text{eff}}, \log g, [\text{Fe}/\text{H}]$	$T_{\text{eff}}, \log g, [\text{Fe}/\text{H}]$
$\sigma_{RV}$	$\sim 2 \text{ km s}^{-1}$	$\sim 4 \text{ km s}^{-1}$
chemistry	$[\alpha/\text{Fe}]$ , abundances for 6 elements	$[\alpha/\text{Fe}]$
SNR	$\sim 40$ (average)	$\sim 30$

should allow to particularly shed light on an issue like the thin-thick-disk dichotomy.

In addition, accurate information on stellar radii, surface gravities and masses delivered by the asteroseismic missions Kepler (Gilliland et al. 2010) and CoRoT (Baglin et al. 2006) have a large impact on the determination of precise distances and ages. Complemented with the astrometric measurements from GAIA (Perryman et al. 2001), an ESA satellite launched early 2014 that provides precise positions, distances and velocities for over a billion stars, and the future ground based follow-up projects like 4MOST (de Jong et al. 2012) the prospects to unravel the history of the Milky Way are promising.

Previous to the large observational campaigns, that now easily gather spectra of several hundred thousands of stars by making use of multi-object spectrographs, it was difficult and rather time-consuming to obtain stellar spectroscopic samples suitable for reliable statistical and proper abundance analysis. Instead, the samples usually contained a few hundred (or even fewer) stars, which had mostly undergone pre-selection based on kinematic probability membership (Bensby et al. 2003; Reddy et al. 2006; Fuhrmann 1998, 2008, 2011). However, these pioneering compilations, being often observed in high-resolution, serve now as references to support the calibration and validation of automated analysis pipelines (AAP) that are needed to handle the data flow of today's surveys.

### 1.3.1 A first look on the counterparts RAVE and SEGUE

In the particular case of RAVE and SEGUE the observational programmes are indeed different regarding their concept and general design, but they are comparable with respect to the data products they deliver. This opens a door to address scientific questions which can be equally explored by using data from either survey. It remains to be seen how the results obtained from each survey compare to each other. As demonstrated in the course of this thesis the choice of the stellar subsets as well as the data's quality and the automatic processing are important aspects with view to a meaningful comparison.

Despite of many similarities and their common scientific goals, the surveys yet differ in several technical details, their target selection and main stellar categories (see Table 1.2 for a quick overview and Chapter 2 for a detailed discussion on the survey's specifications). While

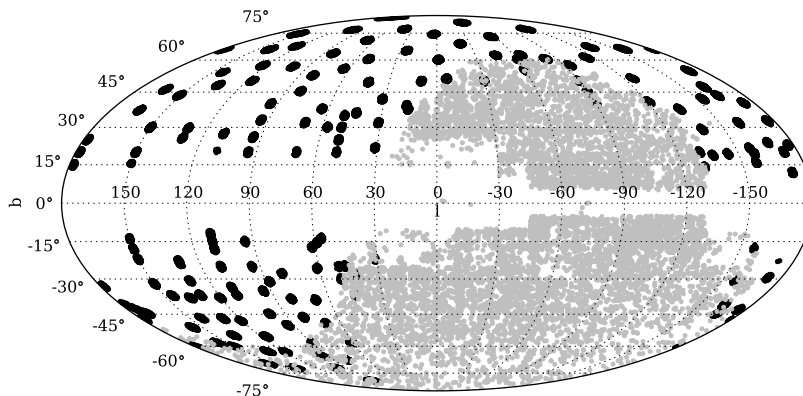


**Figure 1.3:** Comparison of RAVE's and SEGUE's skycoverage. Grey areas mark the RAVE footprint, while the SEGUE pointings are displayed in black.

RAVE aimed for an unbiased sample of stars, SEGUE put its focus on particular subsets of stars with a clear science case in mind. Originally SEGUE was designed to provide radial velocities, stellar parameters and metallicity estimates based on spectra with a large wavelength coverage and thus a sufficient number of spectral features. It turned out that even with its lower resolution  $\alpha$ -enhancement measurements are possible to a certain accuracy. On the other hand, RAVE's primary goal had always been to obtain radial velocities for a large number of stars to enable statistically significant studies of the Milky Way dynamics. Thus, the survey is limited to a very small wavelength region around the Ca II triplet. With the observed spectral measurements in hand the quality was finally proven to be good enough to provide information about stellar atmospheric parameters and the chemistry of the stars too. These developments set them both on the same level of informational content. Only in terms of individual chemical abundance measurements RAVE outplays SEGUE because of its higher spectral resolution which increases the number of reliably measurable elements.

As further layed out in Chapter 2 the survey's reduction and analysis pipelines exploit different methods and techniques to determine the stellar properties for the two independent datasets. This is an important aspect because differing methods give rise to different systematics and biases in different regimes of the parameter space. This can lead to a lack of consistence in the determined stellar parameters, kinematics or chemical quantities that are finally used when studying the properties of the Galaxy.

RAVE and SEGUE cover two contrary parts of the sky. Whereas RAVE scans the southern sky, SEGUE concentrates on the northern celestial hemisphere which puts them into the role of valuable counterparts. Their complementarity provides the unique opportunity to study the Galactic disk's properties in a more complete and global manner by looking through two independent but rather equal eyes into different parts and directions of the Galaxy. Figure 1.3 gives an impression on the skycoverage of both surveys. The RAVE footprint covers almost the complete southern hemisphere as indicated in grey, SEGUE pointings that are sparsely distributed over the northern hemisphere are marked in black. No study so far has taken the advantage to combine the two surveys in the sense of performing a direct comparison of the Galaxy's properties as revealed by different stellar samples selected from the two independent

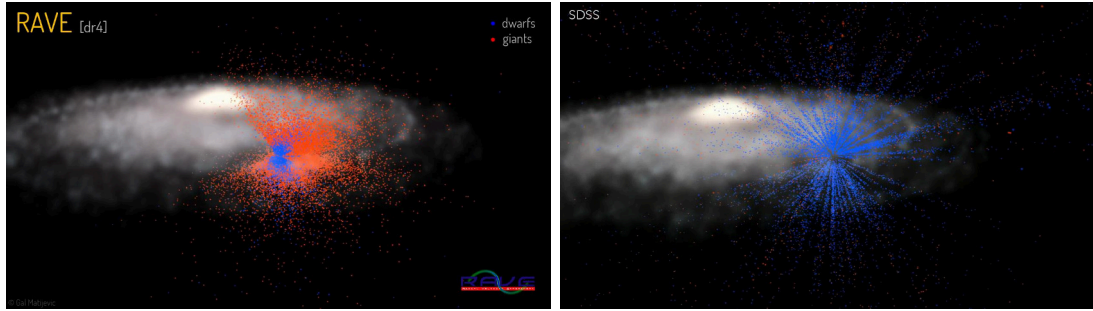


**Figure 1.4:** Illustration of the observed survey volume (spatial distribution) for RAVE (*left panel*) and SEGUE (*right panel*). Approximately at the position of the Sun both surveys are overlaid on a simulation of the Milky Way’s disk. In both cases dwarf stars are indicated in blue, giants in red. Shown are extracted snapshots from movies created by Gal Matijevic.

spectroscopic datasets. But why can such a comparison be realised? Simply, because RAVE is nearly probing the same volume of the Galactic disk with its giant stars, that SEGUE does cover with its dwarfs. Figure 1.4 provides the relevant evidence with giants and dwarf stars marked in red and blue, respectively. RAVE as a magnitude limited survey observes bright targets in the solar neighbourhood with its giant targets located at around 0.5 kpc to 2 kpc and its dwarf targets even closer to the Galactic midplane. SEGUE on the contrary observes mainly dwarf stars up to 3 kpc and probes out into the distant halo up to 100 kpc with its giants reaching much deeper in magnitude. It can be hence assumed that SEGUE dwarfs and RAVE giants probe the same stellar content of the Galactic disk.

## 1.4 Aims of the thesis

In times of rapid progress in the field of Galactic surveys and numerical simulations of galaxies the bottleneck to discovery is no longer the access to data or the lack of computational power, but an issue of analysis and collaboration. More than ever within Galactic science there is a particularly need for a union of modellers and observers to assess the open questions of galaxy formation and evolution in a joint effort. Both fields have reached a level where in terms of covered spatial volume their scales are very similar. Simulations are able to resolve features in the kilo-parsec regime while observational campaigns reach out far beyond the rim of the solar neighbourhood catching objects several kilo-parsecs away from the Sun’s position.

Connecting the two disciplines in a constructive way to enlarge the understanding on the chemo-kinematic properties of the Milky Way disk has been one of the main drivers to realise the present thesis. The presented work intends to make a good case for the further development and exploitation of the rather new and unexplored branch of stellar synthetic surveys, aims to provide new observational constraints on a selection of theoretical models of the Galaxy and for the first time seizes the chance to directly oppose the chemo-kinematic relations of the Milky Way as seen by the independent surveys RAVE and SEGUE.

### Inverse modelling

After the past years’ discoveries no Galactic scientist can deny that the Galaxy presents itself as a complex and sophisticated system, showing non-equilibrium features like moving groups (Dehnen 1998; Bovy & Hogg 2010; Antoja et al. 2012) and velocity gradients (Siebert et al. 2012; Williams et al. 2013) as well as detectable substructure, such as streams in the stellar

halo (e.g. Belokurov et al. 2006). These continuously unveiled findings in combination with the complications and effects introduced by the survey selection functions prevent to easily pin down the exact underlying physical properties and true distribution functions of the Galaxy. One way out is the method of inverse modelling: rather than correcting the observations for their biases before comparing to (physical) models, the selection effects (functions) are introduced to the models in order to make predictions on what an observer would see if the model was true. That way the models can be tested for their validity, the observations can be used to constrain the models and the predictions of various models can be directly compared to each other allowing to evaluate the model's quality that can only be determined in a model-to-model comparison. Also, the effects of the survey's selection biases can be studied in detail, i.e. how biases influence parameter distributions and relations as revealed by the observations.

By following the population synthesis approach the current thesis concentrates on generating two synthetic versions of the SEGUE survey, one based on TRILEGAL, the other on the basis of the chemo-dynamical model by Minchev et al. (2013). These mocks of the SEGUE survey than serve the assembling of synthetic mock equivalents to a particularly selected subsample of SEGUE stars (G-type dwarfs). Analysing the observed stars' properties and comparing those to the mock predictions builds the core of this work's chemo-kinematic analysis of the Milky Way disk. Thereby, the confinement to a single stellar type and thus a limited range in stellar parameter space has the positive side-effect that differences between observed and predicted parameters are minimised which otherwise may arise due to flaws in the automatic reduction pipeline concerning certain types of stars.

## Combining RAVE and SEGUE

At the start of this thesis the spectroscopic surveys RAVE and SEGUE were the only ones providing an extensive sample of disk stars within and beyond the solar neighbourhood with parameters of acceptable uncertainty that include reasonable distances and well determined chemical abundances. As such, they were the first to enable the investigation of a disk volume much larger than covered by the Hipparcos satellite mission and the GCS. With the goal to explicitly extend the knowledge gathered by the latter pioneering projects the two datasets were hence chosen as the main source of stellar samples for the present work's analysis. In this connection the opportunity to be involved in both surveys' collaborations was a great benefit. It allowed to actively getting in touch with the persons in charge for the automatic processing steps and the data products, thereby learning on how to properly deal with the delivered parameters and their drawbacks and having access to additional data products that are not yet publicly available.<sup>16</sup>

Because SEGUE's potential to provide constraints to theoretical models, especially helping to calibrate population synthesis codes like TRILEGAL or GALAXIA, has been relatively unexplored in the past this work is in uncharted waters. Also, joining SEGUE and RAVE in the way described in Section 1.3.1 is a new and worthwhile effort. Equally analysing and comparing stellar samples from the two different surveys allows for a sanity check of their automatic pipelines and the quality of the determined parameter and enables to validate that generic features and correlations in the Galactic disk are present no matter of the dataset under investigation. Obvious biases in either of the surveys that could result from restrictions and limits given by the processing tools or the selection algorithms are given a chance to be detected too.

---

<sup>16</sup>The organisation of a workshop called "Galactic Archaeology with SEGUE", taking place at the Leibniz Institute for Astrophysics Potsdam in July 2011, gave an additional opportunity to get in contact with the SEGUE man in charge.

## Structure of the thesis

After a general introduction to the field of Galactic Science with its observational and theoretical aspects and subfields in this chapter, Chapter 2 gives a more detailed view into the two major projects RAVE and SEGUE, which are the rich source of observational samples for this thesis' research. The survey's specifications and their automatic pipelines for stellar parameters and chemistry are discussed noting the expected observational uncertainties. Chapter 3 highlights the assemblance, characteristics and calibration of the thesis' main stellar sample, a compilation of SEGUE G-dwarfs used as the observational reference to constrain the studied models. Chapter 4 then describes the different procedures and codes needed to obtain spectro-photometric distances, proper motions and orbital parameters for either the observed or the mock stars under investigation in this work's analysis. As such, Chapter 2 to 4 deal with the preparatory work, while the analysis and results are presented in Chapter 5 through 8.

Among the latter, Chapter 5 puts the focus solely on the observed SEGUE G-dwarf sample, carefully exploring its selection biases and discussing several ways to correct them. The selection function examination is then followed by a chemo-kinematic analysis that includes a first observation versus model comparison shedding light on how the selection effect corrected SEGUE sample stands up against the predictions of the chemo-dynamical MCM model. Since this approach experiences clear limits concerning the empirical corrections, the following two chapters concentrate on the synthetic realisations of the models. The inverse modelling comes first into play in Chapter 6 where it is applied to test TRILEGAL's capabilities. The next chapter then lays out how the  $N$ -body distribution of the MCM model is transformed into an observable populations of stars using the code GALAXIA. This line of action allows to repeat the comparison performed in Chapter 5, clarifying which of the observed caveats between the MCM model and the observations may results from the model itself or problems with the bias corrections.

As a last step Chapter 8 aims to approach the chemo-kinematic nature of the Milky Way by comparing the properties found by SEGUE with those revealed by RAVE. Thereby, any of the problematic selection effect corrections, in particular the compensation for the actually covered disk volume of the surveys, can be neglected by assuming that RAVE and SEGUE suffer from similar biases due to their cone shaped observing volume. Finally, Chapter 9 summarises the results, puts them in the general context and concludes with an outlook on further work.

By that structure this dissertation presents a fairly unique approach to study the chemo-kinematic and -dynamic structure and evolution of the Galactic disk, involving both the status quo in observational and theoretical Galactic science.

This chapter focuses on the two spectroscopic Galactic surveys, RAVE and SEGUE, whose observations provide the ground base for the observational part of the analysis performed within the framework of this PhD thesis. The question why those two surveys are suited to study the chemo-kinematic properties of the Milky Way's disk have already been answered in the introduction, along with a brief summary on their comparability and complementarity.

Here, the projects itself are presented in more detail including a discussion on their similarities and differences regarding specifications, design, target selection approaches as well as their automatic parameter pipelines as those are needed information for the forthcoming chapters.

## 2.1 RAVE

The Radial Velocity Experiment (Steinmetz et al. 2006, RAVE) is a large spectroscopic survey of the southern hemisphere which has aimed to observe up to half a million stars. The project started in April 2003 and took its last observation in April 2013. By then 574 630 spectra had been taken on 483 330 individual objects. So far, the collected data is presented in five catalogue releases: DR1 in 2006, DR2 in 2008, DR3 in 2011, DR4 in 2013 and DR5 in 2017 (Steinmetz et al. 2006, Zwitter et al. 2008, Siebert et al. 2011, Kordopatis et al. 2013, Kunder et al. 2017). All of those contain general descriptions of the project. All information for the RAVE stars analysed in this thesis are taken from RAVE DR4, a dataset that was available since March 2014 and that includes spectra for 482 430 stars, together with information about stellar parameters, distances, proper motions, photometry and chemical abundances for most of the observed objects.

The observations have been performed at the UK Schmidt telescope at the Australian Astronomical Observatory (AAO) in Siding Spring, Australia, using the multi-object spectrograph 6dF (Watson et al. 2000) where in total three field plates, each with 150 robotically positioned fibres are used. The spectra have a medium resolution of  $R = \lambda/\Delta\lambda = 7\,500$  and cover the wavelength region around the Ca-triplet from  $8\,410\text{ \AA}$  to  $8\,795\text{ \AA}$ . This allows a reliable determination of the line-of-sight velocity via the Doppler effect using the Ca II lines that are still strong enough even for observations with low SNR. With regard to the Gaia space mission (Prusti 2012) the RAVE spectral coverage matches the wavelength region of the Gaia satellite's radial velocity spectrometer. The survey provides spectra not only suitable for accurate radial velocity mea-

measurements with typical uncertainties of a few  $\text{km s}^{-1}$ , various other properties can be derived as well. This includes the atmospheric stellar parameters effective temperature,  $T_{\text{eff}}$ , surface gravity,  $\log g$  and an overall metallicity,  $[\text{M}/\text{H}]$ , complemented by individual chemical abundances for a limited number of elements that are obtained by a separate chemical pipeline (Boeche et al. 2011). The determination of the main stellar parameters based on different analysis techniques are extensively described in the various data releases. However, Section 2.1.2 and 2.1.3 give a short introduction to the latest stellar parameter pipelines (DR4) and the chemical abundance pipeline.

### 2.1.1 Target selection

In order to avoid any kinematic or chemical biases the RAVE survey was designed to have a selection function as simple as possible. RAVE targets are randomly selected on the southern hemisphere in the magnitude interval  $9 \leq I \leq 12$ . A mild colour cut ( $J - K_s > 0.5$  with  $J$  and  $K_s$  being 2MASS magnitudes) is only introduced for stars near the Galactic plane and bulge. SEGUE on the contrary exhibits a rather complex selection function (see Chapter 5) suffering from several target selection biases e.g. due to specific colour cuts. Further details on the RAVE selection function and the completeness of the survey can be found in Appendix A.1.

RAVE does not select particular stellar types. As a survey with a limiting magnitude of  $I \approx 12$  it samples the brightest stars in the stellar disk, probing dwarfs at distances of hundreds of parsecs and giants out to a few kilo parsecs. Since RAVE operates in the wavelength region around the Ca-Triplet the selection of targets in the  $I$ -band has been the preferred choice. However, back in 2003, there was no suitable photometric infrared catalogue available for the southern hemisphere. This led to an initial input catalogue based on  $I$ -band magnitudes derived from the Tycho-2 photometry (Høg et al. 2000) complemented by photographic  $I$  magnitudes from the SuperCOSMOS Sky Survey (Hambly et al. 2001) to compensate the incompleteness of Tycho-2 at the faint end of the magnitude range.

Initially, the observing fields have been selected excluding regions with a Galactic latitude of  $|b| < 25^\circ$ . This was meant as a precaution to minimise the effects of dust and avoid superposition of target stars when using the 6dF wide fibres with an angular diameter of  $6.7''$ , being especially problematic in crowded regions. Later, RAVE was extended to lower Galactic latitudes ( $5^\circ < |b| < 25^\circ$ ) towards the Galactic anti-centre direction in order to be able to also observe the outer disk. The introduction of a colour criterion  $J - K_s \geq 0.5$  for targets in those added regions assured the selection of cool giant stars (mostly K-giants), which at the faint magnitude limit of the survey, are bright enough to probe far out into the stellar disk.

With the availability of  $I$ -band magnitudes from the comprehensive DEep Near Infrared Survey (DENIS) (Epchtein et al. 1997) in 2005 a new input catalogue was compiled. This catalogue contains DENIS objects in the magnitude range  $9 < I < 12$  that have a successful cross-match in 2MASS. Additionally, to get more bright objects north of the celestial equator potential targets were selected by constructing DENIS  $I$ -band magnitudes from 2MASS  $J$  and  $K_s$  (Skrutskie et al. 2006). It is clear that the various input sources generate some inhomogeneity in the RAVE dataset. An extensive description of the various RAVE input catalogues can be found in the DR4 paper (Kordopatis et al. 2013).

### 2.1.2 The stellar parameter pipelines in RAVE

In previous RAVE data releases (DR1-DR3) the stellar atmospheric parameters are estimated based on a  $\chi^2$  optimisation technique and the library of synthetic template spectra from Munari et al. (2005). To find the most suitable combination of effective temperature, surface gravity,

metallicity and  $\alpha$ -enhancement describing the observed object, a synthetic model spectrum is constructed that best matches the properties of the observed spectrum. Thereby the model is a weighted sum of several template spectra with known parameters (Zwitter et al. 2008, Siebert et al. 2011).

Yet, automated pipelines that rely on the minimisation approach have the drawback to sometimes falsely converge in secondary minima of the distance function. The distance function represents the difference between the observed and the set of synthetic spectra. Careful analysis and investigations have revealed that astrophysical parameters determined by the method described above are likely suffering from biases and interdependencies between the stellar parameters. Hence for DR4 a new RAVE pipeline has been established, an updated version of the Kordopatis et al. (2011) pipeline, which combines two different methods to derive stellar parameters from a spectrum: DEGAS (DEcision tree alGorithm for ASTrophysics) and MATISSE (MATrix Inversion for Spectral SynthEsis; Recio-Blanco et al. 2006). The first one is a decision-tree method which uses a discrete grid of template spectra to find the best matching model. The set of parameters DEGAS has converged on is then used as starting values for MATISSE, a projection algorithm that is able to interpolate between spectral grid points and as such better suited for spectra with higher SNR which provide more spectral information. In comparison to other algorithms DEGAS manages to produce the most accurate results if the SNR is low and the distance function shows many secondary minima. Hence MATISSE is only run as a second step to get more precise parameters if the SNR is sufficiently high.

The new pipeline also takes the photometric information from 2MASS into account by introducing a photometric temperature range prior. Kordopatis et al. (2013) demonstrate that the results are thus more robust and less affected by biases as a result of spectral degeneracies. In terms of calibration the new DR4 catalogue benefits from a variety of new calibration datasets<sup>1</sup> which include RAVE spectra with high resolution observations (e.g. Ruchti et al. 2011) and stars from open and globular clusters. In total, 809 stars were selected as reference. They mainly served to calibrate the RAVE metallicity,  $[M/H]$ . A detailed description of the calibration and validation of the DR4 pipeline is given in Kordopatis et al. (2013).

### Uncertainties of the DR4 pipeline

The total parameter uncertainties of the pipeline can be computed for each individual object in every estimated parameter as the quadratic sum of the internal and external error. Whereas the internal errors represent the pipeline's ability to deal with the spectral degeneracies and the signal-to-noise, the external uncertainties give evidence how well the true spectrum is matched by the synthetic template.

The internal uncertainties are determined by computing the stellar properties of a set of artificially created spectra with known parameters using the Besançon population synthesis model (Robin et al. 2003). Internal errors are listed for different stellar types and SNR values in Table 1 and 2 of Kordopatis et al. (2013). They are available for each individual object from the database. The external uncertainties are estimated by comparison with the high resolution calibration datasets. External errors for the main stellar parameters are listed in Table 5 of the latter reference, separated into dwarfs and giants for various temperature and metallicity ranges.

---

<sup>1</sup>For DR4 calibration datasets of observed spectra have been obtained using (1) the heterogeneous PASTEL catalogue (<http://pastel.obs.u-bordeaux1.fr/>) which contains information on stars with atmospheric parameter determinations available from high-resolution spectroscopy, (2) the high-resolution thick disk stars by Ruchti et al. (2011) and a sample of RAVE-like spectra a stars belonging to the open clusters M67 and IC4651 observed with the 2.3m telescope at Siding Spring Observatory (SSO). For more information on the datasets see Section 4.1 or Table 3 in Kordopatis et al. (2013).

**Table 2.1:** External uncertainties for RAVE giant stars in DR4.

Giants				
Parameter range	$N$	$\sigma(T_{\text{eff}})$	$\sigma(\log g)$	$\sigma([\text{M}/\text{H}])$
$T_{\text{eff}} > 6\,000$	8	263	0.423	0.300
$T_{\text{eff}} \leq 6\,000, [\text{M}/\text{H}] < -0.5$	273	191	0.725	0.217
$T_{\text{eff}} \leq 6\,000, [\text{M}/\text{H}] \geq -0.5$	136	89	0.605	0.144

A subset of this table, relevant to the sample of RAVE giants adopted in Chapter 8, is shown in this work’s Table 2.1.

### 2.1.3 The RAVE chemical pipeline

Although RAVE was designed as a radial velocity survey the successful performance of the RAVE chemical pipeline demonstrates that a resolution of  $R \sim 7\,500$  provides enough visible lines for a more sophisticated chemical analysis, even for stars with SNR of 20. For DR4 an updated and improved version of the original RAVE chemical pipeline (Boeche et al. 2011) has been employed. This new version uses as input the normalised, RV-corrected and wavelength-calibrated spectra together with the stellar parameter estimates from the DR4 stellar parameter pipeline. In what follows the general features and improvements are outlined.

The pipeline works based on an equivalent width (EW) library that comprises the EW of all lines visible in the RAVE wavelength range (line list contains 604 atomic and molecular lines). The library contains information about the EWs for a set of grid points that cover the parameter space in the range  $[4\,000, 7\,000]$  K in  $T_{\text{eff}}$ ,  $[0, 5.0]$  dex in  $\log g$  and  $[-2.5, +0.5]$  dex in  $[\text{M}/\text{H}]$  and five levels of abundance in the range  $[-0.4, 0.4]$  dex relative to the metallicity in steps of 0.2 dex. This allows to reconstruct a curve of growth (COG) for every line by fitting the five abundance points with a high order polynomial.

Individual lines are reconstructed assuming a Voigt profile and summed up to create a model spectrum on-the-fly adopting the stellar parameters from DR4. Finally, the best-fitting model is found by minimising the  $\chi^2$  between the models and the observed spectrum. A new feature of the improved pipeline is the consideration of line blending. This reduces the overestimation of abundances especially towards high metallicity. Briefly, the method adopted is the following: if a line  $l_0$  with  $\text{EW}_0$  is blended with some lines  $l_i$  with  $\text{EW}_i$  the ratio  $\text{EW}_r = \text{EW}_0 / \sum \text{EW}_i$  is calculated with  $\text{EW}_0$  and  $\text{EW}_i$  assuming isolated lines. After synthesising the blend composed by  $l_0$  and  $l_i$ , and from this measuring  $\text{EW}_{\text{tot}}$ , a corrected EW of the line  $l_0$  is calculated as  $\text{EW}_{0,\text{corr}} = \text{EW}_r \cdot \text{EW}_{\text{tot}}$ . Generally, lines are considered as blended if they are closer than  $0.2 \text{ \AA}$ . Even with these precautions blending issues can still occur in very metal rich stars, a common caveat in low and medium resolution surveys. A more detailed description on the line blending issue is given in Kordopatis et al. (2013).

The chemical pipeline is able to measure elemental abundances for six elements including iron (Fe), nickel (Ni) and the  $\alpha$ -elements magnesium (Mg), silicon (Si), aluminium (Al) and titanium (Ti). Besides an estimate for  $[\text{Fe}/\text{H}]$  the chemical pipeline also provides a value for the  $\alpha$ -abundance of the star that is computed as

$$[\alpha/\text{Fe}] = \frac{[\text{Mg}/\text{H}] + [\text{Si}/\text{H}]}{2} - [\text{Fe}/\text{H}] \quad (2.1)$$

The reliability of the abundance measurements for the individual elements depends on the SNR of the spectrum and the type of star. Since the lines of dwarf stars are generally weaker, some elements, e.g. Ti, can only be estimated with confidence for giants. Internal uncertainties are estimated based on a sample of synthetic spectra with known stellar parameters and metallicities. The precision of the abundances is evaluated at different levels of SNR. The uncertainties are influenced by the element itself as there are differences in the number of lines and the intensity of the lines for the different elements. External errors of the chemical pipeline are determined by comparison with high resolution reference spectra. The estimated uncertainties depend on each element ranging from 0.17 dex for Mg and Al to 0.3 dex for Ti and Ni. The uncertainties for  $[\text{Fe}/\text{H}]$  and  $[\alpha/\text{Fe}]$  are approximately 0.23 dex and 0.15 dex, respectively. Detailed information about the external errors are listed in Table 1 of Boeche et al. (2011).

## 2.2 SEGUE

*The Sloan Extension for Galactic Understanding and Exploration* (SEGUE, Yanny et al. 2009) is a spectroscopic sub-survey of the *Sloan Digital Sky Survey* (SDSS, York et al. 2000) and one of the three main projects in SDSS-II. The survey shared the observational capacities of the wide-field 2.5m telescope at Apache Point Observatory in Sunspot, New Mexico (Gunn et al. 2006), with the SDSS Legacy survey and the Supernova Survey and performed its observations in a period from 2005 to 2008. The main goal of the survey is to investigate the kinematic and chemical substructure of the Galactic Halo and disk leading to a better understanding of the assembly and enrichment history of the Galaxy. For that purpose SEGUE-1 (SDSS-II) has obtained low-resolution ( $R \sim 2\,000$ ) spectra of around 240 000 objects in a wavelength range from 3 900 Å to 9 000 Å, covering an area of approximately 3 500 deg<sup>2</sup> of the northern hemisphere. In SDSS-III the survey has been continued (SEGUE-2) obtaining yet another 120 000 spectra. Contrary to SEGUE-1 which had a focus on the high-latitude thick disk and halo, SEGUE-2 spectra were almost exclusively taken to explore the outer and more distant halo. The processed dataset from SEGUE-1 and SEGUE-2 were made publicly available as part of the SDSS Data Releases 7 (DR7, Abazajian et al. 2009) and 8 (Aihara et al. 2011a), respectively.

Two fibre-fed spectrographs, providing 640 fibres in total, were used to sample the stellar spheroid in 200 pencil beams sparsely spaced around the sky at intervals of 10 to 15 degrees. Each pencil beam has a circular area of 7 deg<sup>2</sup>. A certain amount (7% to 12%) of fibres was reserved for sky signal and further calibration purposes. Each of the line-of-sights was observed twice, performing one exposure for bright ( $14.5 < r_0 < 17.8$ ) and one for faint ( $17.8 < r_0 < 20.2$ ) objects going as deep as 20.3 mag in the SDSS  $g$ -band. Concerning the saturation the SDSS spectrograph reaches its limits at  $g \approx 14$  mag for an exposure of 300 s.

Although SEGUE takes low resolution spectra, it is possible to measure radial velocities and astrophysical parameters, such as effective temperature, surface gravity and metallicity. The radial velocities with typical uncertainties around 4 km/s are measured by cross-correlating the SEGUE spectra against a set of selected templates from the ELODIE high-resolution spectroscopic survey (Moultaka et al. 2004). The fundamental stellar parameters are determined by the SEGUE Stellar Parameter Pipeline (Lee et al. 2008a,b, SSPP), which uses multiple techniques to determine each of the astrophysical parameters and will be described in more detail in Section 2.2.2.

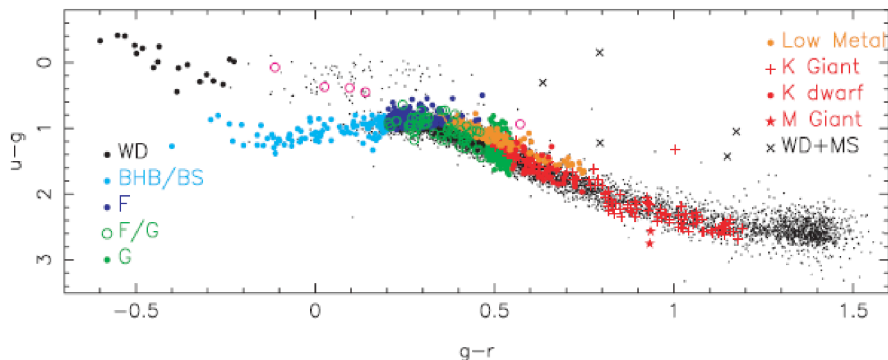


**Figure 2.1:** Location of different SEGUE target selection categories in the  $u - g$  versus  $g - r$ -diagram. Figure courtesy of Yanny et al. (2009).

### 2.2.1 Target selection

SEGUE was designed to study and characterise the largest structures in the Milky Way stellar disk and halo with a particular focus on the chemo-dynamical formation history of the Galaxy. In order to achieve these general goals the target selection strategy included the sampling of near-by objects, mainly dwarfs within the disk, as well as bright giants far out in the stellar halo. Different stellar types were targeted at a variety of colours and apparent magnitudes which cover a distance range from a few (e.g. white, M and K dwarfs) to hundreds of kpc (blue horizontal branch stars, red K-giants). Thus most of the fibres on each line-of-sight were devoted to objects that probe the spheroid substructure and global properties of the thin and thick disk components. As a result the selection function of the survey presents itself as rather complex. More details on the SEGUE selection function are discussed in Chapter 5, especially focussing on the stellar type of G-stars, which is the only SEGUE target category that is subject in this work.

To be able to select spectroscopic targets in a larger range of sky directions outside the available SDSS imaging footprint (mainly Northern Galactic Cap with  $b > 35^\circ$ ), SEGUE has performed an additional imaging survey of  $3500 \text{ deg}^2$ . The SEGUE *ugriz* photometry augments the imaging data from the SDSS and Legacy Survey and adds data to the overall footprint, especially at low latitudes and the Southern Galactic Cap. Building-up on this the target selection for the spectroscopic observations for SEGUE-1 is based on the SEGUE *ugriz* photometry (York et al. 2000). SEGUE-2 targets are later selected based on SDSS DR7 *ugriz* photometry. Since then the overall SDSS photometry has undergone several re-calibrations leading to slight differences between the photometry used in this thesis (from DR9) and the SEGUE target photometry.

SEGUE uses various photometric and proper motion cuts to select different spectral types of stars. Targets of a certain spectral type, that are finally assigned to a fibre, are randomly selected from the overall sample of possible (photometric) candidates that particularly fulfil the target selection criteria for this stellar category. Figure 2.1 shows the SEGUE target selection categories in the colour-colour diagram. G-type stars are marked in green.

In the context of SEGUE stellar categories the G-type stars play an important role and are the most extensive targeted sub-sample. Among the long living objects on the main-sequence they belong to the most luminous ones. They carry precise information on the Milky Way disk and its evolution since their lifetime is assumed to be longer than the age of the disk. Due to their richness in metal-lines they allow good velocity and abundance determinations. G-stars are located at intermediate distances (0.5 kpc to 4 kpc) sampling the entire SEGUE magnitude range.

Approximately 375 fibres have been allocated to G-type stars for each line-of-sight, creating a large and unbiased sample of stars that effectively probes the detailed structure of the Galactic components.

### 2.2.2 The SEGUE Stellar Parameter Pipeline (SSPP)

The SEGUE Stellar Parameter Pipeline uses multiple techniques for different ranges of temperature, surface gravity and metallicity to estimate the stellar astrophysical parameters. Every method is valid within a specific range of  $g - r$  and SNR. Following this multiple approach the SSPP enables one to obtain stellar parameters for stars from a variety of stellar types and evolutionary state that cover a wide range in  $T_{\text{eff}}$ ,  $\log g$ ,  $[\text{Fe}/\text{H}]$ , colour and SNR. Final values for each astrophysical parameter are computed as an average based on all valid estimators for each particular star. The DR8 version of the SSPP provided 11 estimators for  $T_{\text{eff}}$ , 10 for  $\log g$  and 12 for  $[\text{Fe}/\text{H}]$ . A summary of them together with their valid ranges in colour and SNR can be found in Table 5 of Lee et al. (2008a). In the revised SSPP version for DR9 some of those techniques are no longer used. More information on the exclusion of several estimators, the calibration, specific improvements and modifications being applied to the SSPP in preparation for the ninth data release are either outlined below or discussed in Appendix B.1. How these changes affect the stellar parameter estimates obtained from different versions of the pipeline is illustrated in Section 3.3. There the stellar parameters from DR8 and DR9 are directly compared for the set of G-dwarf stars assembled for this thesis.

Generally, the set of estimating techniques can be divided into the following types: Firstly, methods that use atmospheric models (e.g. from Castelli & Kurucz 2003) and template spectra in combination with spectral fitting techniques like the  $\chi^2$  minimisation. These try to find the most likely set of stellar parameters by fitting the observed spectrum with synthetic templates to determine the best matching model spectrum with known properties (e.g. Allende Prieto et al. 2006). Examples are the SSPP estimators `ki13`, `k24`, `NGS1`, `NGS2`, `WBG`, `CaI1` and `CaIIK1`. Secondly, two methods (`ANNSR` or `ANNRR`) follow the approach of artificial neural networks (see e.g. Re Fiorentin et al. 2007) and thirdly, there are a couple of estimators classified as line index calculation methods (`HA24`, `HD24`, `CaIIK2` and `CaIIK3`). They deliver parameter estimates based on equivalent width measurements of atomic and molecular lines. An overview about the individual SSPP estimators can be found in Lee et al. (2008a), which together with Lee et al. 2008b, Allende Prieto et al. 2008b and Smolinski et al. 2011 provides detailed information on the SSPP.

#### Validation of the SSPP

Pipelines such as the SSPP that aim to estimate atmospheric stellar parameters for a variety of stellar categories (including dwarfs and giant stars) need to be able to cover a large range in  $T_{\text{eff}}$ ,  $\log g$  and several magnitudes in metallicity. To check whether the SSPP is adversely affected by any systematic offsets and to obtain a better handling on the uncertainties of the determined parameters validation of the pipeline is essential. In case of the SSPP this has been done with a set of open and globular clusters (Lee et al. 2008b) as well as a set of SEGUE field stars with high-resolution observations.

In the context of refining the SSPP for DR9 the sample of calibration field stars covered 126 SEGUE stars that were re-observed with several high-resolution spectrographs on larger telescopes (HDS on Subaru, HRS at HET, HIRES and ESI at KeckI and II and UVES at VLT). Those high-resolution spectra were analysed in a uniform way to obtain consistent stellar parameter estimates that can serve as calibration reference. In so doing, the SSPP estimates could be

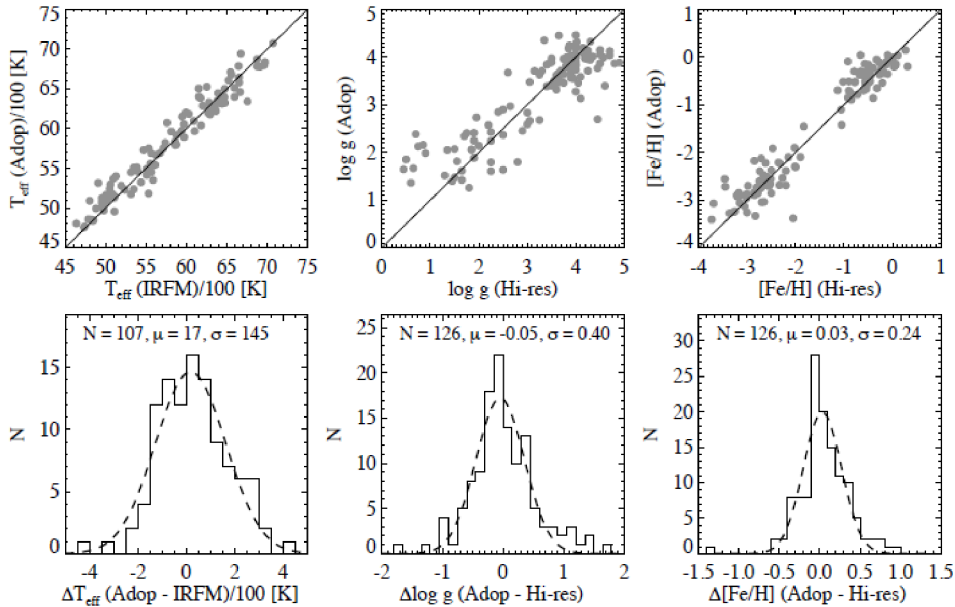


**Figure 2.2:** Comparison of the re-calibrated SSPP  $T_{\text{eff}}$  (*left panels*),  $\log g$  (*middle panels*) and  $[\text{Fe}/\text{H}]$  (*right panels*) with the temperature, surface gravity and metallicity obtained from high-resolution spectra of 126 stars. The high-resolution temperature estimate is directly calculated using only the IRFM.  $\mu$  and  $\sigma$  are the mean and standard deviation from a Gaussian fit to the sample. The sigma represent very conservative upper limits for the external errors of the pipeline. Figure taken from Ahn et al. (2012).

refined and re-calibrated through a high-resolution comparison. To re-calibrate each single SSPP method the offsets between the SSPP results and high-resolution parameters were fit and the resulting relations used to correct the individual estimators. Figure 2.2 compares the re-calibrated SSPP parameters with those from the high-resolution analysis. It should be noted that the surface gravity (middle panel) for very cool giants is overestimated by more than 1.0 dex. Moreover, the  $\log g$  estimates for dwarf stars with  $\log g > 4.0$  dex tend to be underestimated, assuming that the high resolution values represent a solid basis. It seems that a simple linear relation as function of surface gravity is not sufficient to reproduce the gravity estimates comparably well in the low and high  $\log g$  regime. How this particular underestimation of  $\log g$  for dwarf stars affects this thesis' sample of SEGUE G-dwarf stars is discussed in Section 3.3.1. More details on the cluster and field star high-resolution analysis and the calibration of the SSPP estimators are given Ahn et al. (2012).

### Optimal SSPP estimators for G-dwarfs

After the exclusion and adjustment of several estimators (for details see Appendix B.1 and B.2) and the overall calibration with high-resolution data the SSPP used for DR9 delivers already improved adopted values for each stellar astrophysical parameter in contrast to the parameter set published with DR8. Still, among the remaining SSPP estimators some of them can be less suited for particular stellar types. The detailed examination by Schlesinger et al. (2012), that focussed on the SEGUE G- and K-dwarf stars, finds that certain techniques are not appropriate

and as accurate for cool dwarfs than others. This mainly concerns surface gravity and metallicity estimators. The corresponding sets of SSPP techniques considered to be appropriate are:

$$\begin{aligned} \log g : & \quad \text{NGS1, NGS2, ANNSR, ANNRR, CaI1, KI13} \\ [\text{Fe}/\text{H}] : & \quad \text{NGS1, NGS2, CaIIK1} \end{aligned}$$

It is hence possible to optimise the DR9 stellar parameters even further, specifically for cool dwarf stars. By calculating own average parameter estimates according to the above subsets, this has been conducted for the G-dwarfs analysed in this work. The exact computation is explained in detail in Section 3.2.1.

### $[\alpha/\text{Fe}]$ -abundances of SEGUE stars

With respect to chemistry, the pipeline is able to measure  $[\alpha/\text{Fe}]$  ratios (Lee et al. 2011a) of SDSS spectra with  $\text{SNR} > 20$  for stars with atmospheric parameters in the range  $T_{\text{eff}} = [4\,500, 7\,000]$  K,  $\log g = [1.5, 5.0]$  dex and  $[\text{Fe}/\text{H}] = [-1.4, +0.3]$  dex over the range  $[\alpha/\text{Fe}] = [-0.1, +0.6]$  dex. The low spectral resolution prohibits to determine abundances for individual  $\alpha$  elements, instead an average  $[\alpha/\text{Fe}]$  ratio is obtained by quantifying the overall behaviour of  $\alpha$ -element sensitive features in the spectrum in the specific wavelength region around  $4\,500 \text{ \AA}$  to  $5\,500 \text{ \AA}$ . The region contains a large set of metallic lines, mainly Mg I, Ti I and Ti II lines which are the main contributors to the SEGUE  $[\alpha/\text{Fe}]$  ratio. More information about the  $[\alpha/\text{Fe}]$  determination process can be found in Lee et al. (2011a).

### Uncertainties of the SSPP

The multiple approach design of the SSPP allows to empirically determine internal uncertainties for each derived parameter based on the range of values that are reported by the different methods. In averaging several estimates the internal error is computed as the standard error of the mean according to  $\sigma/\sqrt{N}$ . This leads to an internal scatter estimate that significantly underestimates the actual errors by a factor of 2 to 3 (Allende Prieto et al. 2008b). The underestimated uncertainties may be due to those methods not being completely independent, which happens in case of estimators that rely on the same information obtained from a spectrum. Moreover, many methods share the same spectroscopic indicators (lines or colour indices) or models (e.g. Kurucz's model atmospheres).

Lee et al. (2008a) lists typical internal uncertainties in temperature, surface gravity and metallicity to be around 70 K, 0.18 dex and 0.07 dex, respectively. Combining those with external uncertainties from the comparison with high-resolution (141 K, 0.23 dex and 0.23 dex) the typical total uncertainties of the SSPP can be estimated as  $\sigma(T_{\text{eff}}) \approx 160$  K,  $\sigma(\log g) \approx 0.3$  dex and  $\sigma([\text{Fe}/\text{H}]) \approx 0.25$  dex over the temperature range  $4\,500 \text{ K} \leq T_{\text{eff}} \leq 7\,500 \text{ K}$ .

In the the process of re-calibrating and improving the SSPP for DR9 the external uncertainties have been revised too. Figure 2.2 shows that typical systematic uncertainties are of the order 150 K in  $T_{\text{eff}}$ , 0.4 dex in  $\log g$  and 0.25 dex in  $[\text{Fe}/\text{H}]$ . Because the SSPP errors vary significantly over parameter space, the stars are split into subsamples covering different regions of the temperature, surface gravity and metallicity space. Table 2.2 shows those error estimates that are particularly important for this thesis's stellar SEGUE sample. Total uncertainties for the stellar parameters of the SEGUE G-dwarfs are adopted in a similar way as for the RAVE stars. Internal and external errors are combined in quadrature. Based on Table 2.2 the external error is assumed to be a fixed value of 180 K in  $T_{\text{eff}}$ , 0.3 dex in  $\log g$  and 0.2 dex in  $[\text{Fe}/\text{H}]$  for all SEGUE stars in the sample. The temperature uncertainty is chosen slightly larger than the

**Table 2.2:** External uncertainty estimates for SEGUE dwarf stars as determined for DR9 based on the comparison with high-resolution data.

	Temperature Range		Gravity Range		Metallicity Range	
	5 200 K to 6 200 K		> 3.5		> -1.5	
	$\mu$	$\sigma$	$\mu$	$\sigma$	$\mu$	$\sigma$
	[K]	[K]	[dex]	[dex]	[dex]	[dex]
$T_{\text{eff}}$	19	153	-2	132	-3	129
$\log g$	-0.095	0.273	-0.115	0.261	-0.071	0.290
[Fe/H]	-0.017	0.195	0.050	0.236	0.032	0.236

values in Table 2.2. The main reason for this being that the IRMF temperature was adopted and used to calibrate individual estimates of  $T_{\text{eff}}$ . With a typical uncertainty of 70 K to 100 K for the IRMF estimator and the scatter from the high-resolution comparison of around 150 K the error will be roughly around 180 K (private communication with Young Sun Lee). The assumed uncertainty in  $[\alpha/\text{Fe}]$  is 0.1 dex, a precision that can be achieved from spectra with  $\text{SNR} > 20$ .

This chapter focuses on describing the needed steps in order to compile a sample of SEGUE G-dwarf stars with good quality parameters. These main-sequence late-type stars are particularly useful to study the Galactic evolution because they are both numerous and long-lived with atmospheres reflecting their initial chemical composition. Hence, they serve as snapshots of the various stellar generations that formed at different times and places in the history of the Galaxy and they are suited to obtain large and homogeneous samples of objects whose chemical and kinematic properties can well be studied from a statistical point of view over a large volume in the disk. That is why the current thesis focuses on the compilation and investigation of a sample of local SEGUE G-dwarfs in the disk.

### 3.1 Data assembly

Every data product that has been obtained in any of the various SDSS projects is released to the scientific community and the general public through a website called the SDSS SkyServer<sup>1</sup>. The SkyServer holds the entire database of the Sloan Digital Sky Survey free of charge and provides a variety of tools to view and download the SDSS data. Among those tools is the CASJobs<sup>2</sup> which is an sophisticated online web environment that allows easy access to the SDSS Catalogue Archive Server (CAS). This searchable database can be queried through SQL which is the Standard Query Language usually used to obtain data from large databases. With respect to the SEGUE dataset under investigation for this thesis the CAS has been the main source of information.

In terms of SEGUE so far the official data releases contain information about photometry, astrometry (including proper motions), radial velocities, stellar parameters and with a general metallicity estimate also partial information about the chemistry. However, in order to perform a detailed chemo-dynamical analysis the knowledge about  $[\alpha/\text{Fe}]$  abundances, often used as an age proxy, is essential. This is also the reason why in the long term  $[\alpha/\text{Fe}]$  abundances will be published in a value added catalogue for the entire community, adding to the SSPP parameter already available through the CAS. Currently  $[\alpha/\text{Fe}]$  values for SEGUE objects are only accessible

---

<sup>1</sup><http://skyserver.sdss.org/dr12/en/home.aspx>

<sup>2</sup><http://skyserver.sdss.org/casjobs/default.aspx>

to members of the SEGUE collaboration.

The analysis on SEGUE stars presented in this thesis is entirely based on parameters that have been published with the SDSS DR9. This includes the main stellar parameters, the photometry, radial velocities and proper motions being all obtained from the DR9 context of the CAS. The  $[\alpha/\text{Fe}]$  values are extracted from the SEGUE RERUN 122 file.<sup>3</sup> In case of the previous data release (DR8) the results of the final SSPP run based on the DR8 version of the pipeline can be obtained from the RERUN 116 file. Note, that the latter is used when comparing the stellar parameters and how they have changed from DR8 to DR9 for the same stars (see Section 3.3).

In the framework of this work the data mentioned above is complemented with additional information on distances. These are used together with the proper motions to obtain information on the stellar motions and orbital properties. With the knowledge about the stellar motions an extensive chemo-dynamical analysis is possible. A description of the employed distance code is given in Chapter 4, which lays out the computation of the complete set of kinematic parameters.

### The data flow

The data flow of this thesis is illustrated by Figure 3.1. Shown is a schematic chart that gives a comprehensive overview and summarises the various data products and codes as well as selection and calibration steps that all together have led to the assembling of the final compilation of SEGUE G-dwarfs.

The top half of the schema shows the different processing steps performed and the data products obtained and provided by the SEGUE collaboration in the survey's framework. Hence, the diagram starts with the original target selection of spectroscopic candidates based on SDSS and SEGUE photometric targets. From the resulting SEGUE spectra, when observed and processed through the general SDSS pipeline and the SSPP (light red boxes), information on radial velocities and stellar atmospheric parameters could be obtained and were provided. Those data products together with further observational data relevant to the SEGUE G-dwarf sample compilation, such as recent SDSS photometry, extinction and proper motions are colour coded in purple.

The second half of the schematic chart illustrates the actual selection steps as performed and laid out in detail as part of this work. Taking the pipeline outputs and SDSS database information as the starting point blue boxes mark additional calibration processes that were needed in order to improve the original parameters with respect to the aims of this thesis. Those two major working steps where collaboration played a role are highlighted in yellow: the development of a spectro-photometric distance code delivering distances to SEGUE stars and the modification of the selection effect corrections presented in Bovy et al. (2012c). The latter had to be adapted for the SEGUE sample analysed in this thesis. Finally, the hexagon covers the compiled selection of SEGUE G-dwarfs that not only possess stellar parameter estimates but distances and information on kinematics and their orbital properties (red boxes).

## 3.2 SEGUE G-dwarfs from DR9

This section gives an overview about the selection criteria and quality limitations that have been applied to the overall SEGUE dataset in order to compile a G-dwarf sample suited for a robust and statistically significant chemo-dynamical analysis.

---

<sup>3</sup>The RERUN 122 is the final SSPP run that provided the parameters published in DR9.

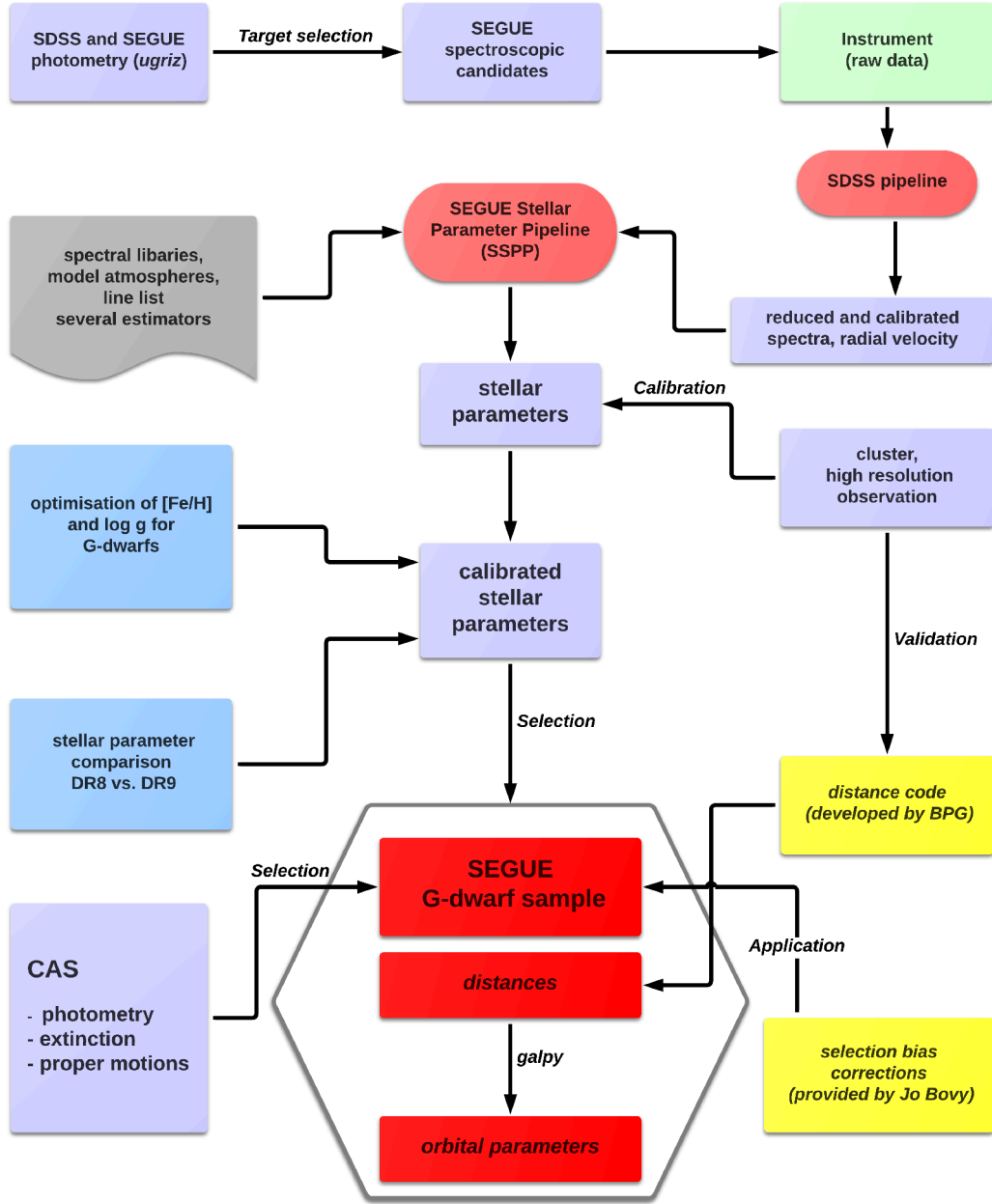


**Figure 3.1:** Schematic chart describing the data flow with respect to the assembled stellar SEGUE G-dwarf sample. Purple boxes correspond to observational data from various sources or the parameters obtained thereof, while blue boxes correspond to parameter calibrations performed as part of this thesis. The most collaborative parts, including the development of a distance code for spectro-photometric distances and the modification and adoption of the Bovy et al. (2012c) selection effect corrections for this thesis, are marked with yellow colour. The red boxes in the hexagon indicate the final selection of SEGUE G-dwarfs for which additional information on distances, kinematics and orbital properties are obtained.

**Table 3.1:** Conversion from  $E(B - V)$  to extinction for the SDSS *ugriz* filter system.

Band	$A_{\text{filter}} / (E(B - V))$
<i>u</i>	5.155
<i>g</i>	3.793
<i>r</i>	2.751
<i>i</i>	2.086
<i>z</i>	1.479

### 3.2.1 Extraction of G-type stars

The SDSS-III archive has been queried via CASJobs to download the complete sample of G-type stars available in DR9. Thereby a simple colour-magnitude cut is applied to the SDSS DR9 photometry serving as the primary selection criterion. An alternative to the pure photometric selection would have been to exploit the SDSS bitmask<sup>4</sup> system. Yet, as discussed in Chapter 5 bitmasks are only used to obtain additional information on the composition and possible contamination of the G-type sample by other stellar types.

All selected stars are spectroscopically observed as part of the SEGUE sub-survey. In particular, the query is designed to select objects that are observed as part of SEGUE-1, since neither SEGUE-2 nor the SDSS program have targeted the G-type star category explicitly. However, some SEGUE-1 stars belong to the group of objects with repeat observations or additionally possess observations in one of the other two programs. This is important to know if one aims to exclusively use parameters that are obtained from the spectroscopic observation with the highest quality. Hence, in case of objects with multiple observations the query is built such that it assures the extraction of the best spectra available for each object. If this observation turns out to be not the one from SEGUE-1, the stellar parameters from the SEGUE-2 or the SDSS spectrum are used instead. The SQL code and a detailed description of the multi-part query employed in the selection process can be found in Appendix B.4

#### Photometric selection

From the overall SEGUE-1 sample stars are selected using the colour-magnitude-criterion for SEGUE G-type stars that covers a range in colour and magnitude of  $0.48 < (g - r)_0 < 0.55$  and  $r_0 < 20.2$ . The cut is applied to the absorption-corrected and dereddened photometry of the objects as indicated by the magnitudes with zero index. The total extinction  $A(\lambda)$  in each individual SDSS filter band, which is needed to correct the apparent magnitudes, is provided for each SDSS objects and can be downloaded together with the photometry from the SDSS archive. The reddening,  $E(B - V)$ , which is required to obtain  $A(\lambda)$  is determined along the line of sight of each individual object based on the extinction maps by Schlegel et al. (1998). More details about the conversion from reddening to total extinction can be found in Stoughton et al. (2002). Table 3.1 lists the conversion factors that are used for the SDSS *ugriz* filter system.

<sup>4</sup>The concept of bitmasks uses the bits in an integer as “toggles” to indicate whether certain conditions are met. As such it allows to directly select particular types of objects from the entire SEGUE dataset. In case of SEGUE the bitmasks can be used to (1) figure out to which SEGUE stellar category a star belongs to according to its actual photometry and astrometry and (2) to recap for which target type category the object was originally assigned a fibre for.

**Table 3.2:** The Table lists the number of stars in the SEGUE G-star sample at various stages along the selection and definition process.

sample stage	number of stars
CAS sample	46 307
sample with valid parameters ( $T_{\text{eff}}$ , $\log g$ , $[\text{Fe}/\text{H}]$ , RV, PM, $[\alpha/\text{Fe}]$ )	38 668
sample after parameter optimisation	35 009

Each target that meets the above colour-magnitude criteria is extracted whether or not it has been originally a G-star candidate in SEGUE-1. Due to changes in photometry for different SDSS data releases, stars that have been observed and targeted as G-star candidates may not satisfy the G-star colour criteria anymore (and vice versa). As a result, the size and composition of this work G-star sample differs from the ones that were photometrically selected for previous studies (Bovy et al. 2012c, Liu & van de Ven 2012) which used photometry from earlier data releases. One advantage that comes with the photometric selection is that the entire SEGUE G-star sample can be explored. Still, this goes along with the disadvantage that contamination due to overlapping target categories may not be completely negligible.

The applied query results in an initial sample of 46 307 G-type stars. However, as shown by the bitmasks some of the stars were originally targeted as K-giants, low metallicity stars or K-dwarfs which are the SEGUE target categories overlapping with the G-type stars. More details on the contamination of SEGUE G-star samples by overlapping SEGUE target categories is given in Section 5.1.1.

Starting from the initial sample all objects with undetermined stellar parameters (effective temperature, surface gravity and metallicity), radial velocity or proper motion are excluded. This leaves a number of 38 668 G-type stars with the full set of valid DR9 parameters as listed in Table 3.2.

### Calculation of adopted optimised stellar parameters

In Section 2.2.2 it has been already mentioned that some of the SSPP parameter estimators are not appropriate for cool dwarfs, ruling out e.g methods that are by purpose designed for hotter or evolved stars. This applies especially for some of the metallicity and surface gravity estimation methods. However, the aim is to compile a statistically significant sample of G-dwarfs with stellar parameters of good quality. That is why for this work’s analysis the surface gravity and metallicity estimates are particularly optimised for the stellar type of interest. Thereby, a quality improvement is achieved as follows: by using a simple biweight average algorithm<sup>5</sup> for both,  $\log g$  and  $[\text{Fe}/\text{H}]$ , an average parameter estimate is calculated based on those sets of appropriate methods listed in Section 2.2.2. In addition to this selective use of SSPP estimators only parameter estimates from estimators actually being valid for an individual star are incorporated into the biweighted average. Thereby, valid means that the star and its observation satisfy the

<sup>5</sup>The routine developed for that is adopted from IDL routines which compute the centre and dispersion (mean and sigma) of a distribution using bisquare weighting. The original IDL routines are `biweight_mean.pro` (Last modification: October 2002) and `robust_sigma.pro` (Last revision: June 2010) which can be found at [http://idlastro.gsfc.nasa.gov/ftp/pro/robust/biweight\\_mean.pro](http://idlastro.gsfc.nasa.gov/ftp/pro/robust/biweight_mean.pro) and [http://idlastro.gsfc.nasa.gov/ftp/pro/robust/robust\\_sigma.pro](http://idlastro.gsfc.nasa.gov/ftp/pro/robust/robust_sigma.pro), respectively.

$g - r$  and SNR criteria<sup>6</sup> of the estimator. Whether an estimator is valid or not is indicated by a specific SSPP flag<sup>7</sup> that is listed for each individual estimator as part of the pipeline output. It turns out that, according to the flags, for some of the stars none of the methods that could be used for the optimisation procedure are valid. This limits the sample of G-type stars with optimised parameters to a number of 35 009 objects, even though the procedure has been applied to all stars with a full set of parameters (see Table 3.2 line 2). Given this, in any further sample selection steps only those remaining 35 009 G-type stars are considered.

The biweight average routine outputs an error estimate, sigma, for the mean values it determines. Thereby, sigma is based on equation (9) of Beers et al. (1990) and represents an outlier resistant measure of the dispersion about the centre of the distribution and is as such analogue to the standard deviation. In order to get an absolute error, sigma has to be divided by  $\sqrt{N}$ . The error for the optimised parameters is thus calculated basing on the following formula

$$\sigma_{\text{opt}} = \frac{\sigma}{\sqrt{N}} \quad (3.1)$$

where  $N$  is the number of estimators that incorporate into the average. This error estimation is similar to the internal scatter estimate of the SSPP that has been already discussed in Section 2.2.2. Generally, it results in very small uncertainties for the optimised values. These are indeed compatible with the error in each individual SSPP method and the error of the adopted average value from the SSPP but underestimate the internal SSPP uncertainty by far.

### 3.2.2 Compiling a G-dwarf sample

So far, most studies that deal with G-dwarf samples (Lee et al. 2011b; Bovy et al. 2012c; Liu & van de Ven 2012; Schlesinger et al. 2012) have relied on a cut in surface gravity to separate dwarf from giant stars. However, cuts in stellar parameters instead of observable space can lead to strong biases. One of those is illustrated in Figure 3.2 which shows the  $\log g$  dependence on  $[\text{Fe}/\text{H}]$  for this work's compilation of G-type stars and this based on DR8 (left) and DR9 (right) SSPP parameters (optimised parameters).

The plot reveals an obvious difference in the shape and location of the distributions for the two data releases. For stars with  $4.0 \text{ dex} < \log g < 5.0 \text{ dex}$  the DR8 panel indicates an almost flat behaviour and only a slight decline to lower surface gravity values in the higher metallicity regime. This suggests that there is a moderate dependency between surface gravity and metallicity in DR8. Indeed, a slight dependency for  $\log g$  with  $[\text{Fe}/\text{H}]$  is expected due to the colour-magnitude cut that is applied as part of the selection process. In case of G-type stars the cut preferentially selects low metallicity stars at higher surface gravity, while the high metallicity stars tend to have lower gravity values in general (see the set of theoretical stellar isochrones in Figure 5.6). This directly influences the shape of the distribution in the present diagram. The extent of the dependency is demonstrated by the black contours in both panels.

When using optimised DR9 parameters (right hand panel) instead there is a stronger dependency than in DR8 which clearly exceeds the described effect of the colour cut. It seems that the surface gravity of the high metallicity stars is systematically underestimated with respect to the low metallicity stars. In addition, for the entire distribution there is a systematic shift of about 0.2 dex to 0.3 dex compared to DR8. These findings suggest that a flat cut in  $\log g$  is

<sup>6</sup>A detailed listing of the  $g - r$  and SNR ranges for individual SSPP DR9 methods is given in Table 2 of Rockosi et al. (in prep.).

<sup>7</sup>The flag (the indicator variable) is either set to zero (method is dropped), one or two (method is valid for both). A two (only set for  $[\text{Fe}/\text{H}]$ ) labels those estimating methods that produce the most reliable estimates of the parameter. Hence, in case of the  $[\text{Fe}/\text{H}]$  only methods where the flag is equal to two are considered in the average.

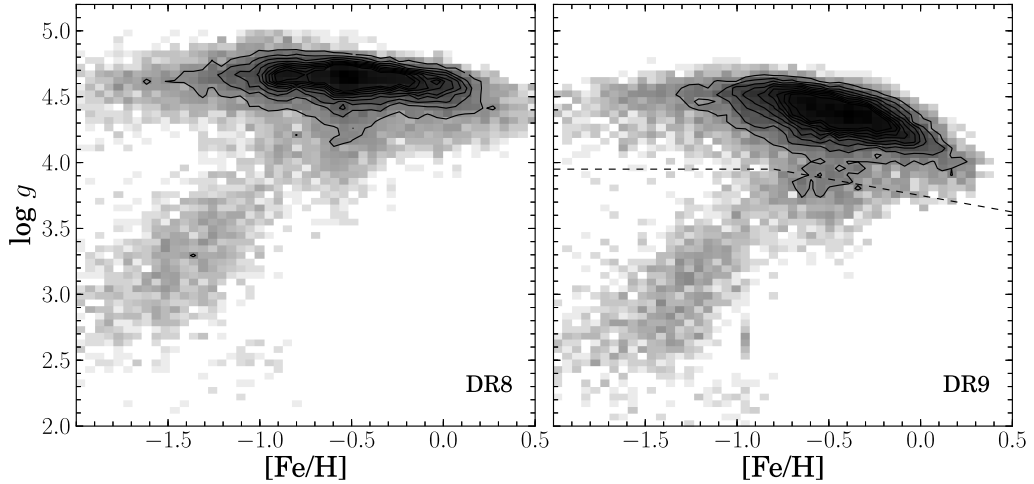


**Figure 3.2:** Density distribution of the G-type star sample with optimised stellar parameters in the  $[\text{Fe}/\text{H}]$ - $\log g$ -plane. Shown are the SSPP parameters from DR8 (*left*) and from DR9 (*right*). All quantities are optimised for G-stars. The contours indicate the extent of the dependency between surface gravity and metallicity. The dashed line in the DR9 panel marks the empirical selection boundary that is used to separate dwarf from giant stars. The line corresponds to Equation 3.2.

not recommended when using DR9 parameters (see similar results in Schlesinger et al. 2014) but requires an individual treatment as described below.

### An empirically determined $\log g$ cut

To account for the dependency between surface gravity and metallicity giants are separated from dwarfs according to the following empirically-determined relation:

$$\log g > \begin{cases} 3.95, & \text{if } [\text{Fe}/\text{H}] < -0.8 \\ -0.25 \cdot [\text{Fe}/\text{H}] + 3.75, & \text{if } [\text{Fe}/\text{H}] > -0.8 \end{cases} \quad (3.2)$$

The dashed line in Figure 3.2 (right panel) depicts the boundary between giant and dwarf stars as given by equation 3.2. It is evident that a straight conservative cut in  $\log g$  at a fixed value would have been sufficient when using the DR8 parameters, not so in case of DR9 where one would likely eliminate the high metallicity stars. The introduced individual cut makes sure that the G-dwarf sample still embeds objects at higher metallicity. The application of the empirically determined  $\log g$  cut selects 28 604 stars to be G-dwarfs.

### Quality restrictions

For each stellar object the SSPP uses only parameter estimates from valid estimators in order to obtain an average parameter value for each stellar astrophysical parameter. In addition, for this work the  $\log g$  and  $[\text{Fe}/\text{H}]$  values have been separately optimised for each of the selected stars. Either assures to obtain a G-dwarf sample with a parameter set of reliable quality. However, the quality of the selected sample can be increased by paying attention to additional quality parameters and flags that are also part of the SSPP output. In the present case two important

quality indicators are the `CC_MGH` and `CC_CAHK`<sup>8</sup> parameters. Due to an error in the pipeline for the methods NGS1, NGS2 and CaIIK1 some stars possess very incorrect parameters. By selecting stars with `CC_MGH` > 0 and `CC_CAHK` > 0 those objects can easily be removed from the sample. See Table 3.3 for their fraction among the G-type stars crucial to this thesis.

Also, to indicate whether quoted atmospheric parameters may be in doubt or to point out possible anomalies that might apply to a given stars, the SSPP provides a number of flags, among them critical and cautionary flags. Especially the second category of flags is mainly provided for users consideration being not necessarily a cause of concern. All flags are combined to a set of five letters that are listed for each star in the `FLAG` column of the SSPP output table. For detailed information on the SSPP flags and the meaning of each individual letter consult Section 7 of Lee et al. (2008a). If an object is classified as a normal star because its spectrum has passed all crucial SSPP tests and the stellar parameters are considered as well determined, the five letter combination is `nnnnn`. If instead the spectrum exhibits certain features one or multiple of the five placeholders may feature a different letter. With respect to the present G-star sample the majority of stars is flagged as normal. Nevertheless, a couple of stars are labelled with the combinations `nnnGn/nnngn`<sup>9</sup> or `nnBnn`<sup>10</sup>. Those indicate that the stars have strong/mild G-band features or show a discrepancy in the  $H\alpha$  strength when measured directly or predicted from  $H\delta$ . After careful consideration, all stars with a letter combination other than `nnnnn` remain in the G-type star sample because the specified flags are only warning flags which are not accurate to 100%, the majority of G-band feature stars have been targeted as G-type stars and the G-dwarfs are mostly cooler than the limit mentioned in footnote 10.

The sample is further limited to objects with a signal-to-noise ratio of  $\text{SNR} > 20 \text{ \AA}^{-1}$ . This limit in SNR is recommended by Lee et al. (2008a) given that spectra with a  $\text{SNR} > 20 \text{ \AA}^{-1}$  are at least required to allow a reliable estimate of the alpha-enhancement. Other studies of SEGUE G-dwarfs (Bovy et al. 2012c; Liu & van de Ven 2012) even included stars with a SNR of  $15 \text{ \AA}^{-1}$ , claiming that the uncertainties in  $[\alpha/\text{Fe}]$  are not increased by much. The G-dwarf sample analysed in Lee et al. (2011b) on the other hand is restricted to stars with  $\text{SNR} > 30 \text{ \AA}^{-1}$ , making sure to include only stars with high  $[\text{Fe}/\text{H}]$ ,  $[\alpha/\text{Fe}]$  and small errors in radial velocity that allows a reliable separation of thin and thick-disk population stars solely based on chemistry. Since one aim of this thesis is to perform an analysis where chemical and kinematic information are combined at the same time in order to disentangle thin and thick disk stars and their corresponding correlations and properties, the decision has been made to not be as restrictive as the latter authors are. The cut at  $\text{SNR} > 20 \text{ \AA}^{-1}$  allows to obtain a sufficient number statistic and assures that the chemistry is reliable enough for a thorough chemo-dynamical analysis.

In addition to the previous quality criteria another two criteria are set, one on the reddening along the line-of-sights of the stars and the other on their magnitude. In order to minimise the effects due to uncertainties in extinction only line-of-sights with reddening values of  $E(B - V) < 0.3$  and stars with a  $r$ -band magnitude of  $r_0 > 14.5$  remain in the sample. The cut in magnitude is applied to avoid problems with saturation which is a know issue for SEGUE

<sup>8</sup>The `CC_MGH` and `CC_CAHK` parameters represent correlation coefficients between the observed spectrum and the synthetic spectrum with SSPP adopted parameters  $T_{\text{eff}}$ ,  $\log g$  and  $[\text{Fe}/\text{H}]$  for the spectral regions  $4500 \text{ \AA}$  to  $5500 \text{ \AA}$  and  $3850 \text{ \AA}$  to  $4250 \text{ \AA}$ , respectively.

<sup>9</sup>Objects with G-band features are possibly carbon-enhanced stars and mostly metal poor. Indeed, all considered G-type stars with those flags span a range in  $[\text{Fe}/\text{H}]$  from  $-1.5 \text{ dex} < [\text{Fe}/\text{H}] < -1.0 \text{ dex}$  dominating the low metallicity tail of the metallicity distribution. The target categories they have been initially assigned to are either the G-stars or the low metallicity stars.

<sup>10</sup> The measured  $H\alpha$  strength is not within the strength of the  $H\alpha$  line as predicted from  $H\delta$ . The relation between  $H\alpha$  and  $H\delta$  breaks down for stars cooler than  $5800 \text{ K}$  because the  $H\delta$  lines are too weak. The flag can hence be ignored for stars with temperatures lower than this limit.

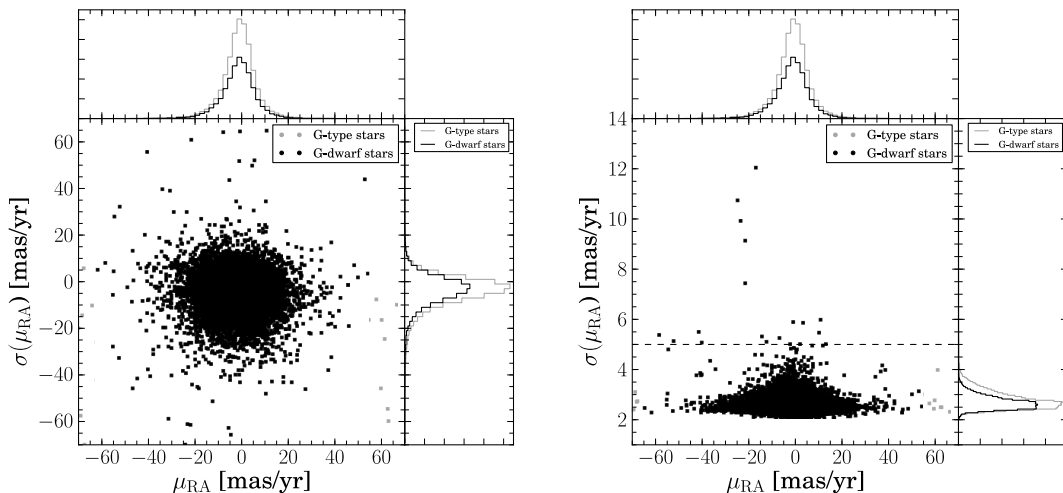


**Figure 3.3:** SDSS proper motions for the SEGUE G-type stars. *Left panel:* 2D distribution of the proper motions for SEGUE G-type stars with optimised parameters (grey dots) and the SEGUE G-dwarf sample (black dots) that has been cut according to the selection criteria described up to this point. *Right panel:* Distribution of uncertainties in absolute proper motion error for the two samples displayed on the left. The quality cut that should assure a G-dwarf sample with good quality kinematics is indicated by the dashed line.

stars brighter than this limit. The SDSS saturation limit varies over the instrument and hence influences the completeness of the bright end of the sample.

### Compilation of a disk sample with good quality kinematics

To obtain a sample of disk stars with distances and kinematics that allow to reliably investigate chemo-dynamical properties in the Galaxy, the final G-dwarf sample is restricted to local disk stars. Note, that at this point in the selection process kinematic parameters and distances are already used to restrict and clean the sample, even though the stellar kinematics are first introduced throughout the next chapter. The inclusion of the kinematic information at this stage allows to present the entire set of selection criteria being applied to get the final SEGUE G-dwarf sample at once.

As a first step stars with  $[\text{Fe}/\text{H}] < -1.5$  and rotational velocities  $v_\phi \leq 40 \text{ km s}^{-1}$  are removed from the sample. These latter two restrictions should avoid contamination by halo stars which are more metal poor than disk stars and have smaller velocities or move even on counter-rotating orbits. To ensure a sample with kinematic parameters of reasonable precision a quality cut is applied to the uncertainty in proper motion. The left hand panel of Figure 3.3 shows the range in proper motion that is covered by the SEGUE G-type stars. The grey dots represent the full G-star sample with optimised parameters while the black dots display the G-dwarf sample with all cuts applied being described up to this point. The figure's right panel shows the typical uncertainties in proper motion for the same samples on the left. Evidently, the uncertainties in proper motion are in general small with a peak around 2.5 in  $\sigma(\mu_{\text{RA}})$ . Thus, only a minor fraction of stars is excluded due to the cut at  $\sigma(\mu_{\text{RA}}) = 5 \text{ mas/yr}$  (dashed line in the right panel of Figure 3.3). It should be noted that the SDSS astrometry and proper motions have been improved and corrected for DR9 with respect to former DR7 and DR8 values. The latter were affected

**Table 3.3:** Summary of the selection criteria that define the G-dwarf sample of this work.

parameter	sel. condition	note	# of stars
$\log g$	see Eq. 3.2		28 604
CC_MGH	$> 0$	remove stars with incorrect SSPP parameters	28 499
CC_CAHK	$> 0$	remove stars with incorrect SSPP parameters	28 498
SNR	$> 20$	cut required to ensure reliable abundances	23 985
$E(B - V)$	$< 0.3$ dex		23 787
$r_0$	$> 14.5$	avoid issues with saturation	22 986
[Fe/H]	$> -1.5$ dex	avoid contamination from halo	22 226
$v_\phi$	$> +40$ km s <sup>-1</sup>	avoid contamination from halo	21 240
$\sigma_{\mu_{\text{RA}}}, \sigma_{\mu_{\text{DEC}}}$	$< 5$ mas/yr	sample with reliable distances	21 221
distance	$\leq 3$ kpc	local sample with reliable kinematics	18 244

by several errors in the astrometric calibration. Further details on the fixed and improved SDSS astrometry can be found in Ahn et al. (2012) and Aihara et al. (2011b). In order to give insight into the origin and properties of the SDSS proper motions being in this thesis, the kinematics chapter contains a subsection solely dedicated to the proper motions.

As a last restriction distances are required to be less than 3 kpc from the Sun. Focussing on a local volume ensures that the distance estimates and proper motions are reliable with moderate errors that allow to obtain accurate space motions and well-defined stellar orbits. The distance distribution and the corresponding distance errors of the final SEGUE G-dwarf sample are shown and described in Chapter 4, together with the actually used distance code.

### 3.3 Stellar parameter systematics between DR8 and DR9

As outlined in Section 2.2.2 the SSPP has undergone a couple of modifications providing improved stellar parameters for all stellar SDSS objects within the scope of DR9. A natural consequence are systematic changes in the determined parameters with respect to earlier parameter sets. But how did the SSPP data products really change and are the new parameters a change for the better? This section aims to shed light on the transition from DR8 to DR9 by comparing stellar parameter estimates from both corresponding SSPP versions for a defined sample of stars.

Given the differences in the  $\log g$  scales as discussed in Section 3.2.2 there needs to be a significant discrepancy in the  $\log g$  values determined for DR8 and DR9. Moreover, as said before the surface gravity seems to be underestimated in case of DR9. To invest this more qualitatively and to check whether there are similar discrepancies for the remaining stellar parameters Figure 3.4 shows the main stellar parameter distributions for the previously defined G-dwarf sample. For that the DR8 SSPP parameters for [Fe/H] and  $\log g$  have been optimised the same way as presented for DR9. The solid curves represents the DR9 distributions, the dashed curves are for their DR8 counterpart.

Among all shown parameters the most significant deviation is observed for the surface gravity. Compared to DR8 the DR9 parameter estimates show a systematic decrease of about 0.2 dex to 0.3 dex. This finding is indeed in agreement with the fact that the DR9 surface gravity is in general lower by about 0.2 dex (see Rockosi et al.(in prep.)). Possible explanations for the decrease are the following: (1) the surface gravity estimates from the re-analysis of the

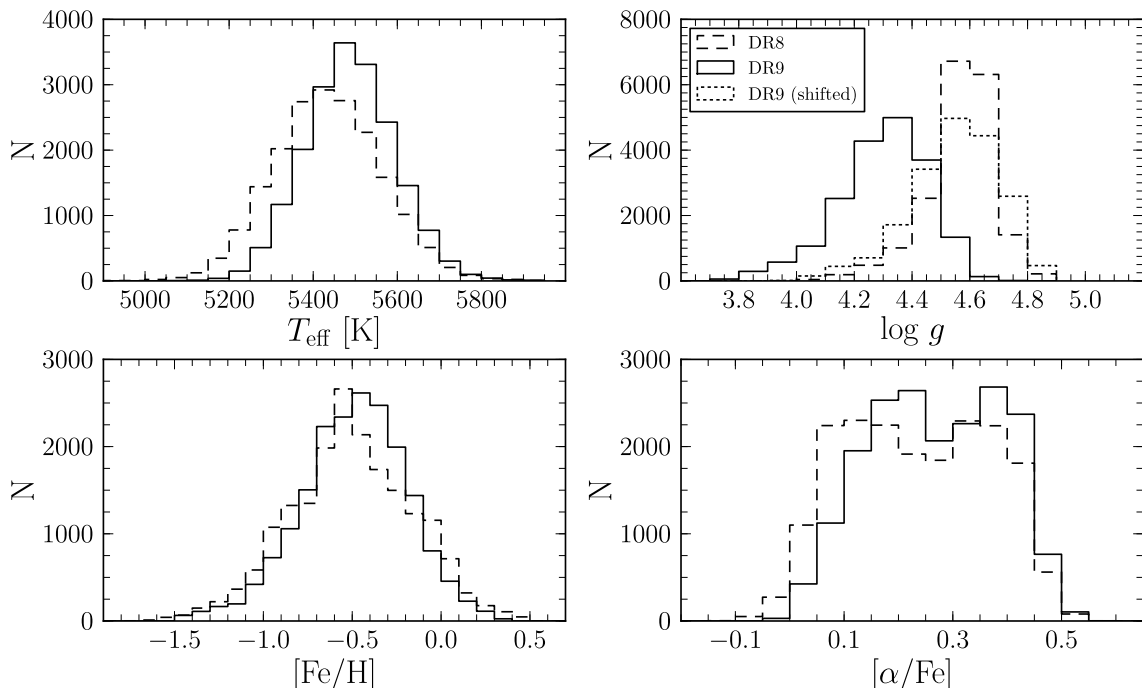


**Figure 3.4:** Comparison of the stellar parameters from the SSPP’s DR8 and DR9 version for this work’s sample of G-dwarfs.

high-resolution spectra that are used to calibrate the DR9 SSPP results are in general lower by 0.13 dex than those from the older high-resolution analysis, (2) for the methods NGS1, NGS2 and CaI1 new grids of synthetic spectra have been used and (3) the line index methods MgH and CaI2 are not considered any longer which may have a substantial effect since those estimators produce higher  $\log g$  values compared to others.

Especially for dwarf stars the re-calibrated final adopted SSPP  $\log g$  values tend on average to be lower by about 0.5 dex compared to the parameter estimates from the high-resolution analysis (see Figure 2.2, middle panels). For sure the overall lower gravity is caused by a combination of the above facts.

Besides the shift in surface gravity, the temperatures in DR9 tend to be systematically larger by roughly 50 K than in DR8. This temperature shift occurs due to the IRMF temperature scale being utilised to calibrate all SSPP temperature estimators and the IRMF temperature estimate being higher on average by about 50 K to 60 K. For the metallicity no obvious systematic shift is visible. Still the shape of the distributions differs slightly in the sense that the peak of the DR9 metallicity distribution has moved to a higher value. Also in case of DR9 the  $[\text{Fe}/\text{H}]$  distribution is considerably smoother than that from DR8. From Figure 3.4 and even more obvious from Figure 3.5 the  $\alpha$ -enhancement values have changed as well. Not only that the whole distribution is shifted to higher values by about 0.1 dex, the distribution seems to be compressed as well. Because the SEGUE  $\alpha$ -determination is independent of the SSPP surface gravity the systematic change in  $\log g$  is considered not to be the main reason for the change in  $\alpha$ -abundance. Moreover, the observed shift is likely a consequence of the change in effective temperature because  $T_{\text{eff}}$  is the only SSPP parameter that is directly used in the  $\alpha$ -estimation process. For more details on this issue see section 2.3 of (Lee et al. 2011a).

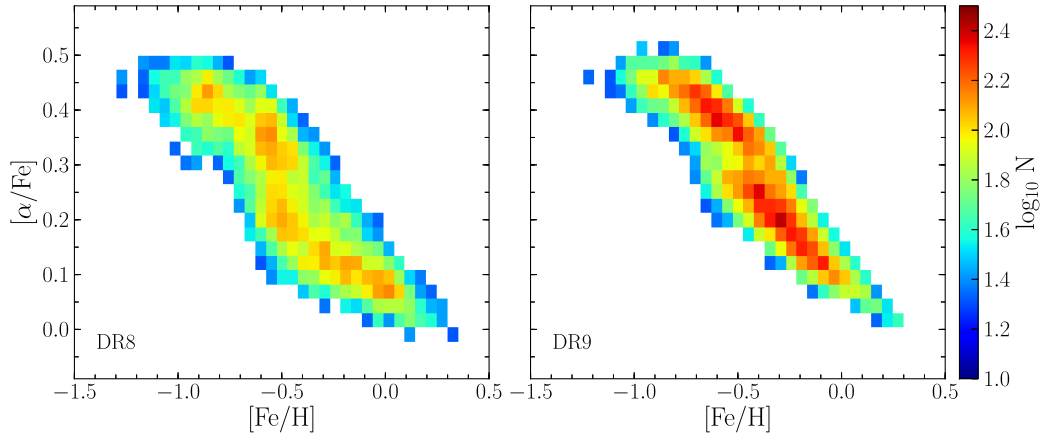


**Figure 3.5:**  $[\alpha/\text{Fe}]$ - $[\text{Fe}/\text{H}]$ -diagram (chemical abundance plane) of the final G-dwarf sample. The sample’s location is shown based on the SSPP parameters from DR8 (*left panel*) and DR9 (*right panel*). Compared to DR8 the DR9 distribution appears slightly compressed and shifted to higher values by about 0.1 dex.

### 3.3.1 Calibration of $\log g$

The comparison to DR8 has shown that the DR9 surface gravity is lower by a non negligible amount. Also, especially for dwarf stars the calibrated DR9 gravity values show large differences compared to the high-resolution analysis which suggests much larger gravities (see previous paragraph and Section 2.2.2). As only the relative gravity scale is important to separate dwarfs from giants the absolute surface gravity values are crucial when computing e.g. spectro-photometric distances. Any systematic under- or overestimation of the surface gravity will lead to an under- or overestimation of the spectroscopic distances. If the surface gravity is too low, the object seems to be brighter than it is, thus the distance will certainly be overestimated and vice versa. Hence, it has been decided to calibrate the SEGUE DR9 surface gravity values by applying a shift of 0.25 dex and thus increasing the  $\log g$  of each object in the G-dwarf sample by the same amount. The extent of the shift is empirically determined from the comparison with DR8. The shifted DR9  $\log g$  distribution is illustrated by the dotted histogram in the upper right panel of Figure 3.4. A weakness of this calibration is certainly that the surface gravity is increased by a fixed value which does not account for the dependency between  $\log g$  and metallicity that is seen for the DR9. The shift may thus overcorrect the surface gravity for the low metallicity stars but still underestimate the  $\log g$  for the high metallicity stars in the sample. Nevertheless, the following chapters demonstrate that this ad-hoc shift of the surface gravity results in more realistic distance estimates and agrees much better with the predictions from theoretical population synthesis models.

## 3.4 Discussion

The application of several quality restrictions and selective parameter choices has reduced the number of about 35 000 pre-selected SEGUE G-type stars with optimised stellar parameters (see Table 3.2 and Section 3.2.1) to a final selection of about 18 000 G-dwarfs. All of these remaining stars satisfy the criteria listed in Table 3.3 and build a statistically significant sample with well defined kinematic and chemical properties. Those are, by the end of Chapter 4, complemented

with a complete set of phase space and orbital parameter information as determined based on the objects spectro-photometric distances.

Yet, in spectroscopic samples the occurrence of observational selection effects and biases is inevitable regardless of the scientific user's own putatively careful performed selection. The previously presented sample not excluded. Each limitation on the object's parameters put by the user's hand can lead to a bias that is introduced to the final collection of stars used to analyse the properties of the Galaxy. Prominent examples for user created biases arise due to restrictions in photometry, such as the colour cut in  $g - r$  that is discussed in this chapter and that extracts only G-type stars from the entity of SEGUE stars. However, a large fraction of selection biases commonly arises as a consequence of the design and target selection procedures of today's large stellar surveys. In case of SEGUE one main selection bias in the survey's stellar population owes to the limited number of spectroscopic fibres that is available for each line-of-sight. Hence selection effects can be present in datasets before any other selection is later applied to a stellar sample by the analysing end user.

The attentive scientist who aims to extract chemo-kinematic constraints for the Milky Way by analysing a sample, such as the roughly 20 000 SEGUE G-dwarfs, must hence ask himself the following: How do selection effects and biases influence the overall properties and chemo-dynamical relations found in my sample? How can those influenced relations possibly lead to incorrect and misleading conclusions on the dynamical structure and composition of the Galaxy, especially when comparing the observations to predictions from theoretical models of the Milky Way?

The answer to these questions will be given in Chapter 5 by thoroughly investigating and accounting for the complex selection effects that affect the present work's G-dwarf sample and could hence tamper any conclusion drawn from it. As such, this thesis joins the previous studies on SEGUE G-dwarfs presented by Bovy et al. (2012c,a) and Schlesinger et al. (2012) which claim that the ensemble of these stars has to be treated with caution due to biases.



Present-day stellar spectroscopic surveys systematically cover the main Galactic components, thereby providing insights on how the stellar chemical abundances and kinematic properties are distributed throughout the Galaxy. In order to efficiently use these information for chemodynamical studies it is necessary to get a robust handle on the kinematic parameters and, in particular, their uncertainties. Now that GAIA's first data has been released precise distances are available for many stars in the Milky Way. The science presented in this thesis however had to do without the GAIA distance measurements. Therefore, the stellar distance has been the most uncertain and problematic variable when computing stellar kinematics because the distance crucially affects the precision and hence the interpretation of the stars' motion inside the Galaxy. Yet, it is impossible to compute 6D-phase-space coordinates and stellar orbits within the Galactic potential without complementing the astrometry and radial velocities with information on the proper motions and, of course, a distance measure to the star. Therefore, a large effort was spent on the development and verification of a general purpose method that allows to determine reliable spectro-photometric distances to stars from a variety of stellar surveys. The basics of the adopted distance code are outlined in the first part of this chapter (Section 4.1) followed by a short discussion on the employed proper motions in Section 4.2. Finally, Section 4.3 deals with the computation of phase-space coordinates and Section 4.4 describes how stellar orbital properties are estimated based on an existing python module for orbit integration and related errors are obtained by use of a Monte Carlo technique. All implemented methods are mainly applied to the SEGUE G-dwarf sample which is introduced and analysed in Chapter 3 and 5. However, the same procedures are also employed for the RAVE giant sample as discussed in Chapter 8 as well as they are used for the most part to calculate kinematic parameters for the synthetic mock star samples that are created and compared to the SEGUE observations in Chapters 6 and 7. Overall, the determination of stellar dynamics, especially the set up, testing and improvement of a proper statistical framework to determine reliable distances, was a major task and accounts for a significant part of the time spent for the current thesis.

## 4.1 Distances

One of the major problems in modern Galactic astrophysics is to determine accurate distances to stars falling beyond the volume covered by the Hipparcos satellite mission (Perryman et al. 1997) which obtained precise astrometric parallax estimates to stars in the close vicinity of the Sun ( $d \leq 100$  pc). Being independent of any physical assumption about the nature of the object the accuracy and availability of these direct and fundamental distance measurements, forming the lowest rung of what is called the *cosmic distance ladder*, relies only on the distance to the object itself. That is because with increasing distance the parallax gets very small complicating a precise measurement in the range of milliarcseconds. As a result, for a long time reliable distances to more distant stellar objects were rare and restricted to a specific class of astronomical objects, called *standard candles*. These physical distance indicators (e.g., Cepheids, RR Lyrae stars) have known luminosities that, in combination with observable quantities, such as their apparent brightness, allow to obtain a distance estimate via the distance modulus. But their low number statistic prevents any significant chemo-dynamical mapping and exploration of the Galaxy. With precise parallaxes for over one billion stars the GAIA-satellite will put things right in the near future allowing to draw an unprecedented detailed chemo-dynamical picture of the Milky Way. While waiting for GAIA much effort is spent though to develop new methods that employ available measured physical stellar properties. For example, Ivezić et al. (2008) determined a photometric parallax relation to obtain photometric metallicities and distances for more than 2 million SDSS stars. Common to most of the newly emerged approaches is however the determination of distances by fitting to theoretically computed stellar evolutionary models, i.e. comparing the observed location of a star in the  $T_{\text{eff}} - M_V$ -plane to isochrones or evolutionary tracks given spectroscopic observables like effective temperature, surface gravity, metallicity and  $\alpha$ -enhancement in combination with photometric information. Using the absolute magnitude,  $M$ , of the best-fitting model and the distance modulus ( $m - M$ ), with  $m$  being the apparent magnitude, the stars' distance can then be estimated according to

$$d [\text{pc}] = 10^{\frac{m-M}{5}+1}. \quad (4.1)$$

With the advent of large-scale stellar surveys, among them, RAVE, SEGUE, APOGEE and Gaia-ESO, photometry and spectroscopic parameters with sufficient accuracy are available for a significant large number of stars. Much attention has therefore been devoted to develop sophisticated statistical methods to best exploit these information in order to determine physical parameters of stars, masses, ages, extinction or distances. These methods include frequentist approaches, e.g. by Breddels et al. (2010) or Bayesian analysis of increasing complexity (Jørgensen & Lindegren 2005; Takeda et al. 2007; Burnett & Binney 2010; Bailer-Jones 2011; Casagrande et al. 2011; Schönrich & Bergemann 2014). With the latter techniques being systematically applicable, there is a general trust in routines that spectro-photometrically determine stellar properties which are not directly or hardly accessible by measurements, thus enriching the data product of the stellar surveys. This allows for characteristic studies of the stellar populations in the Milky Way, both in the intrinsic stellar properties, such as age-metallicity relations (Holmberg et al. 2007; Casagrande et al. 2011) or in their kinematics (Carollo et al. 2010; Schönrich et al. 2011). Regarding the distance estimates the above methods certainly have a clear drawback compared to the parallax distance measurements. They depend on the accuracy of the measured stellar parameters that have to be very precise to obtain reliable distance estimates.

### 4.1.1 The method

In the context of stellar distances several authors have presented methods to determine spectrophotometric distances, for the most part based on the framework of statistical inference<sup>1</sup>. Among the most recent publications is a series of papers dealing with distances to RAVE stars (Breddels et al. 2010; Zwitter et al. 2010; Burnett & Binney 2010; Burnett et al. 2011; Binney et al. 2014) and a couple of works introducing distances to APOGEE stars (e.g. see Hayden et al. 2014; Schultheis et al. 2014; Rodrigues et al. 2014). With respect to SEGUE stars so far no such works exist in the literature. Presumably, one of the main reasons for this is the resolution (and the SNR) of the SEGUE spectra which is low in comparison to the medium and high resolution observations taken within the RAVE or even the APOGEE projects. The lower resolution leads to larger uncertainties in the measured parameters increasing the risk to get potentially less precise distances. In fact, to date the majority of known studies using stellar samples from SEGUE still rely on photometric distance estimates (e.g. Lee et al. 2011b; Bovy et al. 2012c; Cheng et al. 2012; Liu & van de Ven 2012) considering solely the spectroscopic SSPP metallicity estimate, if at all. At this point the current thesis comes into play which, for the first time, provides spectro-photometric distances to SEGUE G-dwarf stars that are calculated by exploiting the general purpose distance code, hereafter BPG distance code, presented in Santiago et al. (2016). The code realisation and distance determination was led by B. Santiago (Universidade do Rio Grande do Sul, Porto Alegre, Brazil) with support from other members of the SDSS-III Brazilian Participation Group (L. Girardi, H. Rocha-Pinto, E. Balbinot) and a significant contribution from a group of people from the Leibniz Institute for Astrophysics Potsdam (D. Brauer, F. Anders, C. Chiappini). Originally, the code was developed to compute distances to SEGUE stars but it was then gradually adapted to successfully deliver distances for APOGEE and RAVE objects. As a result, the latter distance framework could be used to compute distance estimates to SEGUE G-dwarf and RAVE giant stars, the two groups of stars that are both analysed, discussed and compared in this thesis.

In short, based on the Bayesian approach of Allende Prieto et al. (2006) and in the style of Burnett & Binney (2010) the BPG distance code builds the probability distribution function (PDF) over a set of stellar evolutionary models given the observed and comprehensive set of spectroscopic and photometric parameters and quoted uncertainties thereon for any individual stellar object in order to find the star’s most likely distance. In other words: the aim is to identify the most likely set of stellar “intrinsic” variables, i.e., the true initial metallicity,  $[M/H]_t$ , the age,  $\tau$ , the initial mass,  $M$ , the heliocentric distance,  $d$ , and the true sky positions  $l_t$ ,  $b_t$  of the star, considering the measured quantities  $T_{\text{eff}}$ ,  $\log g$ ,  $[M/H]$ ,  $[\alpha/\text{Fe}]$ , as well as the magnitude ( $m$ ), the star’s colours and coordinates ( $l, b$ ). The present section points out the general scheme of Bayesian analysis and highlights the special features and planned improvements of the adopted distance code. For further details the interested reader is referred to Santiago et al. (2016).

### The Bayesian analysis framework

One of the great advantages of Bayesian inference is given by the possibility to characterise a system by using prior knowledge about the problem under consideration incorporating specific priors into the statistical analysis. In the current case, the adopted Bayesian method makes use of a couple of simple priors concerning the age, mass, metallicity and stellar density distribution of the three Galactic components (thin and thick disk, halo) in order to build a model prior

<sup>1</sup>A first introduction into the subject of Bayesian inference are the articles by Pont & Eyer (2004) and Jørgensen & Lindegren (2005) that describe the general methodology on how to estimate a value and an error for stellar properties like distance, metallicity, age and mass.

probability for each evolutionary track. This unique model probability is then considered as a multiplicative factor in the posterior probability distribution function (PDF), which is the probability of a model being correct given the observed data and the prior knowledge. The core of Bayesian analysis however is the fundamental but simple statement given by Bayes:

$$p(\text{model} \mid \text{data}) = \frac{p(\text{data} \mid \text{model}) p(\text{model})}{p(\text{data})} \quad (4.2)$$

where *data* stands for the relevant measured observables (stellar parameters and photometry) of an individual star and *model* represents the star's specified initial parameters (mass, age, metallicity, distance and location). According to Bayes' theorem the posterior probability distribution function (PDF) can then be expressed as:

$$p(\mathbf{x} \mid \bar{\mathbf{y}}, \sigma_{\mathbf{y}}) = \frac{p(\bar{\mathbf{y}} \mid \mathbf{x}, \sigma_{\mathbf{y}}) p(\mathbf{x})}{p(\bar{\mathbf{y}}, \sigma_{\mathbf{y}})} \quad (4.3)$$

with the vector  $\mathbf{x} = [l, b, d, M, \tau, [\text{M}/\text{H}]]$  representing the six ‘‘intrinsic’’ variables of the stellar evolutionary model that characterises the star and  $\mathbf{y} = [T_{\text{eff}}, \log g, [\text{M}/\text{H}], \text{colours}, m]$  being a vector containing the relevant stellar observables. The star's actual measured values of the observed quantities and their uncertainties are termed  $\bar{\mathbf{y}}$  and  $\sigma_{\mathbf{y}}$ , respectively.

In the computational process of estimating the set of ‘‘intrinsic’’ parameters and their uncertainties, factors independent of  $\mathbf{x}$  can be neglected. They represent the proportionality constant in Equation 4.3 and serve as such as the normalisation of the posterior PDF which is of no relevance to the problem to be solved. Hence, Equation 4.3 simplifies to:

$$p(\mathbf{x} \mid \bar{\mathbf{y}}, \sigma_{\mathbf{y}}) \propto p(\bar{\mathbf{y}} \mid \mathbf{x}, \sigma_{\mathbf{y}}) p(\mathbf{x}) \quad (4.4)$$

The two factors on the right-hand side of the Relation 4.4 are:

1. The likelihood, i.e. the probability that the parameter set  $\bar{\mathbf{y}}$  is measured given the measurement uncertainties  $\sigma_{\mathbf{y}}$  and the model characterised by its intrinsic parameters  $\mathbf{x}$ .
2. The prior probability of the model given by the product of a number of priors.

Assuming independence and Gaussian errors in the observed data, the likelihood is defined as the multivariate Gaussian:

$$p(\bar{\mathbf{y}} \mid \mathbf{y}(\mathbf{x}), \sigma_{\mathbf{y}}) = \prod_i \frac{1}{\sigma_{y,i} \sqrt{2\pi}} \exp\left(-\frac{(y_i - y(x)_i)^2}{2\sigma_{y,i}^2}\right) \quad (4.5)$$

where  $\mathbf{y}(\mathbf{x})$  represent the true observables corresponding to the ‘‘intrinsic’’ stellar values  $\mathbf{x}$  of the model. Thereby,  $\mathbf{y}(\mathbf{x})$  supersedes  $\mathbf{x}$  in the likelihood factor of Equation 4.4 under the assumption that the stellar model can be used to map from  $\mathbf{x}$ -space to  $\mathbf{y}$ -space. Furthermore, the knowledge of the Galaxy is reflected by defining the prior probability density,  $p(\mathbf{x})$ , of the model parameters as:

$$p(\mathbf{x}) = p(M) \sum_i p_i(\tau) p_i(\mathbf{r}) p_i([\text{M}/\text{H}]). \quad (4.6)$$

Assumed are a Chabrier-type initial mass function  $p(M)$  (Chabrier 2001) and different age, metallicity and spatial distributions for the basic Galactic components following the scheme used in Burnett et al. (2011). Also, the specifications for the Galactic structural parameters, the power-law density profile of the spherical component as well as the normalisation for the three

spatial density profiles are adapted from Burnett et al. (2011). For more details on the priors see also Section 2.1 in Santiago et al. (2016).

Finally, for each “intrinsic” parameter  $x$  of  $\mathbf{x}$  an expectation value and an estimated error  $\sigma_x$  thereon can be determined by calculating the 1st (mean) and 2nd (variance) order moment of the posterior PDF according to

$$\langle x_k \rangle = \int x^k p(\mathbf{x} | \bar{\mathbf{y}}, \sigma_{\mathbf{y}}) dx \quad (4.7)$$

where  $k \in [1, 2]$  and the integration is over all evolutionary models that satisfy  $|y(x) - \bar{y}| < 3\sigma_y$ . As such, the final distance estimate,  $d$ , is the weighted mean distance over all models within  $3\sigma$  of the data with the weight being the posterior probability of each model. For a discussion on the uncertainty estimate see Section 4.1.3.

#### 4.1.2 Special features and further add-ons

Even though the method presented in Santiago et al. (2016) is similar to many other approaches, it has a couple of specific features. First, the code is applicable to stars from each spectroscopic survey as long as the following information is available: (1) measures of physical stellar properties  $T_{\text{eff}}$ ,  $\log g$ ,  $[\text{Fe}/\text{H}]$  or  $[\text{M}/\text{H}]$  and  $[\alpha/\text{Fe}]$ , (2) photometry in the optical or Near Infrared (NIR) wavelength range and (3) estimates on interstellar extinction because the photometry needs to be dereddened in order to perform a direct comparison to the theoretical models. The current version of the code further relies on the PARSEC isochroneset by Bressan et al. (2012), both, for optical and NIR evolutionary tracks, and is flexible in the sense that it can be accomodated to the availability of the spectroscopic and photometric parameters. Distances to stars are provided even for reduced sets of parameters and can be calculated based on the following four distinct sets of observables:

1.  $\bar{\mathbf{y}} = \{[\text{M}/\text{H}], T_{\text{eff}}, \log g, \text{magnitude, colours}\}$
2.  $\bar{\mathbf{y}} = \{[\text{M}/\text{H}], T_{\text{eff}}, \log g, \text{magnitude}\}$
3.  $\bar{\mathbf{y}} = \{[\text{M}/\text{H}], \log g, \text{magnitude, colours}\}$
4.  $\bar{\mathbf{y}} = \{[\text{M}/\text{H}], \text{magnitude, colours}\}$   
plus a simple cut in  $\log g$ :  $|(\log g)_{\text{obs}} - (\log g)_{\text{model}}| < 0.5 \text{ dex}$

The information content decreases from 1 to 4, so does the reliability of the distance estimates. Most uncertain is set 4 because it does not implicitly consider the surface gravity of the star which is the most important parameter to discriminate between dwarf and giant models. If possible, priority should hence always be given to the results from set 1 or 2. For many spectroscopic surveys the  $[\text{Fe}/\text{H}]$  abundance is the only available measure for the stellar metallicity content, missing any information about the more general estimate  $[\text{M}/\text{H}]$ . Stellar evolutionary tracks however are only available for different values of  $[\text{M}/\text{H}]$  and do not yet properly account for the star’s  $[\alpha/\text{Fe}]$ -enhancement. Thus, as long as  $[\alpha/\text{Fe}]$  values are available for the star of interest, the BPG distance code adopts

$$[\text{M}/\text{H}] = [\text{Fe}/\text{H}] + [\alpha/\text{Fe}] \quad (4.8)$$

in order to bring the metallicity scale of the observations and the theoretical models to approximately the same level. Besides, in the near future the BPG distance code will also deliver individual estimates on the amount of interstellar extinction between the observer and the stars of interest. The required add-on thereon is currently being implemented and similar to the method described in Rodrigues et al. (2014).

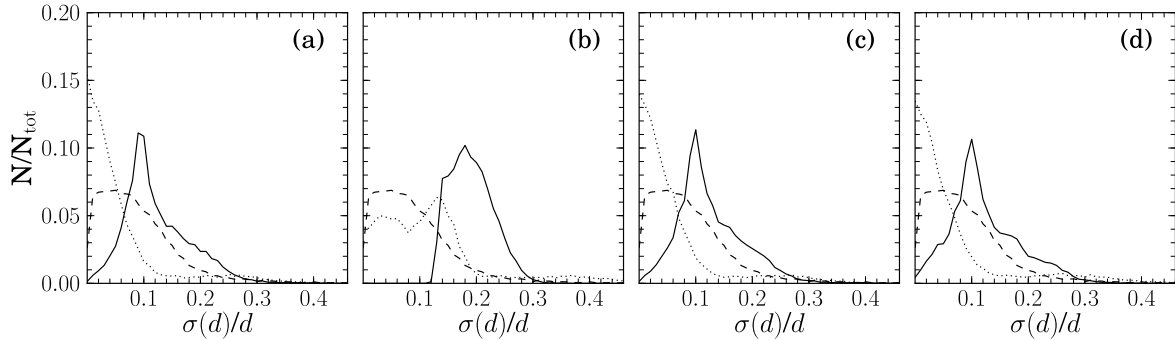


**Figure 4.1:** Distribution of distance uncertainties computed according to the different parameter sets introduced in Section 4.1.2. Parameter sets 1 to 4 correspond to panels (a) to (d). *Solid line:* rms uncertainty based on the model pdf, *dotted and dashed lines:* *internal* and *external* error as defined in the text. The plotted uncertainties are those of the stars in the final SEGUE G-dwarf sample described in Chapter 3.

### 4.1.3 Uncertainties

With respect to the calculation of realistic distance uncertainties Santiago et al. (2016) exploits several directions which result in three different reported error estimates for each star: (1) the *rms uncertainty* that is based on the second-order moment taken over the posterior probability distribution (Equation 4.4) and calculates as  $\sigma_d^2 = \langle d_2 \rangle - \langle d_1 \rangle^2$  where  $\langle d_2 \rangle$  is the second and  $\langle d_1 \rangle$  the first order moment of the PDF, (2) an *internal uncertainty* that is given by the difference between the weighted average distance (1st moment) and the distance corresponding to the peak in the multivariate model probability distribution which is defined by the model with the highest posterior probability. As such this internal estimate is ideal to get a hint on the complexity of the model pdf. The uncertainty should for example be small for a single peaked, widely symmetric PDF, and (3) an *external uncertainty* which is the maximum difference among the four distance estimates based on the different parameter sets (1 to 4). This external uncertainty helps to shed light on the actual sensitivity of the distance estimates to the set of used observables.

Figure 4.1 illustrates the distribution of relative uncertainties for the sample of SEGUE G-dwarfs. Each panel corresponds to one of the four different choices of  $\mathbf{y}$  listed in Section 4.1.2. The *rms*, *internal* and *external uncertainties* are represented by the solid, dotted and dashed lines, respectively. It is striking that in panel (b) the *rms* and the *internal* uncertainties tend to be larger when no colour information is used in the distance determination. The apparent increase may result from the comparatively larger uncertainties in the spectroscopic (especially true for the SEGUE  $\log g$  estimates) than photometric parameters. Besides, the *rms* distribution for all panels, but panel (b), shows a clear asymmetry. The fact that stars with lower  $\log g$  values, at the transition from dwarf to sub-giant stars, exhibit distinctively larger distance errors is one of the main points discussed in the next section. They are shown to cause the tail in the *rms* distribution.

### 4.1.4 Method validation

For the purpose of validation the BPG distance estimates have been compared to independent distance measurements based on astrometric parallaxes, asteroseismology and cluster isochrones for a couple of reference samples from several surveys covering both, the optical and NIR. These references comprise (1) a sample of 582 very nearby ( $d < 60$  pc) FGK stars from the Hipparcos

**Table 4.1:** Properties of reference star clusters observed with SEGUE. Cluster distances (distance moduli), ages and mean metallicities are taken from the WEBDA database in case of open and the Harris (1996) catalogue for globular clusters.

cluster	$m - M$	$\log(\tau)$	[Fe/H]	$E(B - V)$
M2	15.30	> 10	-1.65	0.04
M3	15.04	> 10	-1.50	0.01
M13	14.26	> 10	-1.53	0.01
M15	15.08	> 10	-2.37	0.10
M67	9.79	9.41	0.00	0.03
M92	14.59	> 10	-2.31	0.02
NGC2420	12.45	9.05	-0.26	0.04
NGC6791	13.06	9.64	+0.15	0.14

mission (ESO-HARPS Sousa et al. 2011), (2) a sample of 120 red giant stars in the CoRoT field LRa01 with  $\log g$  and distance estimates derived from CoRoT lightcurves (Miglio et al. 2013a,b) and complementary spectroscopic parameters from APOGEE (Ahn et al. 2014, ASPCAP), (3) the RAVE giant star sample discussed in Boeche et al. (2013a) and (4) stellar members of well studied open and globular clusters (with observations from APOGEE and SEGUE). In a nutshell, the quantitative comparison of all references shows that the adopted method does perform well, not only in a relative but for most comparison samples also in an absolute sense. Despite a clear one-to-one correlation, the typical relative random scatter in distance for the HARPS stars with parallaxes and precise atmospheric parameters is 20% or less, with a slight systematic trend to underestimate the distances by approximately 10%. A reassuring behaviour is also seen for the stars in the CoRoT sample indicating a small shift in the absolute scale of about 15% and a similar amount of rms scatter ( $\leq 20\%$ ) that increases for stars with  $d > 3$  kpc. Moreover, a reasonable agreement within the expected uncertainties with only a small systematic trend but a large scatter is seen for the RAVE giant stars when comparing the BPG and the Binney et al. (2014) distances that originate from a similar approach. Additional to the external observational references, the code was tested on a set of simulated mock stars from PARSEC models well recovering the input distances without showing systematics. As expected though, the errors in the BPG distance estimates to the mock stars increase with increasing uncertainties in the observables,  $T_{\text{eff}}$ ,  $\log g$ , [Fe/H] used in the computation. A detailed discussion of the complete reference set can be found in Santiago et al. (2016) Section 3 or in Section 4.1.6 of Anders (2013). The present work focusses on the reference sample of stellar clusters with SEGUE observations.

### SEGUE - cluster comparison

Figure 4.2 illustrates how for a subsample of cluster stars with SEGUE observations the spectrophotometric BPG distances compare to the host cluster distances which are obtained from isochrone-fitting and publicly available from the literature. Pertaining to the cluster properties, all needed reference information, e.g., cluster age, distance and main metallicity are retrieved from the WEBDA database (Paunzen 2008) in case of open clusters and from the Harris (1996) catalogue for globulars. As the main source for information on the spectroscopic and photometric parameters of the individual cluster stars serves the SDSS data published as part of DR9 (Ahn

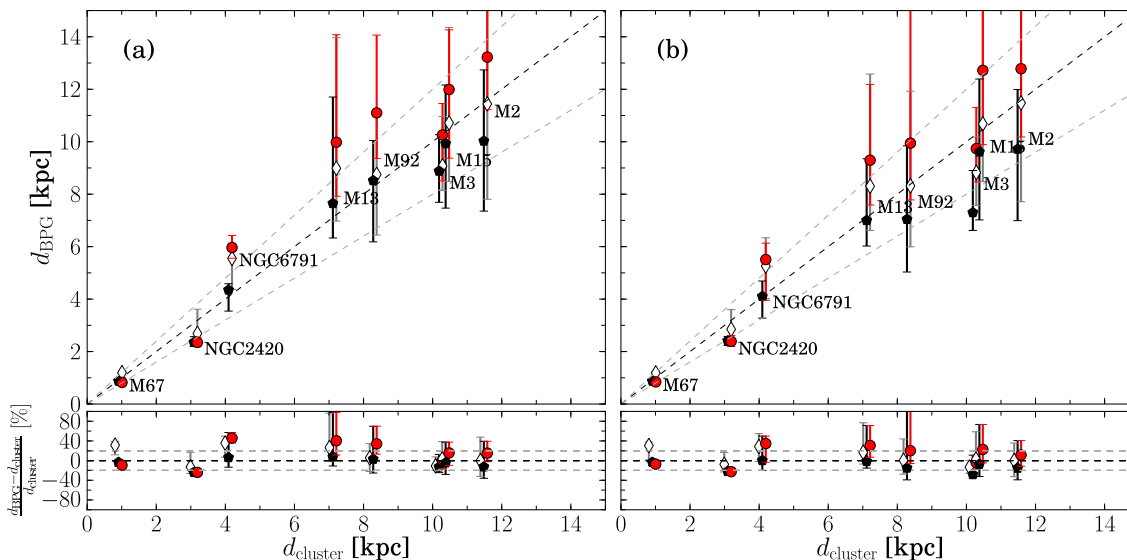


**Figure 4.2:** Comparison of the BPG distances and the host cluster distances obtained from isochrones for a subsample of clusters with SEGUE observations. Panels (a) and (b) represent the results based on the parameter sets 1 and 2 as defined in Section 4.1.2. For each cluster the median distance and the 60% quantiles (as error bars) are shown assuming the following different scenarios: *open diamonds* - uncalibrated SSPP DR9 parameters with field priors, *black pentagons* - a  $\log g$  shift of 0.25 dex and field priors and *red circles* - a shifted  $\log g$  and a simple prior in cluster age. For visibility the different symbols are offset with respect to  $d_{\text{cluster}}$ .

et al. 2012). As a necessary step the photometry is corrected for extinction and reddening and  $[M/H]$  values are calculated according to Equation 4.8 employing the individual  $[\alpha/Fe]$  information for each SEGUE object. The final sample of considered SEGUE clusters holds eight star clusters as labeled separately in Figure 4.2. Each of them possess at least five confirmed members with successfully determined BPG distances. Table 4.1 lists the main properties of these eight clusters which are selected from the full cluster sample that comprises 11 clusters with members observed by SEGUE adding up to a bit more than 1000 stars. Part of those cluster stars have also been used as reference objects to calibrate the SSPP (Lee et al. 2008b). In the present case however the complete set of spectroscopic and photometric parameters with associated uncertainties could only be acquired for 593 of the above mentioned cluster members. For most of the remaining stars no SDSS *ugriz* photometry was available from the SDSS database preventing the usage of parameter set 1 (see Section 4.1.2), hence leading to their disregard.

For those stars with valid distances panel (a) and (b) of Figure 4.2 exemplarily represent the cluster comparison with distances based on parameter sets 1 and 2. Each cluster is indicated by its cluster-averaged spectro-photometric distance estimate, with three of them having mean distance estimates below 6 kpc. As further discussed below the various symbols encode different  $\log g$  calibrations and priors used in the distance determination process illustrating and underlining the importance and influence of quantities such as the surface gravity. In case of the open diamonds that correspond to the usage of the original SEGUE data taken from DR9 there is a clear correlation with no strong systematic in the estimated distances for the three closest clusters but the code tends to overestimate the distances by roughly 25% to 30% for a significant fraction of the stars in the more distant globular clusters beyond 6 kpc. Part of that systematic overestimation is likely caused by the SEGUE DR9  $\log g$  scale which, as investigated and dis-

**Table 4.2:** Summary of the mean ( $\Delta d$ ) and rms relative residuals ( $\sigma_{\Delta d}$ ) for the SEGUE cluster distances individually listed for the parameter set 1 and 2 and obtained for the different computation options as discussed in the text and depicted with separate symbols in Figure 4.2. Also given is the total number of stars with successful distances.

SEGUE clusters with	$N_{\text{tot}}$		$\Delta d \pm \sigma_{\Delta d}$ [%]	
	Set 1	Set 2	Set 1	Set 2
field priors	419	537	$14 \pm 43$	$10 \pm 39$
log $g$ shift by +0.25 dex, field priors	425	547	$-2 \pm 35$	$-8 \pm 31$
log $g$ shift by +0.25 dex, age priors	385	515	$13 \pm 39$	$10 \pm 44$

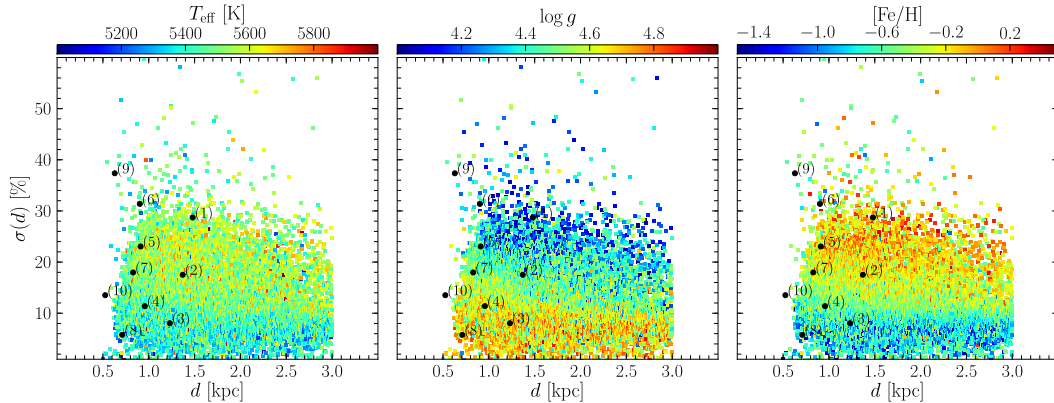
cussed in Section 3.3.1, exhibits an offset compared to the DR8 scale, obviously underestimating the surface gravity by about 0.2 dex to 0.3 dex. Replacing the DR9 gravity with the DR8 values as a sanity check results indeed in a much better match to the model values. Also, as shown later in Chapter 6 (Figure 6.10) the apparent discrepancy is supported by predictions from TRILEGAL, a population synthesis model, which reveals that there is a non-negligible systematic shift between the SSPP DR9 scale and the theoretical Padova stellar evolutionary models. Demonstrably, the log  $g$  values for SEGUE main-sequence and subgiant branch G-type stars are lower by about 0.25 dex than the surface gravities of a comparable sample of TRILEGAL G-type mock stars whose stellar parameters are based on stellar evolutionary tracks of similar metallicity and temperature. The lower surface gravities tend to make the stars overluminous putting them to larger distances because their parameter sets are more frequently matched to subgiant and giant models. Correcting for this effect by applying a shift of 0.25 dex to the log  $g$  values of the cluster members reduces the systematics at larger distances to roughly 15% with a clear improvement for the recovered cluster mean distances as demonstrated by the black pentagons. The global mean offset relative to the reference distance is reduced, although the rms relative residual remains high. The plot also shows the results when adopting a simple cluster age prior (red circles). The age prior has a sizeable effect on the distance estimates in the sense of increasing them in particular for the more distant clusters. For more details Table 4.2 lists the total number of stars with successful distances, the mean relative distance residuals,  $\Delta d$ , and the corresponding rms scatter,  $\sigma_{\Delta d}$ , for each of the different calculations represented by the three symbols.

In conclusion, there is a general agreement between the BPG distances and those from CMD fitting as long as the SEGUE DR9 surface gravities are calibrated. This is especially true for the three nearer clusters below 5 kpc where the rescaling in log  $g$  has only a small effect. The problematic overestimation for the more distant cluster resides, specially if the DR9 log  $g$  data is used without recalibration, but is momentarily put aside as distance estimates up to 3 kpc are the only ones necessary for this work.

#### 4.1.5 Distances for SEGUE G-dwarfs

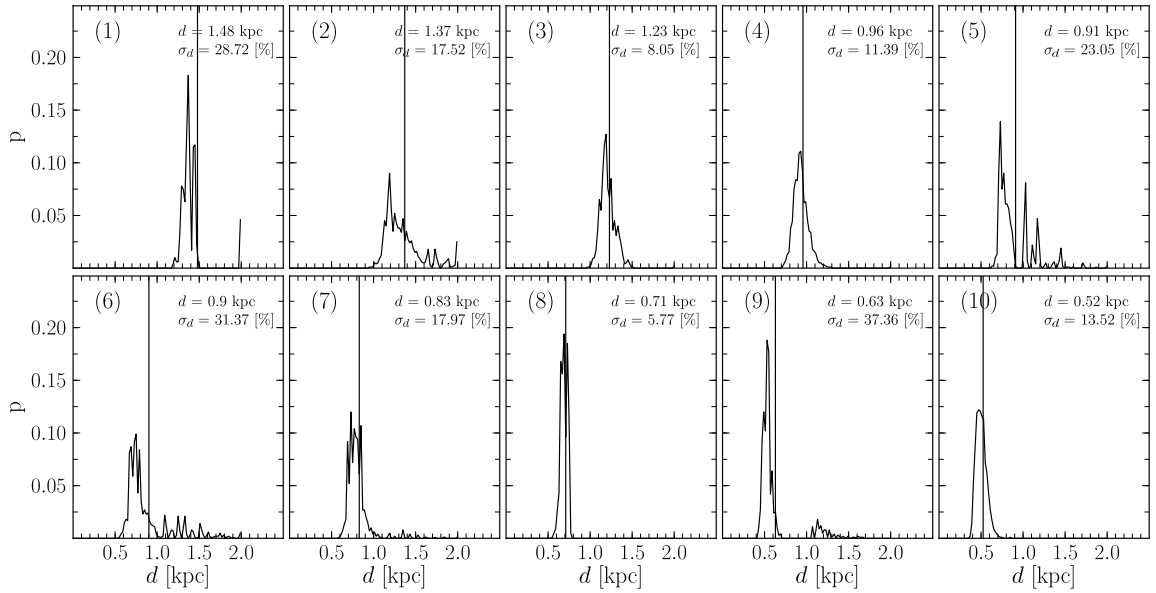
Distances for this thesis' main stellar sample of 35 009 SEGUE G-type field stars as defined in the previous chapter are computed by following the same procedure as for the SEGUE cluster stars, thereby adopting the setup that uses field priors and the recalibrated DR9 surface gravity values. As demonstrated by means of the cluster stars the applied calibration in log  $g$  is a necessary step, at least, to guarantee reliable distances to the SEGUE stars.

Figure 4.3 shows the BPG distances as a function of their uncertainties for the final selection



**Figure 4.3:** BPG distance estimates for the sample of SEGUE G-dwarfs as a function of their uncertainty (relative scale). The dependency on the three main stellar parameters  $T_{\text{eff}}$ ,  $\log g$  and  $[\text{Fe}/\text{H}]$  is separately shown in colour code. The 10 stars representing the test sample as mentioned in the text are indicated and labeled with individual numbers.

of SEGUE G-dwarf stars. From left to right the panels illustrate how both quantities depend on the three stellar parameters  $T_{\text{eff}}$ ,  $\log g$  and  $[\text{Fe}/\text{H}]$  that are indicated by the colour coding. The distances of the G-dwarf sample are a combination of estimates originating from parameter sets 1 and 2. For a small percentage of stars the distance code failed to predict an estimate based on both, the spectroscopic and photometric information which is why the set 2 estimates are used in cases where the set 1 distance is missing. The uncertainties plotted in relative scale on the  $y$ -axis are the internal rms errors based on the second-order moment of the posterior PDF. For consistency, the rms uncertainty is used as the standard error estimate for all stellar distances to the observed stars presented and analysed in this work. From Figure 4.3 and 4.1 it is evident that the majority of SEGUE G-dwarfs have distance errors around 10%. However, for stars with lower  $\log g$  values, higher metallicities and temperatures there is a general tendency to possess an uncertainty above 10% which causes the tail towards 20% or higher in the rms distribution (solid line) of panel (a) in Figure 4.1. In addition, Figure 4.3 shows a slight flaring in the relative uncertainties for the closer stars indicating that the absolute uncertainties seem to be independent on the distance itself and off the same order for near and far G-dwarfs with comparable stellar parameters. As a natural consequence this leads to larger relative errors if the actual distance is small. The reason why predominantly the G-dwarfs at the lower  $\log g$  limit of the sample experience larger distance errors is that those stars are the most likely to be effected by luminous and evolved stellar evolutionary models during the distance determination. Depending on the extent of their uncertainties in the stellar parameters, they may be part of the transition region between dwarf and giant stars rather than the main sequence. The fact that actual G-dwarfs may be (miss)interpreted as subgiants results in posterior PDFs that are more complex, even double peaked, which leads to larger uncertainties in their distances and to the observed behaviour. In order to further investigate this issue a sample of 10 randomly chosen test stars has been selected with distances below 1.5 kpc and relative uncertainties between 8% and 40%. The position of these stars is given in Figure 4.3 each of them labeled with an individual number. Assuming that the distance determination for stars with lower  $\log g$  is influenced by a larger variety of stellar models there should be a clear difference in the distance PDFs for the test stars 1, 5, 6 and 9 when compared to those of the remaining test objects. And indeed, Figure 4.4 reveals that the few stars with clear substructure in their marginalised distance PDF have the largest



**Figure 4.4:** Set of marginalised PDFs (see description and details in the text) for the sample of 10 chosen test stars. The average-weighted BPG distance estimate, determined as the 1st order moment of the posterior PDF over all stellar evolutionary models within  $3\sigma$  of the data, is marked in each panel by the solid line. Its value and uncertainty is also given in the upper right corner.

relative distance errors and belong to the group of stars closer to the subgiant region. Basically, the marginalised PDF is the integral of the multivariate posterior PDF over the entire parameter space except for the absolute magnitude and hence distance. And in practice, the presented PDFs are computed by binning the evolutionary models according to the distance estimate they yield for a given star, adding their unnormalised posterior probabilities in each bin and dividing the result by the sum of the unnormalised posterior probabilities over all models. The solid vertical line marks the average BPG distance which, in most cases, does not correspond to the main peak of the marginalised PDF. A fact that is expected because the multiple peaks of the marginalised PDF correspond to models with very different absolute magnitudes assigned to them but with sizeable posterior probabilities. Certainly, a fraction of models for giant stars have significant probabilities producing a higher tail in the distance distribution. The degree of the giant models contaminating the distances of the SEGUE G-dwarf sample should, as already mentioned above, relate to the uncertainties in the observables. Pertaining to this, Figure 4.5 gives a good illustration on how the errors in the stellar parameters can have an impact on the distance determination of particular stars in the sample. Again the 10 test stars are indicated with their individual uncertainties (i.e., combining the internal and external SSPP error to a total error) in temperature and surface gravity plotted as errorbars. In retrospect, the applied total errors may have been a too conservative assumption. A reduction of the errors using the internal uncertainties of the SSPP as estimated based on the duplicate spectra and later done in Chapter 6 for the TRILEGAL mock sample would have certainly helped to narrow down the range of models that are considered within the distance code for each star. To conclude, the errors in the observables are essential because the distance method is very sensitive to their extent. How sensitive is illustrated in Santiago et al. (2016) Section 2 by means of a simulated sample of mock stars with varying uncertainties in the stellar parameters.

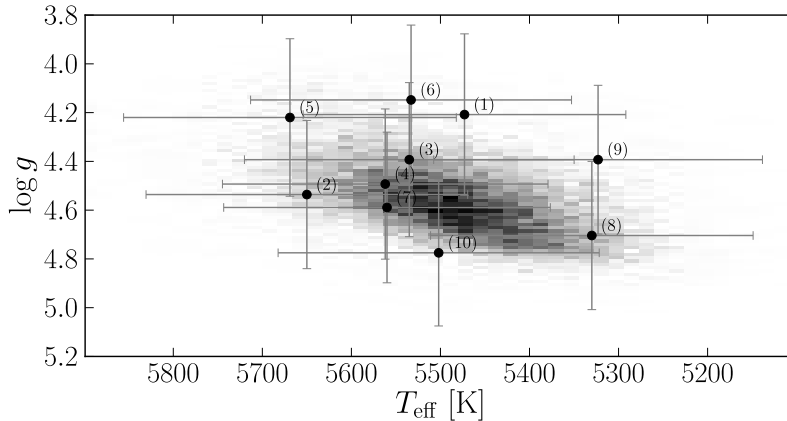


**Figure 4.5:** The SEGUE G-dwarf sample in the  $T_{\text{eff}}\text{-log } g$ -plane. Additionally indicated are the positions and the extent of the stellar parameter uncertainties for the 10 test stars whose marginalised distance PDFs are shown in Figure 4.4.

## 4.2 Proper motions

Besides the distance the proper motion is the second crucial quantity that affects the determination of the stellar kinematics because it is comparably uncertain with respect to the radial velocity or spatial positions of the star. At present the two proper motion catalogues with sufficient sky coverage are the PPMXL (Roeser et al. 2010) and UCAC-4 (Zacharias et al. 2013). Even though they could have been used to homogeneously obtain proper motion estimates via crossmatch for both, the analysed RAVE and SEGUE sample, it has been decided to rely on the proper motions provided as part of the surveys’s data products. Hence the employed astrometric source catalogues vary for the different samples that are discussed in the following chapters. While the current section gives more details on the proper motions released by the SDSS collaboration the specifications on the sources used for the RAVE sample can be found in Chapter 8. How proper motions are obtained for the theoretical comparison samples of G-dwarf mock stars (from TRILEGAL and GALAXIA) is clarified in Chapter 6 and 7.

### Computation of proper motions for SDSS objects

As most of the SDSS footprint is imaged only once in the course of the whole project proper motions can not be obtained from the SDSS photometry alone. Instead, the SDSS collaboration has created a proper motion catalogue by matching the SDSS observations to catalogues of objects derived from surveys that rely on photographic Schmidt plates (e.g. POSS I+II). Munn et al. (2004) gives an overview on how SDSS proper motions are generally computed by combining the SDSS astrometry with positions from the US Naval Observatory (USNO)-B catalogue (Monet et al. 2003). The USNO-B is an all-sky catalogue that provides positions, proper motions and magnitudes in various optical bands and it is a compilation of digitalised photographic plates from several surveys conducted during the past 50 years. Before SDSS proper motions could be computed based on a linear fit to the USNO-B positions in each epoch on the one hand and the SDSS positions on the other hand, the object positions on the USNO-B plates had to be recalibrated using SDSS astrometry of galaxies that provide a stationary reference frame. This procedure allows to obtain absolute instead of relative proper motion estimates. The combination of the two catalogues also has a positive effect on the uncertainties. Due to the recalibration with SDSS astrometry the systematic USNO-B errors are replaced by the smaller systematic errors in

more accurate SDSS positions. Also the statistical uncertainties are decreased by roughly 20% (Munn et al. 2004). As both catalogues share the same errors after the recalibrational process the systematic errors cancel out in the proper motion determination when combining both catalogues. Besides, the larger errors on the photographic plates are compensated by far by the long baseline that results from the large epoch difference.

### Calibration and improvement of the SDSS astrometry in DR9

In case of DR9 the SDSS astrometry is calibrated against the Second USNO CCD Astrograph Catalogue (UCAC2, Zacharias et al. 2004) and has been fundamentally improved with respect to DR8 where the imaging suffered from several errors in the astrometric calibration as described in an erratum Aihara et al. (2011b) published shortly after the DR8 data release. Specific information on the changings and improvements can be found in Ahn et al. (2012). In detail, UCAC2 provides positions and proper motions that are supplemented with 2MASS photometry for over 99% of the objects and the current epoch positions of the catalogue are CCD based and obtained with USNO 8 inch Twin Astrograph. In the calibration process the UCAC2 positions are first propagated to the SDSS epoch using the UCAC2 proper motions for declinations up to  $41^\circ$  north. Further, as UCAC2 does not cover the whole sky an ‘internal’ UCAC data release, called r14, is used as supplement. Both together allow full sky coverage. Then the bright stars detected on the SDSS r-band CCDs are directly matched to stars in the UCAC astrometric reference catalogue having a precision of 70 mas at the catalogue limit of  $r = 16$  and a systematic error of less than 30 mas. A more detailed description of the astrometric calibration is given in Pier et al. (2003).

## 4.3 Space motions

Given the BPG distances as determined and discussed in Section 4.1.5 and the line-of-sight velocities and proper motions from DR9, the stellar space velocity in the Milky Way’s Galactic coordinate system is calculated for each star in the G-dwarf sample. The components  $U$ ,  $V$ ,  $W$  are derived by taking into account that the peculiar motion of the Sun with respect to the Local Standard of Rest (LSR) is  $(U, V, W)_\odot = (11.10, 12.24, 7.25) \text{ km/s}$  (Schönrich et al. 2010). Additionally, for all stars in the sample the position in Galactocentric Cartesian coordinates  $(x, y, z)$ , the Galactocentric radial distance,  $R$ , and the velocities  $v_R$  and  $v_\phi$ , which are the radial velocity and the rotational velocity around the Galactic centre, are obtained by assuming  $R_\odot = 8 \text{ kpc}$  and  $V_{\text{LSR}} = 220 \text{ km/s}$ . Uncertainties for positions and velocities are determined performing a Monte Carlo simulation with 100 realisations for each star in a similar manner as in e.g. Gratton et al. (2003) or Boeche et al. (2013a). In the simulation, the initial values for distance, radial velocity and proper motion (input parameters) are varied according to their individual uncertainties which are used as the  $1\sigma$  of a normal distribution assuming that the uncertainties of all quantities follow a Gaussian behaviour. Most likely the errors in distance are not Gaussian but the assumption is made for simplicity. From the 100 realisations an average value and a standard deviation as uncertainty is finally computed for each quantity.

## 4.4 Orbits

Disentangling the stellar populations of the Galaxy by means of their orbital characteristics has become a powerful tool in Galactic chemo-dynamical analysis. In the scope of this thesis the

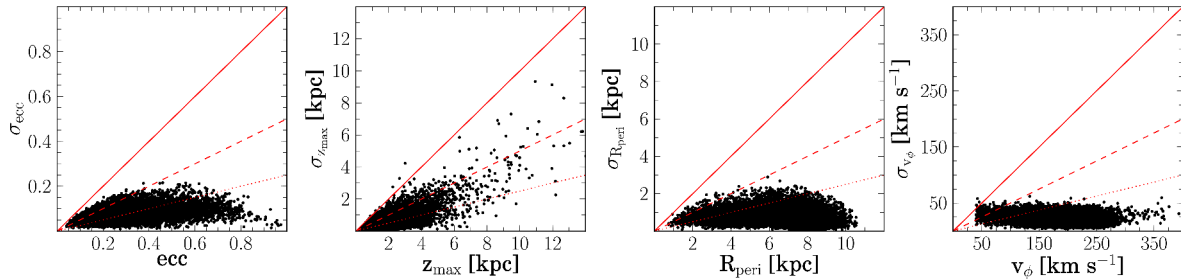


**Figure 4.6:** Comparison of stellar orbital parameters and their uncertainties. Both, parameters and uncertainties, are determined via Monte Carlo. The solid, dashed and dotted red lines represent the 100%, 50% and 25% error.

orbit parameter calculation for any of the analysed samples is based on the `GALPY`<sup>2</sup> python module (Bovy 2015). By use of the complete set of phase space information (RA, DEC,  $d$ ,  $\mu_{\text{RA}}$ ,  $\mu_{\text{DEC}}$ ,  $v_{\text{los}}$ ) and the `SCIPY` routine `odeint` individual orbits are numerically integrated for each star over a time of at least 2.5 Gyrs or 6 radial turns around the centre of the Galaxy. Thereby, the time step size for the integration is defined that small that smooth and stable orbits are guaranteed. From the resulting orbits quantities like the peri-,  $r_{\text{peri}}$ , and the apocentre,  $r_{\text{apo}}$ , radius, are obtained which represent the star’s maximum and minimum distance from the Galactic centre. Additionally, the maximum height above the Galactic plane,  $z_{\text{max}}$ , reached by the star along its orbit, and the eccentricity,  $e$ , are determined with the latter being defined as  $e = (r_{\text{apo}} - r_{\text{peri}})/(r_{\text{apo}} + r_{\text{peri}})$ . The assumed potential for the Galaxy is a standard three-component Galactic potential, composed of a Hernquist bulge (Hernquist 1990), a Miyamoto-Nagai disk (Miyamoto & Nagai 1975) and a NFW dark-matter halo (Navarro et al. 1996) which is defined such that the model Galaxy’s rotation curve is recovered to be flat and the circular velocity at the solar position is  $v_{\text{circ}}^{\odot} = 220 \text{ km/s}$ . The values for the solar motion and the position and velocity of the Sun are the same as in Section 4.3.

### Uncertainties

Both, the final value and the uncertainty of each parameter that is extracted from the orbits is determined via Monte Carlo similar to the procedure described in the previous section. Figure 4.6 shows a suite of orbital parameters as a function of their corresponding uncertainties for the sample of SEGUE G-dwarf stars. The solid, dashed and dotted red lines represent the 100%, 50% and 25% error. Considering that the orbit integration depends on two rather uncertain quantities, the distance and the proper motion, the plot illustrates that the overall cut in distance at 3 kpc and the restriction in proper motion error at  $5 \text{ mas/yr}$  still allow to obtain orbital parameters for the SEGUE stars with acceptable errors.

<sup>2</sup>Documentation and source code can be found at <https://github.com/jobovy/galpy>.

---

## Chemo-kinematic constraints from the SEGUE G-dwarf sample

---

In the chapter at hand the focus is given to the investigation and consideration of the selection effects and observational biases that affect this work's selection of SEGUE G-dwarfs and that need to be accounted for before drawing any scientific conclusion. While the first part of the chapter is dedicated to the analysis of the present biases and the development and application of proper corrections to the sample of G-dwarf stars itself, the second part goes beyond this by dealing with the deduction of chemo-kinematic constraints to be compared with model predictions at face value.

It turns out that the main biases to be discussed in the following are associated with (a) the selection procedure of the survey (spectroscopic target list and target sampling), (b) the relationship between the stars observed by the survey and the underlying stellar population the targets were selected from and (c) the partial volume coverage of the survey which is missing the close parts of the disk. Due to the combination of the previously mentioned selection effects the characteristics of any stellar spectroscopic sample (a subsample representing only a portion of the underlying photometric population) do not properly reflect those of the parent population. But how representative is a spectroscopic object and its properties than?

Only an unbiased view can help to constrain common models which try to explain the dominant processes involved in the formation and evolution of the Milky Way. To infer new insights on the stellar properties and chemo-dynamics of the Galaxy a new and challenging approach is thus taken in this thesis and presented in this chapter. The observed SEGUE G-dwarf sample is corrected in such a way that its properties resemble the stellar structure of the global volume around the Sun, which in theory can then be directly compared to the quantitative predictions from models, e.g., the chemo-dynamical model presented in Minchev et al. (2013) which is considered in this thesis. Thereby it is essential that each applied selection effect correction is critically reviewed with respect to its validity and reliability because, as outlined later, some corrections are extremely model dependent and based on strong assumptions. However, this new approach of fully correcting the dataset is only one among various ways. Another is presented in Chapters 6 and 7 which, instead of correcting the data, deals with mock versions of the G-dwarf sample to be discussed and compared to different models. As such the forthcoming two chapters are meant to complement this chapter's results.

## 5.1 Accounting for selection effects and biases in the SEGUE G-dwarf sample

Numerous selection biases have been identified to particularly impact the SEGUE G-dwarf sample. Common to many of them is their falsifying influence on the metallicity distribution function. Because SEGUE aims to address a variety of scientific questions the survey targeting concept embraces a larger number of target categories. Every type covers a different portion of the parameter space. The stellar range of metallicity and age is thus not sampled equally for all stellar categories which has a net effect of favouring metal-poor stars for the entire sample. The main metallicity biases introduced by the original SEGUE target selection are listed below:

1. The G-dwarf colour range is overlapping with colour-magnitude criteria of other SEGUE target categories such as K-dwarfs, K-giants and low metallicity stars. All of which are biased toward metal-poor stars, this leading to a bias in metallicity.
2. By construction, the amount of spectroscopic fibres is for each line-of-sight limited to the same number regardless of the stellar density in the observed region on the sky. This leads to a metallicity bias in favour of low metallicity stars.
3. The  $(g - r)$  colour cut to select G-dwarfs isolates a different stellar mass range at each metallicity which results in a bias against metal rich stars because lower mass stars are more abundant than high mass stars in a given volume and the cut preferentially selects low mass stars in the low metallicity regime.

Biases (1) to (3) are complemented by a selection effect that arises due to the limited survey volume which in case of SEGUE has a cone like shape around the Sun. The survey volume has direct influence on the ratio of observed metal-rich to metal-poor stars which for SEGUE thus differs from the ratio that one would infer from stellar number counts in a more general volume around the Sun. Basically, metallicity distribution functions can be significantly tampered depending on the survey under investigation and its covered volume.

All of those mentioned selection effects have to be accounted for in order to correctly reproduce the chemical and kinematic properties of the studied G-dwarfs in the Galactic disk. A detailed description on how those biases can be corrected is hence given in the next subsections. These parts of the chapter also shed light on the different methods described in Bovy et al. (2012c,a) and Schlesinger et al. (2012), two authors that have developed selection bias corrections for SEGUE stars and that serve as example and measure for this thesis. In particular, the corrections developed and computed by Jo Bovy are of special interest. The present thesis greatly benefits from his preliminary work and kindness to support the following study with selection effect corrections that are based on his original methods that are extensively laid out in Bovy et al. (2012c,a) and Rix & Bovy (2013). In a joint effort the corrections have been tailored to be specifically valid for the particular set of stars analysed in the current work. As such those adoptions are a main part of this thesis. Changes and variations from the original methods are indicated along with the descriptions in this chapter.

As explained in Chapter 3 selection effects in a sample can not only originate from the survey's observing structure and selection algorithms and decisions itself. The scientific user can introduce additional biases into its selection of stars by choosing particularly those stars with high quality stellar parameters. Since resulting biases are hard to quantify they will not be investigated and specifically corrected within the framework of the following chapters. Yet, possible implications will be outlined during the analysis whenever it is necessary.

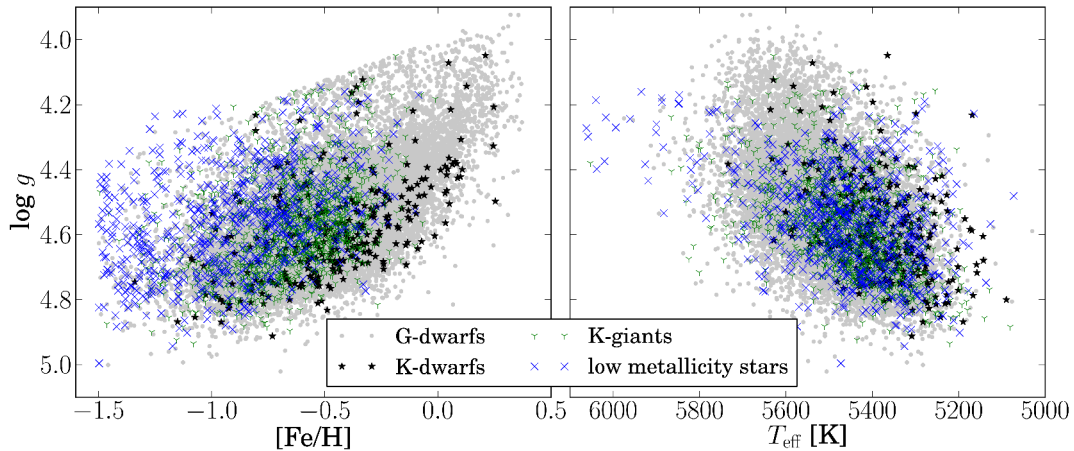


**Figure 5.1:** Overlap of different SEGUE target type categories with the G-type star category. Displayed are the stars of this work’s G-dwarf sample. The majority of stars has originally been targeted as G-type candidates (grey dots). Still, around 2 400 stars have been assigned fibres in one of the overlapping categories (see legend).

### 5.1.1 Correction for the SEGUE target-type

As a result of the survey targeting scheme the selection criteria for different SEGUE stellar target-type categories, being mainly cuts in the colour-magnitude and proper motion parameter space, overlap. Thus, in the target selection process each photometrically observed SDSS object that satisfies the criteria of more than one SEGUE target-type category is considered as possible candidate for several spectroscopic stellar samples. In case of the G-dwarfs their specific colour-magnitude range overlaps with the parameter space of the low metallicity star and K-giant target categories. Both of them are biased towards lower metallicity objects. A contamination by those categories may hence bias the G-dwarf sample in favour of low metallicity stars. Figure 5.1 illustrates the composition of the G-dwarf sample assembled in this work. The majority of the stars has been originally targeted in the G-star category. Nevertheless approximately 2 400 stars were assigned to fibres in different categories. The location of those stars in the plot confirms that the contaminating categories are biased towards metal-poor stars. The effect of other target types within the SEGUE G-dwarf sample (only essential for samples purely selected based on photometry) has been previously studied by Schlesinger et al. (2012) concluding that G-dwarfs are only mildly affected by the metallicity bias. One reason for this is that G-dwarfs are allotted more SEGUE fibres in general reducing the number of stars with equal properties that have been assigned to other categories. Nevertheless, target-type weights for the entire SEGUE G-dwarf sample (selected from DR9 using bitmasks in `segueTargetAll`) are publicly available and can be downloaded as a value added catalogue from the SDSS SEGUE webpages<sup>1</sup>. A detailed description on the computation of those target-type weights is given in Section 4.7.1 of Schlesinger et al. (2012). Figure 5.2 shows the metallicity distribution function for the sample in Figure 5.1 after and before application of the weights. The change in the overall distribution is indeed marginal. Compared to the corrections that compensate for the selection function or the survey volume the target-type weights have small impact on the shape of the MDF. Since they are not available for all stars in this work’s G-dwarf selection the target-type correction is neglected in all further steps of the analysis.

<sup>1</sup>[http://www.sdss3.org/dr10/data\\_access/vac.php](http://www.sdss3.org/dr10/data_access/vac.php)

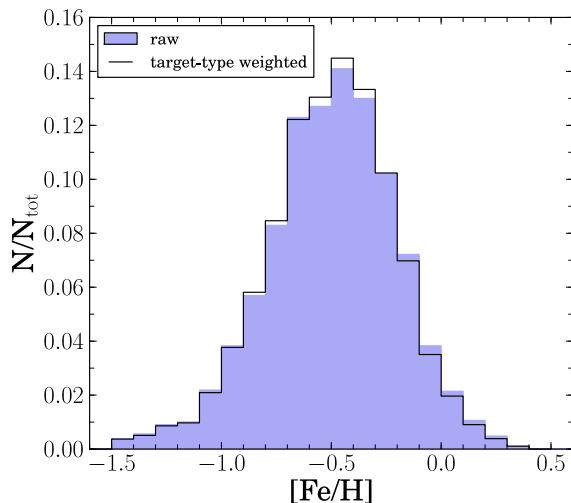


**Figure 5.2:** Metallicity distribution function for the SEGUE G-dwarf sample. The two histograms show the raw distribution (filled histogram) on the one side and the sample’s distribution after application of the target-type weights from Schlesinger et al. (2012) on the other side. Target type weights for the SEGUE G-type stars have been provided in a value added catalogue (see text and footnote).

### 5.1.2 Correction for the SEGUE selection function

One key aspect in order to obtain a realistic picture about the spatial distribution of the G-dwarfs is to understand the SEGUE selection function. This function is defined as the fraction of spectroscopically observed SEGUE targets with respect to the number of objects in the underlying photometric population. The observed number of G-type stars is then the underlying number of stars multiplied with the sampling selection function. In the case of SEGUE the selection function is strongly influenced by the limited and fixed number of spectroscopic fibres available for each line-of-sight. This fact leads to the undersampling of regions with high stellar density that are mostly located at low latitudes and dominated by high metallicity stars. Consequently, the more metal-poor stars at high latitudes are favoured and a bias is introduced against high metallicity stars in the MDF of the entire survey. This incompleteness of the spectroscopic survey can be corrected by comparing the spectroscopic number density with the number counts gained from the complete SDSS photometry for the underlying population in the same volume. To deal with this issue, two different methods have been laid out in the recent literature that present weights to correct for the selection function of the survey. In what follows, both are briefly discussed.

#### Selection function weights

To account for the fact that SEGUE does not have an unlimited amount of fibres the study presented in Schlesinger et al. (2012) calculates and uses the so called “ $r$ -magnitude weights”. Because each line-of-sight possess a different distribution of stellar spectral types and number of stars the weights are determined on a plate-by-plate basis. For each plate the number of spectroscopic G-type targets is compared in  $r_0$ -magnitude bins of width 0.5 to the photometric population of stars that satisfy the colour-magnitude criteria of G-type stars. The inverse of this ratio is the weight that is assigned multiplicatively to each spectroscopic target to resemble the photometric parent distribution.

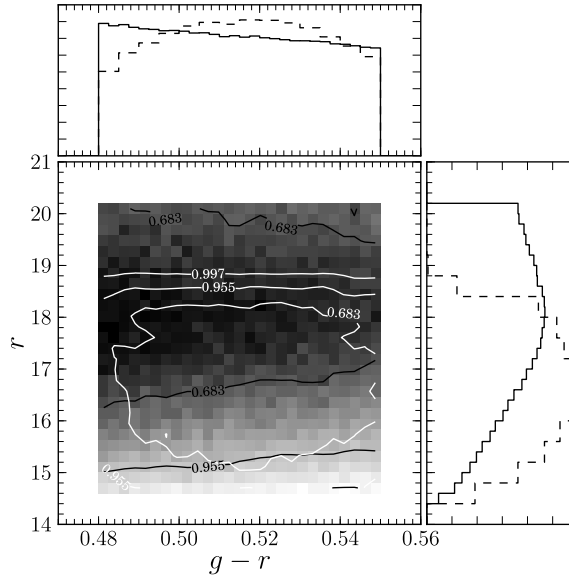


**Figure 5.3:** Number density distribution of the photometric sample of SDSS G-type star candidates (linear density grey scale, black contours, solid histogram) falling within the SEGUE G-star colour-magnitude target selection box defined by  $0.48 < (g-r)_0 < 0.55$  and  $r < 20.2$ . Overplotted is the spectroscopic G-type star sample (white contours, dashed histogram) being selected from DR9, cut in signal-to-noise at  $\text{SNR} > 20$  and limited to objects with an extinction of  $E(B-V) < 0.3$ . As indicated in both cases, the contours contain 68 %, 95 % and 99 % of the distribution.

In addition to the problem of limited fibres another important aspect of the selection function is that the spectroscopic objects cover a limited range in magnitude which is defined by the SNR that still allows to determine reliable stellar parameters from the spectra. The effect of a SNR limit on the spectroscopic stellar sample of SEGUE G-stars has been investigated in detail by Bovy et al. (2012c). Due to its importance the effect of the SNR is shortly discussed below, along with a general description of those steps that are undertaken to determine the individual selection function weights needed for this work’s analysis. As mentioned before this part is strongly geared to the work by Jo Bovy.

Because the surface gravity is not determined in advance for the targets that are assigned fibres in SEGUE, correction weights are calculated for all suitable objects, i.e. with valid stellar parameters, among the G-type stars initially downloaded from the CAS (see Chapter 3). In preparation for the calculation only two additional cuts are applied to this selection of stars: the sample of objects is limited to line-of-sights with  $E(B-V) < 0.3$  and all targets with  $\text{SNR} < 20$  are removed. The SNR cut ensures spectra with good quality and proper parameters. However, it also defines the volume covered by the spectroscopic sample.

It is assumed that the G-star targets are selected independently from each other and sampled uniformly in the G-star colour-magnitude range within the area limits and the apparent magnitude range of the spectroscopic plates. To recall, SEGUE’s observational concept is based on the distinction between bright (stars with  $r < 17.8$  mag) and faint plates (stars with  $r > 17.8$  mag). Still, for calibration purposes some stars were observed on both plate types. Due to changes between the target photometry (DR7 and before) and the photometry (DR9) used for the present work it happens that stars, which were actually on bright plates, are now part of the faint plates and vice versa. This creates a category of stars, referred to as mix-up stars, with magnitudes

close to the bright-faint plate boundary which turn out to have a significant effect on the magnitude distribution of the final G-dwarf sample (see Figure 6.8 and discussion in Section 6.3). Considering the description of the selection function the latter issue is not specifically taken care of by the assumed selection function model (see Equation 5.1). However, those stars are kept when computing the selection function weights.

To obtain an estimate for the selection fraction that represents the ratio between the entries in the spectroscopic catalogue and the number of objects in the photometric catalogue as a function of position, colour and apparent magnitude it is necessary to infer how many photometric objects within the SEGUE pointing footprint could have been targeted as G-type stars. Hence, the photometric G-star target candidates are selected in the area of every SEGUE line-of-sight by querying the SDSS DR9 imaging table of the CAS for all objects that satisfy  $0.48 < (g-r)_0 < 0.55$  and  $14.5 < r < 20.2$ . The query requires every object to meet several quality criteria which are specified by certain photometric flags in the SDSS data tables (see Stoughton et al. 2002). The objects need to be **primary** detections with stellar point spread functions which requires a **type** flag equal to 6. The objects must not have the flags set for saturation (**saturated**), being close to the edge of the plate (**edge**), interpolated PSF (**psf\_flux\_interp**) or inconsistent flux count (**bad\_counts\_error**). In case the centre of the object is interpolated (**inter\_center**), there must not be an indication of a cosmic ray (**cosmic\_ray**).

Figure 5.3 shows the number density distribution of the potential photometric G-star target candidates in the colour-magnitude plane. The distribution of the spectroscopic sample of SEGUE G-type stars (after a cut at  $\text{SNR} > 20$  and at  $E(B - V) < 0.3$ ) is overlaid and indicated by white contours. From this plot it is evident that the selection function is dependent on colour and apparent magnitude. While the spectroscopic sampling is quite satisfactory in  $(g - r)$ , the selection becomes incomplete at the faint end of the  $r$ -band magnitude which is expected due to the cut in signal-to-noise. It is also clear from the figure that the depth in magnitude is not the same for all SEGUE plates because the SNR cut does not result in a clear cut in  $r$ . In Bovy et al. (2012c) it has been investigated how the SNR cut effects relatively shallow or deeply integrated plates. In their Figure 9 they show that the faintest observable object differs a lot from plate to plate and that the SNR limit results in a fairly sharp  $r$ -band cut for each individual plate.

### Selection function model

The selection function model takes into account that the selection function is dependent on position, colour and apparent magnitude. The model assumes that the function is given for every plate by a hyperbolic tangent cutoff centred on  $r_{\text{cut}} - 0.1$  mag, with a width parameter whose natural logarithm is  $-3$  (0.05 mag) such that the total width of the cutoff is about 0.2 mag. The cutoff magnitude in the  $r$ -band,  $r_{\text{cut}}$ , is determined by identifying the faintest targeted object on each plate that still satisfies the signal-to-noise limit of  $\text{SNR} > 20$ . The nominal limit  $r_{\text{max}}$  for bright or faint plates is 17.8 mag and 20.2 mag respectively. In case the apparent  $r$ -band magnitude of the faintest object is larger than  $r_{\text{max}}$ ,  $r_{\text{cut}}$  is set to the latter limits. Equation 5.1 gives the expression for the plate-dependent selection function according to:

$$S(\text{plate}, r, (g - r)) = \frac{\text{No. of spectroscopic objects}}{\text{No. of photometric target}} \Big|_{r_{\min} \leq r \leq r_{\text{cut}}} \times \frac{1}{2} \left( 1 - \tanh \left( \frac{r - r_{\text{cut}} + 0.1}{e^{-3}} \right) \right) \quad (5.1)$$

where the colour range is that of the SEGUE G-type stars and  $r_{\min}$  is 14.5 mag for bright and 17.8 mag for faint plates. Outside the intervals  $[14.5, 17.8]$  and  $[17.8, 20.2]$  in apparent  $r$ -band

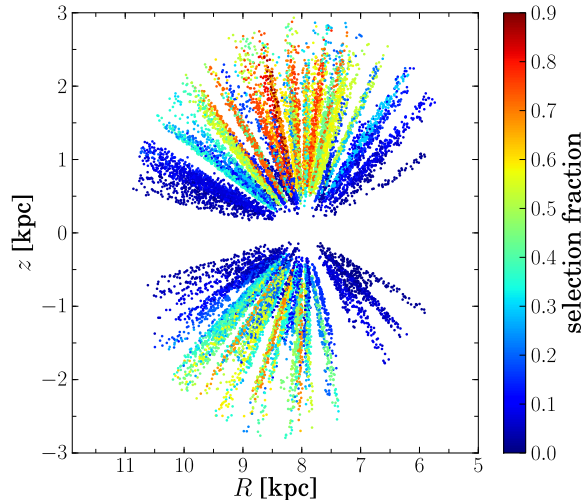


**Figure 5.4:** Fraction of SEGUE G-type star targets that have been successfully observed spectroscopically. Displayed is the same spectroscopic sample as in the previous figure but here as a function of Galactocentric radius,  $R$ , and vertical height,  $z$ . The selection fraction, represented by the selection function weights of the stars in the sample, is colour coded.

magnitude the selection function,  $S$ , is zero. Equation 5.1 shows that  $S$  is a combination of the ratio between spectroscopically observed targets and potential targets from photometry and a hyperbolic tangent function taking care of the overall selection function’s shape at the faint end of the plate where the selection becomes more incomplete. At the bright end of the plate where the influence of the hyperbolic tangent function is negligible the value of  $S$  is equal to the number of spectroscopic objects brighter than  $r_{\text{cut}}$  divided by the total number of targets brighter than  $r_{\text{cut}}$ . Indeed, the selection function model by Jo Bovy (Bovy et al. 2012c) makes the assumption that for each plate  $S$  is constant over a large magnitude range. The selection fraction only drops in the region around the faintest star on the plate. As such it is different to the method of Katie Schlesinger (Schlesinger et al. 2012) whose weights may take better care of variations in the selection fraction as function of magnitude because they are computed for small bins in  $r$ -band magnitude rather than based on an analytical expression describing the whole selection function.

When determining the cutoff of each plate, first as many mix-up stars as possible are resolved, that is assigning each star with  $14.5 < r < 17.8$  to the bright plate of the pair and each star with  $r_0 > 17.8$  to the faint plate. Then the faintest star on each plate is determined and weights are computed. Figure 5.4 displays the fraction of successfully observed spectroscopic G-type targets with  $\text{SNR} > 20$  as a function of galactocentric radial distance  $R$  and current vertical height  $z$  above the plane. It is evident that line-of-sights with high Galactic latitudes are almost completely sampled whereas for pointings within the disk (at low latitudes) only a small fraction of the photometric population has been spectroscopically observed. The effect of correcting for this sampling effect is demonstrated in Figure 5.5. The plot shows the metallicity distribution function (MDF) of the SEGUE DR9 G-dwarf sample in the following cases: biased without any correction (filled histogram) and corrected for the selection function using the weights by Bovy et al. (2012c) (solid histogram) as well as the  $r$ mag-weights by Schlesinger et al. (2012) (dashed histogram). As expected the whole distribution shifts slightly towards higher metallicities, a result of the corrected and changed proportion of low- and high-[Fe/H] stars. In principle, both

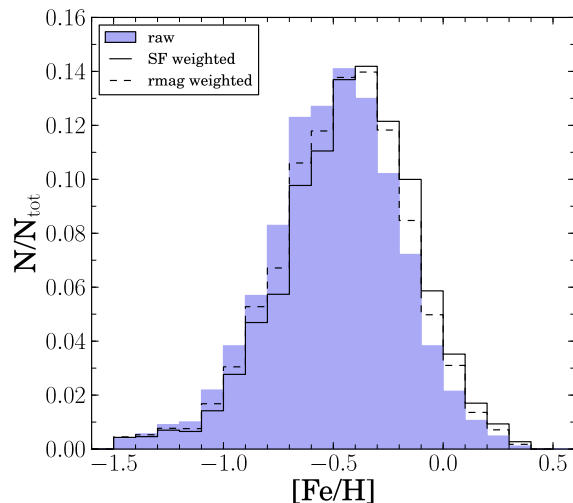


**Figure 5.5:** Metallicity distribution function for the SEGUE DR9 G-dwarf sample. Shown is the uncorrected distribution (filled histogram) in comparison to two different corrected versions of the same distribution. *Solid histogram:* Distribution corrected by the selection function weights of Bovy et al. (2012c); *Dashed histogram:* Distribution corrected by the rmag-weights of Schlesinger et al. (2012).

correction approaches have a similar effect, still the selection function weights by Bovy et al. (2012c) tend to give slightly more weight to stars in the metal-rich tail of the distribution.

### Stars with problematic selection function weights

Preferentially the faintest objects in each line-of-sight exhibit very small weights that turn out to be problematic<sup>2</sup> in the further analysis. The main reason for this issue is that the number of spectroscopically observed faint objects with usable spectra of sufficient SNR is low, whereas the number of photometric targets with faint magnitude is high. The selection function model discussed above takes care of this effect by introducing the tangent cutoff around the position of the faintest objects. Thereby, the model does not make any difference between the bright and faint plates even though for the bright exposures the selection fraction is constant over nearly the whole magnitude range of the plate. Due to the tangent cutoff on both types of plates there are however stars with small weights also on the bright pointings leading to a drop in the sample magnitude distribution at the plate limit. In fact, in case of the SEGUE survey, the discontinuity in magnitude space is introduced by design. Since one has to divide by the selection function weight to resemble the properties of the underlying photometric population the application of small weights is problematic. In fact, it is dangerous and it results in an anomalous, spiky structure of the MDF that gives far too much weight to the low metallicity tail of the underlying distribution because most of the faint stars are low in metallicity. Indeed, the actual intention of the correction is missed which is to achieve that more weight is given to high-[Fe/H] stars correcting for the fact that those are underrepresented in SEGUE. Instead of applying an arbitrary limit directly on the selection function weights that would eliminate all stars with small weights, a more general restriction is performed to handle the issue. A precautions and more consistent solution is to limit the sample to stars that are brighter than

<sup>2</sup>Within the computational process approximately 400 stars even got a zero selection function weight. In order to correct the sample properly the affected stars are removed from the sample.

the centre of the hyperbolic tangent cutoff ( $r_{0\text{cutoff}} - 0.1$ ) of each plate. The remaining stars should have weights closer to the plateau value of  $S$  than to zero. This restriction demands a slight modification of Equation 5.1 as shown in Equation 5.2. The modified selection function model considers only objects up to  $r_{0\text{cutoff}} - 0.1$  but uses the same centre position of the tangent function around  $r_{0\text{cutoff}}$ . The refined selection function weights take into account that all stars in the interval  $[r_{0\text{cutoff}} - 0.1, r_{0\text{cutoff}}]$  are not considered.

$$S(\text{plate}, r, (g-r)) = \frac{\text{No. of spectroscopic objects}}{\text{No. of photometric target}} \Big|_{r_{\min} \leq r \leq (r_{\text{cut}} - 0.1)} \times \frac{1}{2} \left( 1 - \tanh \left( \frac{r - r_{\text{cut}} + 0.1}{e^{-3}} \right) \right) \quad (5.2)$$

Due to the issue with stars both being observed on bright and faint exposures and due to the fact that the photometry has changed from that used for the target selection shifting stars across the boundary at 17.8 mag, the selection seems to be anyway a little odd at that region. Hence, the decision to remove stars that are located at the plate transition seems to be reasonable in order to be able to exclusively work with weights that are well behaved and can be controlled throughout any further analysis of the SEGUE G-dwarf sample. The decision is supported by the findings discussed in Chapter 6. There the comparison of the observed and a G-dwarf mock sample from TRILEGAL reveals an obvious discrepancy in number counts exactly at the region around 17.8 mag in  $r$ -band magnitude, while for the rest of the magnitude range both samples agree well. It will be shown that the discrepancy is caused by the mix-up stars in the observed sample which are by construction not present in the simulated mock sample. With the removal of stars in the transition region of the plate boundaries the final sample of G-dwarfs that is used for the following analyses is reduced in size to a number of 17 499 stars.

### 5.1.3 Correction for the cut in colour-magnitude space

The  $(g-r)_0$  colour cut, which defines the G-dwarf targets, isolates a different mass range at each metallicity. This effect is illustrated in Figure 5.6 showing a set of Padova isochrones (for more details see Figure caption) for a range  $[-2, 0.22]$  dex in metallicity  $[M/H]$  at an age of 10 Gyr. The G-star colour-cut is indicated by the vertical dashed lines overlaid on the isochrones. It is evident that the restriction in colour-magnitude results in a bias. This is because lower mass stars are, according to the commonly accepted mass functions of the Galaxy, more abundant than high-mass stars in a given volume and the cut selects preferentially lower mass stars at lower metallicities. As a result different ranges of the underlying stellar population are sampled for different metallicities. A weight that takes care of this bias needs to correct the number-counts in the given colour range to mass. Ideally, with this correction the mass function should be resembled in correct portions of the entire metallicity range. Such a correction requires stellar-population synthesis models in order to connect the number of observed stars in the particular colour range to the full underlying stellar population.

#### Mass correction weights

The mass function correction presented in Bovy et al. (2012a) depends on the entire set of chemical information that is available for SEGUE stars, including the  $\alpha$ -abundances. How this correction is obtained for the stars analysed in the present work is briefly outline below. For a detailed description of the exact procedure the reader is referred to Appendix A of Bovy et al. (2012a).

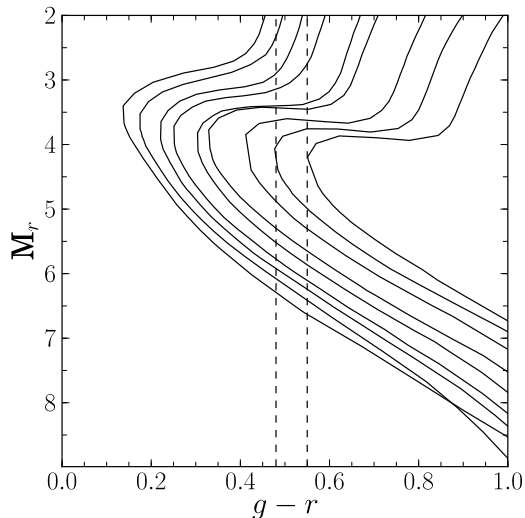


**Figure 5.6:** Isochrone set for a range of metallicities at an age of 10 Gyr. The specific metallicities of the isochrones are  $[-2, -1.5, -1.2, -1.0, -0.7, -0.5, -0.2, 0.0, +0.2]$  dex from left to right. The dashed lines show the  $(g-r)$  colour range for the SEGUE G-dwarfs. The set is based on the theoretical isochrones presented in Marigo et al. (2008) that have been modified with the Girardi et al. (2010) Case A correction for low-mass, low metallicity AGB tracks. The set has been generated and downloaded from CMD 2.5, an online web interface that deals with stellar isochrones and their derivatives<sup>3</sup>.

As the first step the sample under investigation is split into stellar sub-populations, called mono-abundance populations (MAPs), by defining a grid of narrow boxes in the chemical plane that is spanned by metallicity,  $[\text{Fe}/\text{H}]$ , and the  $\alpha$ -enhancement,  $[\alpha/\text{Fe}]$ . Then in order to connect the number of observed G-dwarfs to the full underlying stellar population for each MAP an estimate of the mass fraction in this sub-population is obtained according to the following approach. The total stellar mass in a sub-population is related to the number of G-dwarfs in the given abundance box and calculated as

$$M_{\text{GD}}([\text{Fe}/\text{H}], [\alpha/\text{Fe}]) = N([\text{Fe}/\text{H}], [\alpha/\text{Fe}]) \times \langle \bar{M}_{\text{GD}} \rangle([\text{Fe}/\text{H}]) \times f_{\text{M}}^{-1}([\text{Fe}/\text{H}]) \quad (5.3)$$

where  $N$  is the number of observed stars,  $\bar{M}_{\text{GD}}$  is the average mass of a G-dwarf and  $f_{\text{M}}$  is the ratio of the stellar mass in G-type dwarfs to the total stellar mass in the population. As such  $f$  serves as a re-normalisation of the stellar mass fraction, represented by the spectroscopically targeted stars, in relation to the total mass in G-type stars in a stellar population. Both, the average mass estimate (see Equations A4 and A5 in Bovy et al. 2012a) and  $f$  are calculated based on stellar isochrones in the SDSS photometric system (Girardi et al. 2004; Marigo et al. 2008; Girardi et al. 2010) and a lognormal Chabrier (2001) initial mass function (IMF).

The effect of the colour cut bias is illustrated in Figure 5.7 where the dashed line represents the MDF of the G-dwarf sample corrected for the selection function plus the mass function bias. Clearly, the mass function weights have less impact on the distribution than the selection function correction which produces a distinct change in the distribution's shape and the position of its main peak. This is in agreement with the detailed examination presented in Schlesinger et al. (2012) which indicates that the bias introduced by the colour limit is small compared to the other biases, e.g. the selection function.

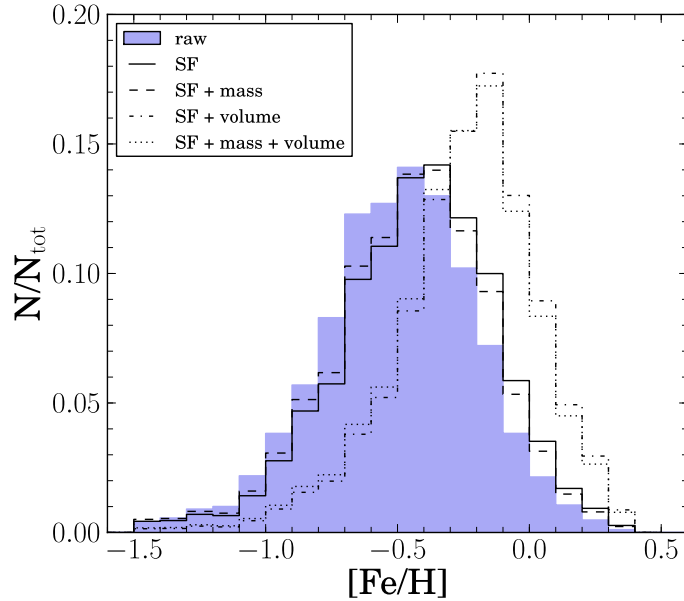


**Figure 5.7:** Comparative overview of the set of discussed bias corrections that are here applied step-by-step to the MDF of the G-dwarf sample in order to demonstrate the corrections’ different effectivity. Displayed is the uncorrected MDF (filled histogram) and several stages of the corrected MDF including the selection function correction (SF, solid histogram), a combination of the selection function weights and the mass function correction (dashed histogram) and finally the additional correction for the ‘global’ volume (dashed-dotted and dotted histograms).

#### 5.1.4 Correction for the survey volume

For a given  $(g-r)$  metal-rich stars are brighter than metal-poor stars, thus the distance range and volume coverage varies with respect to metallicity for the same magnitude range. Furthermore stars with different metallicities show different spatial distributions within the Galaxy. As a result of the combination of both facts one observes different fractions of the total volume that is occupied by a stellar population. In order to correct for this effect the stellar densities of stars in the observed volume need to be extrapolated to a ‘global’ volume, e.g. a cylinder around the solar neighbourhood. Such a correction would then also allow to compare the total number of stars in different components of the Galaxy. More important, for the present work it opens the possibility for a completely new approach in which the metallicity distribution function as well as chemo-kinematic properties, extracted from the SEGUE survey and corrected for the full set of selection effects, are compared to predictions from the chemo-dynamical model of the Milky Way by Minchev et al. (2013). The primary goal thereby is to find new observational constraints for the theoretical model. At the same time the direct comparison can be used to test the reliability and to reveal possible weaknesses of the volume correction which is by itself highly model dependent as will be explained in the next paragraphs.

So far, Bovy et al. (2012a) presents the only method to correct the SEGUE G-dwarf sample for the survey volume. Closely connected to the mass function weights (see previous section) in the current approach weights are computed that correct the number counts within the line-of-sights observed by SEGUE (survey volume) to the number of stars in a column around the Sun (global volume). For each mono-abundance population the total stellar surface density is determined at the solar radius which is an expression for a more ‘global’ quantity that can be obtained through

extrapolation from the actual SEGUE survey volume. In this extrapolation process knowledge about the spatial density of the objects is needed to be able to calculate the fraction of stars in the observed volume with respect to the ‘global’ volume. Bovy et al. (2012c) demonstrates how for sub-populations of SEGUE G-dwarfs an estimate of the spatial-number-density profile can be obtained by fitting stellar density models to the observations in each mono-abundance bin. As the observed star counts do not reflect the underlying stellar distribution the modelling already has to account for (1) the selection fraction of stars with spectra, (2) the fact that a colour-magnitude limited survey corresponds to a colour-metallicity dependent distance-limited sample and (3) the pencil-beam structure of the SEGUE survey. As a result the density of stars is modelled in colour-magnitude-metallicity-position space (for more details see Section 3 in Bovy et al. 2012c).

In the scope of the study it has been shown that the mono-abundance populations of SEGUE G-dwarfs have a simple density structure that can be described by a single exponential in vertical and radial direction and that the inferred scale heights for solar like to more metal-poor and  $\alpha$ -enhanced populations increase smoothly from approximately 200 pc to 1.2 kpc, respectively. As stressed out in Appendix A of Bovy et al. (2012a) the number-density fits are essential to obtain the total number of G-type stars per square pc in each  $[\text{Fe}/\text{H}]$ - $[\alpha/\text{Fe}]$  bin at the solar radius. They help to transform the observed number counts into a number column density  $N(R_0)$  by adjusting the normalisation of the number-density profiles in such a way that, when the density model is run through the model for the SEGUE selection function (see Section 5.1.2), the number of observed stars is predicted.

Following the above procedure number weights are calculated for the G-dwarf sample dealt with in the present thesis. They complement the previous two corrections and are determined for each individual object in the sample. Basically, the correction for the survey volume works such that if one adds up the weights of all stars in the sample one gets the total number of G-dwarfs in the solar neighbourhood per  $\text{pc}^2$ . Following up on the determination of the number density weights it is possible with only one additional step to obtain mass-weighted number counts. Thereby, the main aim is to find a proper estimate of the individual contribution of each mono-abundance population to the surface-mass budget in the solar neighbourhood. This can be realised by relating the number density of G-type dwarfs to the total stellar surface-mass density. As for the mass function correction it requires the use of population synthesis models which can relate the number of observed stars to the mass of the stellar population. How this transformation can be achieved has been already described in Section 5.1.3 (also providing an expression for the total stellar mass estimate of a mono-abundance sub-population (see Equation 5.3)). Replacing the number counts  $N$  in Equation 5.3 with the number-density  $N(R_0)$  results directly in an estimate of the total stellar mass density. If one adds up the mass-weighted number counts for all stars in the G-dwarf sample it results in the total mass of G-type stars in the solar neighbourhood per  $\text{pc}^2$ . The advantage of the latter mass correction is that it allows to get a better picture of the stellar mass distribution in G-type stars in the solar neighbourhood which enables e.g. to test the presence of a bi-modality in chemical space.

### 5.1.5 How do the corrections affect the MDF?

Figure 5.7 summarises how the various bias corrections being discussed so far in this chapter affect the MDF of the SEGUE G-dwarfs. Displayed is the raw distribution (filled histogram) and the corrected distributions after application of (1) the selection function correction (solid), (2) the selection function and mass correction (dashed) and (3) the volume correction on top of (1) and (2) (for number counts - dashed-dotted and for mass weighted number counts -

dotted). Evidently, the volume correction causes a significant change in shape and position of the MDF's main peak such that the metal-rich stars with its mean metallicity around  $-0.15$  dex are dominating the entire distribution. In other words, the correction accounts for the fact that globally most of the mass in a stellar disk sample should be represented by metal-rich disk stars (thin disk) with a smaller mass fraction represented by more metal-poor disk stars (thick disk). Since the metallicity distribution function of the extended neighbourhood around the Sun is an important and widely used observable in order to constrain chemical evolution models it is crucial to free the observations from any artificially introduced biases.

## 5.2 Chemo-kinematic constraints from SEGUE G-dwarfs

The detailed study on the metallicity distribution function and selection effects that influence and shape the latter is an essential step towards the realisation of a unique chemo-dynamical analysis. This comprehensive analysis involves the SEGUE G-dwarf sample assembled and discussed in Chapter 3 as well as population synthesis (TRILEGAL) and  $N$ -body models of the Milky Way and ranges from the present Chapter to Chapter 7. The analysis sample of G-dwarfs contains a number of 17 499 stars after removing all objects with a  $r$ -magnitude close to the SEGUE plate boundary (see discussion at the end of Section 5.1.2). The elementary knowledge about the non-trivial selection biases sets the cornerstone to be able to perform comparisons between observations and theoretical model predictions in various ways and allows to better understand the results and relationships presented in the following sections and chapters.

### 5.2.1 The $[\text{Fe}/\text{H}]-[\alpha/\text{Fe}]$ -plane

As a generation of low and medium resolution spectroscopic surveys SEGUE and RAVE, which probe a volume of a few kpc around the Sun, have been the first projects to provide homogeneous and statistically significant stellar samples with chemical abundance estimates that are feasible to shed light on the chemical history of the Galaxy. In their context, the studies by Lee et al. (2011b) or Boeche et al. (2013a) are the first to probe the abundance distribution of the disk going beyond a few 100 pc. Before, studies on chemical evolution had to rely on the few high-resolution spectroscopic surveys confined to the very local solar neighbourhood and reaching only distances of up to around 25 pc or 100 pc as in the cases of samples assembled by Fuhrmann (1998, 2004, 2008, 2011), Bensby et al. (2003) or Adibekyan et al. (2011). Still, these studies set the ground for the still ongoing discussion about the Galactic chemical-enrichment history. They triggered the interest in stellar chemical-abundance ratio diagrams which are one of the main sources for valuable information on the star-formation and chemical-enrichment history because they encode the chemical composition of the ISM at the time the stars were born. Widely used is the  $[\alpha/\text{Fe}]$  vs.  $[\text{Fe}/\text{H}]$  diagram because iron and  $\alpha$ -element abundances can be obtained with decent accuracy even for lower resolution spectra. Moreover, the timescale<sup>4</sup> in which those quantities are produced and returned to the ISM are different. This fact helps, when comparing the latter two abundance ratios, to constrain the formation history of different Galactic components and populations and provides new insights to internal processes like dynamical mixing. Figure 5.8 illustrates how different high-resolution and the SEGUE DR9 G-dwarf sample distribute in the  $[\alpha/\text{Fe}]$  vs.  $[\text{Fe}/\text{H}]$  abundance plane. The HARPS sample (Adibekyan et al. 2011) restricted to stars below  $d < 0.1$  kpc predominantly represents the metal-rich part of the disk containing a few

<sup>4</sup>While  $\alpha$ -elements like calcium, magnesium or oxygen are mainly produced and released to the ISM by type II SNe at the end of a short-lived massive star's lifetime, heavier elements like iron are predominantly produced by type Ia SNe (Matteucci & Brocato 1990).

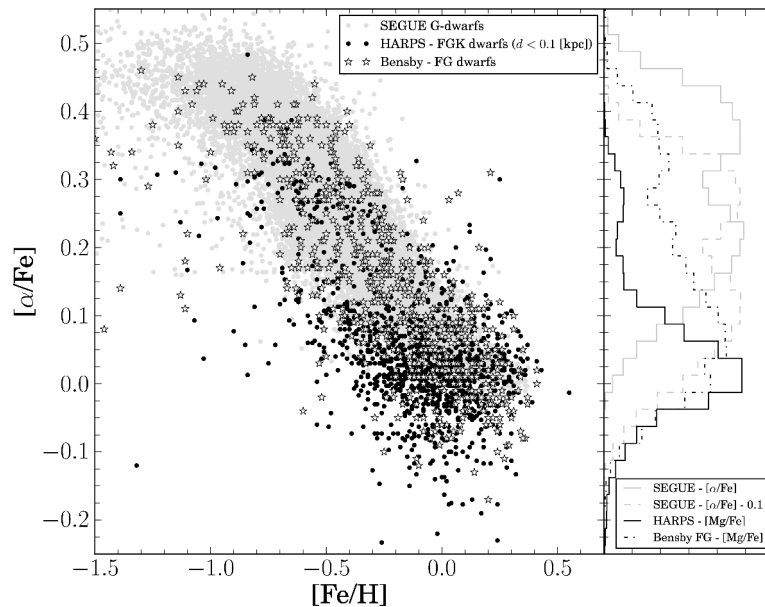


**Figure 5.8:** Distribution of stellar elemental abundances in the  $[\text{Fe}/\text{H}]$ - $[\alpha/\text{Fe}]$ -diagram for the SEGUE G-dwarf sample (grey dots) and for two spectroscopic local high-resolution samples (Adibekyan et al. 2011; Bensby et al. 2014) represented by black dots and open stars respectively. *Right panel:* Corresponding marginalised  $[\alpha/\text{Fe}]$  distributions. The apparent offset in the  $[\alpha/\text{Fe}]$  scale for SEGUE and the high-resolution studies justifies the adjustment of the SEGUE  $\alpha$ -values.

$\alpha$ -abundance enriched stars that reach a maximum  $[\alpha/\text{Fe}]$  ratio of  $\sim 0.4$  dex. Likewise the sample of nearby disk stars (FG-dwarfs and subgiant stars) by Bensby et al. (2014), selected to trace the Galactic thin and thick disk to their extremes, covers the diagram mainly up to 0.4 dex in  $[\alpha/\text{Fe}]$ . A similar coverage of the chemical-plane is reported recently by Anders et al. (2014) studying a disk sample of APOGEE giants. On the contrary, the most  $\alpha$ -enhanced SEGUE G-dwarfs reach  $[\alpha/\text{Fe}]$  ratios above 0.5 dex which is not found in high-resolution and can also hardly be explained by chemical-evolution models (Chiappini et al. 1997). The fact that the SEGUE  $[\alpha/\text{Fe}]$  scale for DR8 tends to be in better agreement with high-resolution (see comparison of DR8 and DR9 abundance ratios for the sample stars in Section 3.3) points also towards a problem in the DR9  $\alpha$ -abundance and supports the decision to empirically adjust the entire scale by decreasing the  $[\alpha/\text{Fe}]$  ratios by 0.1 dex for any further analysis steps. As demonstrated later in Chapter 8, when comparing the G-dwarf properties to those shown by a sample of RAVE giants (selected from a completely independent stellar survey with stellar parameters obtained from a different pipeline and its own  $[\alpha/\text{Fe}]$  scale) a good match in the  $[\alpha/\text{Fe}]$  dependent distribution and relations is only obtained when modifying the SEGUE  $[\alpha/\text{Fe}]$ -scale. Even though, the readjustment does shift the SEGUE stars into a more reasonable  $[\alpha/\text{Fe}]$  range, it does by far not account for the obvious additional compression of the DR9  $[\alpha/\text{Fe}]$ -scale which advises caution.

### SEGUE’s bi-modality in the $[\text{Fe}/\text{H}]$ vs. $[\alpha/\text{Fe}]$ plane: a real feature?

The apparent bi-modality distribution of SEGUE G-dwarfs in the  $[\text{Fe}/\text{H}]$  vs.  $[\alpha/\text{Fe}]$  plane has been firstly described in Lee et al. (2011b) leading to a separation into thin and thick disk popula-

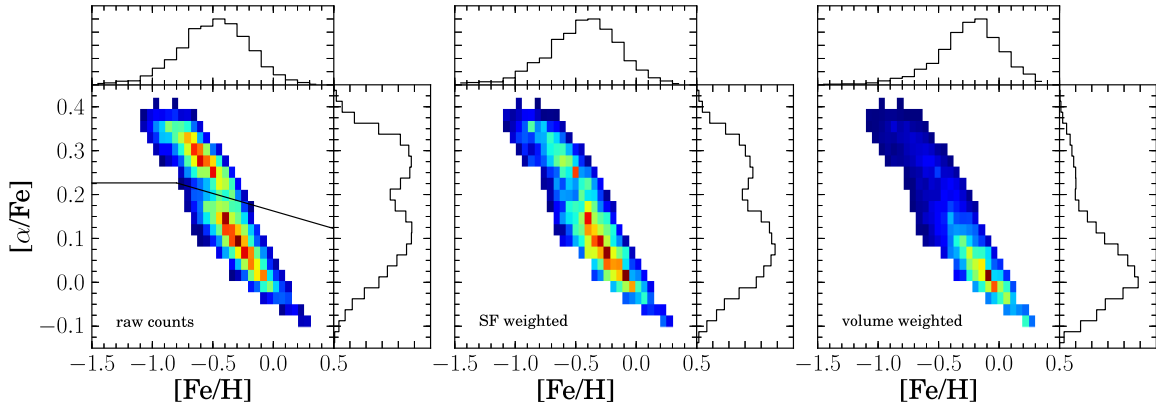


**Figure 5.9:** Density distribution of the SEGUE G-dwarf sample (17 499 stars) in the  $[\text{Fe}/\text{H}]-[\alpha/\text{Fe}]$  elemental-abundance plane. The panels show the effect of (a) NO correction, (b) the correction for the selection function (c) the model dependent volume correction. While the *left panel* shows the raw number counts, the density distribution in the *middle panel* illustrates how the high-latitude and colour-selected SEGUE sample is influenced by the limited amount of spectroscopic fibres. The *right panel* depicts the stellar-mass-weighted and  $|z|$  number count distribution which is corrected for spectroscopic selection effects and represents the total stellar surface-mass densities at the solar radius.

tion stars purely based on chemistry. Studying the chemo-dynamical properties of those chemical separated populations revealed that they represent distinct components in terms of kinematics. Additionally, the chemical division seems to uncover the kinematic structure of each population better than a division on the basis of spatial or kinematic quantities because the hierarchical assembly and internal secular evolution processes possess the potential to diffuse the dynamical memory with time. The left panel of Figure 5.9 shows the unweighted (raw counts) SEGUE DR9 G-dwarf abundance distribution with two maxima in the number density distribution, one in the metal-poor and  $\alpha$ -enhanced and another in the metal-rich and  $\alpha$ -poor part of the diagram. Both are separated by an obvious gap which hypothesises a chemically distinct thick-disk component. Also, local high-resolution studies have found distinct and clearly different abundance patterns leading to strong bi-model abundance distributions in the  $[\text{Fe}/\text{H}]$  vs.  $[\alpha/\text{Fe}]$  plane (e.g. Fuhrmann 2011; Adibekyan et al. 2013; Haywood et al. 2013; Bensby et al. 2003, 2005; Anders et al. 2014) which would favour the presence of a gap and a structural thin-thick disk dichotomy. With respect to Galactic evolution this latter evidence may argue for a scenario with an early thick disk star-formation and a significantly delayed thin disk formation epoch, both separated by a star-formation hiatus (see Two-Infall model by Chiappini et al. 1997). However, the gap’s origin and real presence is still under debate. If nothing else due to the claims recently expressed in Bovy et al. (2012c,b,a). Those contradict the usual picture of only two disk components but advocate a disk structure made up from a continuum of components with different stellar scale heights, suggesting a smooth transition between chemically old and young stars (for details see also Section 5.2.2 and Chapter 6 of Rix & Bovy (2013) Figures 10 through 18).

Because there is yet no clear consensus, much is expected of APOGEE and Gaia-ESO which provide precise chemical abundances over a few kpc within the disk that could help to disentangle. Nonetheless, Figure 5.9 demonstrates that in case of SEGUE the prominent bi-modality is predominantly a result of selection effects. While the marginalised  $[\alpha/\text{Fe}]$  distribution shows a clear double-peak structure in case of the raw number count density distribution (left panel),

correcting for the selection function decreases the number density of  $\alpha$ -enhanced stars already quite effectively compared to the metal-rich ones. A double peak structure is however still visible. To finally assess the elemental-abundance distribution in the solar neighbourhood (at  $R_0$ ) based on any spectroscopically selected sample of stars, it is necessary to properly correct for the survey-specific spatial and mass sampling of the underlying sub-populations. For the SEGUE G-dwarfs the proper mass-weighting (right panel), primarily accounting for the survey volume, leaves only a small but still a hint of a bi-modality in the marginalised  $[\alpha/\text{Fe}]$  distribution. What remains in the right panel is a representation of the stellar surface-mass density of stellar populations with different metallicity at the solar radius. With respect to the Galactic plane the surface-mass density has to increase for populations with smaller scale height (see Figure 5.12 for mean scale height and scale length distribution on the chemical-abundance plane) because the vertical density of stars follows an exponential function. The stepwise correction shows that the strong double-peak structure is mainly a consequence of SEGUE’s very uneven spectroscopic sampling of the underlying stellar population. At the same time however one needs to wonder if the remaining feature is a true one or not. Only a comparison to a model like the MCM model may help to clarify the situation which is why Section 5.3 picks up the issue by discussing similarities and differences between the survey volume corrected SEGUE dwarfs and the predictions made by the MCM model. Also in Section 7.2 the subject is put into focus again by comparing the SEGUE G-dwarf raw sample (without bias correction) to a mock sample of SEGUE G-dwarfs based on the MCM model. In both sections special attention is given to the bi-modality in the elemental abundance plane (see e.g. Figures 5.18 and 7.3.).

### 5.2.2 The spatial and kinematic structure of the disk

The global disk structure and its abundance patterns as seen from the SEGUE G-dwarfs have been studied frequently in the recent past. In exploiting the fact that the  $[\alpha/\text{Fe}]$ -ratio is a rough but adequate proxy for age, it got possible to study changes in the spatial structure with abundance. Connecting those with trends in kinematic properties provides new insights into the formation of the Milky Way’s disk. In particular much effort in studying the spatial structure of the disk and its implication for disk formation is spent in Bovy et al. (2012c) presenting a new approach that focusses on the properties of chemical sub-populations (mono-abundance populations, MAPs) defined in the  $[\alpha/\text{Fe}]$  vs.  $[\text{Fe}/\text{H}]$  plane. For a detailed discussion on their findings see Section 4 and 5 of the latter reference. However, the sample composition and selection in previous studies have been different with regard to the present G-dwarf sample, so have the chemical abundances and distance estimates in use which are crucial for any conclusions on the stellar kinematics (Lee et al. (2011b) and Bovy et al. (2012c) both used chemical abundances from DR8 and photometric distances). Taking a closer look at the properties of the DR9 selected SEGUE G-dwarfs hence serves as a validation of previous results.

#### The elemental-abundance plane in $(R, z)$ -space

Figure 5.10 (raw number density) and 5.11 (stellar surface-mass density) dip more detailed into the abundance distribution of the solar neighbourhood as inferred from the SEGUE G-dwarfs by investigating the  $(R, z)$ -space by means of a grid of elemental-abundance planes. Both plots illustrate the actual position of the stars with the *left* and *right* columns representing the inner and outer disk and the *middle* column focussed on the local solar volume. The density distribution in each subpanel is normalised with respect to this pixel with the overall maximal number of stars. The important take away messages concerning the biased density structure (Figure 5.10) of the disk as seen by SEGUE are the following:

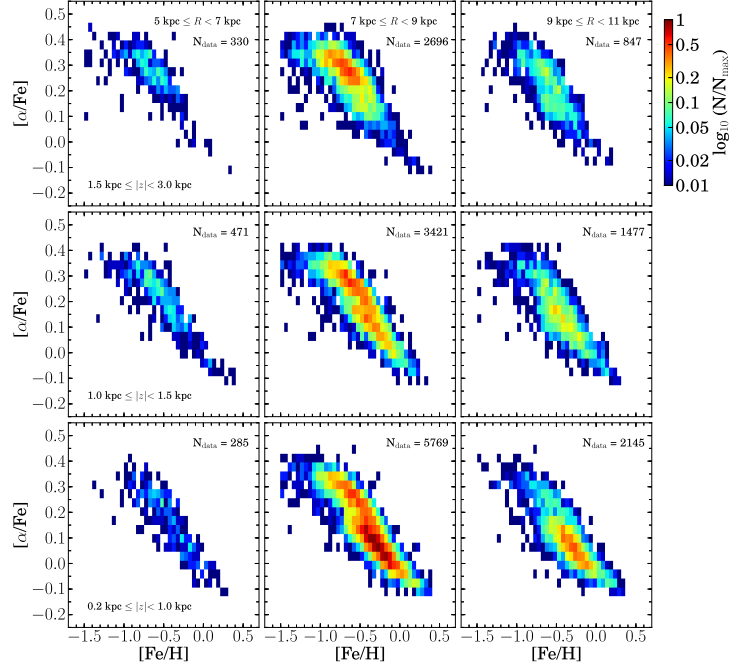


**Figure 5.10:** Elemental abundance plane divided into subgroups of stars in the  $R$ - $z$ -plane. The density distributions represent the raw counts of the G-dwarfs normalised (logarithmic scale) with respect to the pixel with the overall maximum number of stars. For comparison see also Figure 5.11.

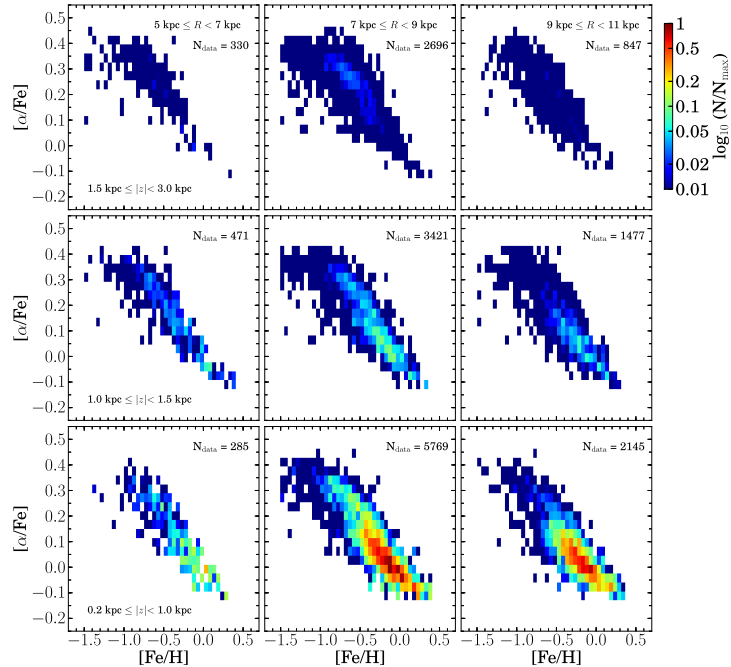


**Figure 5.11:** Same as in Figure 5.10 but for the observed sample of SEGUE G-dwarfs corrected for the survey volume.

(1) the number statistics reveals clearly that SEGUE covers mainly a volume of 1 kpc around the Sun ( $7 \text{ kpc} < R < 9 \text{ kpc}$ ) with the tendency to sample the regions towards the outer disk more extensively than the inner part ( $4 \text{ kpc} < R < 7 \text{ kpc}$ ) which is only sparsely sampled showing very narrow distributions. Concerning the inner disk the focus lies on the higher latitudes covering mainly  $\alpha$ -enhanced stars which, as will be discussed in detail later, biases the metallicity distribution in that radial bin severely against metal-rich stars and (2) independent of the bin in galactocentric radial distance the high latitude ( $z > 1.5 \text{ kpc}$ ) distributions are dominated by thick disk stars while the intermediate heights show a more balanced picture (at least in the local column) with a similar density for  $\alpha$ -rich and  $\alpha$ -poor stars. Towards the Galactic plane the contribution by metal-rich stars is highest although there is a non negligible amount of  $\alpha$ -rich stars present in the low latitude local panel. Overall the selection biased distributions reflect a too thick-disk star dominated density structure of the disk, being consistent with the previously discussed divers selection effects. Figure 5.11 depicts a more plausible stellar density distribution showing again the stellar surface-mass density of the SEGUE G-dwarfs but after taking care of the improper spectroscopic sampling. The general vertical trends laid out above are still visible. However, the proportion of stars observed at various heights has changed dramatically, now showing the peak in number density closely to the plane and a decrease in number counts with increasing height. Additionally, the proportion between thin and thick disk stars in each subpanel is more realistic (see especially the two bottom panels of the local column). It remains to be seen how this corrected density structure compares to the predictions from the chemo-dynamical model by Minchev et al. (2013) when translated into the pure MDF. Yet, in conclusion these maps give a good impression on how the statistical coverage changes with height and radius. From the middle to the left the SEGUE sample loses statistics by a factor of 10 while from the middle to the right the loss in stars is about a factor of 2 to 3. This knowledge is important when showing other constraints as a function of radius.

### The vertical and radial properties of different abundance populations

Figure 5.12 shows how the scale length and height changes for different stellar chemical sub-populations in the DR9 sample. The properties have been obtained as part of the bias correction process by fitting disk models with a single-exponential profile in  $R$  and  $z$  to the sub-populations of stars (see also Section 3 and 4 in Bovy et al. 2012c). Complementing to that Figure 5.13 displays, in colour-code, the distribution in mean orbital radii as well as mean rotational velocity for the same populations. Inferring from these plots and speaking of distinct chemical populations the  $\alpha$ -enhanced, hence older populations, have a shorter scale length, are thus more centrally concentrated, have generally larger scale heights that increase with decreasing metallicity, possess smaller mean orbital radii and rotate slower with respect to the populations close to solar  $\alpha$ -abundance. In contrast, the  $\alpha$ -young populations ( $[\alpha/\text{Fe}] < 0.25 \text{ dex}$ ) have generally longer scale length and shorter scale heights, with an increase in scale length with decreasing  $[\text{Fe}/\text{H}]$  which produces an outward metallicity gradient. A prominent feature that sticks out in all but the vertical scale height distribution is a group of stars within the thin disk, apparently the metal-poor tail of the thin disk with  $[\alpha/\text{Fe}] < 0.25 \text{ dex}$  and  $-0.7 \text{ dex} < [\text{Fe}/\text{H}] < -0.2 \text{ dex}$ . Stars in that region possess distinctively different properties than their surrounding showing rotational velocities that exceed the usual solar velocity and mean orbital radii which suggest an outer disk origin. It should be noted that the distributions in both,  $R_m$  and  $v_\phi$  lose smoothness when implementing the surface-mass weighting (right panels in Figure 5.13). The correction significantly introduces noise compared to the raw distribution (left panels), a tribute to the highly model dependent post-correction.

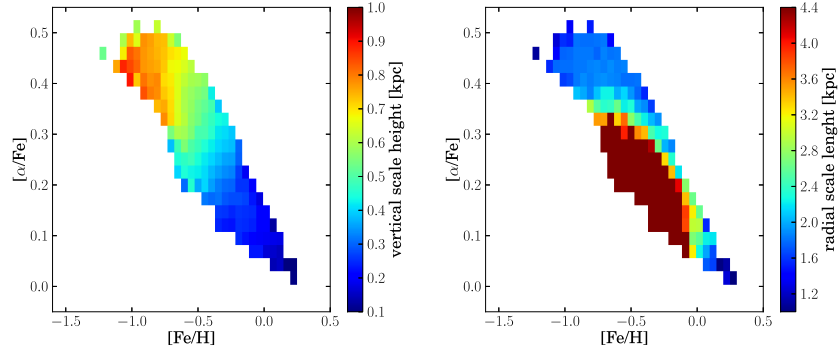


**Figure 5.12:** Distribution of mean scale heights (*left*) and scale lengths (*right*) for different sub-populations in the  $[\text{Fe}/\text{H}]$ - $[\alpha/\text{Fe}]$ -plane.

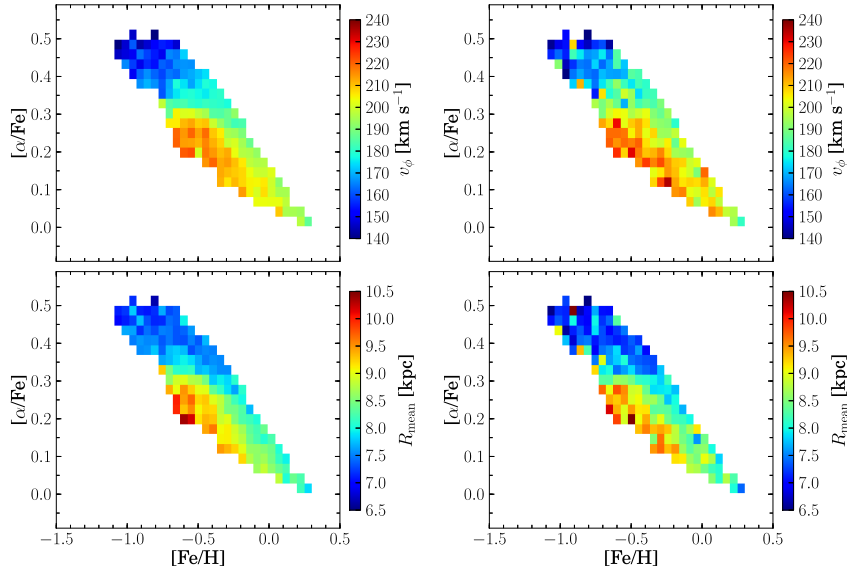


**Figure 5.13:** Raw (*left*) and mass-weight corrected (*right*) distributions of rotational velocity and mean radius depending on  $[\text{Fe}/\text{H}]$  and  $[\alpha/\text{Fe}]$  for the SEGUE G-dwarfs.

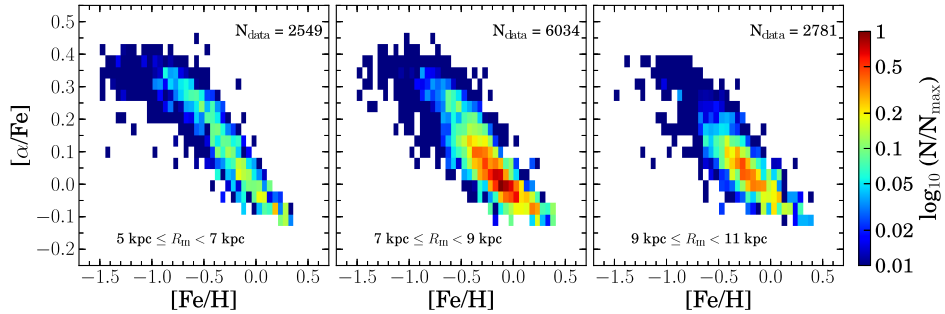


**Figure 5.14:** Volume corrected density plots showing the SEGUE DR9 G-dwarfs in the chemical abundance plane in bins of mean orbital radius. In each panel the sample is restricted to  $z_{\text{max}} < 2$  kpc.

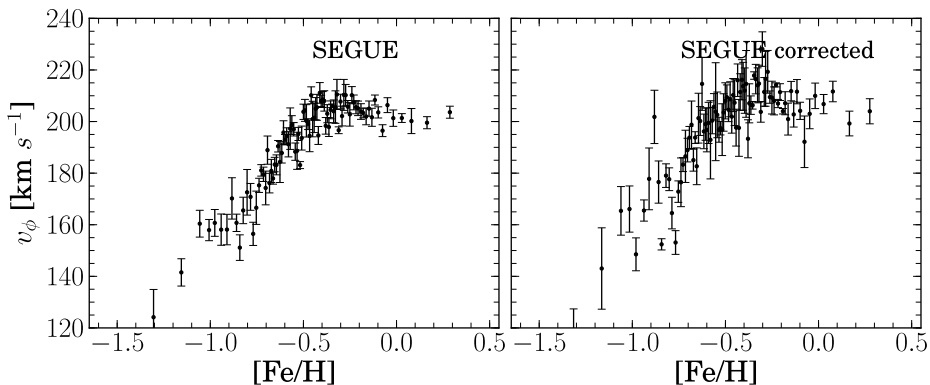


**Figure 5.15:** Correlation of rotational velocity and  $[\text{Fe}/\text{H}]$ . *Left:* G-dwarfs without correction. *Right:* G-dwarfs with selection effect corrections. Dots contains 200 points, error bars are calculated by resampling the 200 stars. The correction for the survey specific spectroscopic sampling is taken into account by calculating a weighted mean in velocity for each dot using the information on the mass-weighting (volume correction).

Still, the main trends are preserved indicating a positive trend of  $v_\phi$  with  $[\text{Fe}/\text{H}]$  for the high- $[\alpha/\text{Fe}]$  populations ( $> +0.3$  dex) and a negative trend of  $v_\phi$  with  $[\text{Fe}/\text{H}]$  for the low- $[\alpha/\text{Fe}]$  populations forming the thin disk (see also section 4 in Lee et al. 2011b). The listed findings strongly favour an inside-out formation scenario of the disk where the inner parts formed earlier than the outer ones. The presence of a shorter scale length for the thick disk, an observational key evidence, has by now be confirmed with various samples. Contrary to APOGEE (see Figure 14 in Anders et al. 2014) or the high-resolution samples by Bensby et al. (2014) the SEGUE G-dwarf sample does not probe beyond  $R = 11$  kpc which is where a certain drop in number of thick disk ( $\alpha$ -rich) stars is observed with respect to the more inner radial bins. Still, Figure 5.14, showing the chemical-abundance plane (mass-weight corrected) for three bins in mean galactocentric radius, indicates a hint for the same finding. Dividing the sample into wide bins of  $R_m$  assures that the contamination by stars on very eccentric orbits, originating from the inner and outer disk and hence only passing by the Sun, is minimised. The most outward bin already evinces a slight decrease in number of thick disk stars with respect to the local and inner Galaxy region. Beyond the outer bin the effect is expected to be even more prominent.

### Correlation between rotational velocity and chemistry

In Lee et al. (2011b) the SEGUE G-dwarf sample is split into a thin and a thick disk population and the  $v_\phi$ - $[\text{Fe}/\text{H}]$  relation for those populations is studied separately (e.g. their Figure 7) without taking care of any selection effect. Contrary, Figure 5.15 of this chapter concentrates on an overall  $v_\phi$ - $[\text{Fe}/\text{H}]$  relation for the entire solar neighbourhood. For clarity the individual stars of the sample are binned in metallicity, with each dot in the plot representing the mean metallicity and mean rotational velocity of 200 stars. From the top panels in Figure 5.13 it is evident that especially the correlation between rotational velocity and  $[\text{Fe}/\text{H}]$  should be influenced by the selection biases because the metallicity range covered by  $\alpha$ -rich and  $\alpha$ -poor stars overlaps (mainly between  $-0.7$  dex  $< [\text{Fe}/\text{H}] < -0.2$  dex). Without correcting the SEGUE specific spectroscopic sampling one expects that the  $v_\phi$ - $[\text{Fe}/\text{H}]$  relation is dominated by the lower velocities of the thick-disk stars (left panel of Figure 5.15). This results in the artificial effect of pulling down the entire distribution towards lower velocity values, especially in the metallicity range populated by both disk populations. And indeed, the right panel of Figure 5.15 indicates a change. When

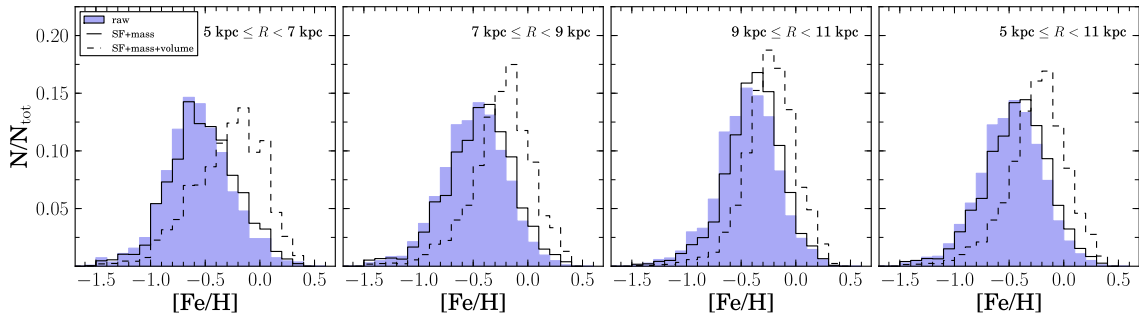


**Figure 5.16:** MDF for the SEGUE G-dwarfs in bins of galactocentric radius. Different stages of correcting the sample are illustrated by separate histograms.

applying the mass-weighting (computing a weighted mean in velocity based on the 200 stars), which favours the thin disk stars and their larger velocities, now the binned data points (dots) in the range  $-0.7 \text{ dex} < [\text{Fe}/\text{H}] < -0.2 \text{ dex}$  clearly exhibit a trend towards larger mean velocities. This proves that the correction is working as expected, shifting the whole distribution slightly to higher mean velocities but preserving the general shape of the biased relation. Even though the correction introduces a lot of scatter there is still a steep slope for the thick disk dominated low metallicity part, a transition region where the velocity is pushed up by the thin disk stars from the outer disk and a plateau around  $200 \text{ km/s}$  for the metal-rich tail. Also the change in slope from positive ( $\alpha$ -rich population) to negative ( $\alpha$ -poor population) is conserved. For the  $v_\phi$ - $[\alpha/\text{Fe}]$ -relation the picture is a little different. The compression in the  $\alpha$ -scale, the fact that both quantities (axes) are affected by the correction and the comparably small  $\alpha$ -range coverage (many orders of magnitudes less than for  $[\text{Fe}/\text{H}]$ ) seem to have a negative influence leading to much more noise than observed for the corrected  $v_\phi$ - $[\text{Fe}/\text{H}]$ -correlation.

### 5.2.3 Variations in the MDF with radial distance from the Galactic centre

Figure 5.16 shows the metallicity distribution at different distances (three radial bins) from the Galactic centre, with filled histograms representing the raw and open histograms illustrating different selection bias corrected distributions. In agreement with the density distributions in the  $[\text{Fe}/\text{H}]$ - $[\alpha/\text{Fe}]$ -plane (Figure 5.10) the peak of the uncorrected MDF for the range  $5 \text{ kpc} < R < 7 \text{ kpc}$  is distinctively shifted to a lower metallicity when comparing the inner (left panel) with the local (middle panel) and outer (right) radial bin. While the local and outer disk distributions are centred around  $-0.5 \text{ dex}$  the MDF towards the centre peaks around  $-0.7 \text{ dex}$  due to the lack of high metallicity stars. A result of the survey sampling, causing a severe bias in this radial bin because SEGUE preferentially observes high latitudes (see also the spatial distribution plots in Figure 6.2) towards the Galactic centre. Even though SEGUE avoids very low latitudes in general the effect is less in the other bins because the observed pointings still reach much lower latitudes there. The same variation in the MDF with radial distance is seen for the TRILEGAL mock G-dwarf sample (see Figure 6.18) presented in the next Chapter - a simulated sample of G-dwarfs created to resemble the observed SEGUE counterpart by applying the same selection criteria and sampling biases to an a priori unbiased TRILEGAL (a population synthesis code to model the content of the Galaxy) simulation of the stellar content in the area covered by SEGUE. This demonstrates that (1) the selection biases can be easily propagated to mock data and (2) the empirically inferred selection function correction for SEGUE G-dwarfs is a proper description. Concerning the bias corrected metallicity distributions the picture changes drasti-

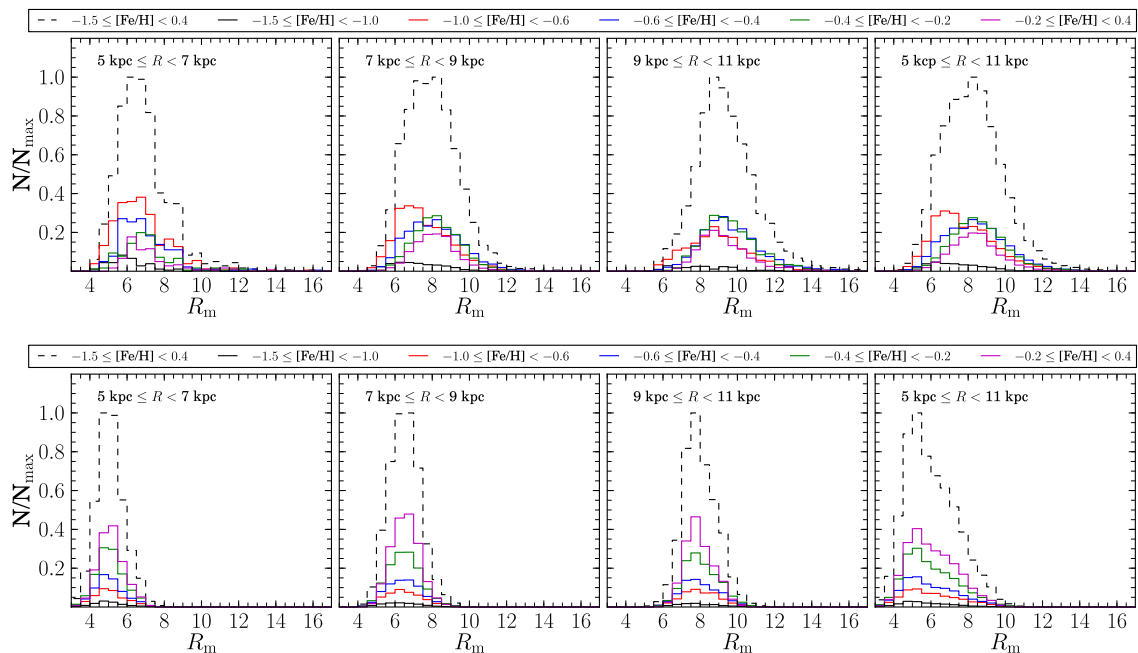


**Figure 5.17:** Mean galactocentric radius distributions for stellar populations with different metallicity bins of current radial distance from the Galactic centre. *Top row:* Biased SEGUE G-dwarf sample without any selection effect correction. *Bottom row:* Volume corrected SEGUE G-dwarf sample. In both rows and all panels the black dashed histogram represents the total distribution which is split into several metallicity intervals as indicated by the colour coding.

cally indicating that only the mass-weight correction (based on the MAP model) can properly account for the severe metallicity bias seen in the inner Galactic disk region. In each radial bin the metallicity distribution’s shape and position is altered such that for the entire galactocentric distances covered by the SEGUE G-dwarfs the MDF peaks around the same range in  $[\text{Fe}/\text{H}]$  (between  $-0.15$  dex and  $-0.2$  dex). A behaviour that has been recently described by Minchev et al. (2014a) based on predictions from their chemo-dynamical model of the Milky Way and that will be further highlighted in Figure 5.22. However, the innermost distribution differs in its width and shape from the solar and outer disk ones. According to chemical-evolution models for the thin disk the metallicity distribution of the inner disk is expected to be broader than in the outer parts, also recently revealed by observational evidence from APOGEE (Anders et al. 2014). In assuming the model dependent correction is reliably reproducing the disk’s abundance distribution at all radii one could be tempted to argue for the presence of a similar trend in the bias corrected SEGUE dataset. But the number statistics for the inner Galactic panel is low compared to the local and outer bin which leads to a larger correction that requires extrapolation of the model to compensate for the deficient amount of available data. This results most likely in a less secure correction and a MDF prone to noise that is introduced throughout the entire correction process (see Figures 5.13 and 5.15). In the future, APOGEE will hopefully complement the inner disk and shed light on this issue because APOGEE suffers less from selection effects.

Adding to the previous findings, Figure 5.17 reveals that, when split into intervals of current  $R$ , the G-dwarf sample shows a certain range of mean galactocentric radii ( $R_m$ ) in each  $R$  bin (represented by the black dashed histogram). More specifically, these ranges in  $R_m$  can be produced by overlaying several sub-distributions, each related to a different population in

metallicity (coloured histograms). Showing the distributions of the biased sample in the top and its volume corrected counterpart in the bottom several things can be seen from this figure, among those how crucial it is to correct spectroscopic sample such as the presented one. The observed picture illustrated in the top panels does not necessarily represent what is actually needed to compare the observations to models.

Obviously, before correcting the sample for biases (top row) the dominating metallicity interval is the one from  $-1.0$  dex to  $-0.8$  dex (red curve) whose distributions especially stick out in the innermost and solar radial ( $5 \text{ kpc} < R_m < 9 \text{ kpc}$ ) and consequently also in the total bin (rightmost panel). It shows that the biased sample gives preference to the low metallicity intervals that are mainly dominated by the  $[\alpha/\text{Fe}]$ -rich stars that best sample the likely thick disk distribution.

When accounting for the volume correction the prominent selection bias affecting the lower metallicity populations disappears. In all  $R$  bins at all  $R_m$  the major contribution to the total stellar population results from the most metal-rich (thin disk) stars. Instead of the red now the purple interval dominates showing an expected contribution of local disk stars that commonly populate the metallicity regime between  $-0.2$  dex and  $0.4$  dex. It is also evident that after the correction the dominant population peaks at the mean of the total  $R_m$  distribution in each radial bin as one would expect. Furthermore, the percentage for the remaining populations decreases with decreasing metallicity. Moreover, a comparison of the corrected red histograms suggests that the overall contribution of the most metal-poor stars in the G-dwarf sample decreases with increasing radius, a trend that is in agreement with several other studies. Current chemo-dynamical models also predict that the fraction of high- $[\alpha/\text{Fe}]$  metal-poor stars decreases towards the outer disk (see Figure 5 in Minchev et al. 2014b). The red curves in the inner and solar bin peak in the range  $5 \text{ kpc}$  to  $7 \text{ kpc}$  with a tail to larger  $R_m$ . This fact is an additional hint that at all  $R$  metal-poor stars preferentially originate from the inner disk.

### 5.3 Comparing the corrected SEGUE observations with model predictions

As previously outlined the inference of chemo-dynamical constraints from observationally biased samples can be dangerous, so is the usage of model dependent corrections. Still, with the present suite of corrections at hand the unique chance to compare the corrected SEGUE G-dwarf sample directly to predictions from models is too promising than to be disregarded.

For the first time it is possible to compare chemo-dynamical properties extracted from SEGUE observations, with the quantitative predictions provided by the chemo-dynamical model of the Milky Way presented and studied in Minchev et al. (2013, 2014b,c).<sup>5</sup> Hence this section explicitly aims to investigate how well the model predictions match with the observations, simultaneously exploring possible drawbacks of the needed but highly model-dependent mass-weighting correction. The focus is thereby solely directed at the metallicity distribution of the solar neighbourhood and its variations within the disk. This is one of the main constraints for chemo-dynamical models. The comparison also aims to determine if the weak but present bi-modal distribution in the chemical abundance plane that is found in the volume corrected SEGUE G-dwarfs is a true feature or a remnant of the selection effects.

<sup>5</sup>A description of the MCM model is given in Section 1.2.2 (pg. 11).

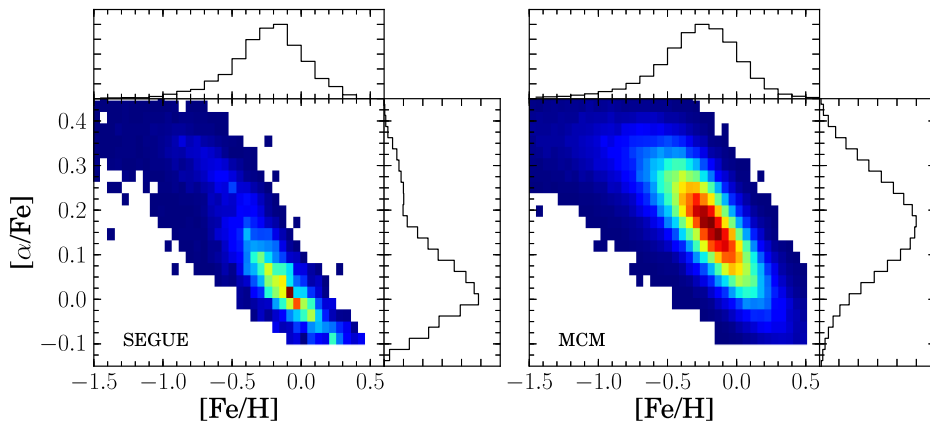


**Figure 5.18:** Density distribution of stars in the elemental abundance plane. Shown are the volume corrected SEGUE G-dwarf sample (*left*) and the MCM model predictions (*right*) based on the simulated  $N$ -body particles. It is to be noted that the distribution in  $[\text{Fe}/\text{H}]$  is rather similar while the  $[\alpha/\text{Fe}]$  abundance histogram shows a significant difference indicating only a double peak in the observations (for an explanation see the text).

### 5.3.1 The chemical plane

As a start Figure 5.18 displays the density distribution in the  $[\text{Fe}/\text{H}]$ - $[\alpha/\text{Fe}]$ -plane for both, the volume corrected SEGUE G-dwarf sample and the simulated  $N$ -body particles of the MCM model. The particle’s chemical properties have been convoluted with observational errors similar to those observed in the SEGUE sample. Also for consistency all selected particles lie within the  $z$  and  $R$  range of the observed SEGUE sample. The core of the density distributions cover a similar range in metallicity shown by the comparable MDFs in the upper panels of the plot, but there is a significant difference in the  $[\alpha/\text{Fe}]$  distributions (right sided vertical histograms). The broad MCM distribution in  $[\alpha/\text{Fe}]$  consists of only one peak that reaches its maximum at about 0.15 dex while the observations show a prominent peak between  $-0.1$  dex and 0.2 dex that represents the metal-rich population of SEGUE stars likely associated with the thin disk component. As already discussed in Section 5.2 this main peak is accompanied by a small bump at higher  $\alpha$  values which is not visible in the model data.

This finding can be interpreted in two ways. First, the peak in the observational data could be a true feature that represents a metal-poor extension to the thin disk leading into a thicker (hotter) component. If so, with the model predictions at hand and the results found by Minchev et al. (2013, 2014b) this component would need to have a different origin than the hotter component of stars that results from internal dynamical processes (e.g. heating, radial migration) in the Galaxy as is seen in the MCM model. The model indeed features particles with typical thick disk properties in kinematics, chemistry and structural parameters. Yet, their fingerprint does not show up as a separate feature in the  $[\alpha/\text{Fe}]$  distribution. Through dynamical mechanisms the model produces a metal-poor (and kinematically hotter, thick disk like) component of stars that serve as an extension of the thin disk. But based on its implemented single disk with thin disk chemistry the model is not able to create a comparable group of stars that result in a second bump in  $[\alpha/\text{Fe}]$ .

Another interpretation is that the peak in the observed data may still be a residual of not perfectly corrected selection effects. If so, there should be no such feature in the model predictions because the model is assumed to be free of any selection effects. And indeed the right panel

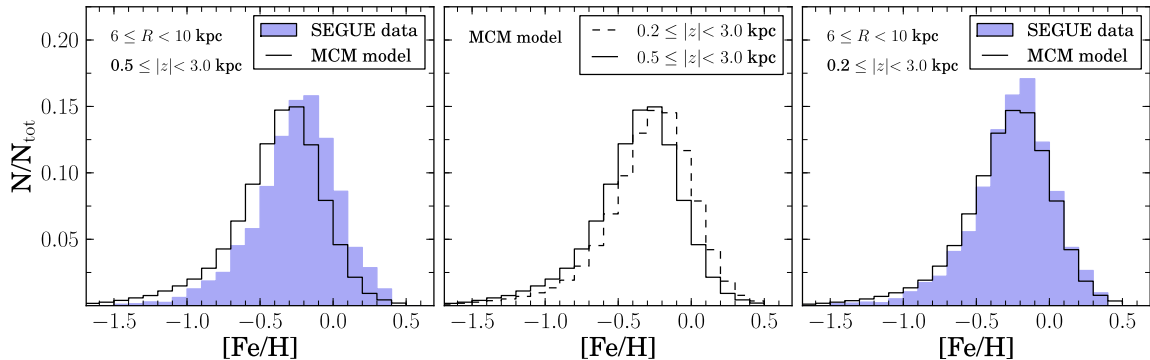


**Figure 5.19:** Selection function, mass and volume corrected MDF for the SEGUE G-dwarfs overlaid by the predicted metallicity distribution function of the MCM model. The model’s metallicity has been convolved with observational errors similar to those observed in the SEGUE sample. *Left and right panel:* MDFs for a range in  $R$  and  $z$ . The choice in  $z$ -range obviously affects the agreement of both, the observations and the model. *Middle:* Variations in the model MDF depending on the chosen  $z$ -range.

of Figure 5.18 does not show a hint of a bi-modal distribution in  $[\alpha/\text{Fe}]$ . However, if in the observations the second peak would be a result of selection effects only, a similar structure should appear in a simulated sample of SEGUE G-dwarfs that is based on the MCM and mocks the observed one. To verify this statement Chapter 7 is devoted to the creation of a stellar mock catalogue of SEGUE stars based on the MCM model. It turns out, as shown and discussed in Section 7.2 (see Figure 7.3) that there is also no indication of a double-peak structure in the compiled MCM mock G-dwarf sample. If the feature is caused by selection effects it should however appear in the mock sample which holds all selection biases of the original SEGUE data. Consequently, it has a lot to commend it that the small but present bump is a true feature.

### 5.3.2 The $[\text{Fe}/\text{H}]$ distribution

Figure 5.19 illustrates how the volume corrected G-dwarf MDF compares to the MCM model MDF. As before the model distribution is based on the characteristics (position and chemistry) of the  $N$ -body particles that belong to the underlying cosmological simulation in the MCM model (see Section 1.2.2). The lefthand panel shows the two MDFs when both, model and SEGUE observations, are restricted to a range in galactocentric radius of about  $6 \text{ kpc} < R < 10 \text{ kpc}$  and a range in vertical height above the midplane of  $0.5 \text{ kpc} < |z| < 3.0 \text{ kpc}$ . The distributions’ slight offset indicates that the stellar distance scale for stars sharing the chemical properties of a certain disk component (thin or thick disk) is different for the model and the observed sample<sup>6</sup>. This implies that even with an identical cut in  $z$ , different portions of the  $[\alpha/\text{Fe}]$ -rich or  $[\alpha/\text{Fe}]$ -poor populations are selected. While the G-dwarf sample still contains a sizeable amount of metal-rich stars at a height of 500 pc, the majority of high- $[\text{Fe}/\text{H}]$  (thin disk) stars in the model reside at lower heights as confirmed by the middle panel. As illustrated the model MDF gets more metal rich when extending the limit in  $z$  down to 200 pc. Consequently, with a change of the  $z$ -range

<sup>6</sup>In contrast, the same cuts in  $R$  and  $z$  applied to the MCM model and an earlier version of the SEGUE DR9 G-dwarfs sample lead to a remarkable match for their MDFs as shown in Figure 11 of Minchev et al. (2014a). Note that back then the spectro-photometric distances for the observed sample had a tendency to be smaller which puts the entire SEGUE G-dwarf sample closer to the plane. A cut at  $|z| = 0.5 \text{ kpc}$  consequently removed most of the metal-rich stars from the sample causing a more metal-poor MDF as observed in the model.

(right panel of Figure 5.19) the agreement of both MDFs improves leading to a remarkable match between model predictions and observations. Apparently the excess of metal-rich SEGUE stars (seen in the bin from 0.5 kpc to 3 kpc) is now compensated in the model MDF by metal-rich stars that are actually closer to the plane where the number statistics of the observed SEGUE stars is insufficient. Whether the observed difference in distance scale is a result of slightly overestimated (see discussion on distance in Chapter 4) distances to the SEGUE stars together with a larger uncertainty in the observation's distance scale or an effect of the model's disk scale height is, at this point, hard to distinguish. Despite the good match of the two total MDFs it is yet unclear how well the MCM model MDF compares to its SEGUE correspondent at different heights and radii within the Galactic disk. As previously discussed in Section 5.2.3 there is a caveat in the SEGUE selection bias corrections, mostly in the inner disk region and at low Galactic heights where the SEGUE survey suffers from low number statistics due to its stellar sampling. This in turn mainly degrades the reliability of the SEGUE volume correction raising the uncertainty for the observed MDFs in those two parts of the disk. How and if this translates into discrepancies with the model MDFs at certain positions within the disk is investigated below.

### Changes in the MDF with vertical height $z$

Figure 5.20 pictures how the observed and the model MDFs match for several  $z$ -bins above the midplane. The discrepant behaviour observed in Figure 5.19 seems to reappear in the two intermediate  $z$ -bins. There, in the range from 0.5 kpc to 1.5 kpc the observed MDFs exhibit more metal-rich stars which leads to a sizeable deviation in the MDFs' high-[Fe/H] tails with respect to the model predictions. If this discrepancy can be explained by a difference in distance scales (scale height respectively) or a problem with the actual volume corrected SEGUE distributions stays open at this point. It turns out that only a similar but independent investigation of the simulated MCM mock SEGUE G-dwarf sample (see Section 7.1.3) helps to narrow down the issue as discussed in Section 7.2.1. In the lowest  $z$ -bin the situation is completely different. Here the model's MDF is dominated by metal-rich (thin disk like) stars showing a pronounced high-[Fe/H] tail and less low-[Fe/H] stars than the observations. Again, this difference may be a result of SEGUE's correction caveat (low number statistics) at low latitudes, yet another reason could be saturation that affects the SEGUE survey at bright magnitudes and that preferentially removes metal-rich stars close to the plane, in addition to SEGUE's target sampling that anyway favours the high latitudes. As mentioned above a closer look to the mocked MCM SEGUE stars provides more insights to the origin of the discrepancy at low  $z$ .

In terms of observational constraints the most important finding however shows up in the highest  $z$ -bin. While the observed MDF is already dominated by a [Fe/H]-poor component of disk stars the model's MDF still comprises a sizeable amount of metal-rich stars missing a MDF that is typical of the thick disk. In general, the peak of the MDF is changing more with height for the observations than for the MCM model. This indicates that, in comparison to the Galaxy's real stellar disk, the MCM model's simulated disk may be too hot and puffed up. Also, the model may be really missing a distinct disk component in addition to its implied thin disk that would then add metal-poor stars more alike the observed ones. If the discrepancy in metallicity at high  $z$  really represents an issue with the metal-poor and  $[\alpha/\text{Fe}]$ -rich disk component of the model a similar behaviour should appear for the inner regions of the Galaxy (probably between a radius of 5 kpc to 7 kpc) where the thick disk component is more prominent than farther out because of its short scale length. So the only way to verify the above assumption is to check the MDF at different bins in galactocentric radius which is done below.

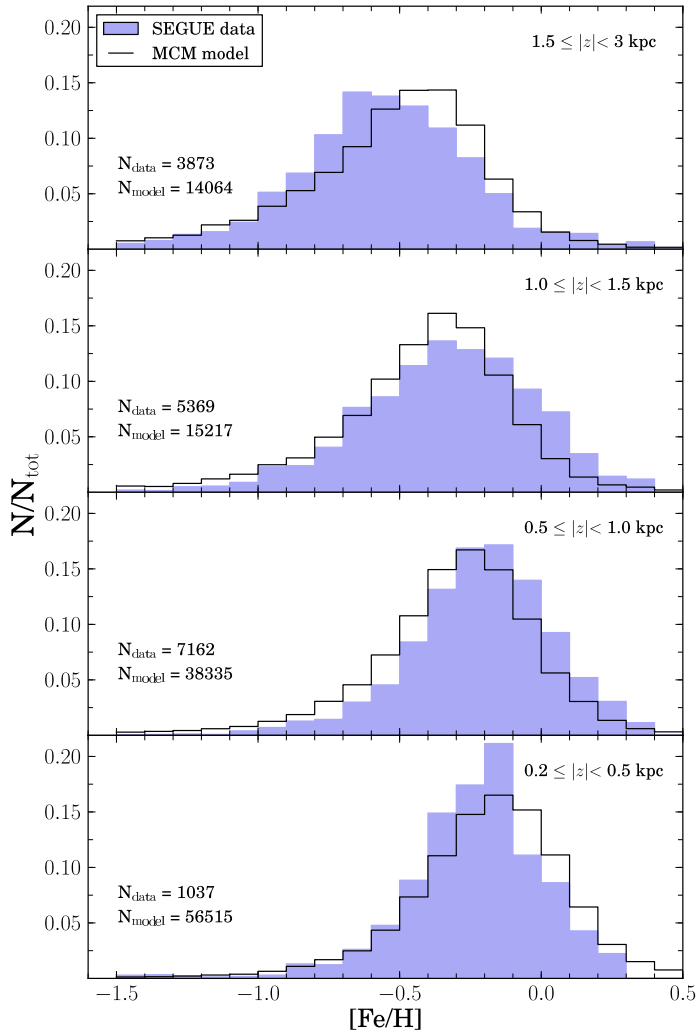


**Figure 5.20:** MDF as a function of vertical height  $z$  for both, the volume corrected sample of SEGUE G-dwarfs (filled histogram) and the chemo-dynamical MCM model. In all subpanels both, the model and the observation, is restricted to a range in radius from 5 kpc to 11 kpc.

### The MDF at different galactocentric radii

In Figure 5.21 the observed (filled histogram) MDF is overlaid by the MCM model’s MDF for several bins in galactocentric radius,  $R$ . With the top row showing SEGUE’s MDFs still uncorrected and the bottom row displaying their fully selection bias corrected correspondents this plot illustrates the significant impact and necessity of the selection bias corrections. Only the volume correction brings the SEGUE distributions into such a good agreement with the theoretical MCM model predictions. Not only that the peak positions are almost identical, there is also little variation in the distribution’s wings. Indeed, in the metal-poor part of the MDF the innermost radial bin shows a less large discrepancy than expected according to the deviations seen in the low metallicity range (thick disk regime) at high  $z$  (see upper panel in Figure 5.20). Instead, the observed MDF indicates only slightly more metal-poor stars in the range  $-0.5$  dex to  $-1.0$  dex. Hence, from the inner disk it is not clear if the MCM model is really missing a distinct metal-poor (thick disk like) component. At that radial range the bias correction could

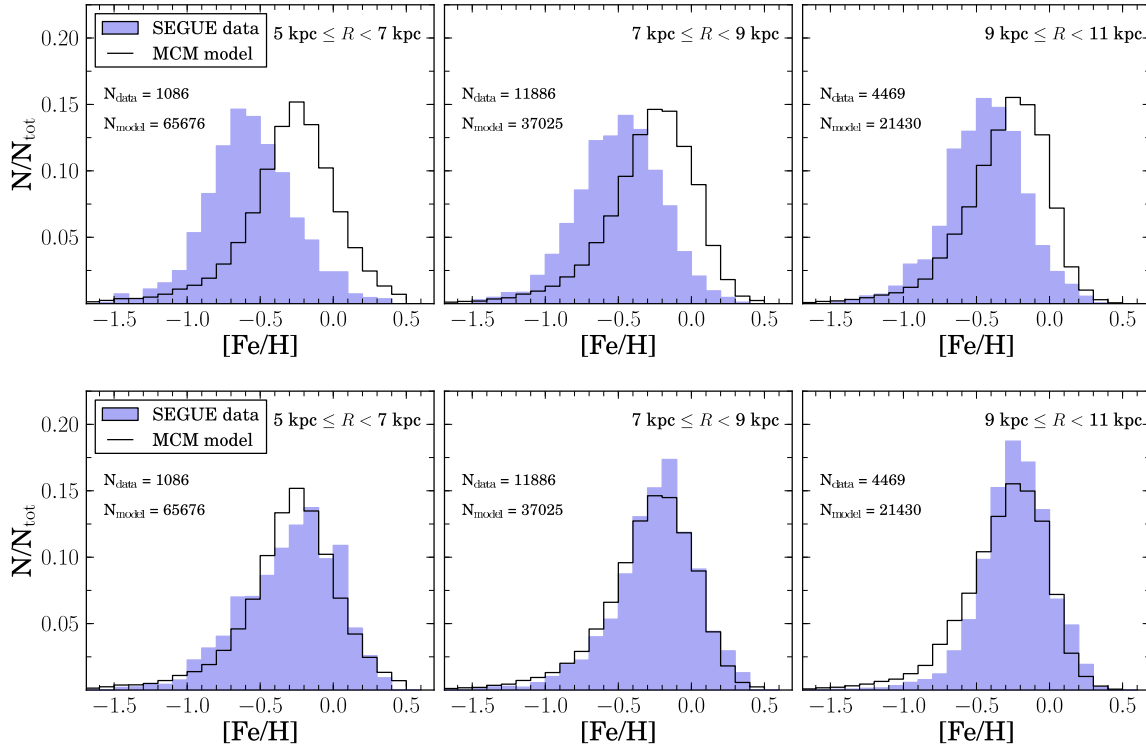


**Figure 5.21:** MDF in bins of galactocentric radius for both, the SEGUE stars (filled histogram) and the MCM model (solid black line). The total number of stars in the radial bins is indicated in each subpanel. *Top row:* MCM model predictions versus SEGUE observations without selection effect corrections. *Bottom row:* Same as in the top row but now with fully corrected (including the volume correction) SEGUE distributions illustrating how significantly the MDF is affected by the corrections.

well conceal important clues. This leaves no doubt that a separate study of on MCM model based mock is imperatively needed in order to distinguish between artefacts and true features.

### Variations in the MDF as a function of galactocentric radius

In order to better compare possible variations Figure 5.22 finally displays the MDF at different galactocentric radii overlayed on top of each other in separate panels for the SEGUE G-dwarfs and the MCM model. Consistent with the findings in Figure 7 and 9 of Minchev et al. (2014b) the peak of the total model distribution for each radial bin is centred on a  $[\text{Fe}/\text{H}]$  value of about  $-0.2$  dex, a slightly lower value, presumably due to the cut at  $|z| > 0.2$  kpc. As a consequence the metal-rich tail is less distinct than originally found in Minchev et al. (2014b). A result that can be explained by the fact that the highest contribution in metal-rich stars usually comes from close to the disk plane (see Figure 9 of the latter reference), a region being excluded in the present comparison. For the observed MDFs (left panel) the situation is different. Even though the MDFs peak around the same value than the model their variation as a function of galactocentric radius is larger. Especially the behaviour of their wings is less clear. As already indicated in Figure 5.21 for the innermost radial bin (blue histogram) a distinct bump appears in the metal-poor tail of the distribution ranging from around  $-1.0$  dex to  $-0.5$  dex. Considering that the model does not show a similar sign and the volume correction for SEGUE stars is the

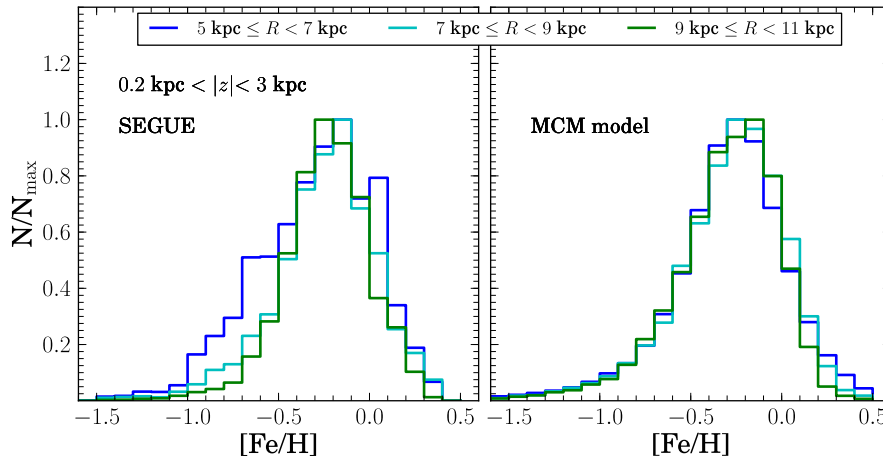


**Figure 5.22:** Normalised metallicity distribution function for different ranges in current Galactic radius, both, for the fully corrected G-dwarf sample (*left*) and the chemo-dynamical MCM model (*right*). In case of the model the peak of the distribution in each radial bin is centred on  $[\text{Fe}/\text{H}] \approx -0.15$  dex. The corresponding observed distributions peak around the same region but possess less defined wings.

most uncertain in the inner Galaxy (compared to the solar and outer radial bin) the feature may be an artefact. The comparison in Section 7.2.1 however reveals a similar excess of metal-poor stars with respect to the MCM mock stars. This may be evidence that the feature observed in the SEGUE data may indeed be a true one.

## 5.4 Discussion

The collection of corrections developed for the stellar type of SEGUE G-dwarfs introduce significant noise and hence uncertainty to the observed distributions and relations. This makes it difficult to read out trends and information with confidence. However, it could be demonstrated that in principle all corrections are well compensating for the observed selection effects. Without doubt they are useful and even necessary when aiming to compare the SEGUE dataset directly to datasets from other surveys or predictions from models. So it is inevitable to at least correct the SEGUE sample for its metallicity biases when comparing its properties to those of a stellar sample of RAVE giant stars which do not suffer from the same selection effects (see Chapter 8). Also, the entire set of biases needs to be taken care of (including the SEGUE survey volume with respect to the global volume around the Sun) in order to compare the SEGUE observations to predictions from the chemo-dynamical model by Minchev et al. (2013) as previously shown. The survey volume correction however is highly model dependent because it includes the extrapolation of the stellar density distribution of the Galactic disk to latitudes only sparsely sampled by the actual SEGUE dataset. Especially this correction has thus to be interpreted with care. This is because it has direct impact on the question whether the discovered differences between the model predictions and the corrected G-dwarf sample are due to problems with the corrections or due to the properties of the model itself.

Using the corrections to trace the 'true' picture of the Galaxy, i.e. the scenario an ideal observer would see from outside the Milky Way, is still a challenging task and far from being perfectly implemented. Yet, a less troublesome but promising solution to wisely use the obser-

vations finding observational constraints for any kind of model is the creation of mock samples. Those mock samples have the advantage that ideally all observational selection effects can be translated to the simulated data in order to obtain an observed realisation of the theoretical model, most similar to the observed counterpart. As long as the selection effects are equally present in the observed and the mock sample a comparison of both is a valuable tool to validate the model. Knowing the influences of the selection biases on the investigated properties allows also to better identify possible discrepancies and variations as true differences between model and observations. If discrepancies that occur in a direct comparison of the observed dataset and the model (current chapter) remain also when the observation is compared to a mock counterpart, they are likely to be caused by true differences between the compared samples. On the other hand, if the differences are only visible in case the observed sample is corrected the correction itself and not the model may be problematic.

In order to complement and extend the findings of the present chapter the following ones concentrate on the creation of two different G-dwarf mock samples. One based on TRILEGAL (Chapter 6), the other as a mock realisation of the MCM model (Chapter 7). As described in the next chapter the main tool needed to generate a proper mock equivalent to the observed G-dwarf sample is the SEGUE survey selection function which is used to downsize the number of simulated photometric objects to match the size and properties of the actual spectroscopic sample. The way this is accomplished is to (a) reconstruct the selection function for each individual SEGUE pointing and (b) compute selection function weights for every simulated G-dwarf. The metallicity bias caused by the colour-cut is naturally introduced as soon as G-type stars are selected only. And the volume correction does not play a role because each mock realisation considers the same volume around the Sun as covered by SEGUE.

## Summary

The main results of the current chapter can be summarised as follows:

- The investigated observational selection effects all bias the SEGUE G-dwarf sample mainly against metal-rich stars. Thereby their impact increases significantly from the bias that can be attributed to the target-type overlap of different categories of SEGUE stars to the bias that results from the limited volume covered by the survey which affects the analysed relation most.
- Figure 5.17 demonstrates that it is possible to obtain a good representation of the real volume characteristics of the Galaxy with SEGUE even with the prevailing biases. Each of those biases has its impact, in combination they reveal the chemo-dynamical structure of the disk as seen by SEGUE.
- Figure 5.18 reveals a significant difference in the stellar density distribution when comparing the survey volume corrected SEGUE G-dwarf sample and the MCM model predictions by means of the simulated  $N$ -body particle characteristics in the chemical abundance plane. While the bias corrected observations show a hint of a bi-modal distribution in  $[\alpha/\text{Fe}]$  there is no sign for it in the predicted model distribution. This finding may indicate the following: either the observationally found feature is still a remnant of the selection effects or the observed sample houses a group of metal-poor stars with properties of a hotter disk component and a different origin that the MCM model is not able to generate by pure consideration of a thin disk (and its chemistry) and dynamical processes such as stellar heating, scattering or radial migration. The comprehension of a SEGUE G-dwarf mock

sample based on the MCM model in Chapter 7 shows that finally the second interpretation is to favour.

- The MCM model shows a shallower change in the peak of the metallicity distribution function than the observations which, if a true feature, indicates that evolutionary processes in the Galaxy's history alone are not enough to account for a thick disk component of the Galaxy as revealed by the observations and shown in Figure 5.20 and 5.21.
- As illustrated in Figure 5.22 the MDF of the volume corrected SEGUE G-dwarfs peaks at approximately -0.15 dex to -0.2 dex in  $[\text{Fe}/\text{H}]$  independent of the stars' galactocentric radius, a finding recently predicted by the chemo-dynamical model discussed in Minchev et al. (2014b). Yet, in the inner disk region (5 kpc to 7 kpc) the SEGUE observations suggest a variation in the metal-poor tail of the MDF as a function of radius that is not matched by the MCM model.



---

## A TRILEGAL mock sample of SEGUE G-dwarfs

---

Among the known theoretical descriptions of the Milky Way that aim to contribute to a better understanding of the structure, formation and evolution of the Galaxy models like TRILEGAL, a population synthesis model, have proven to be particularly useful tools not only to study the stellar content but also to test different Galaxy formation scenarios by comparing the simulated output with observational datasets from Galactic surveys at different wavelength. Since the population synthesis approach makes use of stellar evolution and atmosphere theory those models have a great advantage because their predictions can be directly compared to the observed data. They are able to establish the needed link between observations and model which is missing in case of pure physical models that describe the Galaxy based on distributions and fundamental physical quantities like mass density, ages or phase space coordinates while the real astrophysical observations facilitate information about observable quantities like stellar parameters, apparent magnitudes, proper motions or radial velocities.

The aim of this chapter is to obtain a synthetically generated sample of mock stars that is equivalent to the observed SEGUE G-dwarf sample dealt with in this work by using the TRILEGAL Galaxy model. A comparison of the observed and the mock star sample provides a valuable opportunity to test the Milky Way model for its degree of consistency with observations and its strength to predict what one would expect to observe in real life under the assumption that the TRILEGAL model represents a proper description of the Galaxy and its stellar content. Through a simple comparison of mock and observed stars it is possible to obtain new observational constraints that can immediately help to improve the model under investigation as is shown in the present Chapter.

However, when simulating a specific survey (or a dataset) with TRILEGAL the observational selection effects of the actual parent survey are not a priori present in the simulated mock equivalent. Consequently, they have to be particularly accounted for to allow a direct comparison of the observed and the mock sample. This can be realised in two different ways: either the observed dataset is corrected such that the observations resemble the properties of the underlying photometric population (mainly in terms of stellar number density), this can be implemented e.g., by using information about the survey's actual completeness, or the mock sample is created such that the selection effects are directly applied to the unbiased photometric population of the simulation which is similar to introducing the incompleteness of the observed stellar sample to the simulation. The last chapter has shown how complex the issue of selection effects can get

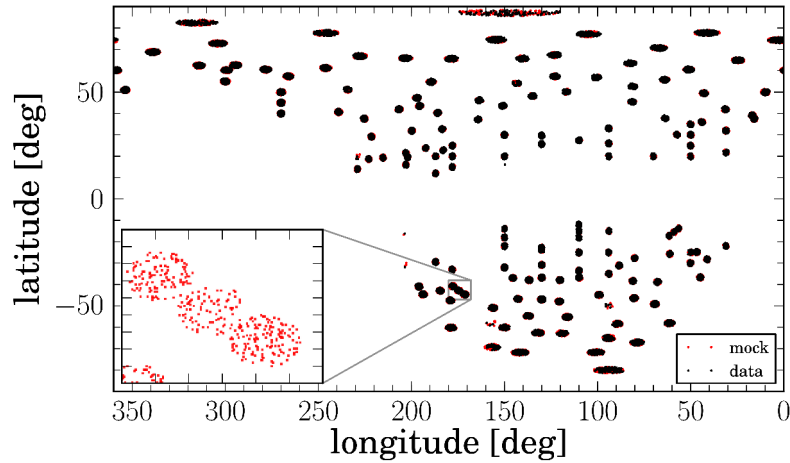


**Figure 6.1:** Spatial distribution (Galactic coordinates) of those SEGUE pointings that contribute to the creation of a TRILEGAL G-dwarf mock sample. *Zoomed panel:* The proximity of some SEGUE pointings leads to an overlap.

for present-day observational Galactic datasets. Not only that most datasets are liable to the selection function of the survey, usually resulting from a non entirely random selection of objects, they can, as demonstrated in the case of G-type stars, also be subject to effects like metallicity biases that arise due to colour cuts. Also the correction can sometimes be very difficult and problematic as previously demonstrated.

Since the introduction of selection effects into the simulation turns out to be less problematic this work makes use of the inverse modelling approach by applying the observational biases to the model output instead of correcting them in the observed sample. In other words, a sample of mock stars is created that resembles the properties and conditions of the Galaxy as seen through the eyes of the model, assuming that the model is a good representation of reality. This procedure allows to select a sample of mock stars in the same way as done for the observed data sample, starting with the target selection by adopting the SEGUE G-star colour-magnitude cut, introducing the same selection biases and final selection criteria. In this process, the uncertainties of the observationally determined astrophysical parameters of the observed stars play an important role. Influenced by many external effects an astrophysical measurement never represents the true value of the quantity of interest but rather is an expression for the most likely value given e.g. the atmospheric conditions, instrument specifications or analysis pipeline. In order to compare observed samples with mock samples it is hence necessary to introduce similar observational uncertainties to the simulation which always predicts the true value of the parameters.

At this point special thanks is given to a couple of members from the Brazilian Participation Group, namely, Eduardo Balbinot, Helio Rocha-Pinto and Leo Girardi who have essentially contributed to the realisation of this chapter’s analysis by running and providing the TRILEGAL simulation of all SEGUE plates, computing the input extinction for each SEGUE pointing and implementing modifications to the model’s code in consequence of the analysis and findings introduced in this part of the thesis.

## 6.1 Simulating the SEGUE survey with TRILEGAL

As a first step the complete set of SEGUE line-of-sights has been simulated with TRILEGAL (version 1.6) creating a catalogue of mock stars that resembles the entity of photometric SDSS objects which serve as potential target candidates for spectroscopy in the celestial area covered by SEGUE. This photometric mock counterpart catalogue has the advantage that, besides photometry (magnitudes) and the positional information, the model delivers additional information on chemistry, ages and kinematics for each mock object. The simulation includes the usual science data pointings from SEGUE-1, SEGUE-2 and special pointings, mainly from SEGUE-1, that serve either for target testing (segtest), calibration purposes (segcluster) or are dedicated to particular regions of interest e.g. the low latitude pointings (seglowlat) that cover line-of-sights below a latitude of  $l = 20^\circ$  or those pointings directed at locations with probable Milky Way structure (segpointed). The list of simulated pointings adds up to a total number of 410 different line-of-sights. A detailed number statistic of the pointings used for the simulation is outlined in Table C.2 of Appendix C. More information and a detailed listing of the SEGUE pointings can also be found on the extensive SDSS-III documentation pages<sup>1</sup>. For illustration purposes Figure 6.1 shows the distribution in Galactic coordinates for all SEGUE pointings that are existent in the observed and the final G-dwarf mock sample.

The simulations were carried out by Eduardo Balbinot using AddStar<sup>2</sup>, a web based tool that was developed and is maintained by members of the Brazilian Participation Group within the framework of LIneA<sup>3</sup>. AddStar uses parallel processing to run TRILEGAL in a more efficient way such that independent pointings are simulated simultaneously. The main input parameters for the simulation are (a) the central coordinates of the SEGUE plates (given in RA and DEC) and (b) the extinction in the direction of the pointing. How the input extinction has been calculated for each pointing is detailed in Section 6.1.1. The simulated area for each pointing covers  $7 \text{ deg}^2$  around the central coordinates. Further parameters that needed to be defined prior to the simulation run are: (1) the magnitude system for the output photometry along with an upper limit (at the faint end) and the resolution in magnitude, (2) the Initial Mass Function (IMF) together with an assumed binary fraction, (3) the position of the sun within the disk with respect to the Galactic centre, (4) the resolution in distance modulus and (5) certain specifications for the stellar components of the Galaxy such as the density profiles of the thin and thick disk as well as the shape of halo and bulge. More information on the input parameter specifications that were used in case of the current thesis as well as an overview about the TRILEGAL output parameters is given in Table C.3 and Table C.1 in the Appendix.

### 6.1.1 Calculation of the input extinction

Values for the Galactic extinction in the direction of each SEGUE pointing are computed based on the Schlegel et al. (1998) maps and passed to the Galaxy model as an input parameter. As a first step in the calculation process the colour excess  $E(B - V)$  is obtained for the central coordinate of the  $7 \text{ deg}^2$  field. In addition the  $E(B - V)$  value is determined for another 1000 locations on the plate which are randomly distributed around the central coordinate. Each of these colour excess  $E(B - V)$  values is transformed into a total  $V$ -band extinction  $A_V$  using the

<sup>1</sup>Table of SEGUE pointings: [http://www.sdss3.org/dr10/algorithms/segue\\_plate\\_table.php](http://www.sdss3.org/dr10/algorithms/segue_plate_table.php)

<sup>2</sup>AddStar is a contribution from the Dark Energy Survey (DES) group in Brazil to the DES collaboration. The tool can be used to create stellar catalogues over a celestial region specified by the user and is based on the TRILEGAL Galactic model of Girardi et al. (2005). The model includes Milky Way bulge, thin and thick disk and halo components

<sup>3</sup>Laboratório Interinstitucional de e-Astronomia

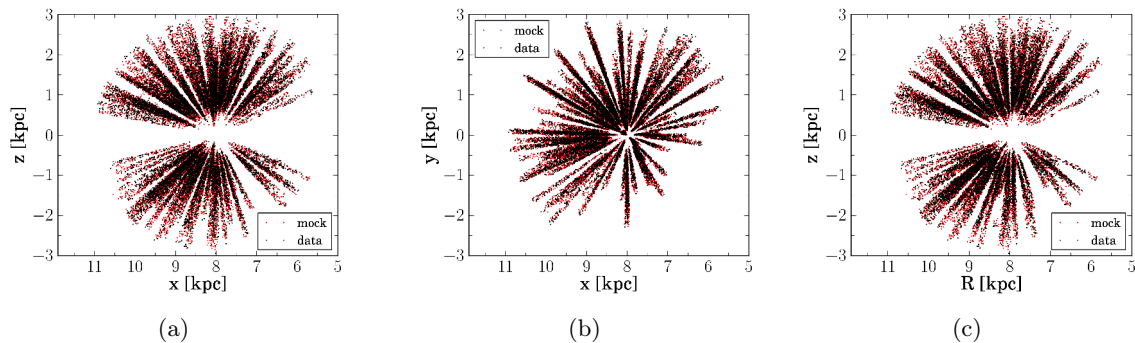


**Figure 6.2:** Spatial distribution of stars in the galactocentric (a)  $xz$ -plane, (b)  $xy$ -plane and (c)  $Rz$ -plane. Observed G-dwarfs are shown in black and the TRILEGAL mock sample is indicated in red. Notice the sparse sampling of the SEGUE survey.

following simple relation

$$A_V = E(V - B) \times R(V) \quad (6.1)$$

assuming a typical value of  $R(V) = 3.1$  for the Galaxy. Then, the entity of  $A_V$  values is averaged, the standard deviation  $\sigma(A_V)$  is determined and the dispersion  $sA_V = \sigma(A_V)/A_V$  is computed.  $A_V$  and  $sA_V$  are finally turned over to TRILEGAL. The Galaxy model itself processes the extinction values for each pointing by applying the central reddening plus a Gaussian noise and returns back an estimate of the extinction  $A_V$  for each single simulated object on the plate. Using Equation 6.1, again the extinction for a particular object can be transformed into an  $E(B - V)$  value to further work with in the analysis.

### 6.1.2 Correction for overlap of SEGUE pointings

Within the set of SEGUE pointings there are a couple of fields that overlap in terms of skycoverage. When simulating with TRILEGAL this directly effects the predicted number counts in the intersecting areas. Since the region of overlap is simulated multiple times, once for each of the intersecting pointings, the number of simulated objects in that particular spot on the sky is overestimated in comparison to the number of stars in the real observational data. One way to account for this issue is to first determine which object on each pointing falls into a region of intersection in order to then assign weights to the affected objects that correct for the overestimation in a second step. The following paragraph shortly outlines how weights are obtained for every simulated star of the photometric SEGUE mock catalogue.

If pointings are overlapping on the sky depends on the distance between their central coordinates. In case of the circular SEGUE pointings ( $7 \text{ deg}^2$ ) the relevant criterium to identify intersections is to check whether for a pair of plates the distance  $d_{AB}$  from the center of plate A to the center of plate B is smaller than two times their radius  $r$  (with  $r = 1.5 \text{ deg}$ ). Assuming spherical geometry the distance  $d_{AB}$  is calculated according to

$$d_{AB} = \arccos(\sin \phi_A \sin \phi_B + \cos \phi_A \cos \phi_B \cos \Delta\lambda) \quad (6.2)$$

with  $\lambda$  and  $\phi$  being right ascension and declination, respectively. If for a pair of plates  $d_{AB} < 2r$  holds true the distance  $d_*$  between each individual star on plate A to the center of plate B is computed and vice versa for the stars of plate B. In case  $d_* < r$  the particular star falls into a region of intersection and is allotted a weight of  $1/2$  if two plates are overlapping or  $1/3$  in case

three pointings are intersecting. How the weights are applied in practice will be described in a later section of this chapter that deals with the extraction of the SEGUE G-dwarf mock sample from the photometric SEGUE mock catalogue.

## 6.2 Creation of a synthetic SEGUE G-dwarf sample

The obtained catalogue of photometric SEGUE mock stars builds the basis to create a mock sample of SEGUE G-dwarfs by applying the same selection criteria as used for the observational counterpart (see Chapter 3) and by using the selection function of the SEGUE survey (as detailed in the previous Chapter). The aim is to obtain a sample of mock stars that resembles its observed counterpart as close as possible by means of stellar type, magnitude range, spatial coverage and sample volume. In other words, the resulting mock sample should be an equivalent model realisation of the SEGUE G-dwarf sample. Therefore it is necessary to determine which SEGUE line-of-sights actually contribute to the final selection of the SEGUE G-dwarfs. This is particularly important because the latter sample covers only a subset of all the pointings simulated with TRILEGAL and the mock sample must contain only objects from pointing in this subset in order to reach the same spatial coverage as its counterpart. Once the subset is identified the overlap among the corresponding simulated pointings is determined as outlined in Section 6.1, assigning an overlap weight to each of the photometric mock objects that are at this stage still all candidates to be finally selected for the mock G-dwarf sample.

### Extraction of G-type stars

Before the colour-magnitude criteria for SEGUE G-type stars can be applied to the photometry of the mock stars the model magnitudes have to be de-reddened. That is because SEGUE's selection criteria have to be applied to extinction corrected magnitudes. However, TRILEGAL's photometry has gone through an internal reddening process where extinction is applied to the output magnitudes that have been directly drawn from the theoretical isochrones (Marigo et al. (2008) isochrones with the Girardi et al. (2010) Case A correction for low-mass, low metallicity AGB tracks). In the present case, the photometry is therefore corrected for extinction by using the following relations:

$$A_\lambda = X \times A_V \quad (6.3)$$

$$\text{mag}_{\lambda,0} = \text{mag}_\lambda - A_\lambda \quad (6.4)$$

with different values for  $X$  depending on the filter. The  $A_V$  values are delivered by TRILEGAL for each individual simulated object. Table 6.1 lists the values for  $X$  that are in internal use by TRILEGAL to add extinction in the five SDSS photometric bands. The  $A_\lambda/A_V$  ratios<sup>4</sup> were once derived by applying the Cardelli et al. (1989) extinction law to the spectrum of the Sun which is by accident also a G-dwarf. Hence, these extinction coefficients are perfectly suited and used to de-redden the TRILEGAL magnitudes of the G-dwarf mock stars in order to be consistent in this matter.

In the extraction process the G-type candidates are selected from the previously discussed subset of pointings on a plate-by-plate basis. Because the stars in the dataset do not entirely sample the original  $r$ -band magnitude ranges of the SEGUE plates ([14.0, 17.8] and [17.8, 20.2] for the bright and faint exposures, respectively) the upper magnitude range limit, that defines up to which brightness simulated G-type stars will be chosen, is adjusted accordingly. In practice,

<sup>4</sup>Provided by Leo Girardi.

**Table 6.1:** Extinction coefficients  $X = A_\lambda/A_V$  as determined by Leo Girardi and internally used by TRILEGAL to redden the theoretically predicted photometry.  $\lambda$  stands for each of the 5 SDSS passbands. For more details see also the text.

	$u$	$g$	$r$	$i$	$z$
$X$	1.56906	1.20585	0.87122	0.68319	0.49246

this means that for each pointing the faintest G-type star in the observed sample sets that faint magnitude limit up to which objects are selected on their simulated counterparts. This is an important step because by experience even the bright exposures of the SEGUE plates do not reach the same depth in  $r$ . By adopting this restriction it should be guaranteed that the sampled volume is similar for the observed and the mock sample. At this point of the process the number of simulated SEGUE mock stars has been reduced to only the G-type like objects on plates that contribute to the observed G-dwarf sample. In terms of selection effects, so far the application of the colour-magnitude cut has certainly introduced the same metallicity bias to the mock stars than is found for the observed stars. Still, the introduction of the even more important selection function of the survey is missing. Its implication and effects on the mock stars is discussed in Section 6.2.2. Prior to that, the next section deals with TRILEGAL’s metallicity distribution function implemented for the thick disk.

### 6.2.1 Modification of the thick disk MDF in TRILEGAL

The literature is rich in studies that concentrate on the chemistry of stellar spectroscopic samples which broadly agree that most of the stars in the thick disk component of the Galaxy have  $[\text{Fe}/\text{H}]$  values between  $-0.5$  dex and  $-1$  dex, with a peak in the range  $-0.6$  dex to  $-0.7$  dex. Also, the results of many authors, e.g., Bensby et al. (2014), Casagrande et al. (2011), Allende Prieto et al. (2006) and Fuhrmann (2008) show that the thin and thick disk’s chemistry overlaps in the region from  $-0.3$  dex to  $-0.7$  dex in  $[\text{Fe}/\text{H}]$ , many studies even indicate that the thick disk extends to solar values or above. Ideally, the same should be observed for the simulated SEGUE G-type stars. However, a first look at their chemical properties revealed that the total metallicity distribution function separates into two distinct peaks. Those are located at around  $-0.2$  dex and  $-1.2$  dex and could be attributed to TRILEGAL’s thin and thick disk components which apparently do not overlap at all in terms of chemistry in the model’s version 1.6 but show a clear dip in the metallicity range  $[-0.7, -0.8]$  dex and a very metal-poor thick disk distribution far beyond the common expectations. The solution was to find a new and suitable template distribution for the model’s thick disk that is constrained by empirical data, resembles the current consensus on the Galactic thick disk MDF as close as possible and can be implemented to TRILEGAL. In this context, a small subsample of thick disk like stars, taken from the high-quality RAVE giant sample presented in Boeche et al. (2013a), seemed to be a proper and the best choice at hand. By fitting their MDF (see panel (g) of Figure 12 (top) of the latter reference) with a lognormal distribution a template could be produced that integrates the empirical shape and peak position (at about an  $[\text{Fe}/\text{H}]$  of  $-0.6$  dex) of the RAVE stars’ MDF into the new definition of the model’s thick disk metallicity properties. A final re-simulation of the entire SEGUE survey (repetition of the steps discussed in Section 6.1) based on the modified TRILEGAL version indicated a clear improvement with respect to a more probable MDF and builds the groundbase to select the final synthetic G-dwarf sample following the descriptions and steps layed out in Section 6.2.

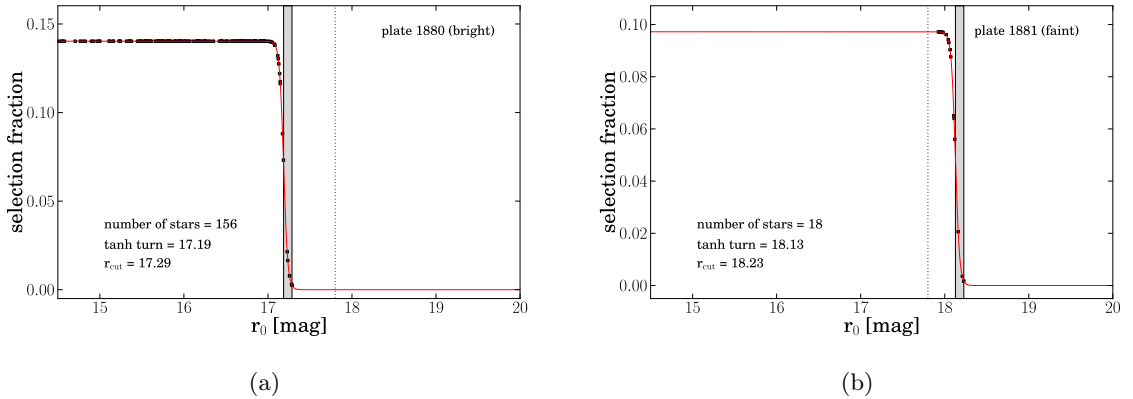


**Figure 6.3:** Reconstruction of the selection function. Exemplarily, panel (a) shows a SEGUE bright plate and panel (b) a SEGUE faint plate. Black points represent the selection fraction of individual stars on the plate, the solid line is the reconstructed fit of the selection function.  $r_{\text{cut}}$  is the  $r$ -band magnitude of the faintest star on the plate. The gray shaded area marks region of the hyperbolic tangent cutoff.

## 6.2.2 Implementation of the SEGUE selection function

In order to properly introduce the selection function into the simulation it is necessary to know the completeness of the survey in terms of G-type stars for each particular SEGUE pointing (see e.g. Figure 5.4). As discussed in the previous Chapter, Bovy et al. (2012c) have found a way to model and describe the SEGUE selection function through a general analytical expression (see Section 5.1.2, Equation 5.1) which allows to directly estimate the selection fraction of G-type stars in the SEGUE survey depending on their magnitude and position on the sky. With this theoretical background and the individual selection function weights that have been exclusively computed (see Section 5.1.2) for this work’s selection of spectroscopically observed SEGUE G-type stars (Chapter 3) it is possible to reconstruct the selection function on a plate-by-plate basis. Thereby, the objects in the observed G-type sample are grouped according to their plate membership, than the relation between the calculated selection function weights and the  $r$ -band magnitudes of the stars is fit assuming a model function similar to Equation 5.1. With the help of those fits it is possible to later calculate a selection function weight for each mock star which can be used in reverse effect to adapt the simulation to the data.

The result of the fitting procedure is exemplarily shown for a bright (left panel) and a faint (right panel) SEGUE plate in Figure 6.3. The black points represent the observed stars. They dictate the shape of the reconstructed function but obviously do not always cover the entire magnitude range. However, the selection function is needed for the whole extent of the plate because the G-type mock stars are distributed over the entire magnitude range. If one wants to consider each mock star as a potential candidate for the final mock sample it is hence essential to be able to determine individual selection fraction values for each G-type mock star depending on its  $r$ -band magnitude using the fit of the corresponding plate. This can only be realised by extending the fit (red line) under the assumption that the model function, backed by the sparse number of data points is valid for the entire plate. Related to the fact that some stars in the observed G-type star sample possess a zero value for their selection function weight (see Section 5.1.2) it is impossible to get a successful selection function fit for every pointing, especially for those where the selection fraction information is missing for all objects. Besides there are a couple of pointings with too few data points to get a reliable fit in the reconstruction process. As

(a) the number of plates without successful fit is reasonably small and (b) in case of mock versus observations it is possible to remove objects on problematic plates in both samples plates without fit are simply not considered in any further steps. As a consequence the SEGUE G-dwarf sample that is compared to the its TRILEGAL mock counterpart differs slightly in terms of number counts from the observed SEGUE sample that is described in Chapter 3.

### Application of the selection function

As illustrated in Figure 6.3 the behaviour of the selection function is different for bright and faint SEGUE plates. For bright exposures the selection fraction is constant over almost the entire magnitude range, dropping off at the very faint end of the plate where the incompleteness of the spectroscopic sample is mainly a consequence of the artificially induced discontinuity at the boundary between the two types of SEGUE plates. However, in case of the faint exposures the modeled decrease accounts for the fact that towards fainter magnitudes the selection fraction has to drop naturally because the spectroscopic sampling gets more and more incomplete with respect to the large amount of available photometric objects.

With the help of the plate dependent selection function fits it is finally possible to calculate an individual selection function weight (similar to selection fraction) for each G-type mock star accounting for the objects angular position and its specific magnitude. In principle, those weights could than directly be used to introduce the selection function to the sample of mock stars by multiplying each object with its corresponding weight. This procedure would have the reverse effect as seen for the correction of the observed sample in Chapter 5. Because the weights are smaller than one the act would result in the needed downsizing effect in terms of number counts weighting the photometric mock stars such that their number appears to be close to the number of stars that are spectroscopically observed.

However, the more common way is to randomly select a fraction of objects from the entire sample of G-type mock stars according to the completeness of the spectroscopic sample. In the present case this can be achieved with the following procedure: the G-type mock stars are binned in  $r$ -band magnitude with a bin width of 0.1 mag. Then, for each bin an average selection fraction (a completeness) is determined based on the individual selection function weights of those mock stars that fall into a particular bin. In the following, the average values serve as representative measures for the percentage of G-type stars that have been observed in each of the magnitude bins. At each magnitude range a corresponding amount of objects is thus be extracted from the total number of available mock stars. In other words, if a magnitude bin with observed stars e.g. exhibits a completeness of 30% an equal percentage of mock stars of similar magnitude is randomly drawn to contribute to the final mock sample. Following this procedure, at this state of the selection process the sample of G-type mock stars is of similar size as its real star counterpart has been after a single cut in signal-to-noise. The latter lead to a sample of approximately 29 000 spectroscopically observed G-type stars that remained from the initial sample queried from the CAS.

In order to validate that the random extraction of mock stars works properly the upper left panel of Figure 6.8 compares the  $r_0$ -magnitude distributions for both methods described above. The dashed histogram shows the mock sample in case the individual selection function weights are applied to each stars on the fly which seemingly downsizes the sample but does not physically reduce its size. The solid histogram represents the randomly drawn and thus number count adjusted mock sample. The fact that both curves match quite well is reassuring and demonstrates that the above procedure produces a randomly generated mock sample suitable to work as a proper comparison sample to the observed dataset of SEGUE stars throughout the

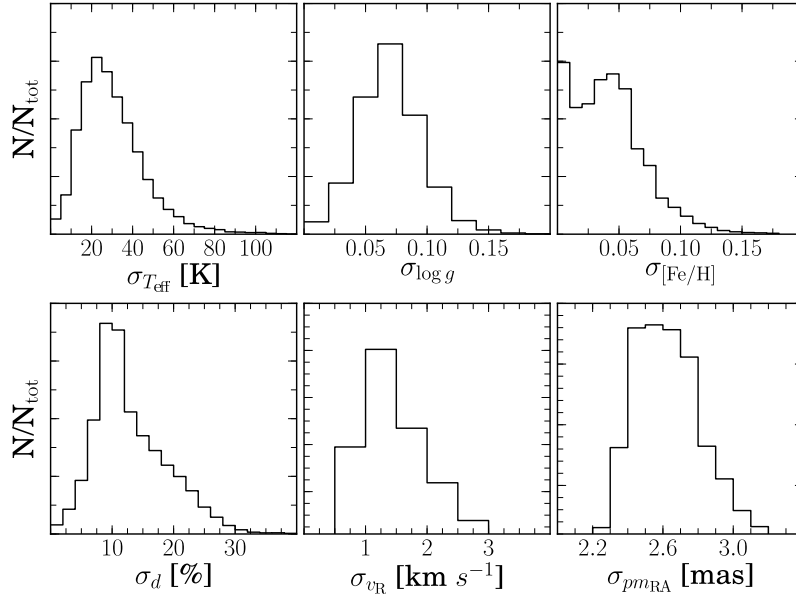


**Figure 6.4:** Uncertainty distributions for stellar parameters, distances and kinematic properties as shown by the SEGUE G-dwarfs. *Top row:* individual internal SPP uncertainties for temperature, surface gravity and metallicity. *Bottom row:* uncertainties in radial velocity, proper motion (RA-component) and distance (as described in Chapter 4).

following analysis.

### 6.2.3 Introduction of observational errors

In case of the simulation none of the output parameters is delivered with a corresponding uncertainty. To obtain a more realistic picture of how well the mock sample compares with the error prone dataset the effect of observational uncertainties needs to be added to the theoretically predicted mock parameters. By construction, the simulated parameter distributions are much narrower and well defined while distributions of parameters that are determined from observed spectra are in general much broader. The main reason for this is the quality of the data that is influenced e.g. by atmospheric conditions, the resolution of the spectra, properties of the instruments in use and the very generalised pipelines that need to be able to determine parameters for a variety of objects. As a result the observed parameters never resemble the true values of the physical quantities but stand for the most likely value given the observational conditions. The simulation however predicts the true physical quantities following the underlying model.

In order to incorporate uncertainties similar to those of the SEGUE G-dwarfs each mock star is associated with a set of parameter uncertainties corresponding to a real SEGUE object. Consequently, the uncertainty distributions for the parameters (including stellar parameters, velocities, distances) of the mock stars are alike those of the observed data sample. This approach is only possible because the SPP provides individual uncertainties for each of its stellar parameter measurements (internal uncertainty). Besides, the spectro-photometric distance, the radial velocities and the proper motions in use possess individual uncertainty estimates too. As illustrated in Figure 6.4 the internal uncertainties for the main stellar parameters however tend to be generally very small, likely underestimating the true observational SEGUE uncertainties (see Section 2.2.2 for a more detailed discussion on the SPP uncertainties). Usually, the precision

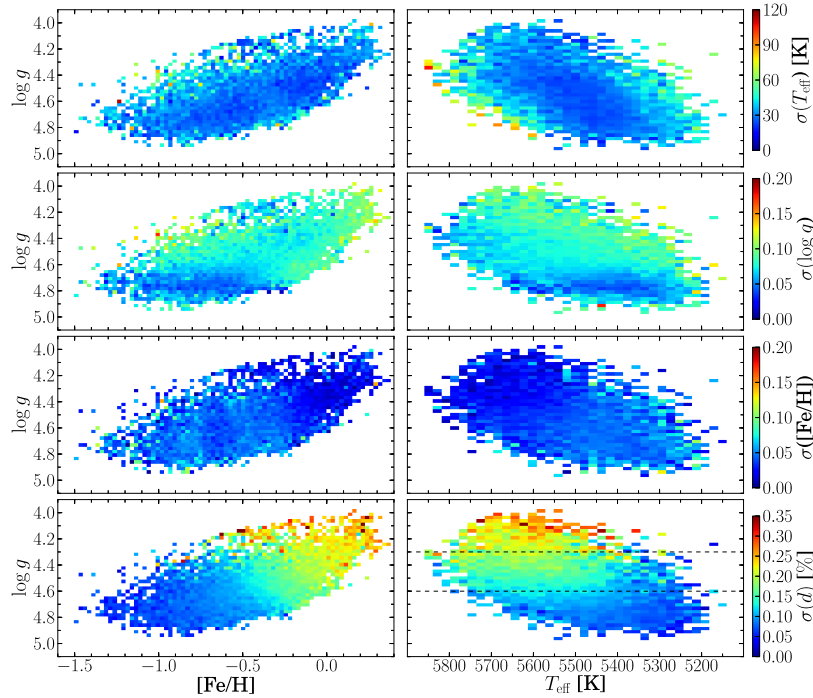


**Figure 6.5:** Mean uncertainties (based on internally determined SSPP uncertainties) for the SEGUE G-dwarf stellar parameter estimates in  $T_{\text{eff}}$  (top row),  $\log g$  (second row) and  $[\text{Fe}/\text{H}]$  (third row), both, as a function of metallicity (left column) and temperature (right column). In addition the distance uncertainties are shown as well (bottom row). In case of the distance uncertainties regions with similar uncertainties (indicated by the dashed black lines) are defined and used to introduce errors to the mock stars accordingly.

of the observational measurement depends partly on the type of star and hence its location in parameter space. However, for a single stellar type (as the G-dwarfs) the uncertainty variations are expected to be minor. Indeed, Figure 6.5 reveals that the main stellar parameters ( $T_{\text{eff}}$ ,  $\log g$ ,  $[\text{Fe}/\text{H}]$ ) can be constrained with similar precision for all objects of the G-dwarf sample. Due to this fact for each mock star a SEGUE G-dwarf is randomly chosen whose suite of internal stellar parameter uncertainties is assigned to the simulated object. Each of these uncertainties is dealt with as the precision  $u(x)$  of the measured physical quantity  $x$ . As such  $u(x)$  is an expression for the probability distribution of the quantity. Under the assumption that the probability distribution in each parameter follows a Gaussian with width  $u(x)$ , an error  $e(x)$  can be generated which is a random value drawn from the probability distribution. These individual random values  $e(x)$  can then be added to the original mock parameter values  $x$ . Indeed, by using the internal SSPP uncertainties as  $u(x)$  the altering effect on the stellar parameter mock distributions is negligible for temperature and  $[\text{Fe}/\text{H}]$  and minimal for the surface gravity. A result being in agreement with the fact that the internal SSPP uncertainties obviously underestimate the true observational uncertainties raising the need to find a more realistic assessment of the SEGUE measurement errors. Approaching this issue, as a test uncertainties of different size are assigned to the simulated stars. Figure 6.6 illustrates how the mock parameter distributions in  $T_{\text{eff}}$ ,  $\log g$  and  $[\text{Fe}/\text{H}]$  change accordingly. The effects become especially clear in the middle panel, showing the surface gravity distribution. Opposite to the internal uncertainties alone (dashed-dot line) a combination of the latter and the external SEGUE uncertainties (180 K in  $T_{\text{eff}}$ , 0.3 dex in  $\log g$

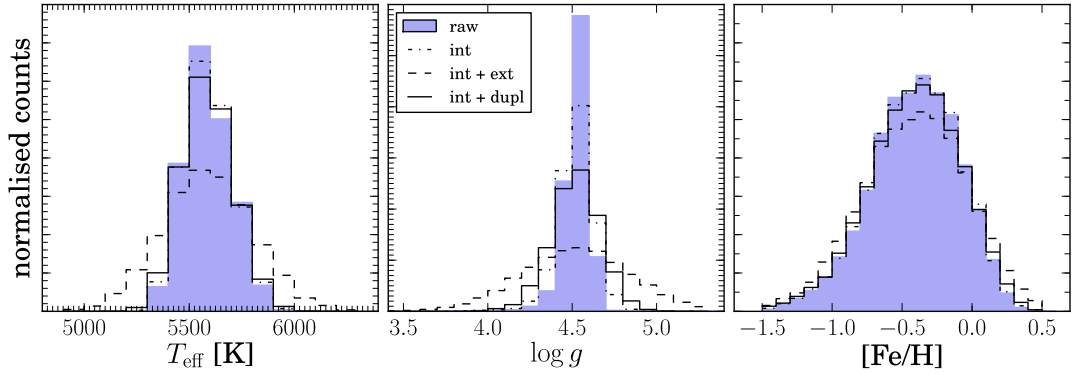


**Figure 6.6:** The plot illustrates the effect of different observational errors on the original stellar parameter estimates as predicted by TRILEGAL for the G-dwarf mock stars. Error free parameter distributions are shown as filled histograms. Additional distributions are displayed with observational errors applied according to (a) the internal errors of the SSPP (dashed-dotted line), (b) the internal plus external SSPP errors (the latter ones have been obtained by comparison with high-resolution samples) and (c) a combination of the internal pipeline error and a more realistic estimate of the internal SSPP error based on duplicates.

and 0.2 dex in  $[\text{Fe}/\text{H}]$ ) leads to a considerable overestimation (dashed line). An effect that is expected because the external uncertainties do not reflect the analysis pipeline’s performance and ability to, e.g., choose the best fitting synthetic template spectrum but set the SSPP results in relation to the parameter scale (systematic offsets) of reference observations. It turns out that the SEGUE stars with repeat observations offer an excellent opportunity to investigate and assess revised and more reliable internal uncertainty estimates. Starting from the roughly 43 000 SDSS stars (SDSS, SEGUE-1 and SEGUE-2) with more than one spectroscopic observation only those objects are considered that satisfy the colour criteria of G-type stars ( $0.48 < (g - r)_0 < 0.55$ ), have a metallicity within the range  $[-1.5, 0.5]$  dex and a signal-to-noise ratio above 10. It is further required that (1) the SNR difference for the two spectra of each duplicate pair is smaller than 10, (2) the SSPP flag is `nnnnn`, (3) the correlation coefficients (`CC_CAHK`, `CC_MGH`) are larger than zero, (4) there are no bad pixels in the spectra and (5) valid stellar parameters are available for both observations of the same object. Using the remaining pairs new internal parameter uncertainties are obtained by inspecting the residual distributions, i.e. the difference between the two measurements, of each parameter for the same object as a function of SNR. Figure 6.7 shows the residual distributions in temperature, surface gravity, metallicity and  $\alpha$ -enhancement for the 1 590 selected G-type duplicate pairs. The colour and metallicity range is indicated within the panels along with the Gaussian mean ( $\mu$ ) and scatter ( $\sigma$ ) of the distributions. The various restrictions imposed on each object already guarantees to obtain parameters that are as reliable as possible. Hence, further outliers are not clipped when computing the sigma of the Gaussian. The Gaussian fits reveal that the internal error estimates of the SSPP are more like  $T_{\text{eff}} \approx 40$  K,  $\log g \approx 0.1$  dex,  $[\text{Fe}/\text{H}] \approx 0.1$  dex and  $[\alpha/\text{Fe}] \approx 0.05$  dex. For  $\log g$  and  $[\text{Fe}/\text{H}]$  this is less than half of the external uncertainties but double the peak value of the original internal error distributions. With this additional information from the duplicates and the original individual internal SSPP uncertainties a total internal uncertainty can be determined for each of the observed stars combining both internal estimates in quadrature to create a new empirically determined  $u(x)$ . The obvious but moderate effect of this combined uncertainty estimate on the mock parameter distributions is depicted by the solid histograms in Figure 6.6. As shown later in Figure 6.11,

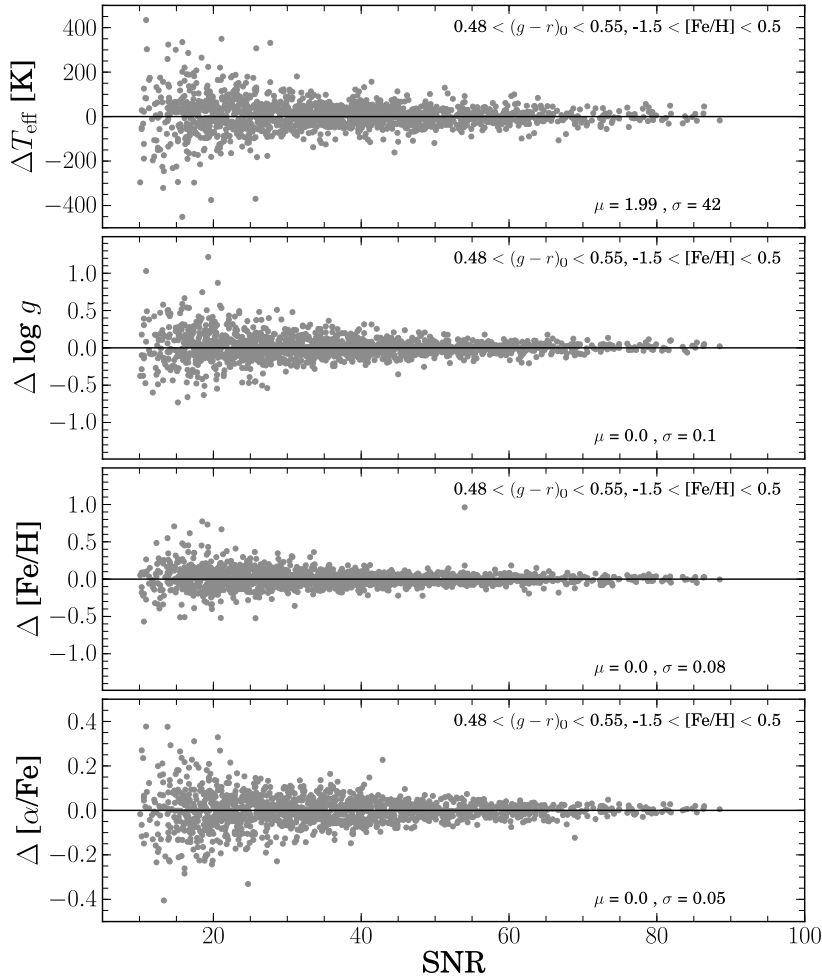


**Figure 6.7:** Comparison of the internal SSPP parameter errors (DR9) as estimated by the cleaned SEGUE duplicate spectra. From all stars with duplicate observations only those stars have been selected that satisfy the following criteria: they show the SSPP flag `nnnnn` and their two spectra show a difference in SNR of less than 10. The colour and metallicity ranges under consideration have been adjusted to match those of the G-dwarf sample.  $\mu$  and  $\sigma$  are the mean and standard deviation of the Gaussian distribution.

the resulting broadening of the mock distributions, especially for the surface gravity, is in good agreement with the shape and width of the true parameter distributions which confirms that duplicates are a valuable component when verifying the internal accuracy of a pipeline.

Besides the stellar parameters, errors are also added to the phase space coordinates of the mock stars. Thereby, the uncertainties in angular position are considered to be negligible and the velocities (in case of TRILEGAL proper motions and radial velocity) are equipped with errors employing the same procedure as for the stellar parameters, but using the observed velocity uncertainty distributions as shown in Figure 6.4 (bottom row). For the distances the situation is more complicated. This is because the individual distance uncertainties as determined by the BPG distance code exhibit larger deviations throughout the G-dwarf sample, mainly correlating with the surface gravity of the stars, the parameter that the distances are most sensible for and

that is the most problematic in case of the SEGUE DR9 parameter set. Note that the distance is the only parameter that relies by itself on the error-prone stellar parameters (and magnitudes) of the stars leading to correlations between the distance and the stellar parameter as well as their uncertainties. For example, the distance uncertainty is strongly dependent on the surface gravity and hence metallicity of the G-dwarf. As extensively discussed in Section 4.1.5 the distance errors are considerably larger for G-dwarfs with lower  $\log g$  values and higher  $[\text{Fe}/\text{H}]$  which are the stars close to the subgiant regime. Hence, the correct way would be to recompute the distances using the error-prone stellar mock parameters and the BPG distance code (see Chapter 4 or (Santiago et al. 2016)) that is also employed for the observed stars. At this point however, the found dependencies are accounted for by dividing the  $T_{\text{eff}}\text{-}\log g$ -parameter space in regions (Figure 6.5, lower right panel) of small variation when assigning distance uncertainties to the mock stars. Thereby, the observed star that donates its uncertainty to the mock star is randomly chosen from the same region the mock star is located in and errors are introduced following the same procedure as described above. The separating borders (dashed lines) are empirically determined according to the colour coded distribution in the plot.

#### 6.2.4 Definition of the final G-dwarf mock sample

Before a final definition of the G-dwarf mock sample is possible several second order quantities have to be obtained for the mock stars including galactocentric spatial positions and velocities as well as orbital properties. The addition of these parameters not only assures that the mock sample can finally be selected in the same way as the observed sample but it also allows to perform a chemo-dynamical analysis that is nearly as detailed as the one that can be carried out for the observed spectroscopical dataset. Radial velocities and proper motion estimates for the simulated stars are delivered by the kinematics module which was added to the original version of TRILEGAL to allow the simulation of 3D phase-space information and is described in Girardi et al. (2012). In short, the kinematics are based on several velocity ellipsoids, each for every Galactic component. The ellipsoids are taken from the literature (Chiba & Beers 2000; Robin et al. 2003; Holmberg et al. 2009) and velocities are randomly drawn from the Schwarzschild velocity distribution. As a very simple approach cylindrical symmetry is adopted for the velocity ellipsoids which is a reasonable approximation at least for local samples around the Sun. For the thin disk an empirical rotation curve is adopted from Dias & Lépine (2005). The validation of the kinematical model has been performed in Rossetto et al. (2011) where the proper motions simulated by TRILEGAL are compared to measured ones for a well-defined subsample of stars with UCAC3 proper motions.

Finally, by following the description layed out in the previous section observational errors are incorporated to the kinematics and distances of the TRILEGAL mock stars and 3D space velocities, Galactic Cartesian coordinates and orbital properties are computed as detailed in Sections 4.3 and 4.4.

#### Application of selection criteria

In the last step to create a SEGUE G-dwarf sample mock equivalent the initially large sample of simulated G-type stars, being pre-selected through the colour-magnitude cut and downsized using the SEGUE selection function, is further diminished by restricting every relevant and available parameter according to the cuts defined in Chapter 3 (Table 3.3). As the set of observed SEGUE stars is selected as a disk sample and TRILEGAL provides information on the Galactic component each simulated star belongs to, only mock stars labeled as disk (thin and thick) stars are kept for the final mock equivalent. The missing cut in signal-to-noise (not available for the

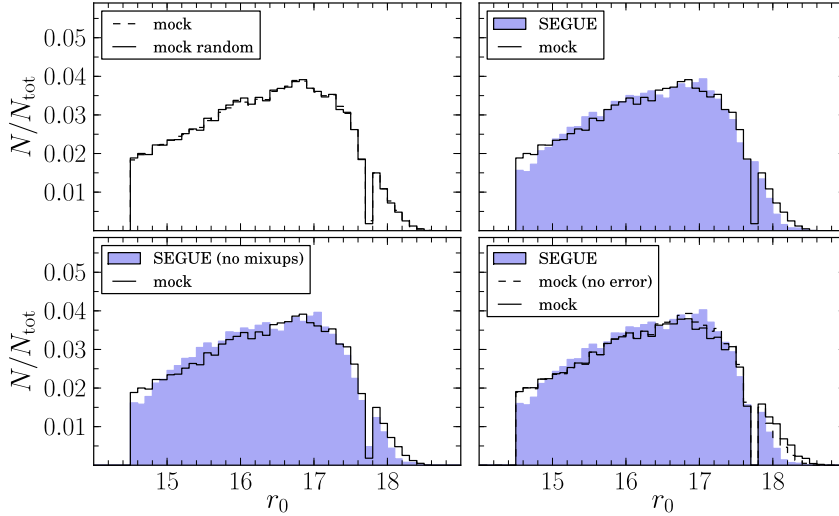


**Figure 6.8:**  $r$ -band magnitude distribution for the mock and the observed G-dwarf sample. *Upper left:* The magnitude distribution of the mock stars hardly differs if the TRILEGAL mock is either created by selecting stars randomly based on the selection function or when selection function weights are applied to each mock stars on the fly (see text for explanation). *Upper right:* Distribution of the randomly selected mock sample in comparison to the observations. *Lower left:* Same as the upper right panel but the group of mix-up stars has been removed from the SEGUE sample leading to a gap around 17.8 mag. *Lower right:* Final distribution for both, the observed and the mock sample, that are used for the following analysis. For reasons mentioned in the text stars around the plate boundary have been removed.

mock stars) is compensated by the fact that the selection function is dependent on the stellar magnitude which is directly linked to the SNR of the observed spectra. Because the utilised selection function fits are determined based on the observed sample after restricting the latter to a  $\text{SNR} > 20$  the SNR cut should be indirectly passed to the mock sample via the selection function.

In order to close the description on how to the mock sample is generated the following listing repeats the major steps:

1. Simulation of the complete set of SEGUE pointings.
2. De-reddening of the TRILEGAL output magnitudes and extraction of the entire sample of G-type stars from the simulated SEGUE plates using the SEGUE colour-magnitude criteria.
3. Pre-selection of only those G-type stars on the subset of simulated SEGUE line-of-sights that also contribute to the observed set of SEGUE G-dwarfs.
4. Reconstruction of the selection function for each SEGUE line-of-sight in the selected subset and removal of all pointings without successful selection function fit from both, the observed and the mock sample.
5. Random selection of mock stars according to the completeness of the SEGUE survey, depending on  $r$ ,  $l$  and  $b$  of the stars. Hence, inevitable introduction of the survey selection biases into the simulated set of stars.

6. Addition of observational errors on the stellar and kinematic parameters of the selected mock stars.
7. Application of similar selection criteria and parameter cuts as used for the observed stars to the suite of stellar and kinematic parameters of the mock stars.

### 6.3 Comparison of the observed and the mock G-dwarf sample

For a faint magnitude limit of  $r < 23$  mag and the sky-coverage of the SEGUE survey TRILEGAL produces a catalogue containing approximately 18 million mock stars. Considering those simulated pointings that contribute to the observed G-dwarf sample and selecting only G-type stars leaves a number of about 201 000 objects. This number is reduced to 26 000 mock stars when choosing stars randomly according to the selection function. The application of the entire set of selection criteria on the error-prone mock parameters finally results in a G-dwarf mock sample with 18 068 stars. A number of stars that is quite in agreement with the size of the observed G-dwarf sample and that underlines the strength of population synthesis models to simulate a realistic content of the Galaxy. Figure 6.8 displays the  $r$ -magnitude distribution of the mock and the observed dataset comparing the TRILEGAL mock sample (black histogram) and the complete observed sample (filled blue histogram) in the upper right panel. A good agreement is expected but still remarkable considering the involvement of the model for the SEGUE selection function when creating the mock sample. Besides the overall match, there is however an obvious discrepancy around the bright-faint plate boundary at 17.8 mag in  $r$ -band magnitude. Expectedly, the mock sample shows a gap at that region while the dataset exhibits an excess of stars in the bin  $[17.7, 17.8]$  mag. As already mentioned in Section 5.1.2 the data sample is affected by a group of stars, the mix-up stars, that populate this transition region. They are a result of the survey's observational concept and the fact that the SDSS photometry has changed over the years. Removing those stars leads to the filled blue histogram displayed in the lower left panel revealing a clear gap between stars on bright and faint pointings similar to the one in the mock. Still, for consistency with the previous chapters and in order to avoid any trouble with stars close to the boundary region for any further analysis steps every star with  $r_0 > r_{0,\text{cut}} - 0.1$  is removed in both the data and the mock comparison sample (see histograms in the lower right panel of Figure 6.8). This leaves 17 971 mock stars with error-prone parameters and 17 186 observed SEGUE stars for the analysis. The latter panel also shows the magnitude distribution of the mock sample selected based on the error-prone parameters after introducing observational errors to the simulated quantities. When comparing the mock sample with and without errors the largest difference in number counts is seen around the plate boundary showing an increase of the number of faint stars in the mock sample under the influence of errors. Concentrating on the mock stars with errors there are basically two specific magnitude ranges that exhibit the most obvious discrepancies in terms of number counts with respect to the observed stars. First, there is an excess of mock stars below 14.8 mag. This indicates that the issue of saturation that affects stellar samples from SEGUE at the bright magnitude end actually extends to larger magnitudes than the current bright limit at  $r_0 = 14.5$  mag. Initially, the latter limit had been particularly set to restrict the spectroscopic G-dwarf sample to avoid problems with the saturation issue in the first place. Second, there are more faint mock stars which may be a hint that the distances of the observed stars are in general larger than those predicted by TRILEGAL. This statement is indeed supported by the fact that the comparison of the distance distributions (see Figure 6.14, upper left panel) indicates an excess of mock stars with distances close to 3 kpc (distance limit of the samples). Usually, the stars with maximum distances are of faint magnitude, most likely

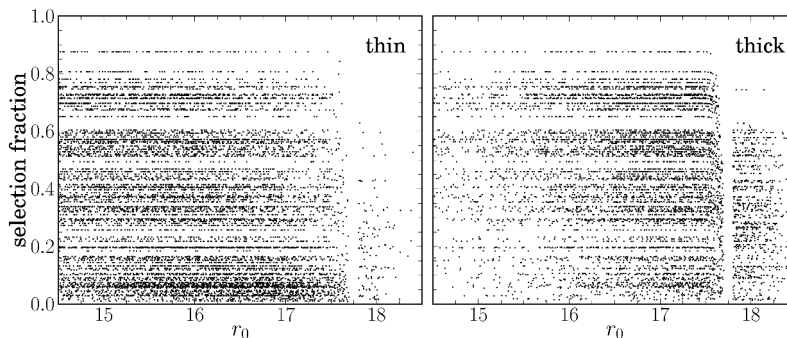


**Figure 6.9:** Selection fraction as a function of magnitude for the thin disk (*left*) and thick disk (*right*) stars in the TRILEGAL mock G-dwarf sample. As expected and in agreement with Figure 5.4 stars closer to the plane (thin disk) possess predominantly a smaller selection fraction indicating the incomplete sampling of the lower pointings. The latter objects also dominate the bright magnitude end. Stars farther away (thick disk) are mainly fainter in magnitude originating from pointings with larger target completeness. Note also that according to TRILEGAL almost all stars on faint plates (above the gap at 17.8 mag) are thick disk stars.

originating from the plates with magnitudes above the gap. If the distances of the observed sample tend to be larger in general faint stars are preferentially moving beyond the distance limit.

### The selection fraction for thin- and thick-disk stars

In conclusion, the magnitude distribution comparison has provided yet another proof that the selection function model is applicable and that the individual selection function weights calculated for the mock stars are properly working. Given that TRILEGAL delivers specific information on the Galactic component each mock star is assigned to, the completeness of the survey can be studied not only as a function of magnitude but also depending on whether the objects are part of the thin or thick disk of the Galaxy. Figure 6.9 illustrates the situation by means of the TRILEGAL mock sample. As expected and in agreement with Figure 5.4 stars closer to the plane within the thin disk (*left* panel) possess predominantly a smaller selection fraction reflecting the incomplete sampling of the lower pointings. The subsample of thin disk mock stars is also dominated by objects with bright magnitudes. Stars in the thick disk being farther away are mainly fainter in magnitude but originating from pointings with larger target completeness. Note also that according to TRILEGAL almost all stars on faint plates (above the gap at 17.8 mag) are thick disk stars.

### Stellar parameter distributions

Moving on to the stellar parameters Figure 6.10 displays the model predicted location of the mock stars (density distribution) in the  $T_{\text{eff}}\text{-log } g$  (top row) and the  $[\text{Fe}/\text{H}]\text{-log } g$ -space (bottom row) in relation to the observed G-dwarfs (overlaid density contours). In particular with respect to the empirical calibration of the DR9 surface gravity (see details in Section 3.3) the comparison of the SEGUE stellar parameters with theoretical predictions based on stellar evolutionary tracks serves as an independent cross-check and validation of the observed absolute parameter scales. As indicated in the panels each column illustrates the position of the dataset according to different versions of the SSPP parameters (*left*: original DR9 parameters, *middle*: DR9 with calibrated

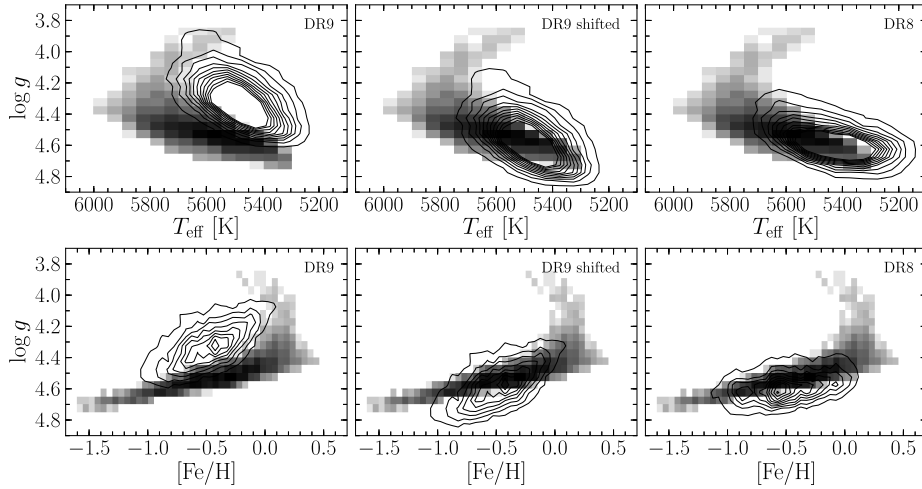


**Figure 6.10:** Location of the TRILEGAL mock and the observed G-dwarf sample, both in the  $T_{\text{eff}}$ - $\log g$ -plane (*upper row*) and the  $[\text{Fe}/\text{H}]$ - $\log g$ -plane (*lower row*). The density distribution indicates the location of the mock sample (sample without observational errors), the data sample is overlaid as contours. From left to right both samples are shown based on different version of the parameter sets.

$\log g$  values only, *right*: original DR8 parameters). The bottom line of this plot is that the population synthesis code predicts  $\log g$  values for the G-dwarfs that are offset to the observations by roughly the same amount than is observed when comparing the  $\log g$  distribution based on the DR8 and DR9 SSPP parameters for the same sample of stars. From the left column it is evident that at a fixed  $T_{\text{eff}}$  and  $[\text{Fe}/\text{H}]$  the observed G-dwarfs possess systematically lower surface gravity values than the mock stars. This displacement in surface gravity provides an independent justification for the need to calibrate the SEGUE DR9 surface gravity as performed in Section 3.3. It agrees also with the findings in Chapter 4 where the spectro-photometric distances to SEGUE cluster stars tend to be systematically overestimated when the original DR9 SSPP  $\log g$  values are used. Without calibration the surface gravities are generally too low putting all stars to larger distances than they actually are. It could be shown that with a shift of about 0.25 dex the cluster distances improved. The current plot also indicates that the dependency which is seen for the data's surface gravity with metallicity is too strong compared to the predicted trend in the mock sample. It is expected that due to the colour cut low- $[\text{Fe}/\text{H}]$  stars have larger surface gravities than high- $[\text{Fe}/\text{H}]$  stars, a fact that is visible in both, the observed and the mock sample. But TRILEGAL predicts a less steep correlation based on theoretical isochrones. In addition, when plotting the observed stars according to their DR8 stellar parameter estimates the  $\log g$  scale of the observed and the synthetic sample are in reasonably good agreement. One may hence argue that the predictions from TRILEGAL can serve as a proper guideline to not only account for the offset but also to align the observed sample and correct for the strong dependency. However, the true shape of the dependency is hard to figure out. This is because the model predictions are based on a particular set of stellar evolutionary tracks which is only one among many that each may lead to a slightly different answer with respect to the dependency. Also the DR8 SSPP parameters do not necessarily have to resemble the reality. More details on the stellar parameter distribution's main peak positions and shapes are given in Figure 6.11 showing the temperature, surface gravity and metallicity distributions for the observed sample with filled and the mock sample with open solid (original mock parameters) and dashed (error-

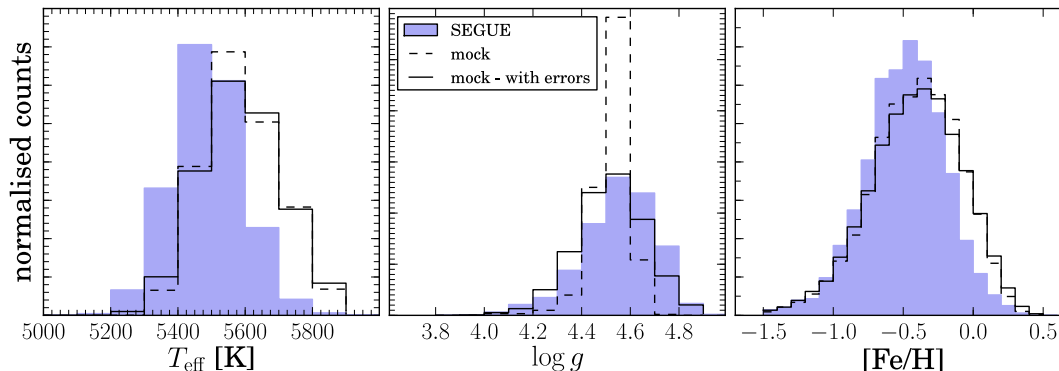


**Figure 6.11:** Stellar parameter distributions for the mock and the observed G-dwarfs. The dashed histogram shows the mock sample before observational errors have been added. The systematic shifts between the synthetic and the observed sample are approximately 100 K in  $T_{\text{eff}}$ , 0.05 dex in  $\log g$  and 0.1 dex in  $[\text{Fe}/\text{H}]$ . The blue shaded histogram in the middle panel represents the calibrated DR9 surface gravity distribution.

prone parameters) histograms. From the top row in Figure 6.10 one could already guess that besides the discrepancy in surface gravity also a non-negligible systematic offset is seen in the temperature scale and a slight difference in  $[\text{Fe}/\text{H}]$  for the model and the observations which is confirmed in Figure 6.11. The width of all three displayed distributions are quite similar, still the peaks are offset by about 100 K in temperature, 0.1 dex in  $[\text{Fe}/\text{H}]$  and 0.05 dex in  $\log g$ . At this point it is important to note that the positions of the peaks in the mock sample are mainly determined by the stellar isochrones incorporated in the model. Hence, the observed offsets might be the result of differences in the parameter scales encoded in the isochrone set applied to generate the mock sample, and the model atmospheres (synthetic templates) employed for the various SSPP estimators. Even though the SEGUE pipeline parameters are calibrated using high-resolution reference samples and cluster members the observed parameter scales may suffer from problems and changes in the zero point. There are obvious variations in the parameters for different SDSS data releases after all. Nevertheless, it should be noted as a final remark to Figure 6.11 that despite the offsets the error-prone mock distributions are well in agreement with the observations in terms of shape and width.

## Velocities

TRILEGAL’s prediction for the radial velocities and proper motions of the mock sample are shown in Figure 6.12 together with the measured velocity estimates for its observed counterpart. The distributions match well in position and shape with a slight offset in the  $\mu_\alpha$  component for the mock stars. The main reason for the good agreement is certainly the fact that the present study considers only local disk dwarf stars of one spectral type which cover a close volume around the Sun. It needs to be seen if stars with larger radial velocities e.g., counter-rotating giants in the stellar halo, would cause a difference between model and observation, especially in the wings of the distribution because TRILEGAL employs a cylindrical symmetry for its velocity ellipsoids which may lead to problems at larger distances.

Knowing which of the mock stars is assigned to the thin or thick disk component of the model’s disk opens the possibility to check what TRILEGAL predicts for the lag in rotational velocity that is observed for the thin and thick disk stars in observed stellar data sets. While the

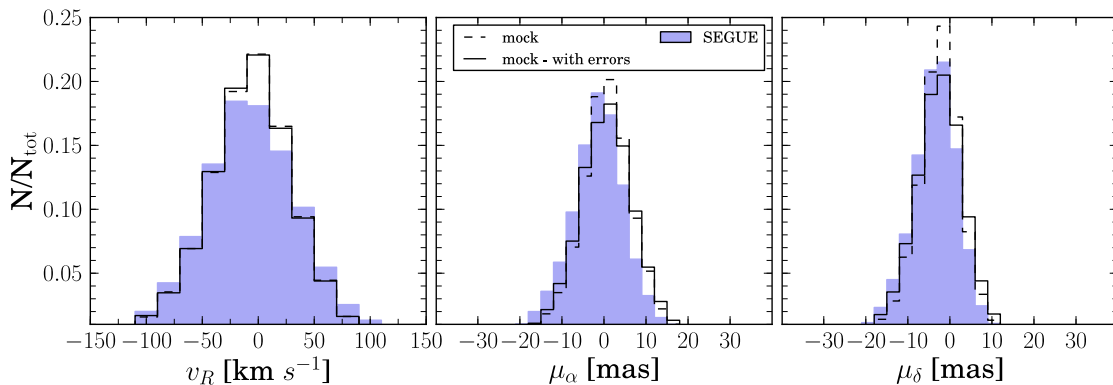


**Figure 6.12:** Comparison of the mock and the observed G-dwarfs' velocity distributions showing the radial velocity on the *left* and the *proper motions in the middle and the right panel*.

model decides on who is a thin or thick disk star the observed stars are divided into subsamples according to a simple separation criterion in chemistry. The empirical division (separation line) in chemical space is shown in Figure 5.9 and can be described by the following relation:

$$[\alpha/\text{Fe}] < \begin{cases} -0.08 \times [\text{Fe}/\text{H}] + 0.2625, & \text{if } [\text{Fe}/\text{H}] \geq -0.8 \\ +0.3265, & \text{if } [\text{Fe}/\text{H}] < -0.8 \end{cases} \quad (6.5)$$

The stars above (below) the separation line are assigned to the thick (thin) disk subsample. Figure 6.13 shows a toomre diagram of galactocentric velocities for the observed (left) and mock (right) stars, indicating their host disk component with black (thin) and grey (thick) symbols. Both splitted sets of stars show a lag between the thin and thick disk component. However, for the mock stars the velocity distribution is much more compact with a lag that is less than the one found for the observed stars whose main velocities are also generally higher in both disk components but similar to the ones found in Anders et al. (2014).

### Distances and further kinematic and spatial properties

Looking at higher order quantities like distances, positions, velocities and orbital properties there is a qualitativ agreement for the model and the observed distributions as illustrated by Figure 6.14. Worth mentioning however is that the mock distance distribution exhibits an excess of stars in the low and high distance tail which coincides with the differences in the magnitude distributions seen in Figure 6.8. Finding the closest star in the data sample being around 250 pc farther away from the Sun than the nearest mock object supports the assumption that apparently saturation effects are affecting the observed sample beyond the  $r$ -magnitude cut at 14.5 mag. Still, the difference in number counts could also be related to a slight offset in the distance scales of the two samples. As already discussed in Section 5.3, the distance scale of the observed SEGUE stars is likely influenced by the problematic DR9 surface gravity and shows a tendency towards overestimated stellar distances. This could also explain why there is a discrepancy around 3 kpc where obviously more observed than mock stars scatter beyond the chosen limit in distance.

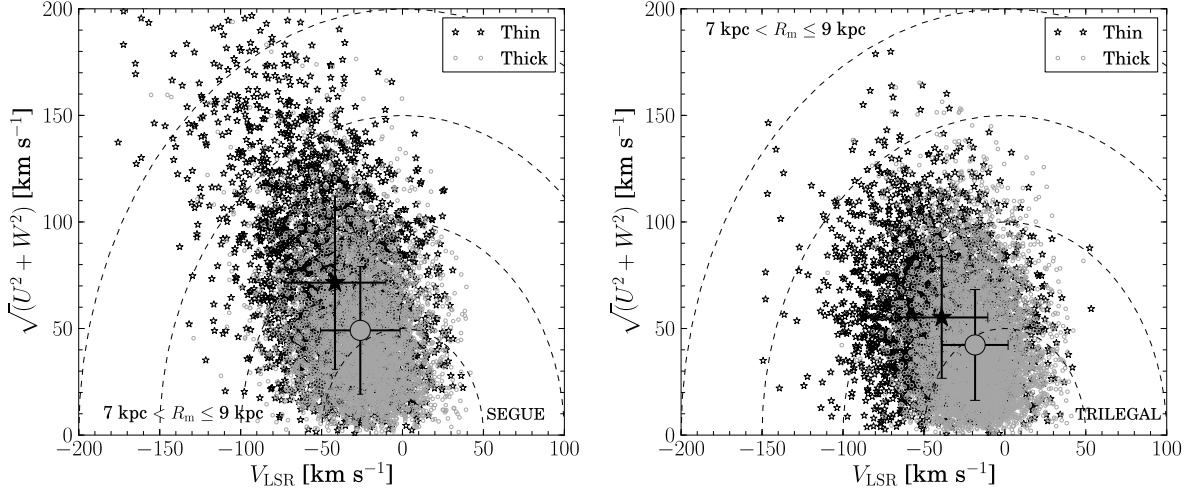


**Figure 6.13:** Toomre diagram (cf. Feltzing et al. (2003)) of galactocentric velocities (with respect to the local standard of rest) for observed (*left panel*) and simulated (*right panel*) stars assigned to the thin-disk (black) and thick-disk (gray) populations. Displayed are only stars with  $7 \text{ kpc} < R_m \leq 9 \text{ kpc}$ . The dashed contours indicate constant space motion.

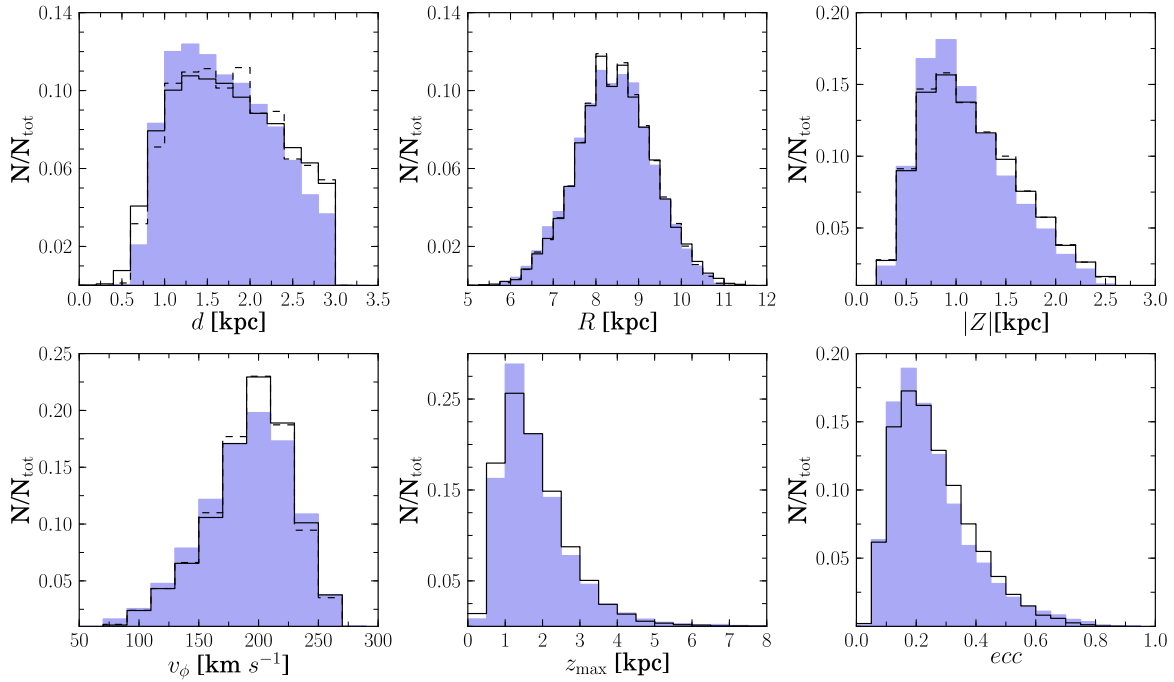


**Figure 6.14:** Overview on several kinematic parameter distributions for the observed (filled histogram) and the mock sample (solid and dashed lines, with and without errors). Note, that due to a low resolution of only  $0.05 \text{ kpc}$  in the simulated TRILEGAL distance, the distribution without errors appears much less smooth than when observational uncertainties are applied.

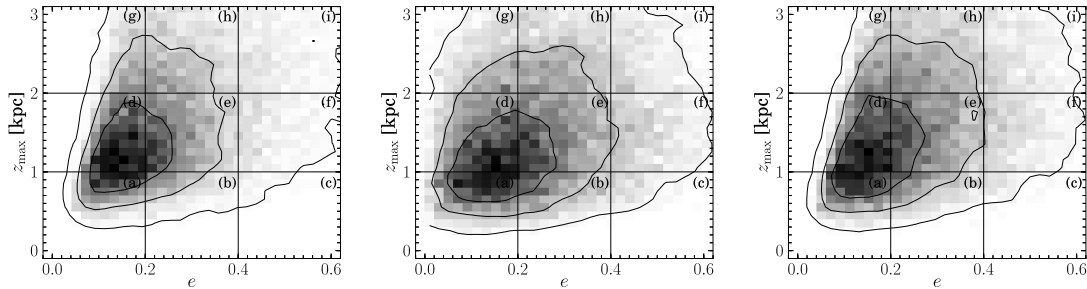


**Figure 6.15:** Density distribution in the  $e$ - $z_{\max}$ -plane. *Left:* SEGUE G-dwarfs; *Middle:* TRILEGAL mock G-dwarfs without errors, *Right:* TRILEGAL mock G-dwarfs with errors.

The two following findings support the suspicion that the observed stars' distance scale may be offset to the one implemented in TRILEGAL. First, in Chapter 5 Figure 5.20 indicated that there is a possible offset in the underlying distance scales when directly comparing the observed MDFs of the bias corrected sample of SEGUE G-dwarfs and their corresponding predictions by the chemo-dynamical MCM model. And second, the analysis of a MCM model based G-dwarf mock sample (presented in Chapter 7) reveals that the distance distribution of both independent mock samples (one based on TRILEGAL, the other on the MCM model) are quite similar (see Figure 7.4) showing the same difference in the distance scale with respect to the observations.

### 6.3.1 Chemo-kinematics of the SEGUE G-dwarfs as predicted by TRILEGAL

TRILEGAL has proven to be able to resemble the spectroscopic G-dwarf sample in terms of number counts and stellar parameters. But when aiming to learn more about the chemo-dynamical correlations within the Galaxy a natural consequence is to ask if or to what extent the model can reproduce the corrections that are seen between the chemistry and present dynamics of the stars in the observed sample. As there are no correlations implemented connecting the stellar chemistry and kinematics in TRILEGAL the model should fail when predicting chemo-dynamical relations. To what extent the model is still in agreement with the observed chemo-dynamics is investigated in the following subsections.

#### Density distribution in orbital parameter space

Figure 6.15 presents the density distribution of the observed and the mock sample in the  $e$ - $z_{\max}$ -plane. Evidently, as indicated by the shape of the density contours, the mock distribution with errors (right panel) compares much better to the observed data (left panel) than the mock without errors (middle panel). Even though population synthesis models like TRILEGAL may not be able to correctly resemble chemo-dynamical relations one of their great benefits are the additional information on ages or stellar components that can help to learn more about the observed sample. Hence, Figure 6.16 dips more detailed into the density distributions dissecting the mock and data sample into subsamples of thin (solid black histograms and contours) and thick (solid gray histograms and contours) disk like stars. Basically, the plot is based on the same thin- and thick-disk sub-groups of stars that were defined in the previous section to study the rotational velocity lag.

Figure 6.16 shows that the density structures of the subsamples agree in principle. However, in case of the mock stars the central density peaks of the thin and thick disk components are much more apart in  $z_{\max}$  direction and less overlapping than the peaks of the observed sample.

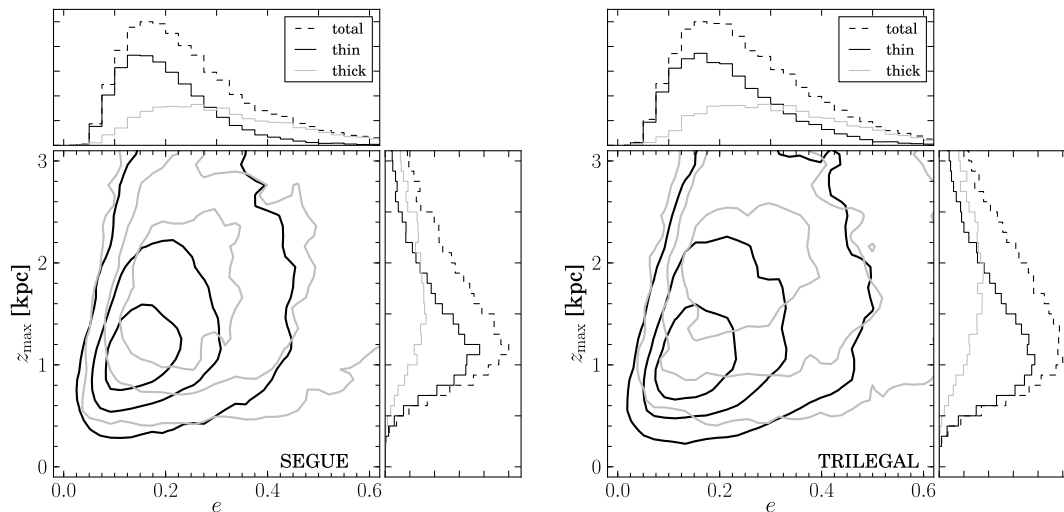


**Figure 6.16:** Density distribution in the eccentricity- $z_{\max}$ -plane for the stellar subsamples of observed (*left*) and mock (*right*) stars assigned to the thin (black contours) and thick (gray contours) disk populations (same division mechanism as in Figure 6.13). The contours contain 34%, 68% and 95% of each sample.

The stronger general overlap of all data sample contours indicates a less clear separation into the two different populations of thin and thick disk stars which is likely a result of the chemical parameter uncertainties, especially in  $\alpha$ -enhancement that affects the star’s position in relation to the chosen division line.

### The MDF with galactocentric radial distance and vertical height above the plane

Similar to Figure 5.20 in the previous Chapter Figure 6.17 and 6.18 illustrate how the metallicity distribution function of both, the observed and the TRILEGAL mock sample, varies when moving outwards in radial distance from the galactic centre or when looking at different ranges in galactic height above the plane. For a better comparability the offset in metallicity (see Figure 6.11) is compensated through a shift of the mock metallicity distribution function by  $-0.1$  dex. This shift to the TRILEGAL mock stars applies for the entire analysis in the present and the following Chapter. As a result, in each  $z$ -bin the peaks of the total MDFs agree well for the two comparison samples (Figure 6.17, left) indicating a similar change in the peak of the MDF with vertical height. This is a surprising result because there are a priori no gradients implemented in TRILEGAL. Regarding the width of the MDFs the model predicts slightly broader distributions at all heights and shows an excess of metal-rich stars in the lowest and highest  $z$ -bin. The overprediction of high- $[\text{Fe}/\text{H}]$  stars could either point to an incorrect MDF for the thin or thick disk which are both put by hand and have an influence on the thin-thick disk star ratio. But it could be also linked to the discrepancies seen in the distance distributions discussed in the previous section. Likely, the difference at low  $z$  is a result of the saturation issue. In any case the finding is in agreement with the contours in Figure 6.16 which suggest a larger number of thin disk mock stars at lower and higher  $z_{\max}$  than are seen for the observed sample. The right panel of Figure 6.17 however concentrates on the ratio of thin and thick disk stars and how the latter changes with height. The thin (black) and thick (gray) disk subsamples for observed (solid) and mock (dashed) stars are the same as discussed in the previous paragraph. The trends and ratios are comparable for both

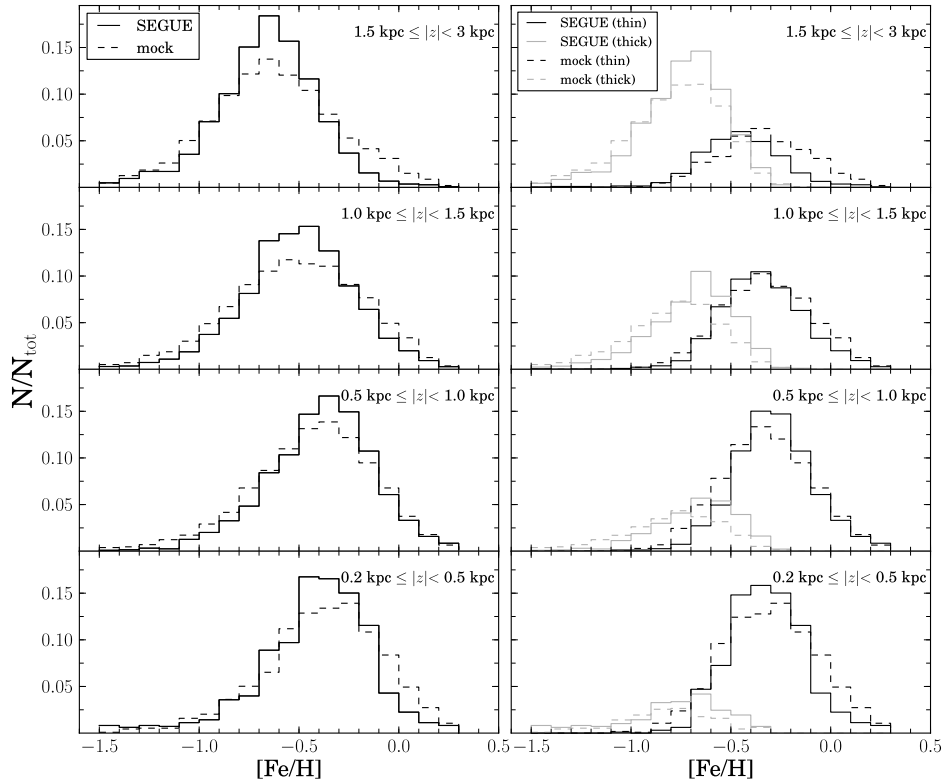


**Figure 6.17:** Distribution of metallicities at different height above the Galactic plane for both, the mock and observed sample. *Left:* entire MDFs. *Right:* MDFs for thin and thick disk subsamples. While the simulated stars are assigned to different Galactic components by the model the observed sample is divided into thin and thick disk stars based on a simple division in chemical space (see Equation 6.5).

samples. While the thin disk metal-rich stars dominate close to the Galactic plane, as expected the thick disk get more important with increasing height. Moving on to the MDF in bins of galactocentric radial distance the left panel of Figure 6.18 shows clearly that the  $[\text{Fe}/\text{H}]$  peak shifts to higher metallicities with increasing radial distance. The fact that the shape and peak positions match remarkably well proves that the selection effects seem to have successfully propagated to the TRILEGAL mock sample which is one of the most important take-away messages of this plot. Especially the good match at radii towards the inner Galaxy, where SEGUE suffers most severely from spectroscopic sampling effects, leading to a unusual metal-poor MDF, confirms this. However, the division into thin and thick disk components (right panel) reveals a generally worse agreement between the observed and the mock stars in radial direction than is seen for the vertical height. Several effects certainly contribute to this finding. For example, the proportion of thin and thick disk stars in the range  $5 \text{ kpc} < R < 7 \text{ kpc}$  should be dominated by the thick disk as a result of the selection effects. This is indeed true for the observed sample but the mock sample shows a well balanced proportion indicating that TRILEGAL predicts too many thin disk stars for the SEGUE pointings towards the inner Galaxy. In addition, the excess of real metal-poor thin disk stars in the outermost radial bin (9 kpc to 11 kpc) is likely a result of the radial metallicity gradient of the real Galaxy's thin disk. According to this gradient, being not present in TRILEGAL, the real thin disk is more metal poor in the outer regions than towards the Galactic centre. Concurrently, the larger amount of thick disk mock stars could be related

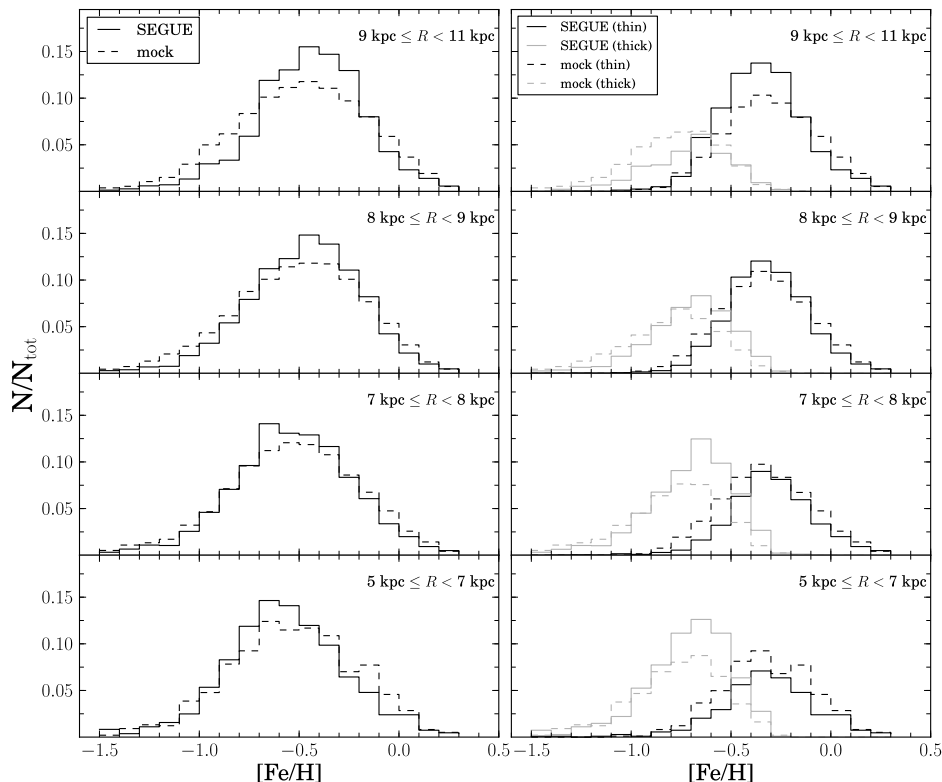


**Figure 6.18:** Distribution of metallicities at different distances from the Galactic center. In all panels the compared samples are restricted to a range in  $z$  from 0.2 kpc to 1.5 kpc.

to the assumed radial scale length of the TRILEGAL disk components overestimating the length of the model’s thick disk. A combination of all these aspects certainly leads to the observed differences between observations and model influencing the thin-thick-disk proportion in each radial bin. The discrepancies may even be intensified by the evolutionary processes like radial migration which shape the observed sample but are absent in the model.

### Orbital families in the eccentricity- $z_{\max}$ -plane

Digging deeper into the chemo-dynamics, Figure 6.19 displays the mock and observed G-dwarfs sub-divided in several orbital families (nine panels) according to their orbital properties eccentricity and maximum height above the plane. The orbital space is split as indicated by the dashed lines in Figure 6.15. Overall, the simple chemical thin-thick-disk star division that is applied to the observed stars seems to be a good approximation matching the model predictions. Both samples reflect the following global trends. For stars with low and moderate eccentricity the peak position of the thin (red lines) and thick (blue lines) disk distributions shifts to lower  $[\text{Fe}/\text{H}]$  values with increasing  $z_{\max}$ . Inferring from the thin-thick-proportions the thin disk dominates at low eccentricity ( $e < 0.2$ ) and low latitudes. Instead, the portion of thick disk stars gains weights with increasing height and eccentricity, predominantly populating the high eccentricity panels which is a natural consequence of their commonly hotter orbits. The high eccentricity panels also indicate the most striking discrepancies in the comparison. Panels (f) and (i) show a clear excess of thin disk mock stars. This seems to be connected to the differences found in the lower panel of Figure 6.18 that sheds light on the MDF of the inner Galactic disk where SEGUE

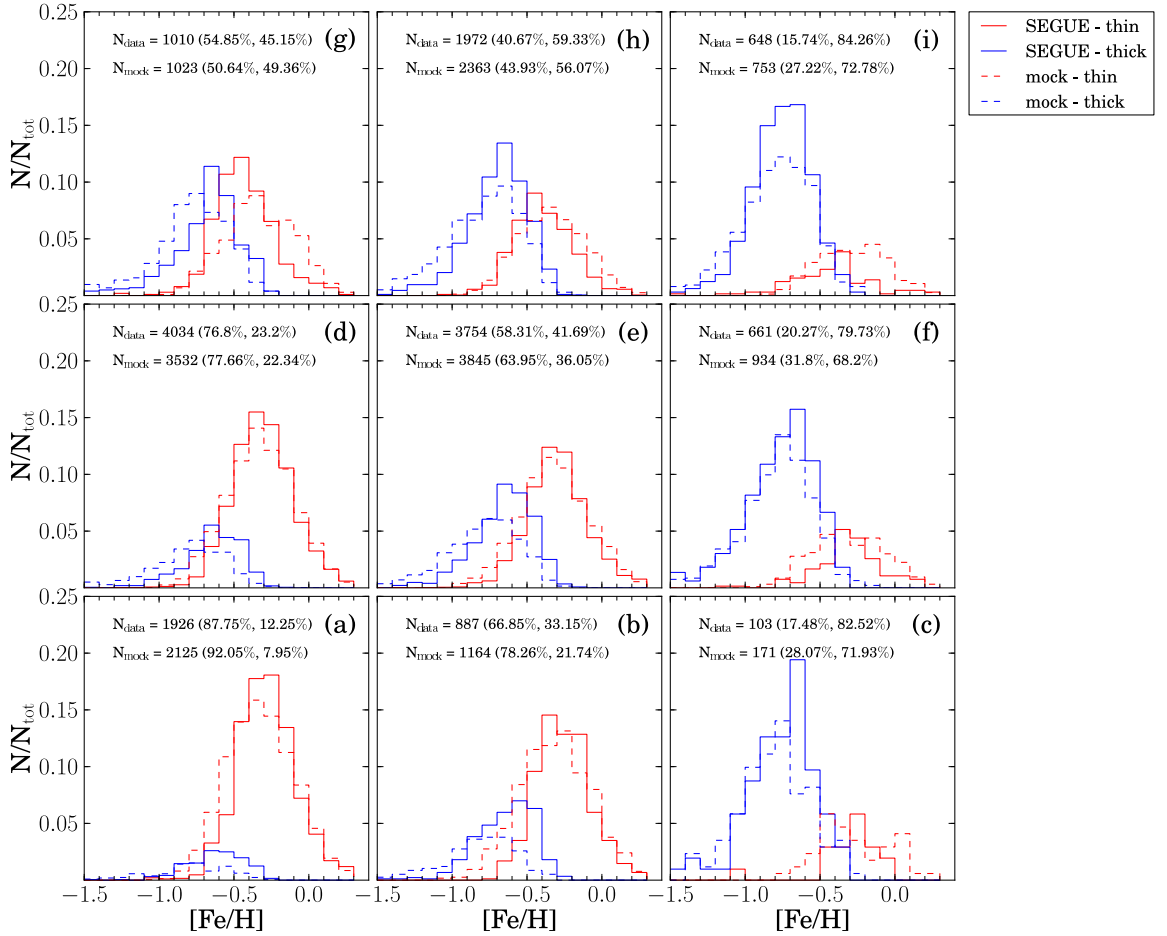


**Figure 6.19:** Normalised MDFs for different orbital families of stars. Both, the TRILEGAL mock and the observed G-dwarf sample are split into subsamples of thin and thick disk stars. The number of stars in each panel is indicated in the upper left corner along with the percentage of stars that have been assigned to the thin and thick disk sub-samples.

is most severely affected by selection effects due to which the thin-thick-disk ratio should favour the thick disk distribution (SEGUE concentrates on higher latitudes towards the inner Galactic radii). As a matter of fact the high eccentricity stars are mainly coming from inner disk regions having small  $R_m$  values. Assuming that the selection effects are well added to the mock star sample the latter should reproduce the amount of observed thin and thick disk SEGUE stars. One reason that could prevent a match is an overprediction of thin disk TRILEGAL stars at latitudes already being populated by thick disk like SEGUE stars, creating a different proportion of thin and thick disk stars.

### Chemo-kinematic relations

It is commonly accepted that the dispersion of each velocity component ( $U, V, W$ ) increases with distance from the Galactic plane. In any case, the dispersion for the thick disk population is substantially higher than for the thin-disk counterpart. Assuming that thick disk stars are preferentially older there is hence a correlation between ages and velocity dispersions too.

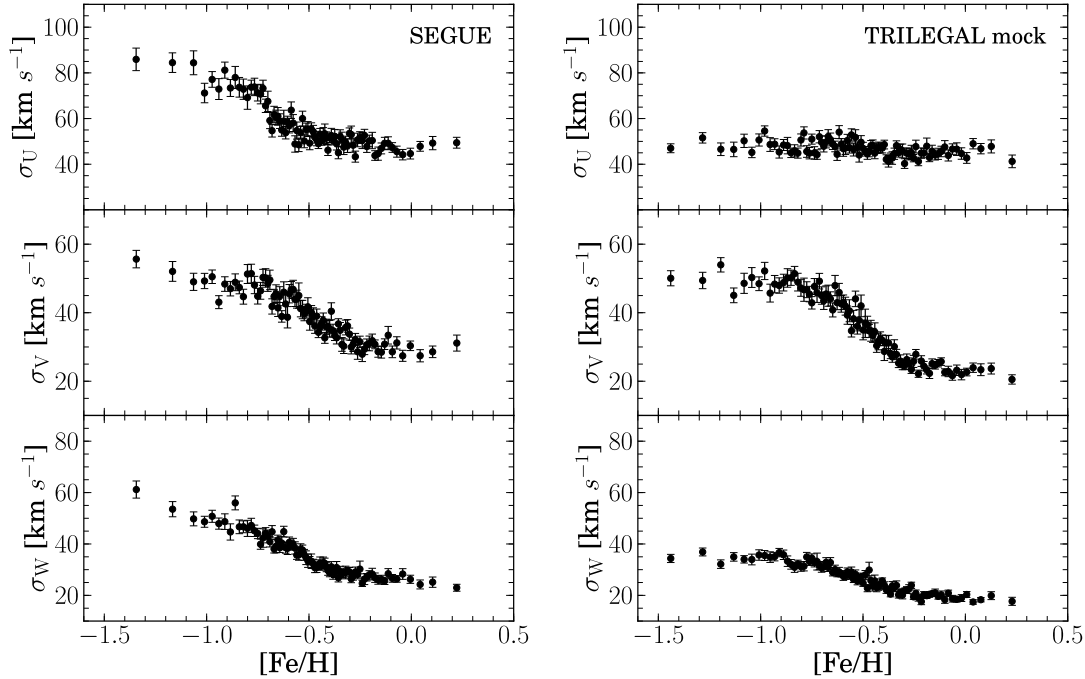


**Figure 6.20:** Velocity dispersion in the three Galactocentric velocity components  $U, V, W$  as a function of  $[\text{Fe}/\text{H}]$ . Shown is the observed sample on the left and the TRILEGAL mock G-dwarf sample on the right. Each dot contains 200 stars. The error bars are calculated in a bootstrapping procedure by resampling the 200 stars 100 times.

Figure 6.20 investigates the variation of the derived  $U, V, W$  velocity dispersion as a function of  $[\text{Fe}/\text{H}]$  for the observed (left panel) and synthetic G-dwarf sample (right panel). It is apparent that TRILEGAL fails to reproduce the differences in velocity dispersion for the thin and thick disk population stars. For the SEGUE stars each velocity component shows a stepwise flat ( $[0.4, -0.3]$  dex), moderate ( $[-0.3, -0.6]$  dex) and steep ( $[-0.6, -1.5]$  dex) slope of the correlation with  $[\text{Fe}/\text{H}]$  where the dispersion increases with decreasing metallicity. Admittedly, at the metal-poor end of the metallicity range there is a group of stars with unexpectedly high velocity dispersion (in radial direction: three leftmost dots, in vertical and azimuthal direction: two leftmost points). Even though the contamination by halo stars should have been removed by setting the cut in rotational velocity at  $v_\phi = 40 \text{ km/s}$  the kinematic properties of those objects seem to be untypical putting them even beyond the thick disk. The check of their distances however reveals that they cover the whole distance range of the G-dwarf sample and have distance errors that are small as well. On the contrary, the mock stars exhibit a completely and almost flat relation with very low dispersion in the radial and vertical component. Only in the  $V$  component the TRILEGAL stars show a similar behaviour as the observations. This confirms clearly that there is no connection between chemistry and kinematics for the TRILEGAL stars.

### Correlation between rotational velocity and metallicity

As already shown by Lee et al. (2011b) there exists a clear gradient of  $v_\phi$  with  $[\text{Fe}/\text{H}]$  at any given  $z$  distance, for both the thin and thick disk population of stars with an opposite sign for the two stellar galactic components. Figure 6.21 adumbrates this behaviour showing the total

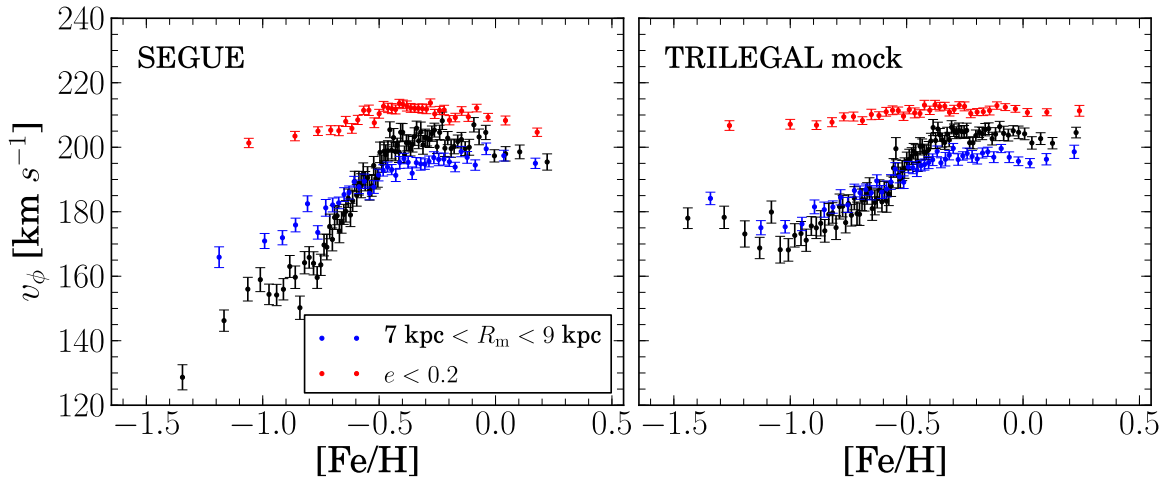


**Figure 6.21:** Rotational velocity as a function of  $[\text{Fe}/\text{H}]$  for both, the observed (*left*) and the simulated (*right*) G-dwarf sample. Shown are the full samples (black symbols), only local stars with  $7 \text{ kpc} < R_m < 9 \text{ kpc}$  (gray) and only stars with  $e < 0.2$  (light gray).

$v_\phi$ - $[\text{Fe}/\text{H}]$ -relation in black dots for the SEGUE G-dwarfs (left panel) and the TRILEGAL mock sample (right panel). For the observations the metallicity range below  $[\text{Fe}/\text{H}] < -0.5$  dex is dominated by thick disk stars with slower velocity indicating a steep positive gradient while stars with metallicity close to solar settle at a plateau value of around  $200 \text{ km/s}$ . The slightly negative gradient seen above  $[\text{Fe}/\text{H}] > -0.5$  dex is mainly a result of the low metallicity thin disk tail created by outer disk stars with larger velocities than usual for the solar neighbourhood thin disk component. Overlaid to the total relation are the correlations for subsamples restricted to a range in mean orbital radius,  $7 \text{ kpc} < R_m < 9 \text{ kpc}$  (dark gray) and eccentricity,  $e < 0.2$ , considering only the very local stars. Their correlations additionally illustrate that the mixture of stars within the observed sample influence the shape of the  $v_\phi$ - $[\text{Fe}/\text{H}]$ -correlation dramatically and tamper the actual correlation of the local solar neighbourhood. Limiting the mean orbital radius to a small interval around the Sun basically eliminates the outer thin disk influence and excludes preferentially thick disk stars from the inner radii which flattens both slopes, above and below an  $[\text{Fe}/\text{H}]$  of  $-0.5$  dex (gray curve). As expected and consistent with the thin-thick-disk proportions in the first column in Figure 6.19 the cut at  $e < 0.2$  keeps mainly stars of the colder thin disk population leading to an almost flat relation at a rotational velocity of about  $210 \text{ km/s}$ .

As TRILEGAL does not account for secular evolution processes within the disk, hence missing the influence of outer disk stars in the solar annulus the mock sample shows a flat relation for all stars above  $[\text{Fe}/\text{H}] > -0.5$  dex. Neglecting the two data points below  $130 \text{ km/s}$  in the left panel on average the most metal-poor observed thick disk stars reach further down in velocity by about  $20 \text{ km/s}$  than their mock counterparts. The latter build a plateau at around  $175 \text{ km/s}$  turning into a moderate positive gradient in the range  $-1.0 \text{ dex} < [\text{Fe}/\text{H}] < -0.5 \text{ dex}$  which is no true chemo-dynamical feature but only a result of averaging the predicted stellar rotational velocities of thin and thick disk component stars that particularly overlap in that metallicity region. This statement is supported by Figure 6.22 showing separate gradients for the subsamples of thin (black circles) and thick (black squares) disk stars. While the observed gradients are similar to those in Lee et al. (2011b) (Figure 7) the gradients are completely flat for the mock sample indicating an average velocity of  $210 \text{ km/s}$  for the thin disk component and  $175 \text{ km/s}$  for the thick disk stars.

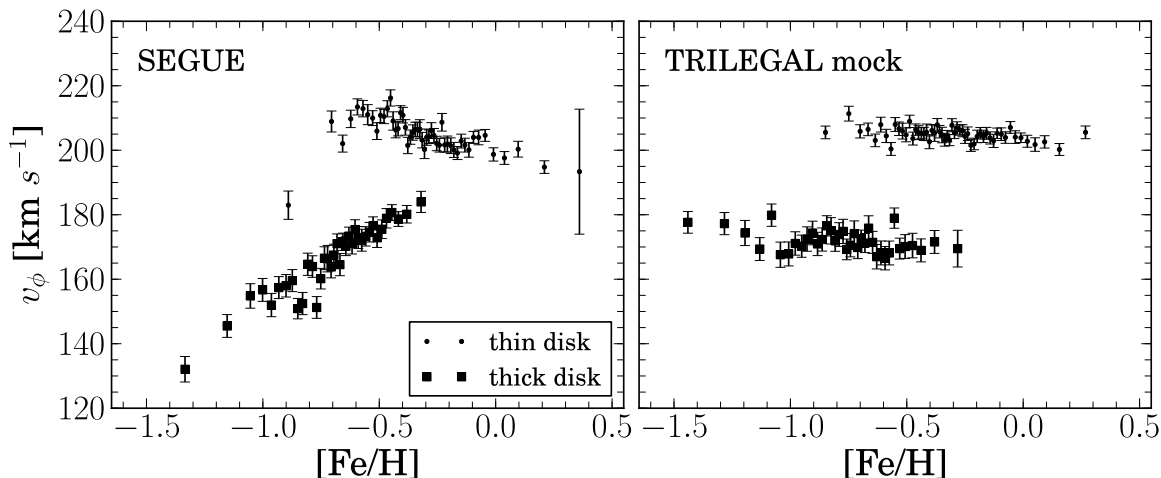


**Figure 6.22:**  $v_\phi$ -[Fe/H]-relation for subsamples of stars assigned to the thin (circles) and thick (squares) disk population. In case of the observed sample (*left panel*) the separation into thin and thick is based on a simple chemical division (see Figure 5.9). The TRILEGAL mock stars are automatically categorised by the model and assigned to a certain galactic population.

## 6.4 Discussion

The TRILEGAL model has proven to be an ideal choice to perform a first exemplary run testing and exploring the mechanisms of the inverse modelling approach. Thereby giving full consideration to the observational selection effects and allowing to handle those independently of observational uncertainties. The good performance in terms of light, mass and density distributions can be explained by the fact that models like TRILEGAL or Besancon were originally designed to match the number counts in the Galaxy. This is achieved by calibrating them with observational datasets from various wide-angle surveys in several wavelength ranges. Regarding the kinematics the TRILEGAL model creates velocity distributions reasonably approximating the observations. With realistic observational error estimates inferred from the SEGUE stellar parameters and introduced to the simulation, the observed parameter distributions can be well reproduced by the model, fitting mainly the distributions width but differing slightly with respect to their peak positions. The shifts found in the parameter distributions clearly illustrate that there is still much uncertainty in the theoretical stellar atmospheres and isochrones. This leads often to different parameter scales for synthetic and observed stellar populations complicating not only the comparison between observations and models but also restraining a feasible combination of different surveys which may have different zero points depending on their pipelines. Concerning this matter, Chapter 8 places an example demonstrating that it is indeed possible to obtain consistent results from stellar samples that are drawn from different spectroscopic surveys, namely, RAVE and SEGUE.

When comparing more subtle properties, such as the metallicity distribution with radial distance from the Galactic center or the gradient in rotational velocity as a function of [Fe/H] the TRILEGAL model obviously encounters problems because there are no such relations implemented between its chemistry and kinematics. While there is an evolution in the mean rotational velocity with metallicity for the observed thin and thick disk stars (see left panel of Figure 6.22) there is no such trend for the two groups of mock stars (right panel).

In the past, most observational studies that aimed to test chemo-dynamical correlations predicted by models relied on methods which assign individual stars to membership in the thin-

and thick-disk populations based on the star's location and kinematics (Sales et al. 2009; Dierickx et al. 2010; Wilson et al. 2011). Yet, with respect to secular processes associated with radial migration, the kinematic division introduces biases that may confound the final interpretations. A less variable property than the star's spatial position and velocity is its chemical signature that conserves the chemical composition of the interstellar medium at the star's birth place. To classify the stars into their likely Galactic component according to their chemical fingerprint (not changing over the stars lifetime) appears hence to be a more secure method. In this context, it is extremely advantageous to know the Galactic disk component each TRILEGAL mock star is assigned to. With the latter information it could be shown that in general the simple chemical division used for separating the observed SEGUE stars (according to their  $[\alpha/\text{Fe}]$  ratio) is robust and results in a good approximation of the model's prediction. Still, the detailed investigation of the thin-thick-disk proportions shows that there are several differences between observed and mock stars. Some of them are likely the results of (1) the lack of evolution within the mock sample or (2) a different distribution of thin and thick disk stars with height. Yet, the simplistic chemical division applied to the observed stars introduces a certain amount of uncertainty.

### Summary

In summary, TRILEGAL is a useful model to demonstrate the effect of observational biases and selection functions and to support people designing new observational projects. But a more sophisticated description of the Galaxy is needed to cope with the presently available photometric and spectroscopic data sets in terms of the Galactic chemo-dynamics. The main results of the present chapter are itemized below:

- The TRILEGAL model works well to generate a mock sample that resembles the observed SEGUE G-dwarf selection in various properties, especially the number of stars.
- The performed chemo-kinematic comparison provides essential constraints on the main abundance gradient and the scale lengths for the thin and thick disk component implemented in TRILEGAL. The discrepancies to the observed data suggests that the scale length of the model's thick disk is too long and that the number of metal-poor thin disk stars is underestimated due to a missing gradient. Therefore, the vertical and radial metallicity gradients inferred from the SEGUE G-dwarfs deliver important insights on how a gradient should look like in TRILEGAL.
- Last but not least, the attempt to obtain a simulated SEGUE G-dwarf sample based on TRILEGAL has led to a significant contribution on revising and modifying the metallicity distribution function (as implemented in version 1.6) of the model's thick disk component. It could be shown that the MDF of a subsample of local thick disk RAVE giants, when used as an empirical representation of the thick disk's chemical properties, serves well in order to constrain the MDF (peak position and dispersion) of the thick disk stars generated by TRILEGAL.



---

## Modelling the SEGUE G-dwarf sample with the MCM model

---

The previous Chapter demonstrated that the TRILEGAL model reaches its limits in reproducing the chemo-kinematic properties of the Milky Way. Evidently, pure population synthesis models are unbeatable in terms of statistical predictions but insufficient in extracting self-consistent chemo-dynamical relations. Hence, chemo-dynamical models with self-consistent evolution and formation history, such as the MCM model are needed. They have the advantage that correlations of age, metallicity and kinematics arise naturally.

In Chapter 5 the latter model is shown to be mostly in agreement with observations from SEGUE. This is particularly true for the metallicity distribution function at different proximity to the Sun and at various distances from the disk plane. However, the direct comparison of the model and the observed sample relies on important and strong assumptions that are part of the correction of selection effects. This leads to a significant element of uncertainty in all distributions and relations that are deduced from the selection effect corrected SEGUE observations.

As a consequence the MCM model is once again, but in a more sophisticated manner, tested in this chapter. Sticking to the approach of inverse modelling a second SEGUE G-dwarf mock sample is created on the basis of the chemo-dynamical model. With this mock realisation it is now possible to better quantify the differences between the model and the SEGUE observations. This is done by repeating the analysis and comparison originally performed in Chapter 5.

Obtaining a MCM mock G-dwarf sample also opens the opportunity to carve out strengths and weaknesses of both, the MCM and the TRILEGAL model. Especially, when comparing the two mock sample versions not only to the observations but to each other. Thereby, the MCM's two most important advantages with respect to TRILEGAL are: (1) the analysis and comparison to the observations will benefit from the realistically modelled dynamical processes in the context of a spatially resolved simulation and (2) more parameters are available, including the  $\alpha$ -enhancement to allow a more complete chemo-dynamical analysis.

### 7.1 Creating a mock SEGUE survey with GALAXIA

The unique feature of the GALAXIA frame-work (see Sharma et al. 2011, and Section 1.2.1) is that the code allows the user to generate stellar populations according to his own model of the Galaxy. This opens the opportunity to build up a stellar catalogue based on the  $N$ -body particle

distribution underlying the chemo-dynamical model by Minchev et al. (2013). However, in order to feed in and process the  $N$ -body realisation of a complete galaxy with several components like disk, bulge and halo the code needed to be adjusted. This was done as part of the PhD thesis by Tilmann Piffl (Piffl 2014) and led to the creation of a MCM mock realisation of the RAVE survey. As a contribution to this work and in accordance with his thesis, Tilmann Piffl, generated a synthetic version of the SEGUE survey that is based on the MCM model. The resulting synthetic stellar catalogue of SEGUE stars serves this thesis as the starting point to obtain a MCM mock equivalent to the observed SEGUE G-dwarfs. Details on the developed and exploited techniques are described and can be looked up in (Piffl 2014). Throughout this chapter only the main procedures concerning the population synthesis process with GALAXIA are outlined.

### 7.1.1 Modifications to GALAXIA

In order to realise a proper population synthesis with GALAXIA that is as consistent as possible with the specifications of the MCM model the following modifications needed to be implemented:

1. GALAXIA's main code is changed such that each mock star which originates from a  $N$ -body star particle inherits the same age and chemistry of its parent particle.
2. The IMF by Scalo (1986) has been added as a second option because it is this IMF that is used by the MCM model. Originally GALAXIA uses the Chabrier (2001) IMF.
3. GALAXIA uses the stellar isochrones by Marigo et al. (2008) which were computed under the assumption that  $[\alpha/\text{Fe}] = 0$ . To approximately correct for this fact the metallicity of each particle is modified according to

$$[\text{M}/\text{H}]_{\text{mod}} = [\text{Fe}/\text{H}] + [\alpha/\text{Fe}] \quad (7.1)$$

In the process of stellar population those isochrones are then selected that are closest to this modified metallicity rather than to the original  $[\text{Fe}/\text{H}]$  value.

### 7.1.2 Stellar population synthesis from an $N$ -body model

In case of the  $N$ -body mode of GALAXIA the spatial and kinematic distribution functions (DFs) are extracted from the mass particle distributions of the model. Essentially, the mass particles are a discrete realisation of the underlying smooth mass distributions which can be transferred to the corresponding density distribution by application of a softening algorithm (see Section 2.3.2 in Piffl 2014). What then happens in the processing with GALAXIA is that each particle is smeared out and transformed into a simple stellar population, distributed in a phase space volume around the particle. Thereby, the mass of the particle is crucial. Because the mass is split into individual stars according to the chosen IMF it is necessary to have an absolute mass estimate for the particles as normalisation for the IMF, in the present case given by

$$m_{\text{particle}} = \frac{M_{\text{tot},\star}}{N_{\text{tot}}} \quad (7.2)$$

where  $M_{\text{tot},\star}$  and  $N_{\text{tot}}$  are the total stellar mass assumed for the entire simulated galaxy and the total number of stellar particles in the model, respectively. For the total stellar mass estimate of the Galactic disk the same value of  $M_{\text{tot},\star} = 7.8 \times 10^{10} M_{\odot}$  is assumed that has been used to create the RAVE mock survey in Piffl (2014). There the latter total mass assumption led to roughly

the same number of stars in the mock survey than actually present in the real RAVE survey. It needs to be seen if the same holds true for SEGUE. In any case,  $M_{\text{tot},\star}$  does not represent the actual stellar mass of the Galaxy but rather acts as a scaling factor which determines the final number of generated stars that enter the synthetic survey. Considering the position and velocities of the mock stars, they are randomly drawn from the phase-space volume around the  $N$ -body particle.

### Resolution of the simulation

An important aspect is the resolution of the simulated  $N$ -body model disk which consists of about two million stellar particles. Similar to the RAVE survey SEGUE covers only a small fraction in terms of stellar number counts and volume of the Galaxy. In particular, the SEGUE G-dwarf sample of which a synthetic copy is created based on the  $N$ -body distribution in this chapter is even more limited to a local volume around the Sun with  $d < 3$  kpc. Consequently, only a small portion of all available mass particles in the simulation would be considered. It is hence a good idea to increase the resolution, doubling the number of particles. This is achieved by superimposing the original particle distribution with a copy of the latter that is rotated by  $180^\circ$  around the  $z$ -axis. As a result the stellar particle mass decreases to  $m_{\text{particle}} = 1.94 \times 10^4 M_\odot$ .

### Softening parameters

Before GALAXIA can finally be used to generate the SEGUE mock observations the softening parameters have to be computed with the smoothing length  $h_i$  being the important quantity to determine for each individual particle. To recall, the softening defines the size of the phase-space volume around the mass particle in which GALAXIA distributes the stellar population that originates from the host particle.

In the present case, each individual smoothing length  $h_i$ , defined as the distance to the  $N_{\text{ngb}}$ -th nearest neighbouring particle, is calculated by use of the publicly available code EnBiD (Entropy based Binary Decomposition; Sharma & Steinmetz 2006). For a description of the exact determination of the smoothing parameters the reader is referred to Section 2.3.4 of Piffl (2014). There the author also discusses the influence and effect of different values for  $N_{\text{ngb}}$  and studies the differences in the smoothing parameters when using a softening in 3D or 6D phase-space. While in the 6D case both the spatial and the velocity smoothing length  $h_r$  and  $h_v$  are considered independently, the latter is fixed to a constant value in the 3D softening case. The investigation reveals that a smoothing in 3D phase-space with  $N_{\text{ngb}} = 32$  results in the most realistic estimates for the spatial softening length with  $h_r$  values of about 200 pc (see Figure 2.5 in Piffl 2014). Consequently, the latter setting is also applied to the simulation of this work's synthetic SEGUE survey. The obtained spatial smoothing length of 200 pc should be small enough to preserve the essential chemical information needed to disentangle different galactic components, at best a thin-and-thick disk dichotomy. However, the current smoothing does not take into account that the density gradient in  $z$ -direction is much larger than in  $R$ -direction. Assuming a spherical phase-space volume around each particle may therefore lead to an overlap of the areas of influence for the particles in  $z$ -direction which could, depending on the smoothing length, mix different populations and erase valuable information. A solution to this issue could be the use of an oblate volume, instead of a spherical one. The effect of the different IMF options, the altered metallicity scale and the smoothing is tested, analysed and described in Section 3.3.2 of Piffl (2014).

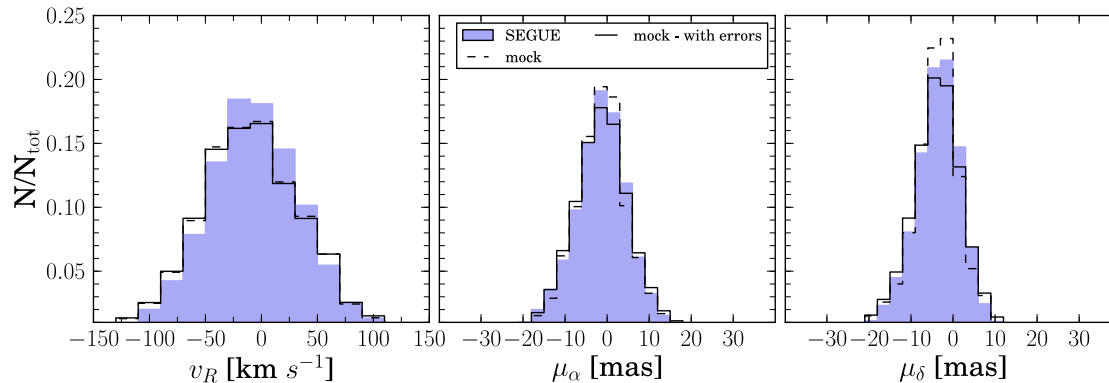


**Figure 7.1:** Velocity distributions for the line-of-sight velocity and the proper motion components displayed for the SEGUE (filled histogram) and the MCM mock sample.

### 7.1.3 Modelling a MCM based SEGUE G-dwarf sample

The selection of a SEGUE G-dwarf sample equivalent from the stellar mock catalogue generated by GALAXIA follows basically the same procedure as described for the TRILEGAL mock catalogue in the previous chapter. The steps discussed in Section 6.2 are gradually applied to the MCM mock stars. This includes the selection of G-type stars, the introduction of the given selection effects (random extraction of stars according to the survey completeness) and observational errors and the application of the specific cuts in  $\log g$ ,  $[\text{Fe}/\text{H}]$  and rotational velocity. However, in case of the GALAXIA mock star catalogue the step of de-reddening the delivered *ugriz* magnitudes of the mock stars is not necessary since those are already dereddened. Still, with view to the kinematic properties, estimates for the proper motions and line-of-sight velocities have to be calculated separately based on the spatial positions, the velocities and the distances of the mock stars. All of which are determined by the MCM model particle phase-space coordinates.

## 7.2 Comparing the MCM, the SEGUE and the TRILEGAL G-dwarf mock sample

While the TRILEGAL mock sample matches the size of the observed SEGUE G-dwarf sample well, the final version of the MCM mock sample contains about 30 000 stars after application of all relevant selection criteria. The discrepancy in number counts demonstrates that the total mass assumption of  $7.8 \times 10^{10} M_{\odot}$  for the model's disk seems to be not universally applicable. The mass serves just as a parameter than determines the number of mock stars in the catalogue. Even if, in case of the RAVE survey, the above mass estimate normalises the IMF such that the number of stars in the MCM based RAVE mock catalogue agrees with the one of the real RAVE survey, this holds not true for SEGUE. Too many SEGUE mock stars are predicted. Considering that the MCM model is not at all trimmed to predict the exact content of the Milky Way, as are the population synthesis models, this finding is not a surprise. Also, as the results in Chapter 8 show the two spectroscopic surveys RAVE and SEGUE do not exactly fit in volume. Compared to RAVE the SEGUE survey samples much deeper in space. Hence, one would expect the absolute number of stars not to fit exactly. Consequently this difference is reflected in the created number of GALAXIA mock stars too.

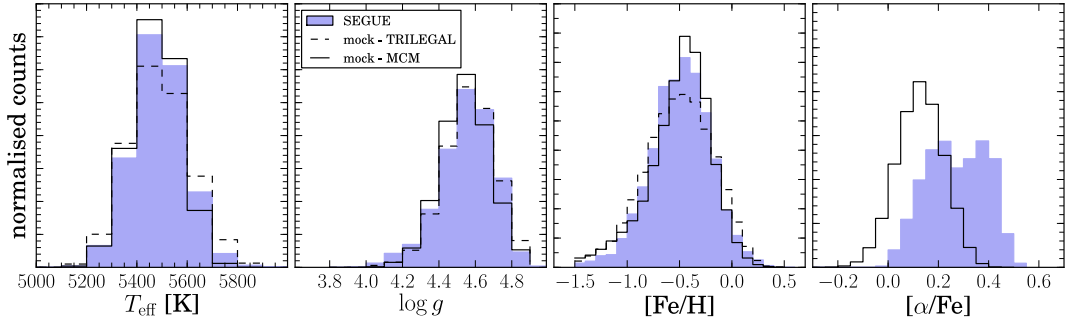


**Figure 7.2:** Same plot as Figure 6.11 with stellar parameter distributions for the SEGUE (filled histogram) G-dwarf stars and the two mock samples. In all parameters, except the  $\alpha$ -enhancement being provided only for the MCM mock stars, the observations and the synthetic samples show similar systematic offsets. All model distributions are based on the error prone mock star parameters.

After all, the magnitude distribution of the MCM mock G-dwarf sample compares well with the one predicted by TRILEGAL showing the same excess of faint stars in the range [17.8, 18.5]mag (see Figure 6.8). Also the density distribution in the eccentricity- $z_{\text{max}}$ -plane is comparable to the one for the observed and the TRILEGAL mock stars revealing similar contours after application of observational uncertainties as illustrated in Figure 6.15.

## Velocities

The predicted proper motion and line-of-sight velocity distributions for the MCM mock sample are overlaid on the observed ones in Figure 7.1. Even though the MCM model concentrates on reproducing primarily the dynamics of the solar vicinity it is still remarkable how well the predictions match the observed velocities of the local G-dwarf population reaching out to 3kpc. The fact that this study compares only a single stellar type of dwarf stars, that populates a very defined range of small velocities, certainly favours the good agreement with the simulated stars. This agreement could be influenced into the negative by the limited resolution of the simulation and could hence chance for the worse if a diverse set of SEGUE stars would be considered of only the SEGUE G-dwarfs. A larger sample of stars would likely show a distribution with extended wings reaching to larger velocities. A recent example for this behaviour is the RAVE survey studied in Piffl (2014) which clearly demonstrated that the MCM model predictions for the proper motions and line-of-sight velocities (see Figure 3.15 in Section 3.3.5 of the latter reference) deviate strongly in the tails of the distributions, i.e., lacking high radial velocity stars with  $v_R > 200 \text{ km/s}$  in the MCM model. Due to the confined SEGUE sample used here this finding can neither be confirmed nor disproved at this point.

## Stellar parameters

Similar to TRILEGAL (Figure 6.11), for the stellar parameter distributions the MCM model predictions are in a good qualitative agreement with the SEGUE observations apart from systematic shifts. Figure 7.2 compares the distributions in  $T_{\text{eff}}$ ,  $\log g$  and [Fe/H] for all three samples, the observed stars and their TRILEGAL and GALAXIA mock counterpart. Plotting the two models on top of each other reveals shifts of equal size for either model with respect to the SEGUE stars. Part of the reason the two models agree is that both of their stellar population algorithms make

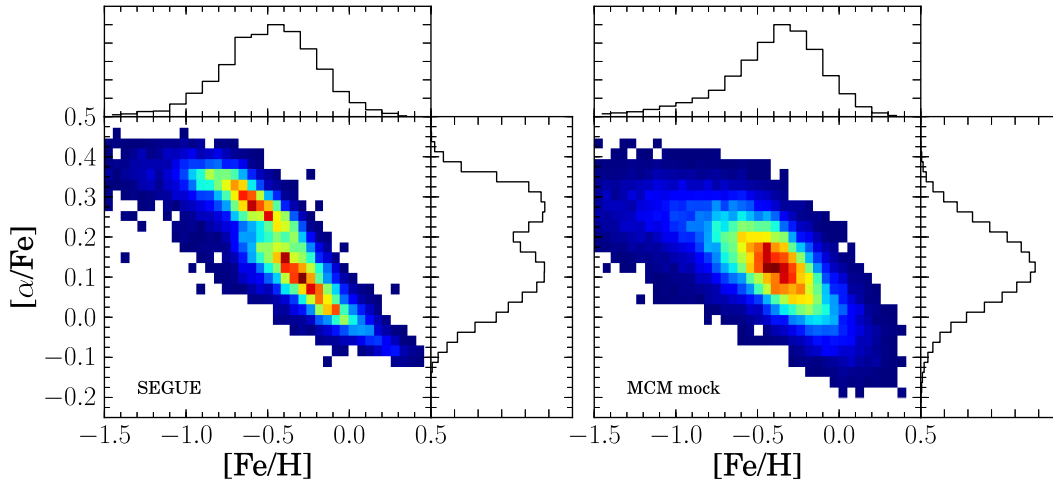


**Figure 7.3:** Density distribution in the elemental abundance plane for the SEGUE G-dwarfs (*left panel*) and their MCM mock equivalent (*right panel*). The distributions are normalised to the total number of stars in each sample.

use of the stellar isochrone set by Marigo et al. (2008). The occurring mismatch in peak positions with respect to the observations however could be partially due to the systematics in the SEGUE parameter pipeline that are observed for the set of DR8 and DR9 parameters (see discussion in Section 3.3). Essentially, the systematic shifts that come to about 100 K in temperature, to 0.1 dex in metallicity and to 0.05 dex in surface gravity are of the same magnitude or even below the external errors reported for the SEGUE parameters. These systematic error estimates that are determined from comparison to high resolution observations are of the order 150 K, 0.4 dex and 0.25 dex respectively (see Table 2.2 and error discussion in Section 2.2.2).

In case of the MCM mock sample it is possible to also investigate the  $[\alpha/\text{Fe}]$  ratio because the chemo-dynamical model provides abundance predictions for several elements, such as magnesium, oxygen, silicon and calcium. In order to obtain an  $\alpha$ -abundance estimate for the mock stars, which is as close as possible to the one determined from the SEGUE spectra, only the magnesium abundance prediction is considered, calculating the  $[\alpha/\text{Fe}]$  ratio as:

$$[\alpha/\text{Fe}] = [\text{Mg}/\text{H}] - [\text{Fe}/\text{H}] \quad (7.3)$$

The rightmost panel of Figure 7.2 compares the  $[\alpha/\text{Fe}]$  distributions for both, the observed SEGUE stars (filled histogram) and the MCM mock stars (open histogram). The first difference that sticks out is the significant systematic shift of both distributions which is of the same order as seen in Figure 5.8. There in Section 5.2 the SEGUE  $\alpha$ -scale is compared to those of different high resolution samples revealing an overestimation of the SEGUE  $[\alpha/\text{Fe}]$  values of about 0.1 dex to 0.2 dex. A similar systematic shift is now seen in comparison to the MCM model. Considering that this overestimation of SEGUE  $\alpha$  values explains the shift to the model the absolute  $[\alpha/\text{Fe}]$ -scale of the MCM model seems to be correct comparing also very well to high-resolution observations. In addition to the shift the SEGUE stars show a double peak distribution while the MCM model distribution exhibits only a single peak. Further insights into this difference are discussed below.

### Elemental abundance plane

The differences seen in the rightmost panel of Figure 7.2 reappear in Figure 7.3 which illustrates how the MCM mock G-dwarf stars (right panel) and the original SEGUE G-dwarfs (left panel) distribute in the chemical-abundance-plane. The observed sample exhibits an extreme bi-modality (very artificial double peak structure) which is, as has been shown in Sections 5.2.1 and 5.3, mainly but not entirely caused by selection effects. The discussion in Section 5.2.1 and the following explanations strengthen the assumption that the second peak at high  $[\alpha/\text{Fe}]$  values, which does not disappear completely even after a careful bias correction, houses a distinct group of stars with properties different than the more metal-rich ones (see Figure 5.18).

There is however no such sign of bi-modality in the model distribution. One may argue that a single peak is expected because the MCM model involves thin disk chemistry only. But given the strong and obvious SEGUE selection effects that have been propagated to the mock stars, the latter should at least have led to a hint of a bi-modality if one assumes that the observed stars' bi-modal distribution is solely a result of selection effects. The apparently unaffected model distribution yet seems to indicate the contrary, supporting the existence of a chemically distinct nature for  $\alpha$ -rich and  $\alpha$ -poor stellar populations. A fact that is in agreement with results from many observational studies (Anders et al. 2014; Fuhrmann 2011; Adibekyan et al. 2013; Bensby et al. 2014) where the two populations of stars appear unambiguously spatially separated in the chemical-abundance diagram.

From the discussions in Section 5.3 and the present findings it is evident that a chemodynamical model of a pure thin disk is by itself not able to produce a gap in the chemical-abundance plane. Neither the model  $N$ -body particles nor the mock sample do show a the bi-modal feature as observed in the real data. If a turbulent early merger phase and the dynamical processes (e.g., heating, radial migration) that act throughout the Galaxy's evolutionary history would be sufficient to create a chemical as well as kinematic thick disk component (clearly separating the simulated stars in a high- and low- $[\alpha/\text{Fe}]$  population), there should be a hint of it in the  $[\alpha/\text{Fe}]$  distribution. But the model lacks any discontinuity even though its oldest stars (see also Minchev et al. 2013, 2014c,b) show properties normally attributed to thick disk stars, including typical thick disk kinematics (such as the rotational velocity lag, larger velocity distribution) and structural (shorter scale length than the younger stars) as well as chemical properties.

This raises the need for a discrete chemical thick disk component (see the two-infall scenario proposed by Chiappini et al. 1997) in order to match the results of today's detailed and precise observational datasets. It remains to be seen what would change if the MCM model is extended to include a combination of a thin and thick disk chemistry following the predictions of the complete chemical evolution model instead of only a thin disk.

### Distances and further kinematic quantities

Adding to the discussion on the distance scale and kinematic parameters in the previous chapter Figure 7.4 displays a copy of the results shown in Figure 6.14 but now overlaid with the predictions from the MCM mock sample. Remarkably, the MCM mock G-dwarfs confirm the TRILEGAL predictions. Especially, the distance distributions are quite similar. This supports the assumptions that has been made concerning the SEGUE stars' distance scale as discussed in Section 6.3. The excess of high- $z$  and high- $z_{\text{max}}$  stars for the models is well in agreement with the larger number of faint stars between  $2.5 \text{ kpc} < d < 3.0 \text{ kpc}$ . The different shape of the MCM mock distribution in galactocentric radius however may be related to the stellar  $N$ -body particle distribution in combination with the applied smoothing.

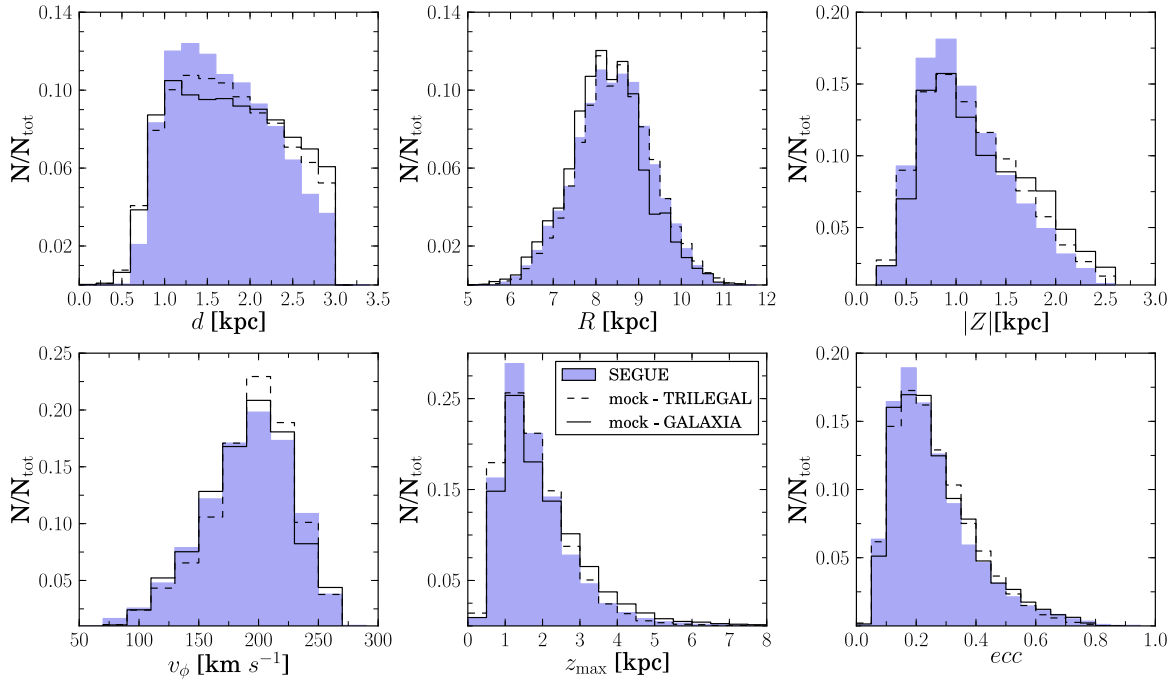


**Figure 7.4:** Overview on several kinematic parameter distributions. Shown are the SEGUE stars (filled histogram) in comparison to the TRILEGAL and the MCM mock G-dwarf sample (dashed and solid line, respectively). The plot is similar to Figure 6.14.

### 7.2.1 Chemo-kinematics of the disk

This section concentrates on the metallicity distribution function and the chemo-kinematic correlations of the Galactic disk as observed by SEGUE and predicted by both models under investigation. As such it adds to the chemo-kinematic analysis in Section 6.3.1.

#### Vertical and radial variations in the MDF

Figure 7.5 displays the MDF for the observed (filled histogram) but biased SEGUE G-dwarf sample and both mock samples (solid - MCM, dashed - TRILEGAL) in bins of vertical height (left) and galactocentric radius (right). For comparability both mock MDFs are shifted to the left by 0.1 dex. Comparing the MCM predicted MDF a second time to the observations, but now my means of the MCM mock stars, has a great advantage: the comparison is independent of the model dependent selection effect correction that needed to be applied to the SEGUE dataset in Chapter 5. This allows to test whether the discrepancies in the MDFs presented in Figure 5.20 are caused by either true differences or by selection effect corrections that strongly shape the MDF of the observed stars.

If the shallow change with vertical height in the peak of the MCM model’s MDF is a true feature, also the MDF of the MCM mock sample should indicate a similar behaviour with respect to the observed SEGUE stars as seen in Figure 5.20. And this no matter of the selection effects present in Figure 7.5. Under the assumption that the bias against metal-rich stars is of the same size in the observed and the mock sample the selection effects should mainly influence the absolute but not the relative positions of the peaks, conserving the difference in the observed and the model predicted gradient. Indeed, the MCM mock sample shows a more metal-rich MDF than the observed SEGUE stars and the TRILEGAL mock sample at heights above  $z = 1$  kpc,

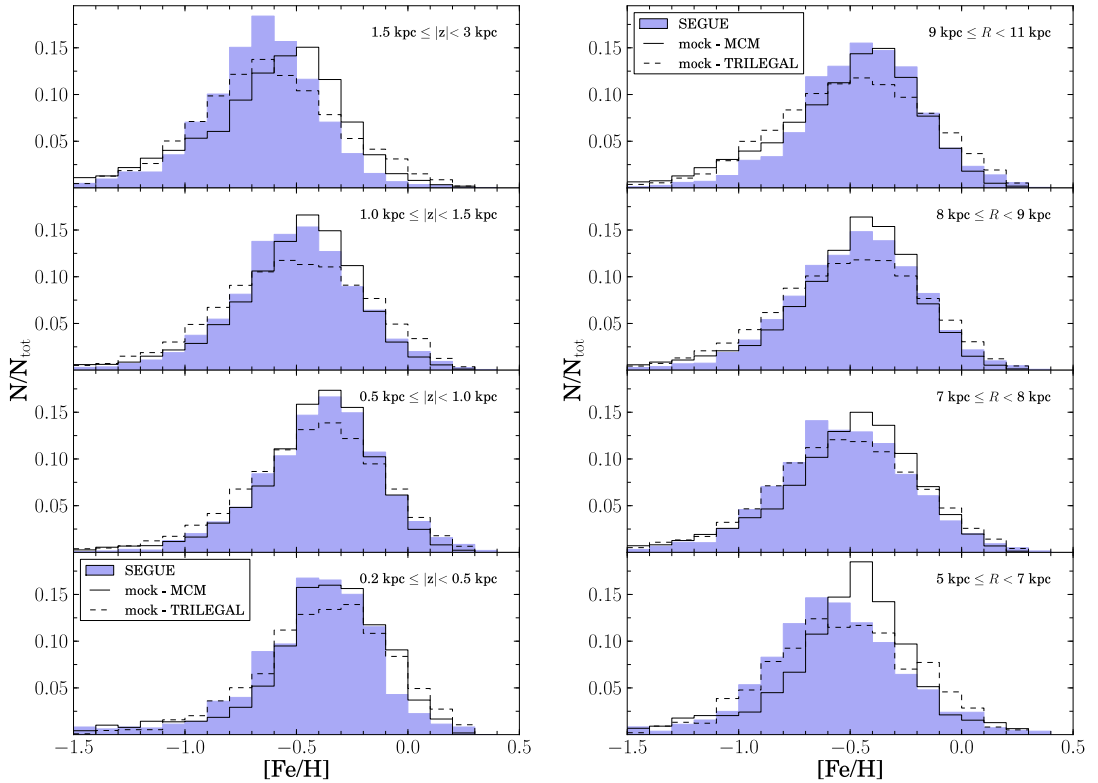


**Figure 7.5:** Distribution of metallicities at different height above the Galactic plane (*left*) and distance to the Galactic centre (*right*) for both, the mock samples based on TRILEGAL (dashed) and the MCM model (solid) as well as the observed stars (blue shaded). For comparability the mock distributions are shifted to the left by 0.1 dex.

leading to a shallow change in the peak of the MDF with vertical height similar to the one found for the chemo-dynamical model. In addition, the innermost radii with  $5 \text{ kpc} < R < 7 \text{ kpc}$  (Figure 7.5, lower right) exhibit a MCM mock distribution being distinctively shifted to high metallicity. Actually, the distribution should appear as metal-poor as the other two samples and that as a result of the survey’s target selection which at these radii primarily samples the latitudes dominated by thick disk stars. The significant discrepancy in the inner Galaxy can hence only arise, acting opposite to the selection effects, if the simulated disk of the MCM model is certainly too hot predicting too many metal-rich stars (more thin disk like) at heights that are expected to be dominated by a certainly less metal-rich stellar population.

Another re-appearing issue is the excess of metal-rich stars in the lowest  $z$ -bin being clearly visible for both model dependent mock samples. In Section 5.3 (Figure 5.20) the named difference showing up between the MCM model and the corrected SEGUE observations could be related to the applied volume correction, if one considers the low stellar number statistics below a height of  $0.5 \text{ kpc}$ . But, in Figure 7.5 the same mismatch seen for the raw SEGUE sample and both mocks confirms that the excess of metal-rich stars is more likely a result of an undersampling of bright stars in the observations due to the problem with saturation. This predominantly eliminates the closer and hence metal-rich stars.

Besides the previous two findings that are comparably easy to explain, it is hard to determine why in Figure 5.20 there is an excess of metal-rich SEGUE stars at intermediate  $z$  (in the range  $0.5 \text{ kpc}$  to  $1.5 \text{ kpc}$ ), while there is no such effect seen in Figure 7.5. If the discrepancy

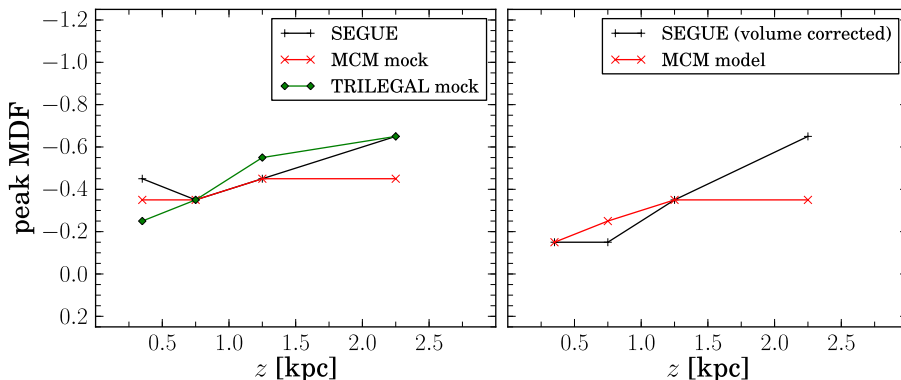


**Figure 7.6:** Variation of the MDF’s peak position with vertical height as inferred from Figures 7.5 and 5.20. Different colours and symbols represent the observed SEGUE G-dwarfs (black), the TRILEGAL (green) and MCM mock (red) stars. *Left:* Results from the current chapter with selection bias effects present in the observations and both model mocks. *Right:* Results from Chapter 5. Contrary to the left panel the SEGUE G-dwarf’s peak positions correspond to fully bias corrected MDFs.

in Figure 5.20 would solely be an effect of the difference in distance scale (see discussion in Section 5.3), a similar deviation should appear in the comparison with the mock stars, which is not the case. It could likely be that the applied volume correction is incorrect exaggerating the observed MDF to be too metal-rich which hence leads to the mismatch. Nevertheless, the exact reason is hard to determine because the better agreement for the mock stars might be either influenced by the selection effects or by the softening which is crucial when transforming an  $N$ -body distribution of mass particles into a synthetic stellar catalogue (see Section 7.1.2).

While in Figure 5.20 the selection effect corrections are the most uncertain factor shaping the observed distributions, in Figure 7.5 the MCM  $N$ -body particle related softening may have an influence on the shape of the MDFs. Also, the selection effects present in both, the raw SEGUE and the model mock samples, contribute to the appearance of the MDFs. This complicates the situation when aiming to disentangle the influence and size of the latter factors. Essentially, the effect caused by the difference in distance scale could be compensated by the smoothing or the selection effects or a combination of both. The assumption of a spherical smoothing volume around the particles likely exaggerates the smoothing perpendicular to the Galactic plane. This may lead to a mixture of stars with distinct chemical properties in different vertical layers which could artificially weaken or in the worse case even completely wash out the underlying vertical metallicity gradient. However, the effects introduced by smoothing, if at all present, are hard to determine considering the list of other issues that play a crucial role in shaping the metallicity distribution functions in Figure 7.5. However, with a mean smoothing length of 200 pc to 300 pc (see Section 7.1.2), which is much less than the actual chosen bin width in vertical height, the mixing of different populations is expected to be minimal.

### The shape of the vertical metallicity gradient

Figure 7.6 displays the trend in metallicity with vertical height for the samples discussed in Figure 7.5 (here left panel) and 5.20 (here right panel). Thereby the plot shows the peak positions of the sample’s MDFs as a function of the four previously used bins in height above the midplane. From this comparison the following is evident:

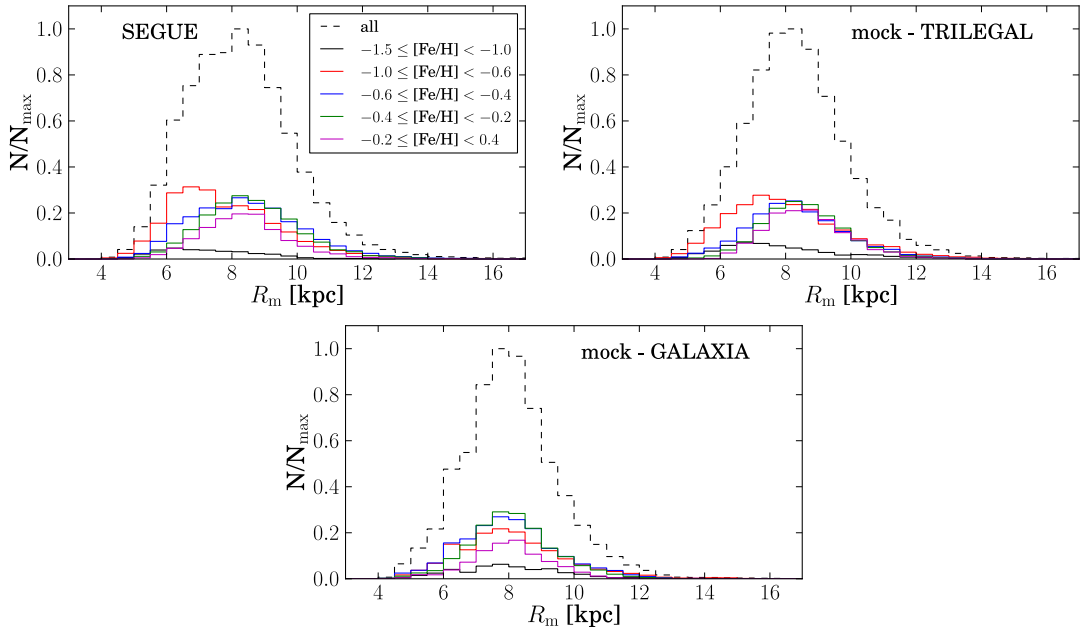


**Figure 7.7:** Distribution of mean orbital radii for different sub-populations in metallicity. *Top row, left:* SEGUE stars, *top row, right:* TRILEGAL mock G-dwarfs and *bottom row:* MCM mock stars.

1. As long as the samples, observed or mock, are influenced by selection effects the MDFs tend to be generally more metal poor. This leads to a displacement along the y-axis for the curves in the left panel with respect to those in the right panel. At the same time the overall trends however remain similar.
2. For both, the SEGUE G-dwarfs and the MCM mock stars, the gradient is less steep in case of the biased samples (left panel) compared to their bias free counterparts (right panel). In both cases the MCM model's gradient is obviously shallower than the observed one.
3. In particular, the gradients of the chemo-dynamical MCM model and the MCM based mock star sample (red lines in both panels) differ visibly, being even shallower for the MCM mock stars while showing less difference in metallicity between the lowest and highest  $z$ -bin than for the model itself. If this is an effect attributed to the smoothing the situation may change with an improved smoothing.

To conclude, the vertical metallicity gradient of the MCM model would certainly be steeper, resembling the observed gradient to a better degree if one adds a separate chemical thick disk component. The results show clearly that the model produces a population of old metal-poor stars which is mostly present at larger heights above the midplane. This population approximately meets the kinematic properties of observed thick disk stars. Nevertheless, those thick disk like effects are not enough to create a gradient as steep as the observations pretend. Especially the mismatch at larger heights points to the need for an additional and pronounced chemical thick disk component.

### Ages and mean orbital radii for stellar populations with different chemistry

Figure 7.7 provides yet another proof that the observational selection effects are properly resembled by the TRILEGAL mock sample but smeared out in case of the MCM mock stars. Similar to Figure 5.17, the present plot illustrates how the distribution in mean orbital radius changes for different populations in metallicity (upper row). Additionally, Figure 7.8 displays the age distribution of each of these different stellar populations as predicted by TRILEGAL (upper row) and the MCM model (bottom row) as a function of the mean galactocentric radius  $R_m$  (for the inner, solar and outer disk region of the Galaxy).

As a result of the uneven sampling of high- and poor-[Fe/H] stars seen for the observed and the TRILEGAL mock G-dwarfs the inner Galaxy ( $4 \text{ kpc} < R_m < 7 \text{ kpc}$ ) is seemingly dominated by metal-poor stars (red histogram for a range in metallicity between  $-1.0$  dex and  $-0.6$  dex). But the shallow vertical metallicity gradient of the MCM model deletes any sign of this selection effect. The different predictions by TRILEGAL and the MCM model seen in Figure 7.7 are reflected in the age distributions. The  $4 \text{ kpc} < R < 7 \text{ kpc}$  bin in Figure 7.8 indicates that for both models the metal-poor population (represented by the red histogram) contains primarily old stars with ages above 9 Gyrs which TRILEGAL assigns exclusively to the thick disk. While in case of TRILEGAL the fraction of younger stars is minimal, the mixture of populations predicted by the MCM model results in a much broader range of ages actually contaminating the metal-poor biased SEGUE sample with younger disk stars.

As illustrated by this plot a fundamental difference between the two models is that TRILEGAL's total age distribution exhibits a clear gap at around 9 Gyrs, clearly separating the thin from the thick disk component. Therewith TRILEGAL's age distribution resembles what one would expect by assuming that the thin and thick disk formation history is radically different as predicted by the two infall model by Chiappini (2009). On the other hand, the MCM model shows a continuous age distribution, which is no surprise considering the usage of a pure thin disk evolution model not being able to create a distinct component of purely old stars. Despite the above difference the two models predict similar age trends with  $R_m$ , namely, the number of metal-poor stars with ages  $< 9$  Gyrs increases with increasing mean radial distance from the galactic centre. Obviously, the effect is weaker for TRILEGAL, which is lacking metal-poor thin disk stars in the outer disk regions due to the radial metallicity gradient. The latter however is not only present in the SEGUE sample but also reproduced by the MCM model explaining the mix of ages that contribute to the metal-poor population. As demonstrated by Figure 8 in Minchev et al. (2014b) the metal-poor wing of the metallicity distribution in the outer disk is by far not exclusively dominated by old stars as it is the case for the inner Galactic disk, but it is a mixture of all ages. Indeed, the fraction of old metal-poor stars decreases with increasing radius. Likely, the relative ratio between the different age distributions of the MCM model are incorrect. Yet they provide, together with the TRILEGAL predictions which satisfy the selection effects but lack any influence of gradients or secular evolution processes, valuable insights in the age structure of the observed SEGUE G-dwarf sample.

### Chemo-kinematic relations

Comparably to Figures 6.20 and 6.21 in Section 6.3.1 the last subsection of this Chapter deals with the chemo-kinematic relations as predicted by the MCM mock stars. While TRILEGAL has trouble in predicting chemo-dynamical relations due to the lack of any a priori implemented correlations and evolutionary processes, the MCM model should show a considerable improvement. Figures 7.9 and 7.10 study the velocity dispersion in the galactocentric velocities  $U$ ,  $V$ ,  $W$  as a function of [Fe/H] and  $[\alpha/\text{Fe}]$  for both the observed (left panels) and the MCM mock stars

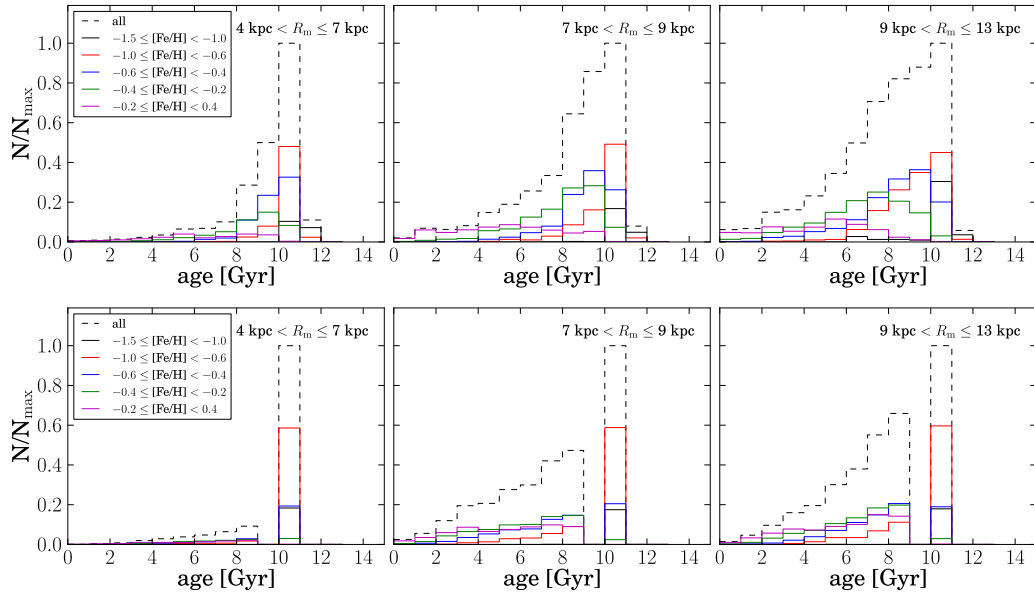


**Figure 7.8:** Age distributions as predicted by TRILEGAL (*bottom row*) and the MCM model (*top row*) for the same sub-populations in metallicity as presented in Figure 7.7. Each panel represents a different bin in mean galactocentric radius  $R_m$ .

right panels, respectively. The overall shape of the observed correlations and the velocity range covered in each of the velocity components are quite well reproduced by the model. Yet, the small change in the MDF’s peak position with vertical height and the missing distinct thick disk component both leave a sign in those plots. This is especially obvious for the inverse S-shape of the observed correlations in Figure 7.9 and the low metallicity, high- $[\alpha/\text{Fe}]$  regime where the discrepancies are largest. Being more severely affected by the bi-modal density distribution present in the sample, in particular the relations as a function of metallicity indicate that there is a clear distinction in the kinematic properties of the observed low- and high- $[\text{Fe}/\text{H}]$  stars. Again this sign is less obvious in the mock sample.

For example, in Figure 7.9 around solar metallicity the dispersion in  $U$  is similar for the observed and the MCM mock stars, rises than marginally in the range  $0 \text{ dex} < [\text{Fe}/\text{H}] < -1.0 \text{ dex}$  for the mock stars while the data sample shows a plateau up to a  $[\text{Fe}/\text{H}]$  value of about  $-0.6 \text{ dex}$ , steeply inclining afterwards to values above  $80 \text{ km/s}$ . Admittedly, the last three dots in the observed SEGUE sample indicate a velocity dispersion more likely attributed to halo stars even though the stars were selected to be disk stars. But the stars between  $-1.0 \text{ dex} < [\text{Fe}/\text{H}] < -0.6 \text{ dex}$  exhibit a realistic velocity dispersion for objects in the thick disk. However, the mock stars settle in a plateau at  $60 \text{ km/s}$  to  $70 \text{ km/s}$  not reaching up to the observed values in the lower metallicity regime. For the  $V$  component the covered velocity range is comparable, still the lack of a chemically bi-modal distribution shapes the correlation differently. Finally, the vertical velocity component shows a much steeper incline for the MCM mock stars than the data sample exaggerating the dispersion for stars above  $[\text{Fe}/\text{H}] = -1.0 \text{ dex}$ . This finding is in agreement with the shallow vertical metallicity gradient that points to a model disk, that is generally too hot and apparently overestimates the velocity dispersion in the Galactic region under investigation. The same overestimation is observed in the  $W$  component displayed in Figure 7.10.

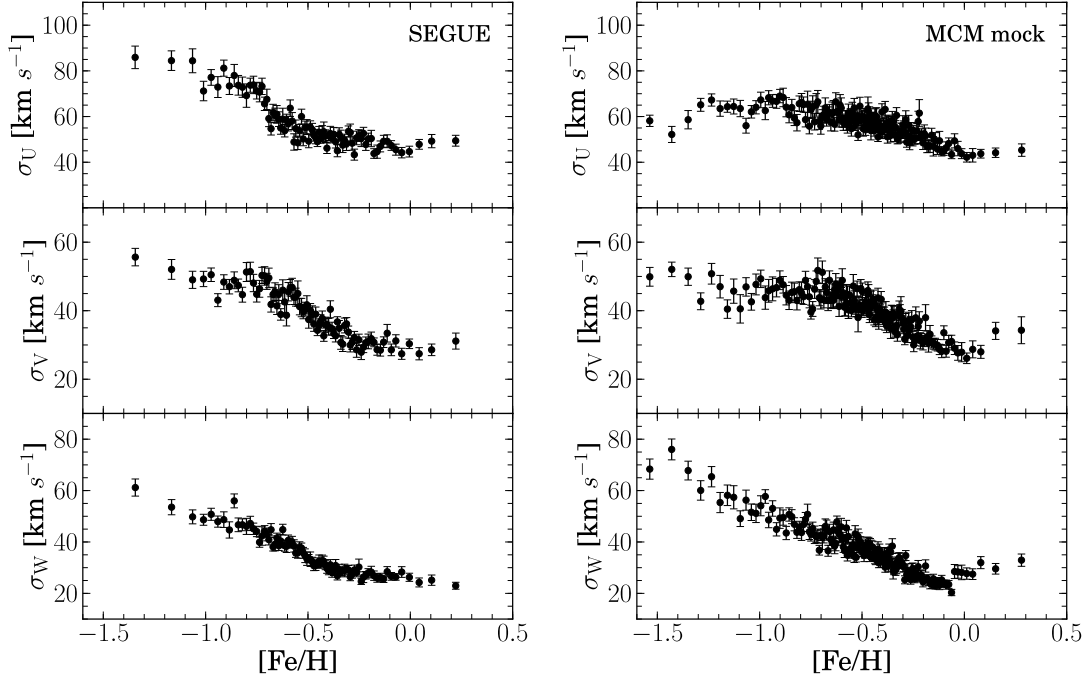


**Figure 7.9:** Velocity dispersion for the three Galactocentric velocities  $U$ ,  $V$ ,  $W$  as a function of metallicity for the observed SEGUE G-dwarfs on the left and the full MCM mock counterpart on the right. Each dot represents the mean of 200 stars and the errorbar in velocity dispersion is obtained by resampling the 200 stars 100 times with replacement. For comparison with TRILEGAL see also Figure 6.20.

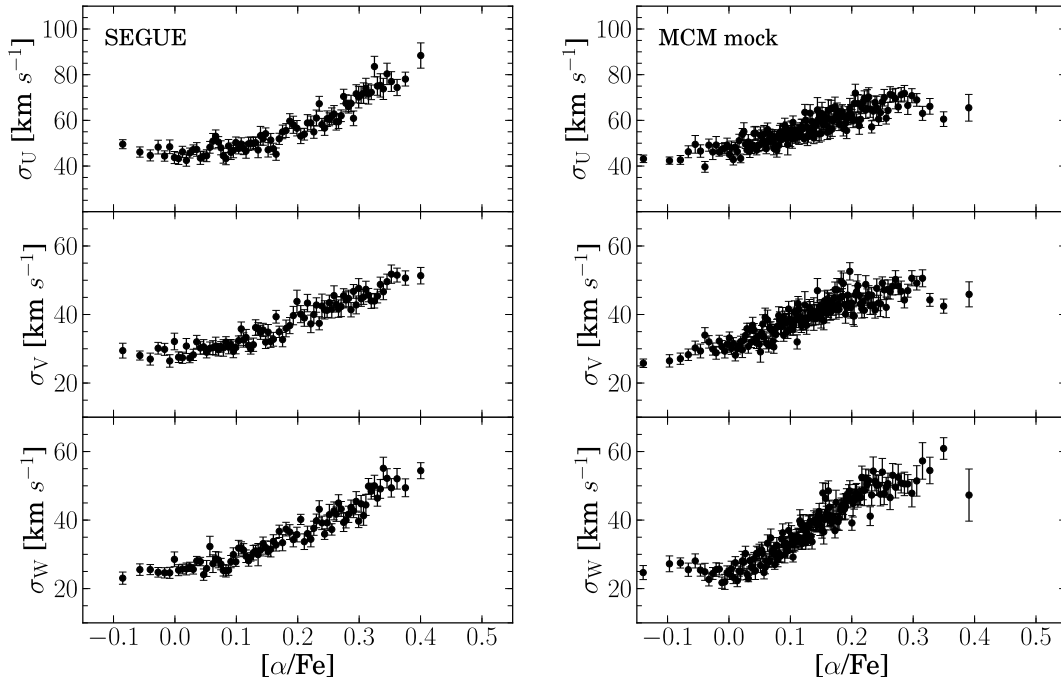


**Figure 7.10:** Same as Figure 7.9 but as a function of  $\alpha$ -enhancement.

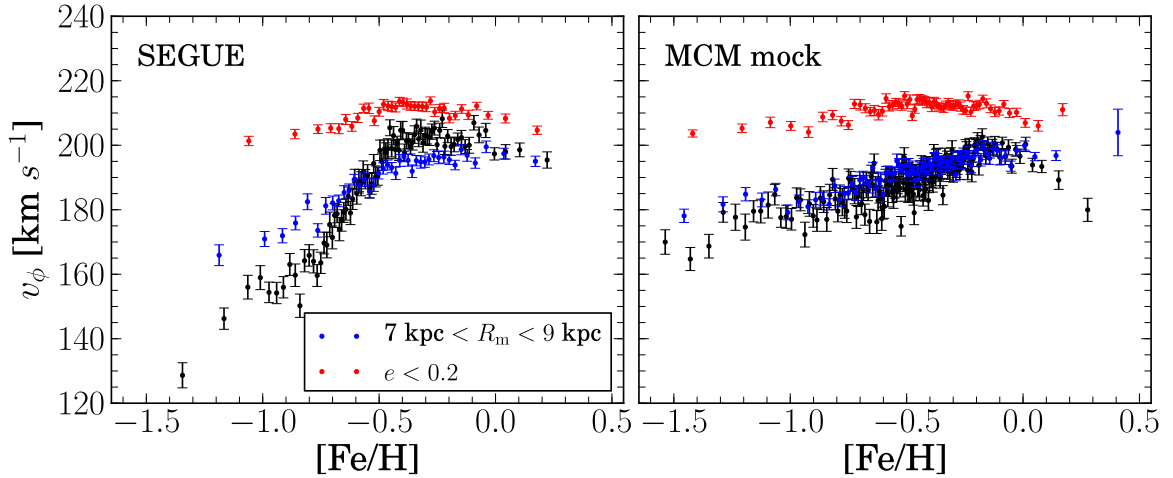


**Figure 7.11:** Correlation of rotational velocity and metallicity for both, the observed G-dwarf sample (*left*) and the MCM mock sample (*right*). Shown are subsamples containing the full sample (black), only local stars with  $7 \text{ kpc} < R_m < 9 \text{ kpc}$  (grey) and stars with low eccentricity ( $e < 0.2$ ).

In summary, common to all three velocity components is the following: the real observations indicate a pronounced inverse S shape for the total correlation. Their metal-rich and metal-poor stars show a flat relation connected by a transition region where the properties of both populations mix and lead to a change in slope. This shape likely points to two separate Galactic components with different properties and formation histories. In contrast, the model based correlations reveal this behaviour only rudimentary, missing the clear difference in velocity dispersion for thin and thick disk like stars. Instead, the relations indicate a smooth and continuous transition which is especially obvious from Figure 7.10. It agrees with the fact that the MCM model is able to increase the velocity dispersion for the oldest stars in the simulation mostly due to secular evolution, heating and scattering them throughout the Galaxy. But, even though this mechanism produces stars with thick disk like kinematics from the plots it is clear that an even hotter disk component is missing.

### Rotational velocity as a function of $[\text{Fe}/\text{H}]$ and $[\alpha/\text{Fe}]$

Figures 7.11 and 7.12 depict the  $v_\phi$ - $[\text{Fe}/\text{H}]$ - and the  $v_\phi$ - $[\alpha/\text{Fe}]$ -correlation for the observed SEGUE G-dwarfs and their MCM mock counterparts, respectively. The correlations confirm the previous findings indicating that the most metal-poor,  $[\alpha/\text{Fe}]$ -rich mock stars are on average  $20 \text{ km/s}$  faster than their observed analogues. Strikingly different is also the overall shape of the total distribution (black dots). While the observed stars show a steep slope for the metal-poor ( $\alpha$ -rich) and a nearly flat behaviour for the metal-rich ( $\alpha$ -poor) stars in both plots, the mock stars continuously decline in  $v_\phi$  with decreasing metallicity or increasing  $[\alpha/\text{Fe}]$ .

By no means the mock stars indicate any break or at least a significantly visible change in velocity as observed for the observed stars at an  $[\text{Fe}/\text{H}]$  value of about  $-0.5$  dex and a  $[\alpha/\text{Fe}]$  value of about  $0.2$  dex. Nonetheless, the model is able to produce a lag in velocity for the more metal-poor stars even if less distinct than for the observations. However, it is hard to determine the exact lag for both samples without splitting them into thin- and thick-disk subsamples. Certainly, the observed SEGUE G-dwarfs would show a lag of similar size of approximately  $40 \text{ km/s}$  as found by Lee et al. (2011b). In turn, Anders et al. (2014) discuss, based on a giant

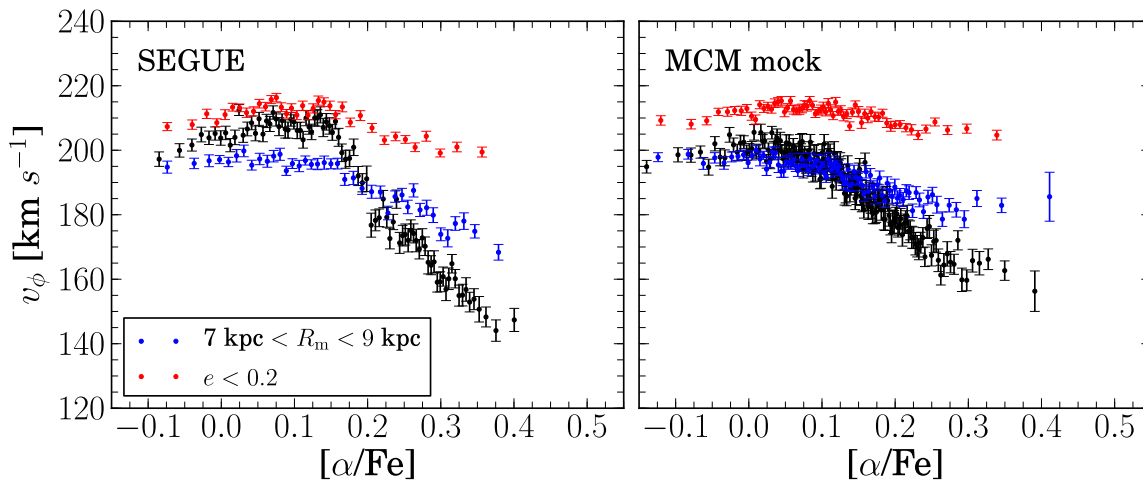


**Figure 7.12:** Same as Figure 7.11 but showing the rotational velocity as a function of  $\alpha$ -enhancement.

sample from APOGEE, that the size of the lag between the chemical thin and thick disk is very much dependent on the exact separation between stars in those two populations determining a range of values from  $20 \text{ km/s}$  to  $70 \text{ km/s}$ .

Interestingly, for the subsamples with only very circular stars (blue dots) that are the ones close to the plane (thin disk, with  $e < 0.2$ ) the match is quite good because here the thick disk component is excluded. Yet, when considering the local stars ( $7 \text{ kpc} < R_m < 9 \text{ kpc}$ ) that include more thick disk like stars the agreement gets instantly worse. By examining the rotational velocity as a function of the stars' chemistry with greater detail Figure 7.13 illustrates the  $v_\phi$ - $[\text{Fe}/\text{H}]$ -relation for several stellar populations in  $[\alpha/\text{Fe}]$  indicated by the different colours. For the observed SEGUE sample there is a clear gap and change in the relations' slope separating the populations above  $[\alpha/\text{Fe}] = 0.2$  dex from those below. As already shown in Figure 6.22, the metal-poor ( $\alpha$ -rich) populations show a positive trend covering a range in  $v_\phi$  from  $140 \text{ km/s}$  to  $180 \text{ km/s}$ . This trend is completely absent for the mock counterpart settling in a plateau between  $160 \text{ km/s}$  and  $180 \text{ km/s}$ . The orange, red and yellow population are however quite comparable. In agreement with the previous results the MCM model is in its present form yet not able to recover the complex velocity structure of the disk which may change with an additional thick disk component.

### 7.3 Discussion

Studying the MCM mock G-dwarfs revealed that indeed the majority of the discrepancies between the MCM model and the SEGUE dataset can be attributed to actual different properties of the model rather than to significant problems with the corrections discussed in Chapter 5. The analysis clearly demonstrates that the chemo-dynamical model is superior to TRILEGAL in terms of connecting the stars' chemistry and kinematics, but has difficulties to match the number counts of the SEGUE G-dwarf sample, a strength of TRILEGAL. Both models however predict comparable distributions for quantities like stellar parameters, proper motions, distances and magnitudes. The resemblance in the models' stellar parameter scale, showing similar shifts with respect to the real parameter distributions, is by construction because both rely on the same set of stellar isochrones (Marigo et al. 2008). Yet, considering the many additional assumptions (e.g, the Initial Mass Function (IMF) which by itself is still highly debated) necessary to generate a

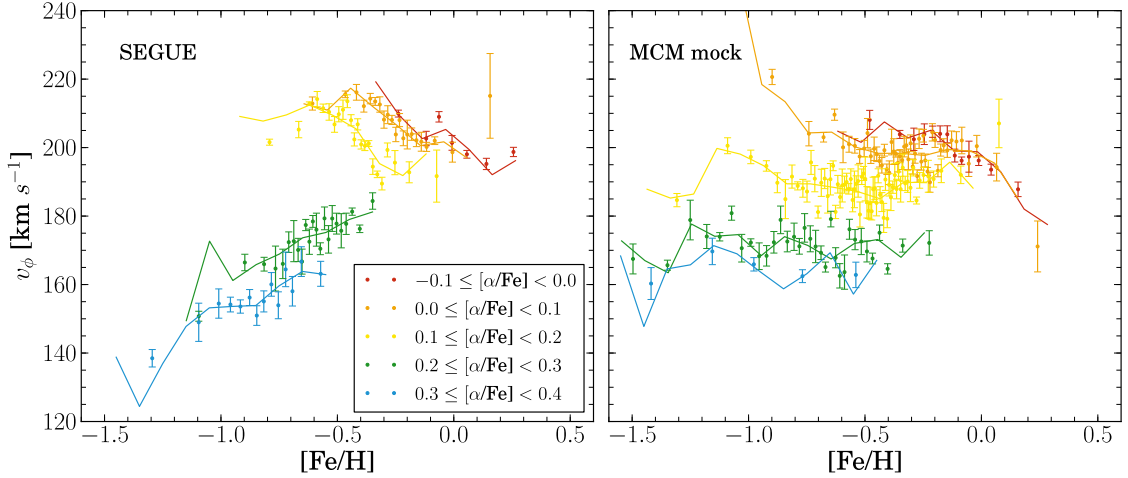


**Figure 7.13:** Rotational velocity as a function of  $[\text{Fe}/\text{H}]$  displayed for the observed (*left*) and the MCM mock G-dwarfs (*right*). The colour-coded curves represent sub-populations with different  $\alpha$ -abundance ratios increasing in  $[\alpha/\text{Fe}]$  from red to blue. Each dot contains 200 stars and the error bars are determined in a bootstrapping calculation. The solid lines trace the trend in each population as determined by calculating the mean velocity in bins of metallicity with a width of 0.5 dex.

synthetic observation the match in the distributions is quite remarkable. The development of reliable stellar isochrone sets for stellar populations with  $\alpha$ -enhanced abundance patterns would for sure help towards a quality-improvement in the field of stellar population synthesis. Currently, there is however no general solution for the problem of differing stellar parameter scales present for synthetic and observed datasets. As long as this is the case stellar parameters should mainly serve as characteristic stellar quantities that enable the user to classify stars relative to each other rather than using the parameters as true physical quantities.

Despite the main issues, namely, the hot nature of the simulated disk or the missing discontinuity in the chemical plane, the MCM model shows the ability to sufficiently reproduce the correlations between chemistry and kinematics as present in the SEGUE G-dwarfs. This gives confidence that the stars in the mock sample have indeed similar statistical properties than the observed counterpart and that the model mirrors important aspects of the Galaxy evolution that leaves its fingerprint in each observational dataset. The direct comparison to the TRILEGAL mock star sample reveals that apparently TRILEGAL’s simulated view of the Galaxy does interfere less with the introduced selection effects reproducing well the biases owned to SEGUE. This leads at least to a better match for the vertical metallicity gradient, as measured by the peak of the MDF, than the MCM mock stars indicate, even though there is no such gradient implemented in TRILEGAL. But of course, it does not compensate for the clear mismatches mostly in the wings of the MDFs.

To conclude, the general consistency of the observations and the two models is a remarkable result. Moreover, the discovered discrepancies and deviations are very useful in order to constrain the two models that are discussed in the present thesis, at best leading to their revision and re-examination. For the future, further constraints could be found if more precise ages, e.g. from asteroseismology are available for any observational dataset. This would allow to study and use the model predicted ages more efficiently.

## Summary

The following list summarises the most important results of the current Chapter:

- Confirming the results found in Chapter 5 the MCM mock stars indicate a vertical metallicity gradient that is too shallow compared to the observed one being an intrinsic property of the simulated  $N$ -body disk. The analysis of the vertical and radial gradient predicted by the model underlines that the MCM model is indeed able to efficiently create a metal-poor thick disk like Galactic component with chemical and kinematic properties different to its thin disk neighbours. But it turns out that the new model of the thick disk, as introduced by Minchev et al. (2013), which intends to induce a thick disk component solely from mergers at early times and radial migration at different stages of the disk evolution, can not completely keep up with the properties of the observed thick disk stars. The latter exhibit, e.g., much lower rotational velocities and larger velocity dispersions. The properties of the oldest stars in the current version of the MCM model are much alike thick disk stars in the solar neighbourhood. The Galactic component they form is produced by two effects: (1) stars are born hot and heated by mergers at early times and (2) radial migration (induced by mergers at earlier times or the bar/spiral features later on) transport old hot stars with thick-disk chemistry from inner disk to solar vicinity.

Based on the findings presented in the current thesis it seems that the MCM thick disk component created through dynamical evolution processes could be interpreted as some kind of additional intermediate thicker component that contributes to the actual thick disk. In either case, the model is yet incomplete pointing to a missing distinct thick disk component which would certainly enlarge the agreement to the SEGUE observations.

- With a thin disk chemistry implemented only, the chemo-dynamical model is not able to predict a gap in the chemical-abundance plane which would be in agreement with SEGUE and many other recent high-resolution data sets that reveal a clear distinction between the abundance patterns of the thin and thick disk. According to Minchev et al. (2013) a kinematic division that follows the criteria of Bensby et al. (2003) leads to a feasible separation of thin- and thick-disk like stars recovering the observed discontinuity in the  $[\text{Fe}/\text{H}]-[\text{O}/\text{H}]$ -space (see their Figure 12). But there is no chance to separate them securely by pure chemistry. Likely, if one would take a distinct chemical thick disk component into account a discontinuity should appear naturally.
- The SEGUE selection effects introduced to the MCM mock stars do not result at all in at least a weak bi-modality in the  $[\alpha/\text{Fe}]$  distribution. This confirms that the bi-modality observed in the SEGUE G-dwarf sample is not exclusively a result of SEGUE's specific observational selection effects, even though the latter demonstrably intensify the effect. The right panel of Figure 5.9 shows that there is still a hint of a distinct density peak for the  $\alpha$ -rich population after correcting for the stellar surface mass density and the survey volume. The assumption that the thick disk is not only the low metallicity extension of the thin disk but chemically a separate component needed to create a gap in the chemical-abundance plane suggests a different origin for each of these components with different formation timescales for the thin and thick disk as claimed by Chiappini (2009).

---

Chemo-kinematics as seen with RAVE and SEGUE - a comparison

---

In the recent past several studies have been performed on the chemo-dynamical properties of the Galaxy using well selected stellar samples from various spectroscopic Galactic surveys (e.g. Lee et al. 2011b, Liu & van de Ven 2012, Anders et al. 2014). One of those stellar samples is a sample of RAVE giants with high-SNR spectra (Boeche et al. 2013a) which was originally used to examine the relations between chemical and orbital properties of local RAVE stars. Therefore, in Boeche et al. (2013a) different stellar families are studied by sub-dividing the  $e$ - $z_{\max}$ -space into orbital sub-populations. In the attempt to obtain more detailed view on the chemo-kinematics of the Milky Way by studying the local disk chemo-dynamics as seen by RAVE and SEGUE the present chapter adopts the previously mentioned analysis technique in order to investigate and compare the orbital families of stars from both surveys (see also Figure 6.19 in Chapter 6).

At first sight the sample of carefully selected Boeche et al. (2013a) RAVE giant stars<sup>1</sup> seems to be the ideal choice as the counterpart to this work's compilation of SEGUE G-dwarfs. Even though RAVE samples Galactic disk stars closer to the midplane, both sets of stars cover roughly the same volume (see Section 8.1.1). Moreover, it is possible to examine the same scientific correlations, because both stellar samples are equipped with comparable data products, including distances and well determined chemical abundances of similar accuracy. However, most appealing is the samples' complementarity in sky coverage comprising both celestial hemispheres (see Figure 1.3). A combination of both datasets hence opens the unique opportunity to explore the global structure of the local stellar Galactic disk in a volume of a few kpc around the Sun. A first illustration on how this work's compilation of SEGUE G-dwarfs and the original RAVE giant sample by Boeche et al. (2013a) populate the  $xy$ - and  $xz$ -plane is given in Figure 8.1.

However, despite of all these positive aspects the final comparison of SEGUE and RAVE stars required a reselection and adjustment of the original Boeche et al. (2013a) sample as the course of this chapter shows.

Yet, the major obstacle to overcome, previous to realising the unprecedented comparison between SEGUE G-dwarfs and RAVE giants, is to exclude the influence of selection effects and to guarantee that both samples are either free of biases or face at least the same effects to a comparable degree. Thereby, the bias in metallicity is a crucial one to be accounted for,

---

<sup>1</sup>The entire sample of Boeche et al. (2013a) giants stars were kindly provided by Corrado Boeche to be used as a reference sample in the course of this thesis.

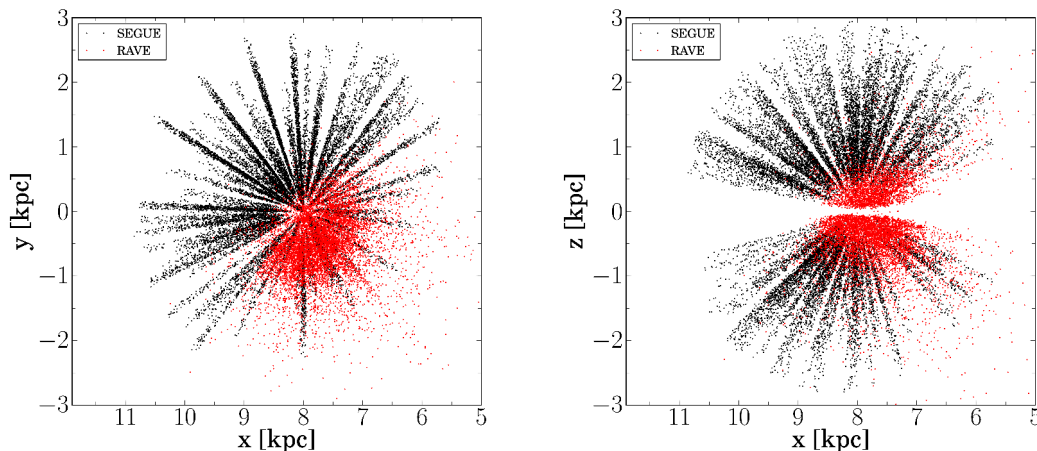


**Figure 8.1:** Spatial distribution of stars in galactocentric coordinates showing the observed SEGUE G-dwarfs in black and the comparison sample of RAVE giants studied in Boeche et al. (2013a) in red. The computation of kinematic parameters as performed for the SEGUE sample is described in Chapter 4. The coordinates for the RAVE sample have been kindly provided by C. Boeche.

because only the SEGUE sample is affected by the latter. Even though RAVE does suffer from incompleteness (see a discussion on the selection function in Appendix A.1) the targeting strategy avoids any bias in metallicity. For the SEGUE G-dwarfs the main metallicity issue can and needs to be resolved by correcting for the selection function and the colour cut of the sample. After the correction the sample can then be directly compared to the RAVE stars. What remains in both samples is the bias due to the incorrect representation of the mass distribution within the Galactic disk which is a consequence of the restrictive survey volume and could only be accounted for by a volume correction.

As previously discussed in Chapter 6 and 7 offsets between parameter scales are not unusual for stellar samples from different surveys or observations and synthetically generated mock samples. Therefore, the RAVE-SEGUE comparison yet presents another interesting aspect: namely to check whether or to what degree the parameter scales of the two independent surveys agree. It would be not surprising to find certain discrepancies because the surveys automatic reduction and analysis pipelines are based on completely different methods. Even for high-resolution observations the stellar parameters can vary a lot for different analysis techniques. Despite possible obvious differences due to the larger number of nearby objects present in the RAVE sample a careful comparison should reveal if RAVE and SEGUE deliver similar chemo-dynamical results overall.

Since the original comparison started with a comparison based on the Boeche et al. (2013a) stars and this work's SEGUE sample the following section sheds light on the original Boeche et al. (2013a) stars and their parameters. Problems and selection biases within the RAVE giant sample that have been detected stepwise while comparing the parameter distributions of stars from both surveys making a re-definition of the RAVE comparison sample necessary in the end are then laid out and motivated in Section 8.2. The section which also discusses the chemo-dynamical relations found from the RAVE-SEGUE comparison.

## 8.1 The RAVE giants from Boeche et al. (2013a)

The Boeche et al. (2013a) sample comprises RAVE stars with the highest quality spectra and abundances. In order to achieve such a selection the following quality criteria have been considered: (1) only spectra with a signal-to-noise ratio of at least 60 are selected on which MATISSE converges to a single point of the parameter space (`Algo_Conv` = 0), (2) the chosen spectra have to be well fit by the reconstructed model spectrum of the chemical pipeline, indicated by a low  $\chi^2$  value ( $\chi^2 < 1000$ ), and the number of defective pixels along the wavelength range of the spectrum have to be small (`frac` > 0.99), (3) every object that is not classified as a normal star according to the classification described in Matijević et al. (2012) is excluded. This morphological information is available for the complete RAVE survey and allows to identify e.g., binaries and peculiar stars within the RAVE sample. In case of objects with duplicate spectra the stellar parameters are used from the observation with the highest SNR as determined by the chemical pipeline.

### Stellar parameters

The usage of RAVE giants as the comparison objects to the SEGUE dwarfs is not only needed to cover the same distance range, giants have a couple of advantages in general, e.g. their stronger spectral lines that allow more certain abundance measurements. Moreover, giants cover a larger range in metallicity and  $\alpha$ -enhancement. Due to their intense absorption lines the chemical RAVE pipeline can obtain metallicity estimates down to  $[\text{Fe}/\text{H}]$  values of approximately -2 dex. With no restriction in metallicity the final cuts chosen to be applied to the RAVE giant's effective temperature and surface gravity of the RAVE giants are  $0.5 \text{ dex} < \log g < 3.5 \text{ dex}$  and  $4000 \text{ K} < T_{\text{eff}} < 5500 \text{ K}$ . This selection ensures that only cool giants are selected and problems with the grid limits of the automated pipeline are avoided by setting the lower limit in  $\log g$ . The resulting RAVE giant sample comprises 9098 stars and is used in the first part of the current chapter.

### Kinematic parameters

In the framework of DR4 the set of available information relevant to the stellar kinematics and dynamics covers radial velocities, proper motions from several sources and spectro-photometric distances. For each of the considered RAVE giants the following analysis uses parameters from DR4 (Kordopatis et al. 2013). An exception however are the proper motions that are taken from Siebert et al. (2011) and as such a mixture of values from PPMX Röser et al. (2008), Tycho-2 Høg et al. (2000), the SuperCosmos Sky Survey Hambly et al. (2001) and the UCAC2 (Zacharias et al. 2004) catalogue because for each object the most accurate proper motion is selected amongst all sources. Even if available in DR4, for reasons given in the course of this chapter the set of proper motions is not updated to values from more recent catalogues, e.g. UCAC3 or UCAC4 (Zacharias et al. 2010, 2013).

For consistency, a set of kinematic quantities, namely distances, velocities, galactic coordinates and orbital properties has been computed for the entire sample of RAVE giants following the methods described in Chapter 4. These information are a complement to the kinematics (phase-space coordinates and second order quantities like stellar orbits) that were originally calculated for the analysis laid out in Boeche et al. (2013a) and that are kindly provided by those authors to be used here as reference. Again, regarding the parameter uncertainties needed for the calculations total errors are adopted for the RAVE surface gravity and temperature by combining the internal and external errors of the RAVE DR4 pipeline. This makes the errors comparable

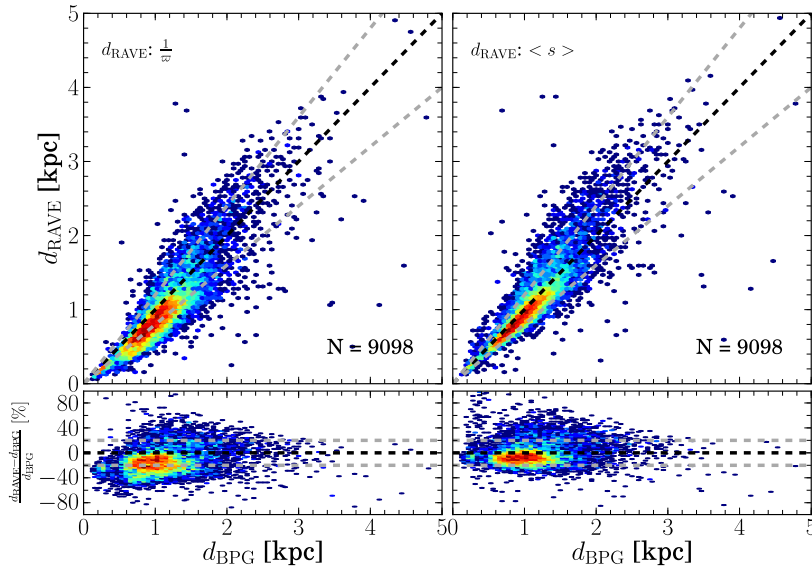


**Figure 8.2:** Evaluation of different spectro-photometric distance estimates to RAVE giant stars. Compared are the distances by Binney et al. (2014) as published with the fourth RAVE data release and the distances as obtained by the BPG distance procedure for the sample of approximately 9 000 Boeche et al. (2013a) giant stars. The density of stars is colour coded showing the highest density in red. The black dashed line indicates the identity line, the dashed grey lines mark a 20% deviation. *Left:* BPG distance (based on pdf) on the  $x$ -axis, RAVE parallax distance on the  $y$ -axis. *Right:* BPG distance on  $x$ -axis versus RAVE pdf distance on the  $y$ -axis.

to those used to compute the kinematic properties of the SEGUE G-dwarfs, an important aspect with view to their direct comparison in the current chapter. The external error estimates for giant stars as computed for the DR4 pipeline are listed in Table 2.1. Errors in  $[\text{Fe}/\text{H}]$  and  $[\alpha/\text{Fe}]$  are estimated to be 0.1 dex and 0.15 dex respectively.

### 8.1.1 Spectro-photometric distances

Spectro-photometric distance estimates for RAVE stars have been determined gradually over the years by Breddels et al. (2010), Zwitter et al. (2010), and Burnett et al. (2011). The method described in the latter reference, a Bayesian approach which served as a guideline for the distance code presented in Chapter 4, has been recently improved and extended as illustrated in Binney et al. (2014). Therefore, DR4 distances to RAVE stars are available as the expectation value of the probability density function over distance, parallax or distance modulus. For the first time extinction, mass and age estimates are also provided for each individual object. Among the three estimates the parallaxes are considered to provide the most reliable distances as claimed by Binney et al. (2014). In addition, the BPG distance code (Santiago et al. 2016) delivers independent spectro-photometric distance estimates to RAVE stars. To recall, the BPG distance estimate is equal to the probability weighted mean distance over all stellar evolutionary models, whose associated observables agree with the actual observable measurements within three times the uncertainties of the observed parameters. Among all datasets (see Section 4.1.4) used to validate the BPG code, the sample of RAVE giants serves as the ideal set of stars to cross-check the implementation of the algorithm. This is because the code uses a similar method and

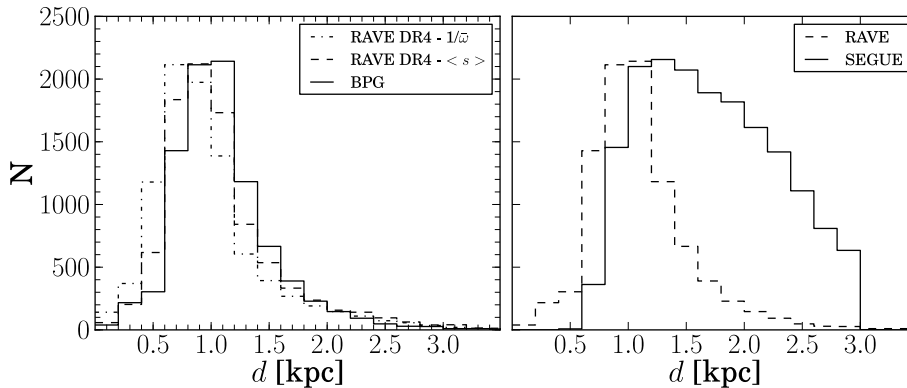


**Figure 8.3:** *Left:* Comparison of different distance estimates for the RAVE giant star sample by Boeche et al. (2013a). Shown are two distance distributions as obtained with the procedure presented in Binney et al. (2014) and one distribution based on the BPG code presented in Chapter 4 or Santiago et al. (2016). *Right:* Distance distributions for the RAVE giant reference sample and the SEGUE G-dwarfs. Even though the RAVE stars tend to be closer to the Sun both samples cover roughly the same volume.

theoretical background as have been used for the original RAVE collaboration distances.

### BPG distances for the Boeche et al. (2013a) sample

For consistency with the DR4 distance estimates the BPG distances to the Boeche et al. (2013a) giant stars are computed based on the same spectroscopic parameters taken from DR4 whereas the photometry has been obtained from 2MASS. To deredden the 2MASS NIR magnitudes in  $HJK_S$  the  $A_V$  extinction values determined by Binney et al. (2014) are adopted for each individual RAVE object in the sample. The conversion between the extinction in the optical and near-IR range is performed by following the transformation equations by Rieke & Lebofsky (1985) (see also Binney et al. (2014), Section 2). Again, as for SEGUE the metallicity scale is brought into better agreement with the stellar evolutionary models that per se do not account for  $\alpha$ -enhancement by use of the  $[\alpha/\text{Fe}]$  ratios as determined by the chemical RAVE pipeline (Boeche et al. 2011). Figure 8.2 shows, for the same set of 9000 RAVE giants, two of the three spectro-photometric distance estimates provided by Binney et al. (2014) (*left panel:* distance implied by the expectation value of the parallax,  $1/\varpi$ ; *right panel:* the expectation value of distance,  $\langle s \rangle$ ) in comparison to the BPG distance. Both panels indicate systematically larger (smaller) BPG distances for stars with  $d_{\text{BPG}} < 1 \text{ kpc}$  ( $d_{\text{BPG}} > 1 \text{ kpc}$ ). However, the systematic trend is less in the right panel. Even though the rms scatter is similar in both panels, the mean residual is smaller for the  $\langle s \rangle$  distances with a value of  $-2.6 \pm 18.6\%$  in comparison to  $-13.6 \pm 19.3\%$  for the parallax distance. As expected the compatibility is larger for the  $\langle s \rangle$  distances because they represent the expectation value directly taken from the distance distribution function which is more similar to the BPG estimates. Basically, the vast majority of the stars have distance residuals well accommodated by the expected uncertainties in the two estimates being compared. Nevertheless, in the distance range that is crucial to the analysis in this Chapter the BPG estimates have a tendency to be generally larger.

As an add-on, Figure 8.3 (left panel) illustrates how the two RAVE distance estimates  $1/\varpi$  and  $\langle s \rangle$  differ for the sample of giant stars, showing the entire distribution to be shifted to smaller distances in case of the parallax estimates. The plot also shows how much the BPG distance distribution is offset to larger distances with respect to the original RAVE curves.

### Comparing the distance distribution for the RAVE and SEGUE sample

The stellar distance is the most crucial parameter that influences the calculation of the stellar kinematic parameter set. The previous paragraph illustrated that distance estimates from different sources and based on different routines can vary essentially for the same stars even if they agree within the expected uncertainties of the quantity. So ideally, when comparing the chemo-dynamical properties of the SEGUE G-dwarfs with the RAVE giant sample one wants to use distances for both datasets that originate from the same computational framework. That way, the kinematic parameter scale of the two independent stellar samples can be homogenised as much as possible and uncertainties can be consistently obtained. For the entire comparison between the RAVE and SEGUE stars the distances of choice are the ones based on the BPG code because those are available for both stellar samples. The resulting distance distributions are displayed in Figure 8.3 (*right panel*). In principle both stellar samples cover the same distance range but there is a clear lack (excess) of RAVE stars for large (small) distances in comparison to their SEGUE counterpart. RAVE, e.g. catches much more nearby thin disk stars. These trends are mainly a result of the different survey sampling strategies and will certainly influence the whole analysis.

## 8.2 Chemo-kinematic relations from RAVE and SEGUE

Adding to the results obtained in the previous two chapters the current section concentrates on discussing the main chemo-dynamical properties and correlations as seen by RAVE and SEGUE. Thereby, the focus is put on the metallicity distribution function (MDF) at various positions within the Galactic disk and as function of the stars' orbital properties. The analysis also sheds light on the kinematic properties, i.e. the rotational velocity as a function of chemistry. In order to compare two samples that are mostly free of biases the SEGUE G-dwarfs are corrected for the survey selection function and the colour-magnitude cut.

Yet, previous to the actual comparison of RAVE's and SEGUE's chemo-dynamics this section starts with the definition of a better RAVE sample more free of biases as the originally chosen sample discussed in the previous section. The need to refine the RAVE reference sample is highlighted in the next section and results directly from the findings made by comparing the MDF of both the selected RAVE and SEGUE stellar samples. As outlined below the original RAVE giant sample is obviously biased against metal rich stars. The main reason for this being the restrictions made in SNR and the RAVE pipeline parameters `frac` and  $\chi^2$ . Based on the detailed check up presented below a new sample of RAVE giants is defined that includes stars with a SNR above 40 (at least needed to still trust the [Fe/H] values) and handles the important  $\chi^2$  parameter more relaxed because the latter kills most of the metal rich stars in the original Boeche et al. (2013a) selection. Distances and stellar parameters of the new samples objects are the same as described in the previous section.

### 8.2.1 The metallicity distribution with galactic distance and vertical height

The MDF as a function of vertical height (*right panel*) and radial distance (*left panel*) from the Galactic centre is displayed in Figure 8.4. The SEGUE G-dwarfs are represented by the filled blue histogram, while the open black histogram shows the distribution of the high-SNR RAVE giant sample (from now on referred to as the RAVE SNR60 giants). Both samples are restricted to vertical heights,  $z$ , between 0.2 kpc and 1.5 kpc and a galactocentric distance,  $R$ , in the range of 6 kpc to 9 kpc. The limitation is necessary due to the samples' uneven coverage in height

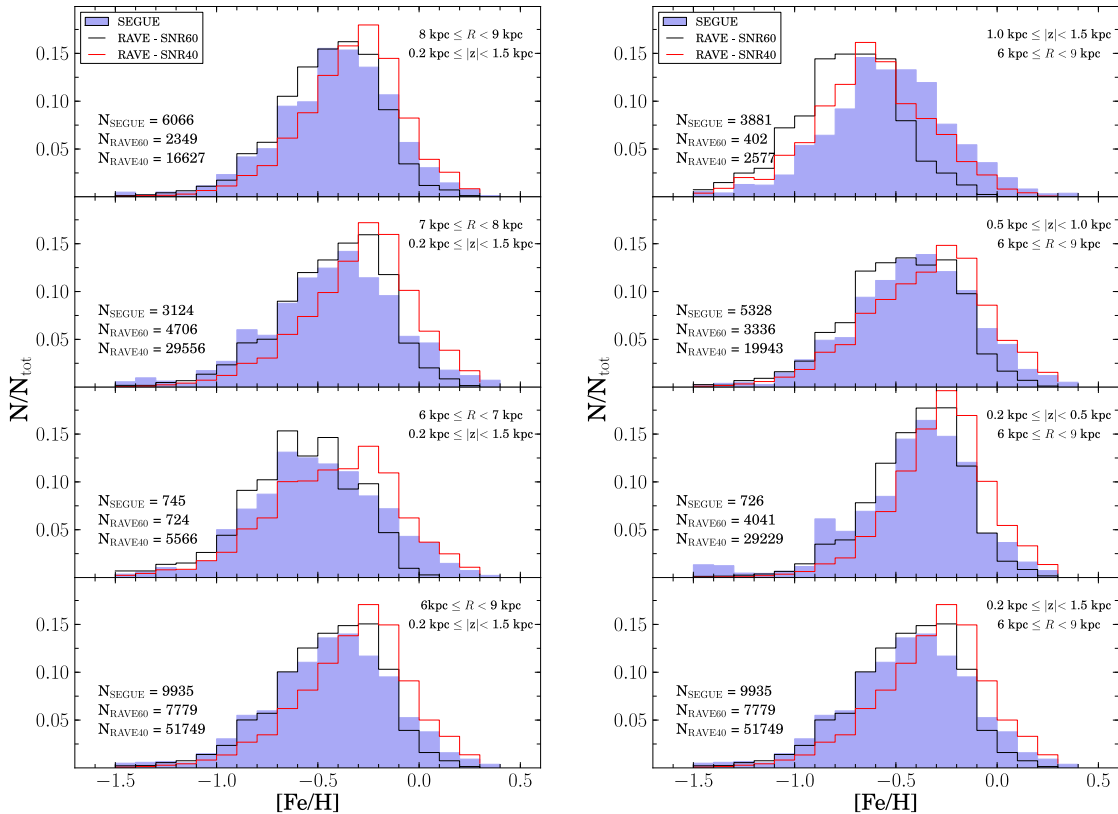


**Figure 8.4:** Displayed are the MDFs in bins of galactocentric radial distance (*left*) and vertical height (*right*) above the plane for the high-quality RAVE giant sample by Boeche et al. (2013a) (black histogram) containing only stars with SNR above 60 and the SEGUE G-dwarf sample (filled histogram). Also shown is a larger RAVE giant sample with a lower cut in SNR at 40 (red histogram). The number of stars in each bin is indicated in the lower left corner of each subpanel. *Lower panels:* no separation in  $z$ -bins.

and radial direction. It guarantees to compare RAVE and SEGUE in those Galactic regions where both surveys provide information for a sufficient number of stars. Mainly, the above limits are determined by the size of the RAVE survey volume being the smaller one which does not include objects beyond  $R = 9$  kpc. This is because RAVE, a southern hemisphere project, predominantly looks towards the centre of the Galaxy. Actually, the distribution in current radius peaks at  $R \approx 7.5$  kpc in case of RAVE giant stars, while the SEGUE G-dwarfs exhibit a peak at  $R \approx 8.5$  kpc because SEGUE samples much farther into the outer Galaxy. Indeed, Figure 8.4 and the following analysis reveal that even with the above limits the obtained results are significantly influenced by the present differences in the stellar number statistics within the chosen ranges and the geometric volume of the two surveys. How exactly their stellar density changes with  $z$  and  $R$  is indicated by the number counts given in each sub-panel. While the number of RAVE stars decreases with increasing distance from the plane, the G-dwarf sample shows, by construction of the SEGUE survey, the opposite behaviour. It is hence advisable to split the samples into sub-samples of stars grouped according to their spatial position.

Along the radial axis of the Galaxy most of the RAVE SNR60 sample concentrates in the bin  $7 \text{ kpc} < R < 8 \text{ kpc}$ , the majority of the SEGUE stars however has radii beyond the Sun's radius at around 8 kpc. Towards the inner Galaxy both samples exhibit a very low number of stars.

In case of SEGUE this is because the survey's observing-cone leads to a lack of stars with low heights especially inwards of  $R = 7$  kpc. The majority of inner disk SEGUE stars is hence located above 1.5 kpc (see Figure 8.1) which excludes them from the comparison. The same geometric reason also induces the distinctively more metal-poor MDF for the SEGUE G-dwarfs in the inner Galaxy as compared to the local and outer radial bin (see selection biases for SEGUE inwards of  $R = 7$  kpc as already discussed in previous chapters). For RAVE the stellar number statistics is not only determined by the sampled volume which probes less close to the plane in the inner Galaxy than in the range  $7 \text{ kpc} \leq R < 9 \text{ kpc}$ . But the RAVE statistic is also influenced by the high signal-to-noise cut ( $\text{SNR} > 60$ ) which gradually reduces the number of stars with increasing distance to the Sun. This fact predominantly affects the innermost radial bin with  $6 \text{ kpc} \leq R < 7 \text{ kpc}$  and the uppermost bin in vertical height with  $1.0 \text{ kpc} \leq z < 1.5 \text{ kpc}$  (top panel on the right). Both of these comprise RAVE giants with distances above 1 kpc. Consequently, those two panels represent only the most luminous giants with the majority of them having a surface gravity of  $0.5 < \log g < 1.7$  and a temperature in the range  $4300 \text{ K} < T_{\text{eff}} < 4800 \text{ K}$ .

At first sight it is not clear why the number of distant luminous RAVE stars should be that low. Though, when analysing the MDFs in Figure 8.4 there are two distinct discrepancies that especially stick out. Both of them concern stars in the inner Galaxy or with heights far above the midplane, indicating that luminous, metal-rich stars may be underrepresented in the high-quality RAVE SNR60 sample. The inner radial bin shows a significant excess of metal-rich SEGUE G-dwarfs with  $[\text{Fe}/\text{H}]$  above solar, while there is even a more obvious mismatch between the survey's MDFs above 1 kpc. There the RAVE giants' MDF peaks by about 0.2 dex lower in metallicity than the SEGUE G-dwarfs distribution. Especially, the lack of metal-rich stars for the inner radii contradicts the general expectations. Usually RAVE should show a MDF dominated by metal-rich stars due to its ability to sample the more dense and metal-rich low- $z$  regions.

It turns out that the above findings can be explained as follows: when selecting a RAVE sample with the constraints outlined in Section 8.1 any giant star with  $T_{\text{eff}} < 4250 \text{ K}$  is excluded. This is a direct result of the quality criterion `Algo_Conv = 0`. The latter assures to select only spectra for which the DR4 RAVE pipeline provides explicit stellar parameter estimates based on MATISSE. MATISSE has the advantage to deliver more accurate results than DEGAS thanks to its ability to interpolate between the grid points of the stellar parameter space. However, especially close to the grid boundaries, e.g., at low  $T_{\text{eff}}$ , the DR4 RAVE pipeline primarily delivers stellar parameter estimates based on DEGAS because MATISSE does not converge sufficiently in those parameter space regions. Restricting the sample to objects with MATISSE results is one way to assure to deal with a homogeneous parameter set. Yet, at the same time the above temperature cut is introduced, generating a metallicity bias against high metal-rich stars for giants with  $\log g < 1.7$ . The cut is most significant for the luminous metal-rich giants because their isochrones lie at lower  $T_{\text{eff}}$  with respect to the luminous but lower metal-poor giants. Figure 8.5 illustrates how the limit in temperature affects the luminous part of the RAVE giant branch. As displayed, the fraction of metal-rich stars (red, orange coloured dots) with  $\log g < 2$  dex is minimal. The fact that the RAVE SNR60 sample is highly biased against low  $\log g$  metal-rich stars certainly affects the shape of each MDF presented for the approximately 9 000 RAVE giants. The effect's size is however hard to quantify at this stage. Yet it is clear that the effect is largest for those panels predominantly containing giants with low surface gravity. This also explains the significant discrepancies compared to the SEGUE G-dwarf MDFs in the inner disk and at larger heights.

The temperature cut however does not explain why in general the distributions of the RAVE sample appear more metal-poor than one would expect for the RAVE survey. Actually, RAVE should outnumber SEGUE in terms of metal-rich stars. And this should be the case even with

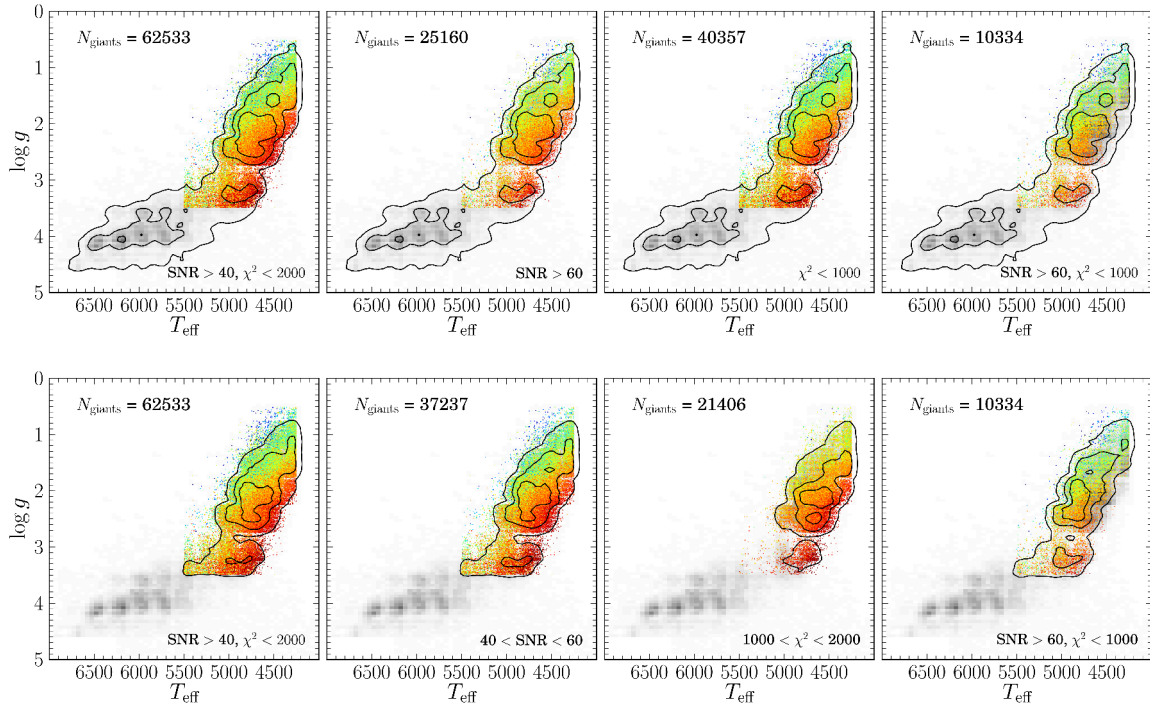


**Figure 8.5:** Hertzsprung-Russel-diagram for the extended sample of RAVE giants (the SNR40 RAVE sample) with parameter limits as discussed in the text. *From left to right:* Application of quality cuts in SNR,  $\chi^2$  or both parameters. The colour coding indicates the metallicity of the SNR40 giants in red (blue) representing the metal-rich (metal-poor) stars. *Black contours (in top row) and grey scale density distribution (in bottom row):* Same sample as the colour coded one but without limits in  $T_{\text{eff}}$  and  $\log g$ .

the chosen radial and vertical limits. But there is no sign of such a behaviour. All radial and vertical sub-groups of stars in Figure 8.4 indicate an excess of metal-rich SEGUE stars. Solely, the total RAVE distribution (both bottom panels) and the MDF for RAVE stars between  $7 \text{ kpc} \leq R < 8 \text{ kpc}$  point towards a more metal-rich dominated distribution. They exhibit at least a small excess of stars with metallicities between  $-0.3 \text{ dex} < [\text{Fe}/\text{H}] < -0.1 \text{ dex}$  close to the expected thin disk's peak in  $[\text{Fe}/\text{H}]$ . Due to these rather unexpected findings it is difficult to state anything on the radial or vertical metallicity gradients as seen by RAVE. Also the peaks and width of both survey's MDFs can be hardly compared. Instead, the significant mismatches seen in Figure 8.4 require a more detailed investigation of the samples' properties, mainly focussing on the influence of the most important selection criteria. The next subsection illustrates that indeed there is yet another bias originating from one of the selection criteria that affects the shape of the RAVE giant's distributions.

### Metallicity biases in the Boeche et al. (2013a) sample

In order to better quantify the biases present in the RAVE SNR60 giant sample Figures 8.5 and 8.6 illustrate the impact of the two main quality criteria,  $\text{SNR} > 60$  and  $\chi^2 < 1000$ , on a larger set of RAVE giants. Basically, the larger sample meets all selection criteria, parameter choices and specifications as listed and discussed in Section 8.1 but the SNR,  $\chi^2$  and  $\text{frac}$  parameter limit. Instead, following the recommendations in Boeche et al. (2011) the extended giant sample

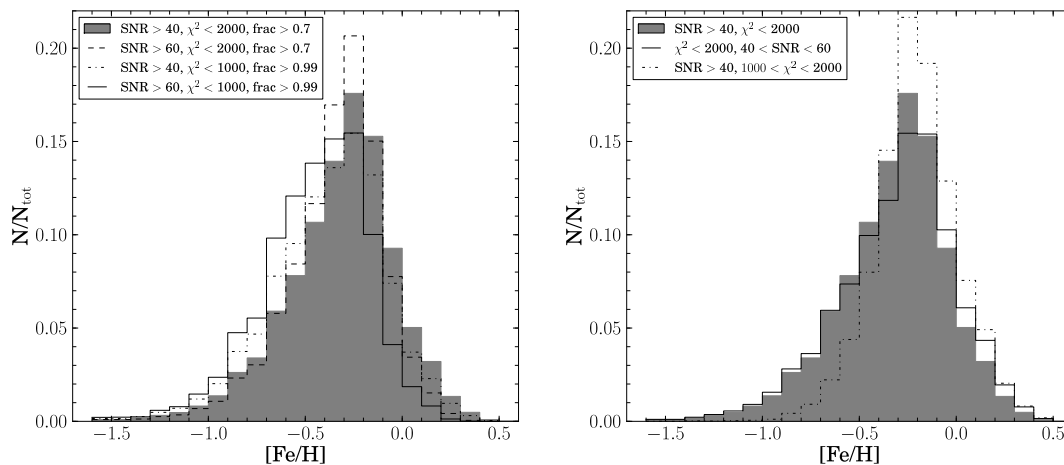


**Figure 8.6:** The plot illustrates how various quality criteria, such as, the signal-to-noise or the  $\chi^2$  parameter of the chemical RAVE pipeline affect the shape of RAVE giants' MDF. Obviously, both, the high SNR cut at 60 and the very conservative  $\chi^2$  limit with  $\chi^2 < 1000$  exclude metal-rich stars.

comprises stars which satisfy  $\chi^2 < 2000$  and  $\text{frac} > 0.7$ , the two main quality criteria of the chemical RAVE pipeline. Also, the SNR cut is less restrictive with a cut at  $\text{SNR} > 40$ , leaving a total number of 62 533 stars. The distribution of the SNR40 giant sample in  $T_{\text{eff}}\text{-log } g\text{-space}$  is shown in the left panels (top and bottom) of Figure 8.5. The colour code indicates the metallicity of the stars with red (blue) representing the most metal-rich (metal-poor) ones. The contours and grey shaded density distribution illustrate the locus of the sample before cutting in surface gravity and temperature. From left to right each panel illustrates the effect of applying a different quality cut or a combination of them. The four middle panels demonstrate how the sample is diminished when changing the cuts in SNR or  $\chi^2$  from 40 to 60 and 2000 to 1000, respectively. Note, that the middle panels of the top row display the stars that remain in the sample, while their equivalents in the bottom row show those stars that are removed after application of the specific criterion. It is evident that the higher SNR limit excludes not only more stars than the  $\chi^2 < 1000$  criterion but also stars with all kinds of metallicities. The more restrictive  $\chi^2$  limit however tends to eliminate primarily metal-rich giants (see colour coding and contours). This finding can be explained as a direct result of the different number of spectral lines visible in the spectra of metal-poor or metal-rich stars. The latter exhibit a line-rich spectrum where spectral effects, such as, line blending are larger than for metal-poor stars, making the stellar abundance determination more complex. Consequently, the match between the observed and the reconstructed spectrum of the chemical RAVE pipeline is less accurate which is expressed by a larger  $\chi^2$  parameter value.

Figure 8.6 shows the metallicity distribution functions for the different samples highlighted in Figure 8.5. The plot underlines that the majority of RAVE giants with  $1000 < \chi^2 < 2000$  have metallicities in the range  $-0.4 \text{ dex} < [\text{Fe}/\text{H}] < 0.5 \text{ dex}$  (right panel, dash-dotted curve). This leads to an obvious change in the shape of the overall MDF for giant stars with  $\text{SNR} > 40$  but  $\chi^2 < 1000$  (dash-dotted line, left panel). Their distribution's peak, located in the range  $-0.2 \text{ dex} < [\text{Fe}/\text{H}] < -0.3 \text{ dex}$ , is still compatible with the maximum as shown by the total SNR40 sample (filled curve, left panel). But the altered shape favours the metal-poor tail due to the large number of missing metal-rich stars. A similar but less strong effect is happening for the SNR limit (dashed curve, left panel). The difference in the  $[\text{Fe}/\text{H}]$  distribution for stars

with  $40 < \text{SNR} < 60$  (dashed curve, right panel) and the entire SNR40 sample (filled curve, same panel) confirms this and illustrates that the cut at high SNR introduces the tendency to also exclude more metal-rich than metal-poor stars, even if the fraction is comparably small. However, in combination both quality restrictions add up to a significant bias against metal-rich giants leading to a highly asymmetric MDF for a sample of stars with  $\text{SNR} > 60$  and  $\chi^2 < 1000$  (solid curve, left panel), comprising very few stars above solar metallicity. For illustration, the left panels of Figure 8.5 display how such a sample distributes in the  $T_{\text{eff}}\text{-log } g\text{-plane}$ .

### Summary and definition of the final RAVE reference sample

Based on this quantitative evaluation the results found for the SNR60 RAVE giants in Figure 8.4 can well be justified. The overall weak metal-rich tail of the RAVE MDFs (black histograms) is likely caused by the very conservative quality selection which turns out to be not suitable for the pursued chemo-dynamical analysis and comparison to SEGUE. Instead, the SNR40 giants present themselves as the better choice, providing a more representative RAVE sample to proceed with in the further comparison to SEGUE. For completeness, the MDFs of the SNR40 giants are displayed as the red histograms in Figure 8.4. They indicate obvious difference in the positions and shapes of the RAVE distributions when compared to the high quality Boeche et al. (2013a) giants (black histograms) clearly changing to the better. With a significantly increasing stellar density of RAVE objects towards the Galactic mid-plane it is expected that any RAVE sample should appear more metal-rich than those from SEGUE. Indeed, the central peaks of the RAVE distributions are noticeably shifted towards larger  $[\text{Fe}/\text{H}]$  values, showing a clear difference and an excess of metal-rich stars with respect to SEGUE. However, even the larger giant sample is influenced by the temperature limit of the MATISSE pipeline. It lacks luminous metal-rich giants with heights above  $z = 1$  kpc and radii in the range  $6 \text{ kpc} < R < 7 \text{ kpc}$ . This leads to a very broad MDF at inner radii that actually should peak fairly sharp at about  $-0.2$  dex to  $-0.3$  dex similar to the other radial bins. Also, for heights between 1.0 kpc and 1.5 kpc the RAVE distribution (red histogram) is too metal-poor compared to the SEGUE one that is thought to represent a plausible distribution at that height.

Before digging deeper into the final chemo-dynamical analysis the properties of the final RAVE giant sample used to compare to the SEGUE stars read as follows: for consistency, the parameter limits of the RAVE sample are, if possible, adapted to those defined for the SEGUE stars, finally leaving 57 745 RAVE stars with  $\text{SNR} > 40$ ,  $\chi < 2000$ ,  $\text{frac} > 0.7$ ,  $0.5 < \log g < 3.5$ ,  $T_{\text{eff}} < 5500 \text{ K}$ ,  $d < 5 \text{ kpc}$ ,  $\sigma(\text{pm}_{\text{RA}}) < 5 \text{ mas/yr}$ ,  $[\text{Fe}/\text{H}] > -1.5$  and  $v_{\phi} > 40 \text{ km/s}$  for the further analysis.

### 8.2.2 Vertical distribution of RAVE and SEGUE stars

Even though the distance range of the two chosen comparison samples is nearly identical ranging from a bit above zero to roughly 3 kpc the actual distance distributions are different as seen in Figure 8.3. These differences are also reflected in the vertical height distributions above the plane being displayed in Figure 8.7. The dashed vertical lines define bins of different height ranges of which the three middle ones (from 0.2 kpc to 1.5 kpc) correspond to the bins used in Figure 8.4 (right plot, first three panels from the top). The distributions in  $z$  reveal that the stellar statistic is similar at intermediate heights between 0.5 kpc and 1.0 kpc. This suggests the following: the results obtained from the comparison of both datasets at intermediate height above the plane should be similar and most robust while the obvious statistical differences at low and high  $z$  are likely to cause variations in the investigated chemo-dynamical relations. Due to this apparent statistical imbalance it is imperative to not only examine the total distributions but to split the

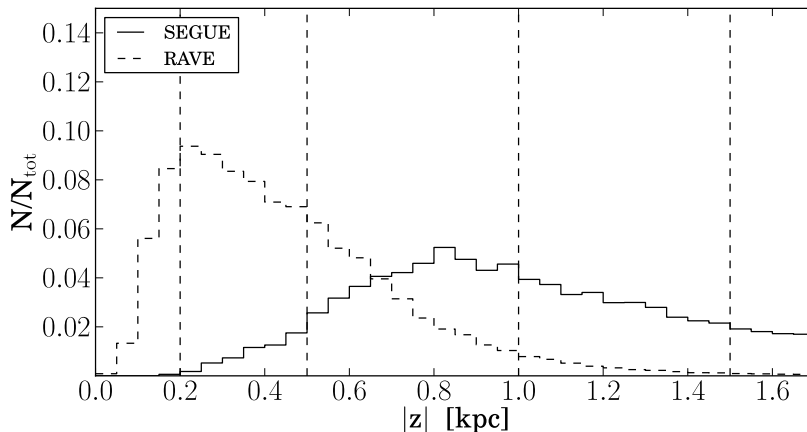


**Figure 8.7:**  $z$ -distribution for the RAVE giants (dashed) and the SEGUE G-dwarfs (solid).

samples in separate bins of vertical height or radial distance as is done throughout the presented chemo-dynamical analysis. Indeed, when linking Figure 8.7 to the results found in Figure 8.4 the domination of RAVE at low  $z$  translates into a more metal-rich MDF (red curve) than seen for SEGUE (filled histogram). Also, the undersampling of RAVE stars at high  $z$  missing mostly the metal-rich giants leads to a RAVE MDF that is apparently too metal-poor. Only at intermediate heights where the spacial sampling is comparable both surveys deliver similar results.

### 8.2.3 Orbital families in the $e$ - $z_{\max}$ -plane

Continuing the comparison the following section concentrates on the orbital properties of both, the SEGUE G-dwarfs and the RAVE giants. As in Chapter 6 the RAVE and SEGUE samples are investigated by grouping their stars into families of similar orbits using the  $e$ - $z_{\max}$ -plane. Whereas the eccentricity describes the shape of the stellar orbit,  $z_{\max}$  is a measure of the stars' oscillation perpendicular to the Galactic plane. Figure 6.15 illustrates the division of the orbital parameter space into nine subgroups of stars, labelled from (a) to (i). By moving rightwards along the grid the eccentricity increases, when moving upwards the maximum height above the plane along the orbit grows. Along with  $z_{\max}$  the stars' vertical velocity  $v_z$  increases as well. With the main interest being the chemo-dynamics of the Galactic disk the selection is intentionally restricted to stars with  $e < 0.6$  and  $z_{\max} < 3$  kpc.

By linking quantities like chemistry, actual position or velocity to the stars' orbital parameters Figures 8.8, 8.9, 8.10 and 8.11 try to explore the complexity of the multidimensional chemo-dynamical space the RAVE and SEGUE stars reside in. For each of the nine orbital subgroups the plots show the stars' distributions in  $[\text{Fe}/\text{H}]$ ,  $[\alpha/\text{Fe}]$ ,  $R_m$ , and  $v_\phi$  (filled blue histogram: SEGUE, open black histogram: RAVE). In order to guarantee a reasonable comparison for both samples the results are based on distance estimates and orbital characteristics that are consistently obtained with the BPG distance code and the python module GALPY (see Chapter 4).

### Comparing differences and similarities between RAVE and SEGUE

As discussed before the number of RAVE and SEGUE stars differs substantially as a function of height. With its maximum at low latitudes the number of RAVE giants decreases gradually with  $z_{\max}$ , while SEGUE lacks G-dwarfs close to the plane but concentrates in the range

$1 \text{ kpc} < z_{\text{max}} < 2 \text{ kpc}$  (see individual number counts indicated in subpanels (a) to (i)). Especially, panel (c) contains only few SEGUE stars revealing a particularly spiky MDF and  $v_\phi$  distribution in Figures 8.8 and 8.11 that are a result of the applied bias corrections. Any conclusions on those subgroups with few stars needs hence to be treated with caution. Still, based on these simple statistical evaluation the combination of both datasets seems once more to be a good idea. At intermediate heights both surveys have comparable statistics while RAVE complements SEGUE at low and SEGUE complements RAVE at high heights, thereby allowing a very global insight to the chemo-dynamics of the Galaxy.

With respect to the expected chemical trends within the Galactic disk both stellar samples show a similar behaviour. For all but the SEGUE stars with  $e > 0.4$  (see further explanation below) the  $[\text{Fe}/\text{H}]$  ( $[\alpha/\text{Fe}]$ ) distributions shift to lower (higher) abundance values with increasing  $z_{\text{max}}$ . Also the MDFs get broader with increasing eccentricity at each of the shown levels in  $z_{\text{max}}$ . For example, from panel (a) to (g) the peak in  $[\text{Fe}/\text{H}]$  moves from approximately  $-0.35$  dex to  $-0.5$  dex and  $-0.25$  dex to  $-0.4$  dex for SEGUE and RAVE, respectively. At the same time, the corresponding  $[\alpha/\text{Fe}]$  distributions show an average increase of roughly 0.1 dex. These findings suggest a transition from thin- to thick-disk like stars in both stellar samples with increasing distance from the mid-plane ending up with samples of local thick disk stars in panel (g). As already mentioned by Boeche et al. (2013a) and proposed by Feltzing & Bensby (2008) the presence of kinematically heated old thin disk stars with thick disk like chemistry cannot be ruled out. After having experienced any kind of perturbation these stars may strongly oscillate through the Galaxy showing high  $z_{\text{max}}$  but low eccentricities. Responsible for this effect could be any of the internal heating mechanisms (e.g. proposed by Villalobos & Helmi 2008; Bournaud et al. 2009; Minchev et al. 2012) that are thought to play a role in thickening the actual old thin disk, hence contributing with stars to the upper panels.

Overall, at all heights RAVE shows a tendency to be more metal-rich than SEGUE. This results in discrepancies and offsets between their MDFs which are likely related to the surveys' different spatial sampling of stars. In fact, a closer look to the group of very local stars ( $e < 0.2$ ,  $z_{\text{max}} < 1 \text{ kpc}$ ) in panel (a) reveals that the distribution in current vertical height peaks around  $z = 0.6 \text{ kpc}$  for the SEGUE dwarfs but at about  $z = 0.25 \text{ kpc}$  for the RAVE giants. The latter hence cover regions of much higher mean metallicity than the SEGUE stars. This illustrates plausibly that the spatial distribution directly translates to the subsamples' individual chemical properties. Both surveys catch slightly different portions of the local thin-disk population whose mean metallicities are offset to each other and tend to be both lower than the actual metallicity peak of the very local and close thin disk stars that is, from Hipparcos or GCS stars, found to be around  $-0.05$  dex (Casagrande et al. 2011; Fuhrmann 2008; Haywood 2001). The height dependency of the metallicity is consistent with the predictions by the chemo-dynamical MCM model of Minchev et al. (2013) (see also Figure 5.20) and findings by Schlesinger et al. (2012).

Along with the gradual abundance trends changes are as well observed in the  $v_\phi$  and  $R_m$  distributions. Most obvious, the mixture of stars with different mean radii contributing to the distributions in each subpanel is essentially influenced by the amount of inner ( $R_m < 7 \text{ kpc}$ ) or outer ( $R_m > 9 \text{ kpc}$ ) disk stars. These are only moderately represented in the local panels (a) to (g) but progressively present as  $e$  and  $z_{\text{max}}$  increases. From left to right the orbital families' peak in  $R_m$  shifts from close to the Sun's position at 8 kpc to 6 kpc for the high eccentricity stars and that independent of height. At the same time, the central peak in rotational velocity moves from  $220 \text{ km/s}$  to values below  $150 \text{ km/s}$ . Overall the  $R_m$  and  $v_\phi$  distributions get equally more asymmetric and develop stronger tails for both surveys. Only for the stars with low eccentricity SEGUE deviates in the sense that when moving from (a) to (g) SEGUE catches successively more stars with local properties that still originate from the outer disk.

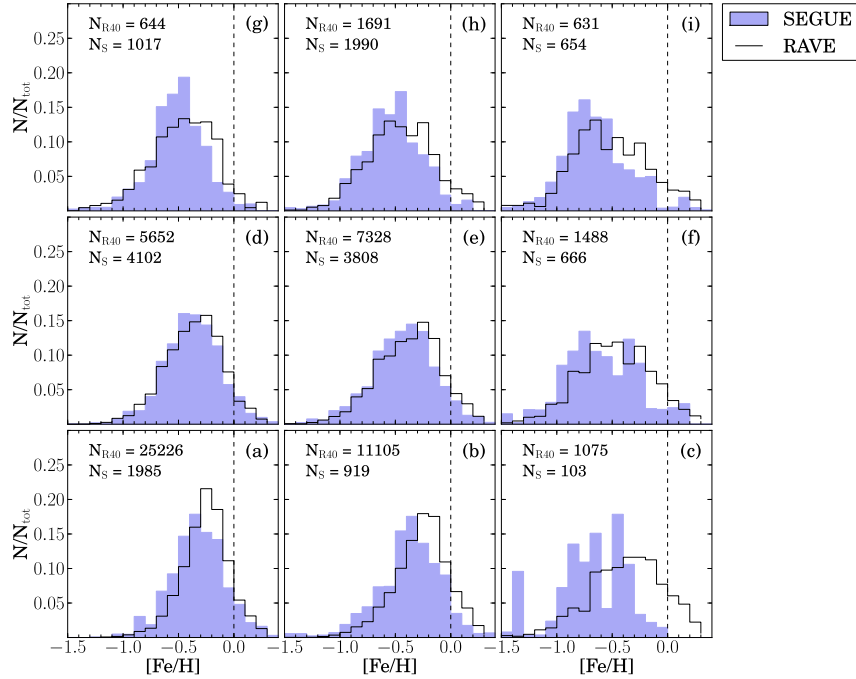


**Figure 8.8:** MDFs for sub-populations of RAVE giants and SEGUE G-dwarfs in the eccentricity- $z_{\max}$ -space. The SEGUE sample is corrected for the survey selection function and the metallicity bias introduced by the colour-cut that selects G-type stars. Number counts for both samples are indicated in each sub-panel.

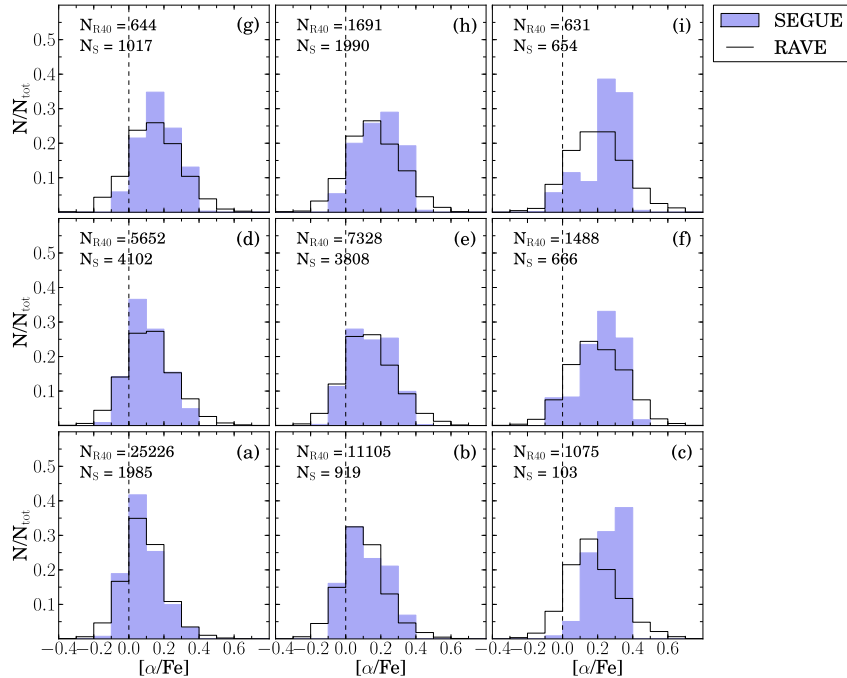


**Figure 8.9:** Distribution of  $\alpha$ -enhancement for the same samples as in Figure 8.8. The SEGUE  $[\alpha/\text{Fe}]$ -value is primarily based on magnesium (Mg) while the RAVE enhancement is a combination of magnesium (Mg) and silicon (Si). Note, that as discussed in previous Chapters, the scale of the SEGUE  $[\alpha/\text{Fe}]$ -values are adjusted leading to a better agreement with RAVE.

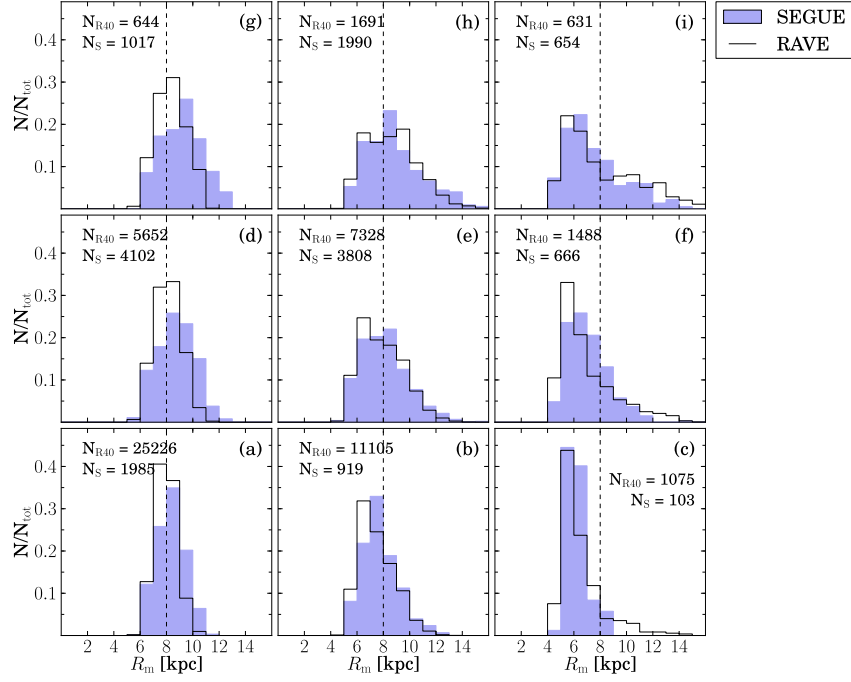


Figure 8.10: Distributions in mean radius for the same samples as in previous Figures.

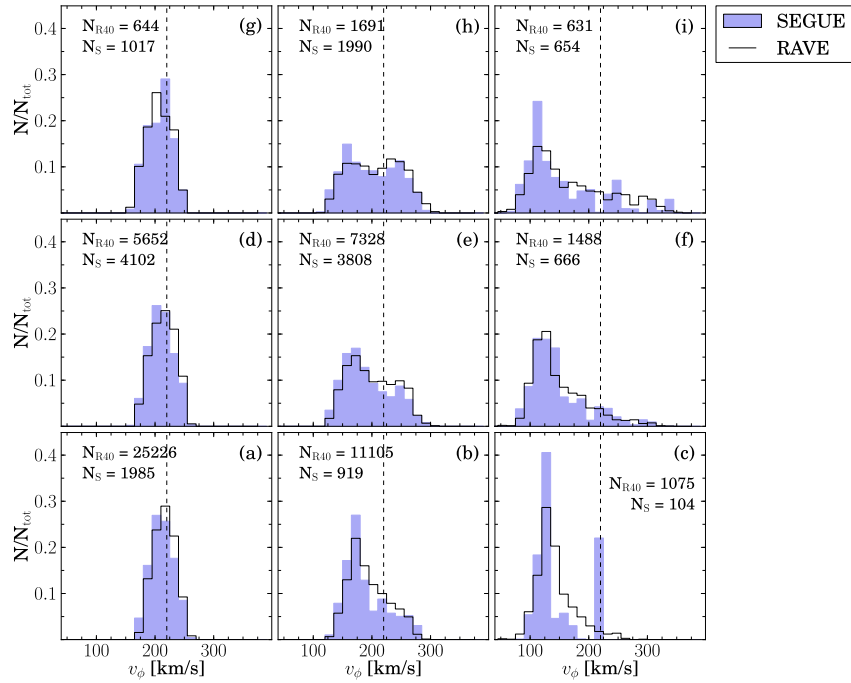


Figure 8.11: Rotational velocity distributions of sub-populations in orbital space displayed for the RAVE giant and SEGUE dwarf sample.

This creates a clear offset to the RAVE distributions which peak at the same position at all heights, just broadening slightly. A contrary behaviour is seen for  $v_\phi$ . Here the RAVE peaks shift from  $220 \text{ km/s}$  to  $200 \text{ km/s}$  (panel (g)) which is in agreement with the chemical gradient. For SEGUE however, the  $v_\phi$  peak stays at the same position, a bit below  $220 \text{ km/s}$  because the SEGUE local thin disk stars do not reach far below  $300 \text{ pc}$  where the rotational velocity is close to solar.

For sure, the cone shaped structure of the survey volumes is, to a large degree, responsible for this specific distribution of stars in the orbital parameter space. This is why the sub-groups of stars with  $e > 0.4$  are particularly interesting. For example, in panel (c) the stellar sub-population is almost exclusively dominated by inner disk stars (with  $R_m = 6 \text{ kpc}$  and  $R_{\text{peri}} = 3 \text{ kpc}$ ). These stars are very frequent and the only stars with low  $z_{\text{max}}$  and high eccentricity that can reach the solar volume as it is observed by the two surveys. As a consequence to the domination by the inner disk the  $v_\phi$  distribution peaks at about  $125 \text{ km/s}$  with a tail towards  $200 \text{ km/s}$ , being more pronounced for the RAVE sample than for the rather confined SEGUE distribution. Knowing about the inner disk influence for star with high  $e$  values (panels (c) to (i)) one would expect the MDFs to be dominated by more metal rich stars. Likely, the metal-poor MDFs for the SEGUE stars can be attributed to the survey's severe selection bias against metal-rich stars in the inner Galaxy (see discussion on this issue in previous Chapters). The same effect is not present for RAVE which indeed catches inner disk stars with high  $[\text{Fe}/\text{H}]$ . Unfortunately, the observed selection effect can only be compensated with a correction for the survey volume as illustrated for the SEGUE sample in Chapter 5. Hence, the RAVE sample would have to undergo the same correction procedure. And this is beyond the scope of this thesis. However, among those high eccentricity panels special interest should be given to the fact that the RAVE distributions reveal a crucial number of supersolar metallicity stars. Especially in panel (c) which is filled with RAVE stars around a  $R_m$  of  $6 \text{ kpc}$  their number is significant. A first indication that RAVE is more metal rich reaching way beyond solar in the inner Galaxy region ( $6 \text{ kpc} < R < 7 \text{ kpc}$ ) could be seen in Figure 8.4. That the RAVE stellar catalogue seems to be rich in supersolar metallicity stars has been recently confirmed by Kordopatis et al. (2015a) claiming that the local MDF declines remarkably slowly up to  $+0.4 \text{ dex}$ . A result that did not show up in the RAVE DR4 metallicity distribution function but appears more clearly now after the application of a new metallicity calibration relation.

The selection bias against metal rich SEGUE stars also partially explains the discrepancies in  $[\alpha/\text{Fe}]$ . With the modification of the SEGUE  $\alpha$ -scale (shift of  $-0.1 \text{ dex}$ , see Chapter 3) the  $[\alpha/\text{Fe}]$  distributions of both surveys are generally comparable. Yet, the high eccentric sub-groups (panels (c) to (i)) show significant deviations. A reason why the agreement between the two stellar samples in those panels gets better with increasing height could be the following: as the observing cones open with height more stars from different radii are caught which seemingly washes out the difference caused by the selection effects in the SEGUE sample. Besides the selection bias issue an important aspect that certainly causes part of the observed differences is the slightly different volume coverage that cannot be compensated by the shift in the SEGUE  $\alpha$ -scale.

Nevertheless, considering all biases and known difference of the comparing samples Figures 8.8 through 8.11 indicate a remarkable good match between the two surveys. This demonstrates that the underlying chemo-dynamical structure of the Milky Way is similarly captured by both surveys no matter of selection biases, stellar type or differences in reduction pipelines.

### 8.2.4 Velocity dispersions as a function of metallicity and $\alpha$ -enhancement

Extending the chemo-kinematic analysis Figures 8.12 through 8.15 shed light on the velocity dispersion in  $UVW$  as a function of chemistry. Again, due to the different stellar density with vertical height the correlations are plotted in bins of current  $z$  (bin size similar to Figure 8.4, right panels). For clarity, the resulting correlations are shown separately for each survey (binning the sample in dots of 100 stars with an error calculated by resampling 100 times with replacement). For comparison the correlation's shape of the particular counterpart sample is overlaid indicated with a coloured line (red). The course of the correlations is determined by applying a Gauss filter to the binned data points and does not represent a fit to the data.

The plots clearly indicate that the middle bin is the one where both samples have a sufficient number statistic (see also Figure 8.7) delivering the most robust results. Whereas for RAVE the number of stars drops very rapid above 1 kpc, the statistic is even more problematic for SEGUE below 0.5 kpc. There the 7 dots of binned data points provide only a hint on the chemo-kinematic relations but prevent to obtain a completely reliable result.

Focussing on the intermediate range  $0.5 \text{ kpc} < z < 1.0 \text{ kpc}$  both stellar samples provide a very similar shape in the dispersion of each velocity component as a function of  $[\text{Fe}/\text{H}]$  (Figures 8.12 and 8.13) and  $[\alpha/\text{Fe}]$  (Figures 8.14 and 8.13). However, the radial component shows the best match while there are small offsets in  $V$  and  $W$  because the RAVE giants feature overall hotter distributions. More specifically, in case of  $[\text{Fe}/\text{H}]$  both samples indicate a flat behaviour (plateau) with an average dispersions in  $U, V, W$  of around  $[50, 40, 30] \text{ km/s}$  up to a  $[\text{Fe}/\text{H}]$  value of about  $-0.5 \text{ dex}$ , followed by a visible and expected incline in velocity dispersion for the hotter and presumably older low metallicity stars.

The same is observed for the dispersions as function of  $\alpha$ -enhancement. Up to  $0.2 \text{ dex}$  in  $[\alpha/\text{Fe}]$  the dispersion stays rather constant for the thin-disk like stars and rises continuously for the  $\alpha$ -rich population. Even if for SEGUE the outlying data points at the edges of the correlations are not taken into consideration, the increase in dispersion is noticeable stronger and more distinct for the thick-disk like SEGUE stars (see  $U$  and  $V$  panels) which only cover up to  $[\alpha/\text{Fe}] = 0.4 \text{ dex}$ . RAVE on the contrary shows a less prominent gradient and populates the region between  $0.4 \text{ dex}$  and  $0.6 \text{ dex}$  where the giants' correlation tends to flatten out again. It remains to be answered why these RAVE stars behave in such a way but it is evident, that there is a true discrepancy between the two samples. Clearly, as a function of  $[\alpha/\text{Fe}]$  the RAVE giants do not match the velocity structure laid out by the SEGUE thin and thick-disk stars. This finding also applies to the bin with stars closer to the plane ( $0.2 \text{ kpc} < z < 0.5 \text{ kpc}$ ).

The picture gets worse for the highest bin in  $z$  at heights of about  $1.0 \text{ kpc} < z < 1.5 \text{ kpc}$  where RAVE hardly shows any change in the dispersion as a function of  $[\alpha/\text{Fe}]$ . Instead the giants exhibit flat relations that are much noisier than the SEGUE counterpart. Considering that the number statistic in this bin is not that different for both samples, one reason for the fewer scatter in SEGUE may be the compression of the DR9  $\alpha$ -scale. Still, the compression can not explain the clear difference in the correlations' shape. While at this heights the SEGUE sample still includes stars with thin disk kinematics (velocity dispersion around  $20 \text{ km/s}$  to  $30 \text{ km/s}$ ), the corresponding high metallicity stars in the RAVE sample show already much higher velocity dispersion. This could be an indication for an issue with the samples' distance scales which directly connects to the stellar density distribution at different  $z$ , determining at what distance above the plane stars with certain chemistry appear. The finding suggests that RAVE is already almost exclusively sampling parts of the thick disk, while SEGUE still samples part of the thin disk. Assuming that the flat behaviour is not related to a problem with the RAVE  $[\alpha/\text{Fe}]$  values at those heights, it is worth testing how the SEGUE sample behaves beyond  $1.5 \text{ kpc}$ .

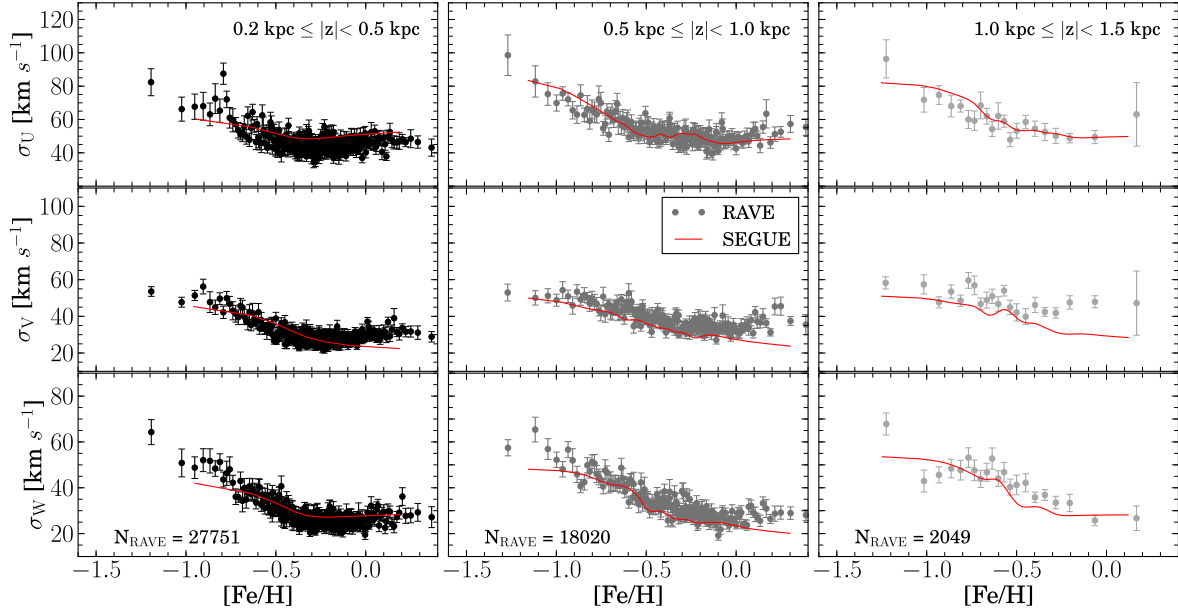


**Figure 8.12:**  $U, V, W$  velocity dispersion for the RAVE giants as a function of  $[\text{Fe}/\text{H}]$  and vertical height above the Galactic plane (see left, middle and right column). Each dot contains 100 stars, the error bar is calculated by resampling these 100 stars with replacement. For comparison the corresponding SEGUE correlations are indicated by the red curves.

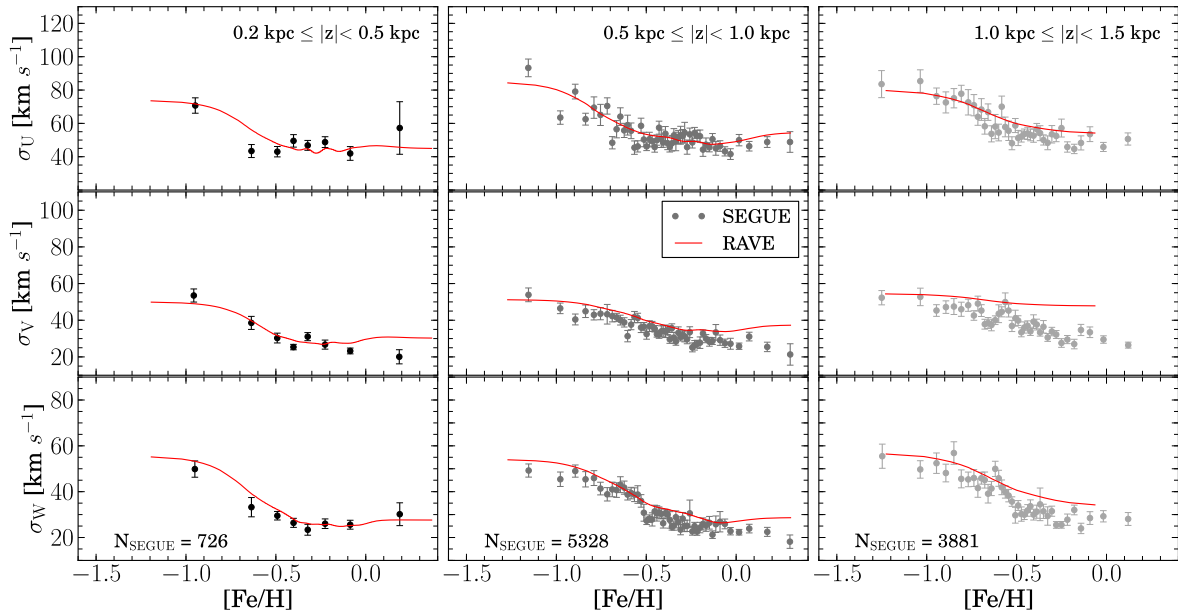


**Figure 8.13:** Same as in Figure 8.12 but for the SEGUE G-dwarfs.

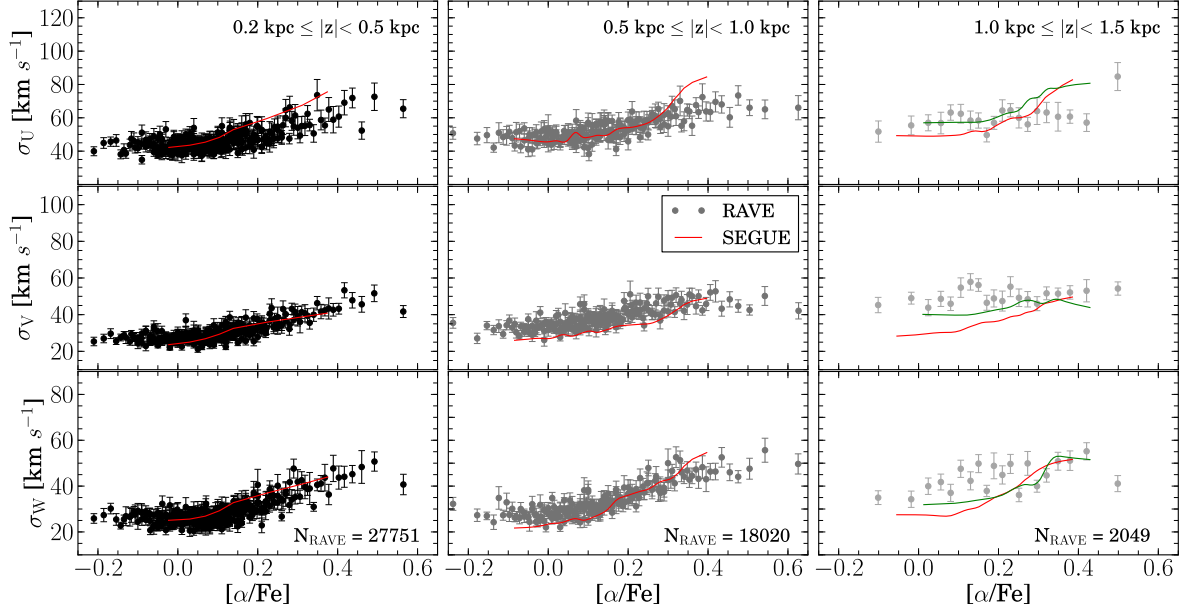


**Figure 8.14:** U, V, W velocity dispersions for the RAVE giants as a function of  $[\alpha/\text{Fe}]$ . Again, the dispersions are shown for three different bins in vertical height. Each dot contains 100 stars, the error bar is calculated by resampling these 100 stars with replacement. The shape of the corresponding SEGUE correlations is indicated with the red curves. For comparison, the additional green curve represents the SEGUE correlation for stars in the range  $1.5 \text{ kpc} < z < 3.0 \text{ kpc}$ .

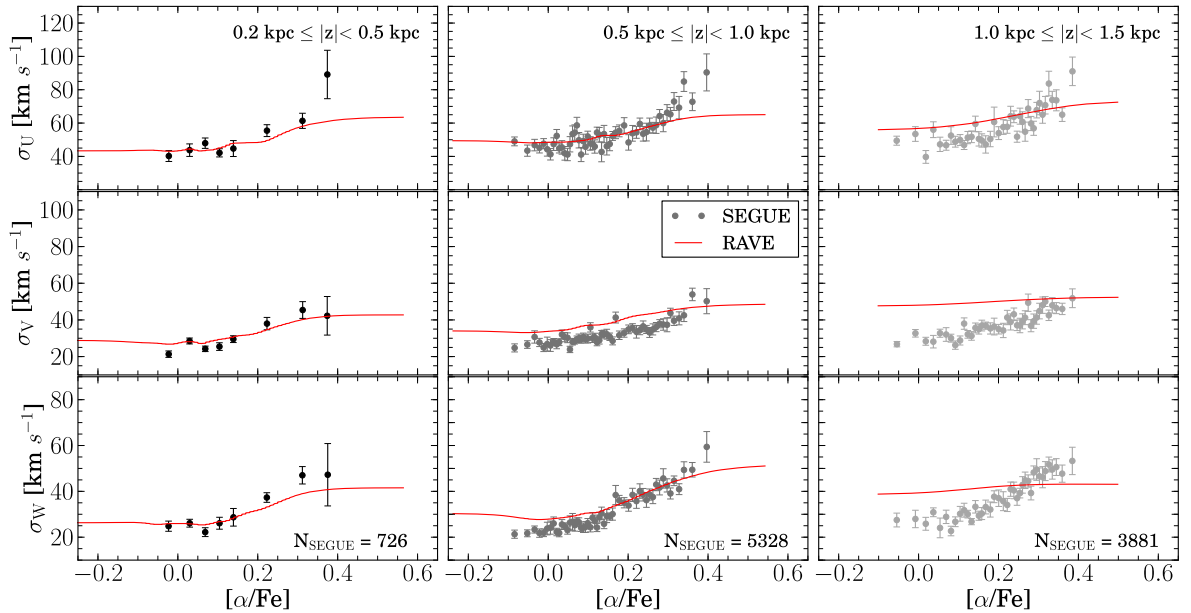


**Figure 8.15:** Same as in Figure 8.14 but for the SEGUE G-dwarfs.

The result is overlaid as the green line in the high  $z$  panels of Figure 8.14. Evidently, for SEGUE stars in the range  $1.5 \text{ kpc} < z < 3.0 \text{ kpc}$  the contribution of stars with thin disk velocity dispersion decreases. As a result the metal-rich part of the SEGUE correlation converges towards the level of the RAVE stars. In the  $V$  component the green line even gets almost that flat as the RAVE data points. In conclusion, even though the RAVE and SEGUE sample cover roughly the same volume, the difference in their spatial sampling seems to cause an offset in the velocity relations as a function of height.

Also the RAVE correlations in Figure 8.14 get progressively flatter with increasing height. A finding that is in agreement with Figure 8.16 which depicts  $v_\phi$  as a function of  $[\alpha/\text{Fe}]$  and  $[\text{Fe}/\text{H}]$  (SEGUE on the left, RAVE on the right hand side) for all stars that populate the intermediate bin in vertical height in the range  $0.5 \text{ kpc} < z < 1.0 \text{ kpc}$ . The plot is restricted in height because at intermediate  $z$  both surveys show a similar number statistics which makes the comparison more reliable. RAVE does catch metal-poor stars with thick disk like rotational velocities (steep slope in the range  $-1.5 \text{ dex}$  to  $-0.6 \text{ dex}$  that reach a mean velocity of  $140 \text{ km/s}$ ) lagging the bulk of thin disk stars that typically build a plateau around  $220 \text{ km/s}$ . Yet, this fact is less obvious from the correlation with  $[\alpha/\text{Fe}]$  (top right panel). The  $\alpha$ -poor stars close to the plane still resemble the properties of the thin disk ( $220 \text{ km/s}$ ) but the decrease in velocity for the  $\alpha$ -rich stars is only moderate down to a mean  $v_\phi$  of  $180 \text{ km/s}$ . It appears that the distinct separation between thin (plateau) and thick (steep slope) disk stars as seen for SEGUE (top left panel) seems to be washed out for the giant stars. This is because the RAVE sample exhibits only a single density peak between solar and  $0.2 \text{ dex}$  in  $\alpha$ -abundance. As a result each bin in  $[\alpha/\text{Fe}]$  contains a mix of stars with a large range in  $v_\phi$  smoothing the distribution. As both surveys are shown without any selection effect correction the picture is different for the SEGUE correlations. Due to the bi-modal distribution of SEGUE stars in the chemical-abundance plane (mainly an effect of the uneven sampling of the stellar populations, see Figure 5.9) the SEGUE velocity distributions are shaped by the influence of the large fraction of metal-poor,  $\alpha$ -rich stars which, in case of the G-dwarf sample, is the only population of stars with lower  $v_\phi$  values. One could now argue that the presently missing correction for selection effects in the SEGUE sample would flatten out the  $v_\phi$ - $[\alpha/\text{Fe}]$ -relation but the analysis in Chapter 5 proves otherwise. Even with the complete set of corrections the relation does not get as flat as for RAVE.

Besides, the shape of the  $v_\phi$ - $[\text{Fe}/\text{H}]$ -relations is not that different for the RAVE and SEGUE sample. Both indicate a slight negative slope for the metal-rich and a similar positive slope for the metal-poor stars. Special to the thin disk part of the relation (above  $-0.5 \text{ dex}$ ) is the influence of more metal-poor stars from the outer disk with larger rotational velocities than typical for the solar neighbourhood causing the rise in mean velocity around  $-0.5 \text{ dex}$  which appears to be stronger for RAVE. Yet, one has to keep in mind that the SEGUE correlations is biased which explains why the entire distribution of data points is pulled down with respect to the RAVE sample.

### 8.2.5 Discussion

The direct comparison of Galactic properties as shown by stellar samples from different spectroscopic surveys can sometimes prove to be very difficult. Not only the resolution and hence the quality of the data products (stellar parameters, distances or velocities) may vary. Also, if the comparing surveys do not have any stars in common, possible issues due to deviations in the parameter scales are difficult to handle. One solution for this problem is the creation of synthetic copies resembling the observed data samples based on the same model. Those copies could then be compared instead. This however requires the models to be as realistic as possible.

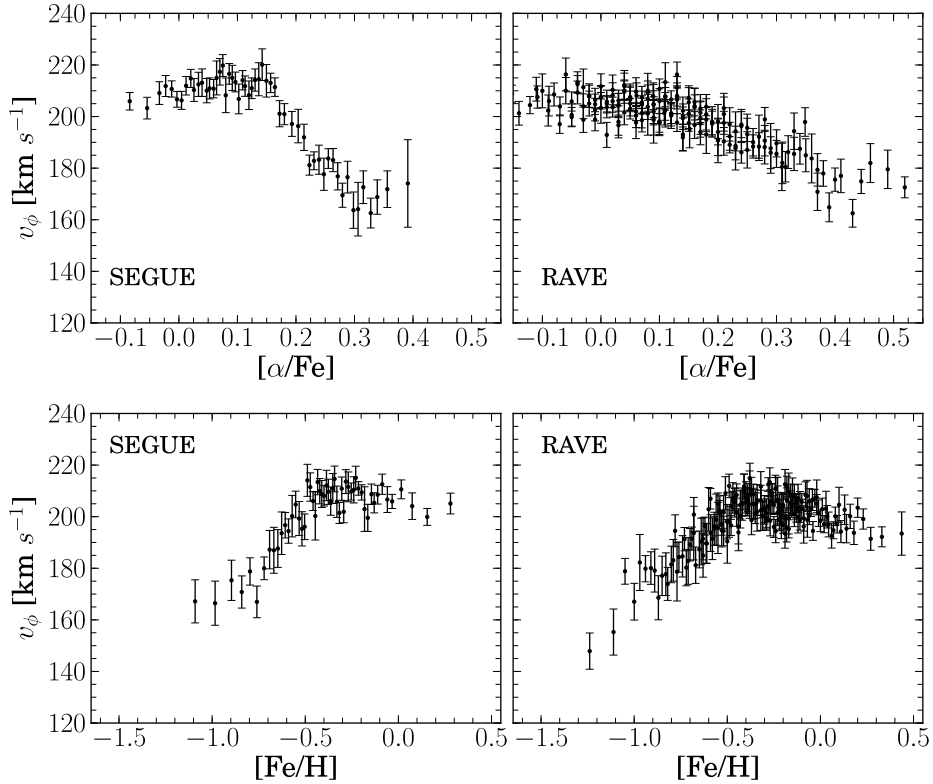


**Figure 8.16:** Rotational velocity as function of  $[\alpha/\text{Fe}]$  (*top*) and  $[\text{Fe}/\text{H}]$  (*bottom*) for the SEGUE stars on the left and the RAVE sample on the right. Here, the SEGUE sample is not corrected for any selection effects.

The creation of a RAVE mock catalogue as presented in Piffl (2014) and the efforts taken in the current work constraining different kinds of Milky Way models are first steps into that direction.

Still the comparison of RAVE and SEGUE proves that it is possible to unravel consistencies about the chemo-dynamical structure within the Galaxy even if the compared stellar samples differ in terms of stellar type and are based on independent parameter pipelines. Of course, deviations due to survey specific issues and differences in parameter scales are not avoidable. But aside from this the presented investigation of chemo-dynamical properties and relations as revealed by the SEGUE G-dwarf and RAVE giant stars demonstrates the following: all general trends are comparably existent in both selected stellar samples, summing up to a consistent picture of the stellar disk above and below the Galactic plane. Certainly important for obtaining this remarkable result is the availability of consistent distances that could be drawn from the same computation routine for both surveys.

The observed differences in the results are expected due to the survey specific sampling of objects that catches slightly different portions of the stellar disk population. Also the survey volumes are concentrated towards opposite directions (inner and outer Galaxy). Some of the differences could be reduced if both samples would be really brought to a similar bias free status. The comparison however shows in depth that this is a rather challenging task. It is hence necessary to interpret all finding in the light of the complicating selection effects and a priori differences of the compared stellar samples. Nevertheless, the two observational dataset show more similarities to each other than the MCM G-dwarfs model mock sample and the observed SEGUE G-dwarfs whose comparison has been discussed in Chapter 7. Sampling marginally

different ranges in  $z$  and  $R$  allows RAVE and SEGUE to really complement each other. Regions where both samples overlap could be especially used to check if the surveys deliver the same answers. Areas where only one of the samples is reliably present can be used to complement the overall view on the stellar structure.

## Summary

As in each of the previous Chapters the present one closes with a summary of the most important results:

- The presented sample of high-quality RAVE giants with  $\text{SNR} > 60$  represents a good example to illustrate how the user can introduce additional selection biases through selective parameter cuts when defining a stellar sample. In case of RAVE there are at least three cuts known that cause a metallicity bias, i.e. a situation where metal-rich stars are underrepresented: (1) the `Algo_Conv = 0` quality criterion of the stellar parameter pipeline causes a cut in temperature that leads to a very strong metallicity bias among stars with  $0.5 \leq \log g < 1.7$ , (2) also a high SNR cut at 60 or above removes metal-rich stars and (3) choosing a conservative limit in the  $\chi^2$  parameter of the chemical pipeline (the  $\chi^2$  determines the match between the observed and the synthetic spectrum) artificially excludes primarily metal-rich stars. Each of these cuts influence the entire composition of the stellar sample. Hence, the take away message of this is that it is inevitable and important to find the right balance when cutting a sample. Sometimes this is however not trivial. If the SNR limit is too low the parameters may not be trustworthy enough but if the limits are too restrictive even a putative high quality sample appears in bad light. Of course, one solution to avoid the metallicity bias for RAVE giants with very low  $\log g$  is to exclude every star below  $\log g = 1.7$  but this would also have a negative affect on the comparison to SEGUE because it eliminates all luminous stars at larger vertical heights and towards the inner Galaxy.
- The distance distributions in Figure 8.3 indicate that both samples cover roughly the same volume but the RAVE giant sample concentrates around 1 kpc while there are only few SEGUE G-dwarfs below that limit. This difference propagates to each of the investigated chemo-dynamical correlations. The RAVE sample does include mainly thin disk stars that are much closer to the plane than the SEGUE sample reaches down in  $z$ . Consequently, the metallicity distribution function is more metal-rich (Figure 8.4 and Figure 8.8) and the mean rotational velocity of the thin disk like stars is closer to the solar value than for SEGUE. Actually, the samples statistics are such that RAVE dominates the lower heights while SEGUE outnumbers RAVE at larger distances from the plane. This leaves the intermediate heights between  $0.5 \text{ kpc} < z < 1.0 \text{ kpc}$  as the ideal region where both surveys have similar statistics and hence show the most conformity and robust results.
- Without the calibration of the SEGUE  $\alpha$ -abundance scale most of the orbital families in Figure 8.9 show an offset of approximately 0.1 dex when comparing the  $[\alpha/\text{Fe}]$  distributions of the RAVE and the SEGUE stars. This discrepancy exactly equals the shift applied to the SEGUE DR9  $\alpha$ -abundances which hence brings RAVE and SEGUE into agreement (as shown in this chapter) and underlines the assumption that the DR9 scale is indeed pretending too high values.
- As expected the RAVE sample shows metallicity distribution functions that are more metal-rich than their SEGUE counterparts. When dividing both samples into subsets of orbital

families of stars they show agreement in metallicity, rotational velocities and mean orbital radii for each of the stellar subgroups. Only for those stellar families with high eccentric orbits the deviations are not negligible (see panels (c) to (i) in Figures 8.8 to 8.11) partly due to the very low number statistics of the SEGUE sample. Finally, Figures 8.12 to 8.16 showing the velocity dispersions at different height above the plane illustrate very well the complementarity of both surveys. At low and higher  $z$  the comparison is hindered by the different statistics. But again at intermediate heights for both surveys the dispersion trend in each velocity component is almost identical (see discussion in Section 8.2.4).

- The main message of this chapter however is the following: the RAVE giant and the SEGUE G-dwarf sample do provide similar answers and insights into the chemo-dynamics of the Galactic disk. And that even though the samples are based on different surveys with parameters from independent pipelines that each suffer from individual issues causing problems in the parameter determination. The direct comparison shows that both samples and hence the surveys complement each other well allowing to explore a significant volume of the disk. Only the selection biases really pose a problem, because they tamper with the correlations and distributions and complicate the comparison between RAVE and SEGUE even if the SEGUE sample is corrected for the most important ones. Also, the applied corrections often introduce a lot of scatter which significantly affects the interpretation of the results. Nevertheless, in those regions where both samples have a good stellar statistic and are not too much influenced by volume geometry effects the agreement between the two surveys is apparent.



---

## Summary and Conclusion

---

This thesis has focused on the chemo-kinematics of the Milky Way disk, exploring and extending the current state of knowledge from an observational as well as theoretical point of view. Thus, the present work does not only compare new observational constraints on the formation of the Milky Way extracted from the two larger pioneer spectroscopic surveys SEGUE and RAVE. It also provides a proper comparison with models (both chemo-dynamic and stellar population synthesis models), thereby connecting the two most important research fields of Galactic science: the Galactic stellar surveys and the modelling of galaxy formation and evolution. Moreover, the presented thesis represents the first study that spotlights the SEGUE dataset in connection with models and simulations of disk galaxy formation.

When aiming to combine and compare observations with theoretical model predictions there are basically two ways for this to be realised:

1. The observational datasets under study are freed from the existing selection effects by subsequent corrections before analysing their properties. In doing so, any obtained results thereof can then directly be compared to model predictions assuming that the observations now mirror an unbiased picture of the Galaxy.
2. The observational selection biases are kept present in the observed datasets while the same are introduced to the model of interest. This again enables a comparison. In this context, the transformation of physical models to the space of observables has presented itself as an effective and fruitful method. The approach allows to compare the properties of basically any model to those revealed by observed datasets, and that in a comparably intuitive and computationally cheap way.

In the attempt to exploit and study the advantages and shortcomings of both stated approaches the previous chapters have taken the reader on a unique journey, that sheds light on the chemo-kinematic structure of the Galactic disk from various perspectives. Thereby the different but complementing methods mentioned above are efficiently combined. In this final chapter the different view points are recapitulated, the main results of the thesis are summarised and future prospects are given.

## 9.1 A stellar sample of SEGUE G-dwarfs

As the main observational testing ground for this thesis serves a compilation of SEGUE G-dwarf stars (selection presented in Chapter 3) that have been assembled from the ninth SDSS Data Release (DR9). Originally, as part of SDSS-II and SDSS-III SEGUE’s full set of observations (including stellar spectra and additional information on photometry, proper motions, stellar parameters, etc.) has already been published in the previous data releases DR7 and DR8. But DR9 is the last SDSS release for which SEGUE’s data products were finally updated. In an extensive revision process the SEGUE Stellar Parameter Pipeline (SSPP) was improved and validated with external high resolution datasets in the time between DR8 and DR9. This revision revealed that in particular the surface gravity (for dwarf stars) and the  $\alpha$ -abundance estimates are systematically deviating from those published earlier than DR9. A fact that shows how essential it is to comprehensively evaluate and document changes, capabilities and limits of the data products at hand, in times of every growing stellar surveys and automatic reduction pipelines.

This is also why as part of the present work careful quality checks and parameter testings have been performed by comparing the DR9 SSPP parameters to those from DR8 for the selected sample of SEGUE stars. And indeed, the comparison to DR8 reveals that for DR9 the SEGUE G-dwarfs exhibit a systematic decrease in  $\log g$  by roughly 0.25 dex with increasing  $[\text{Fe}/\text{H}]$ . A similar discrepancy in  $\log g$  has been recognised by Schlesinger et al. (2014). There is also a general increase in  $[\alpha/\text{Fe}]$  of about 0.1 dex that is accompanied by a compression of the  $[\alpha/\text{Fe}]$  scale. So far, the majority of studies on SEGUE G-dwarfs held on to parameters from earlier data releases, no matter of the DR9 parameters being already available. As such this thesis is one of the few works that investigate the potential of the DR9 dataset.

In that sense the DR9 surface gravity has been carefully used as one of the essential ingredients to determine distances for this work’s compilation of SEGUE stars, rather than using  $\log g$  only to discriminate between dwarfs and giants. As such the presented results are a novelty because, for the first time, reliable spectro-photometric distances have been determined to SEGUE stars based on a Bayesian method. Before, studies on SEGUE G-dwarfs always relied on photometric distances. The Bayesian framework and a number of validity check-ups (testing distances to objects in spectroscopic samples from various surveys and at different resolution) that have been developed in collaboration with the Brazilian Participation Group and further people from the AIP (F. Anders, C. Chiappini) are presented in Santiago et al. (2016) and discussed in this work’s Chapter 4. In this connection it could be shown that based on the DR9 surface gravities distances to SEGUE cluster stars happened to be always overestimated. This finding and the obvious disagreements with predictions from the population synthesis code TRILEGAL (see parameter offsets between the observed and the synthesised mock G-dwarf sample as highlighted in Chapter 6) affirm that an empirical calibration of the DR9  $\log g$  values had been necessary in order to build up this work’s chemo-kinematic analysis. Yet, negative effects due to uncertainties that may have been introduced that way are assumed to be small in consideration of the fact that all presented comparisons, to models or the observational reference sample of RAVE stars, indicate an overall good agreement with respect to parameter distributions and chemo-kinematic relations. Despite these promising results the entire thesis demonstrates that today’s business with automatic parameter pipelines, that are meant to be dedicated to as much different stellar objects as possible, is a tough one. Without a responsible handling by the user, who needs to question the published datasets and parameters in use, reliable research is hardly possible.

In preparation to all comparisons being performed in this work the most challenging task concerned the careful evaluation of the unavoidable selection biases, mainly present for spectroscopic

datasets. The selection effects often mask real information that is hidden in the observational datasets. Thus, their understanding is of essential importance to the proper comparison of models and observations. As demonstrated throughout the thesis they are a key ingredient to the process of creating a meaningful realisation of the models under investigation, i.e. they provide the needed information to simulate how an observer would notice the Galaxy if the model was true. Selection effects are a serious issue, but it turns out that the selection biases affecting the SEGUE G-dwarfs can well be handled and properly accounted for by application of individually determined correction weights as discussed in Chapter 5. Those corrections are capable of eliminating the bias against metal-rich stars that not only rises from the special target sampling of the SEGUE survey and colour-cuts in the sample. The metallicity bias is mainly a result of the limited survey volume. All of these aspects tamper with the sample’s chemical properties. By investigating the influence of each correction separately it could be confirmed that the bi-modal distribution in chemistry, that is seen for SEGUE stars and that argues for the presence of a separate thin and thick disk component in the Milky Way, is indeed enhanced by the various selection effects. Still, the inspection and the comparison to models shows that the double peak structure in density space ( $[\text{Fe}/\text{H}]-[\alpha/\text{Fe}]$ -plane) can not be an effect of selection alone contrary to the claims of Bovy et al. (2012a). The volume correction, that corrects the disproportion of thin and thick disk stars with respect to the local volume around the Sun, does not completely remove the bi-modal distribution in  $[\alpha/\text{Fe}]$ . A result that is in agreement with studies based on high-resolution observations that indicate a clear gap between stellar members of the thin and thick disk (Anders et al. 2014; Hayden et al. 2015; Kordopatis et al. 2015b). The same result is also confirmed when analysing the model based mock samples of the SEGUE G-dwarf sample (see below): the mock G-dwarf sample of a model that has no distinct thin-thick disk separation (as in the MCM model) does not show the discontinuity in the  $[\text{Fe}/\text{H}]-[\alpha/\text{Fe}]$ -diagram despite the biases at play in SEGUE. Even with that said the volume correction has yet to be treated with care. Especially at low galactic latitudes and in the inner disk regions the correction tends to be less reliable because there the spatial sampling of SEGUE is only sparsely. Still, SEGUE allows to obtain a good representation of the real volume characteristics of the Galaxy even with its prevailing biases.

## 9.2 Constraining models of the Galaxy

Based on the detailed chemo-kinematic analysis of the stellar sample of SEGUE G-dwarfs this thesis has also aimed to find new observational constraints on two conceptually very different models of the Galaxy: the population synthesis code TRILEGAL as an analytical description of the Milky Way, and the chemo-dynamical model by Minchev et al. (2013), a hybrid model that combines a cosmological re-simulation of a Milky Way like galaxy with a semi-analytic chemical evolution model for the Milky Way.

As part of their analysis the models’ potential and capabilities have been thoroughly tested by means of synthetic stellar samples of mock G-dwarfs. Those were built to resemble the observed G-dwarf sample as close as possible (see descriptions and analysis in Chapters 6 and 7). Mocking the SEGUE G-dwarf sample with all its biases allowed for a one-to-one comparison in stellar parameters, chemistry and kinematic relations. Previous to the actual mocking process the most important preparatory task was the evaluation (see first section of Chapter 5) and reproduction of the SEGUE selection function. Despite its complexity and variation with position angle the selection function could be well recovered for each area of interest within the SEGUE footprint discriminating between SEGUE’s faint and bright exposures. For the entire process an earlier study on the SEGUE G-dwarf selection function by Bovy et al. (2012c) turned out to be very

helpful.

The use of GALAXIA, a code that provides a framework to combine models with the basics of stellar physics and evolution, made it possible to not only realise a mock sample based on TRILEGAL but to transfer the MCM model by Minchev et al. (2013) into the space of observables using stellar atmospheres and evolutionary tracks. With GALAXIA's simulated realisation of the SEGUE survey at hand it then allowed to assemble a G-dwarf mock sample that comprises the full set of chemo-dynamical properties of the MCM hybrid model. As expected the self-consistent dynamic history of all stars in the MCM model defining its chemo-dynamic relations should finally make the difference to the TRILEGAL mock sample that does not feature relations between chemistry and kinematics.

As a completion to the mock samples' investigation and as a second option to constrain the chemo-dynamics of the MCM model new ground has been broken. Thereby, the main key has been to correct the assembled SEGUE sample for its selection biases including its partial volume coverage (see Chapter 5). Under the assumption to deal with an almost bias free sample of SEGUE G-dwarfs their chemo-kinematic properties have been directly compared to predictions obtained from the MCM model  $N$ -body simulation. An approach that may seem to be venturous due to the corrections' reliability but that turned out to come up with the same results than the MCM mock approach.

In summary, the main results that could be obtained from the three different efforts, which compare the selection of SEGUE stars to theoretical model predictions, read as follows:

- The TRILEGAL model proves to be an ideal choice for exploring the mechanisms of the inverse modelling approach. This approach by itself allows to test the models validity and offers a way to compare predictions from various models with each other as a quality check of just these. As a model designed to match the content of the Galaxy TRILEGAL performs well in reproducing a mock sample that shows an exceptionally good agreement with the observations in terms of light, mass and density distributions. After application of observational errors to the model parameters the velocity distributions are reasonably fitted. However, the stellar parameter distributions do match the observed distributions in width but differ slightly with respect to their peak value positions. Due to uncertainties in most of today's stellar atmosphere models and isochrones sets, in particular concerning stellar populations with non-solar abundance patterns, differences in parameter scales are not a rarity. On the contrary, it is a general issue that needs to be resolved because it appears in all combinations of comparisons for synthetic or real stellar surveys as this work's selection of different comparisons (SEGUE vs. TRILEGAL, SEGUE vs. MCM model, SEGUE vs. RAVE) illustrates. Feasible combinations of different surveys are often restrained due to their different pipeline zero points. Most surveys do not have stars in common which would help to adjust their parameter scale differences. Hence, at present one chance to compensate for the issue might be the creation of synthetic copies of the observed datasets based on the same model. In any case the stellar parameters serve as characteristic values to classify stars with respect to each other rather than using them in their original physical meaning.
- With its chemistry and kinematics assigned independently the TRILEGAL model reaches its limits when comparing chemo-kinematic relations. On a first glance the metallicity distribution function as a function of vertical height and galactocentric radius shows a good agreement to the observations. Also a simple separation in chemistry separating SEGUE's thin from thick disk stars results in a good approximation of the model's MDF

predictions for the thin and thick disk component at different regions in the Galaxy. A closer look to the proportions of thin and thick disk stars however revealed more severe differences. These are likely the result of a lack in evolution within the mock sample and a different distribution of thin and thick disk stars with vertical height. Surprisingly, the simple separation into thin and thick disk results in a reasonable well agreement when investigating the MDF for various orbital families ( $e$ - $z_{\max}$ -plane), even though there are no such correlations implemented in TRILEGAL. The lack of chemo-kinematic correlations is most apparent in the velocity regime. SEGUE's thin and thick disk stars indicate an obvious evolution in their mean rotational velocity with metallicity. There is however no such trend seen for their TRILEGAL mock counterpart.

- With all these results this thesis provides essential constraints to the TRILEGAL model concerning the abundance gradient and the scale length of the thin and thick disk as implemented in the current version of the model. The findings suggest that the scale length of the model's thick disk is too long. Also, the metal-poor thin disk in the outer disk region seems to be underestimated due to the missing abundance gradient with height and radius. Yet, equally important is the fact that without a previous revision and modification of TRILEGAL's thick disk metallicity distribution function (as implemented in version 1.6) most of the above results would not have showed up the way they did. Actually, in the attempt to obtain the simulated SEGUE G-dwarf sample based on TRILEGAL the model's thick disk MDF turned out to be too metal-poor. With the help of a subsample of local thick disk giant stars from RAVE, which served to well represent the general thick disk's chemical properties, TRILEGAL's thick disk MDF (peak position and dispersion) could finally be constrained as part of this thesis.
- Altogether it could be shown that the population synthesis models are not sufficient to cope with the complicated structure and evolution of the Galaxy. TRILEGAL has proven to successfully demonstrate the effect of observational selection biases and selection functions. Therefore, it can certainly serve people to design new observational projects. But a more sophisticated description of the Galaxy is needed to deal with the chemo-dynamics observed in present survey datasets. A better candidate to reproduce the chemo-dynamical properties of the Galactic disk has clearly be found in the MCM model. By exploring the model's chemo-kinematic predictions in a direct approach and by compiling a MCM G-dwarf mock sample it has been possible to verify a very important issue. Namely, if discrepancies that appear in the direct approach (i.e. when comparing the  $N$ -body particle simulation of the MCM model to the bias corrected SEGUE sample) can be attributed to actual different properties and real scientific features rather than to significant problems and artefacts due to the selection bias correction. As a matter of fact the former could be confirmed.
- Both approaches reveal that the MCM model is more suitable than TRILEGAL in terms of connecting chemistry and kinematics, well reproducing the correlations found in this work's SEGUE compilation of stars. This gives confidence that the MCM model mirrors important aspects of the Galaxy evolution that usually leaves its fingerprint in each observational dataset. Matching the number counts of the observed SEGUE G-dwarf sample however poses a difficulty. Still, with respect to TRILEGAL the MCM mock sample predicts comparable distributions for quantities like stellar parameters, proper motions, distances and magnitudes. Actually, both models show a strong resemblance in their stellar parameter scales. A finding being justified by the use of the same set of stellar isochrones in the popula-

tion synthesis process. Nonetheless, the models' match in distributions is quite remarkable considering the many additional assumptions needed to create a synthetic observation and that differ for the TRILEGAL and GALAXIA framework. A closer look on both mock samples revealed that, based on their predicted position of the MDF peak with vertical height, apparently TRILEGAL has the ability to better handle the artificially introduced SEGUE selection biases even though no such gradient is implemented in TRILEGAL.

- Regarding the MCM model this work's main result is certainly that evidence has been found which points to the lack of a distinct thick disk component in the model. Based on a simulation of a thin disk (and its chemistry) only the MCM model is able to create a metal-poor Galactic component almost similar to the observed thick disk with chemical and kinematic properties different to its thin disk counterparts. Corresponding signatures are provided by the existence of a change in the metallicity distribution function peak with vertical height and radial distance from the Galactic centre. Yet, the MCM thick disk component, that solely forms from mergers at early times and radial migration at different stages of the disk evolution, can not keep up with the properties of the observed thick disk stars in the SEGUE G-dwarf sample. Those show much lower rotational velocities and larger velocity dispersions typical for old and metal-poor disk stars. Both, the MCM model itself and its mock companion indicate velocity-correlations that does not suffice the observations. Especially, the predicted change in the MDF peak with vertical height that appears in both comparison approaches is much shallower than the observed one. A fact that points at an intrinsic property of the simulated  $N$ -body disk.

A second result that underlines the need of a distinct thick disk is the significant difference revealed by the stellar density distribution in the chemical space. The  $[\text{Fe}/\text{H}]-[\alpha/\text{Fe}]$ -diagram only indicates a bi-modality in the  $[\alpha/\text{Fe}]$  distribution for the observations. If this feature would be a remnant of the selection effects, still remaining in the observations even after the survey volume correction, there should be a similar signature present in the MCM mock G-dwarfs. However, neither the MCM mock nor MCM model itself show a hint of a gap in the chemical-abundance plane which is not only indicated by SEGUE but in agreement with many other recent high-resolution studies that reveal a clear distinction between the abundance patterns of the thin and thick disk. Clearly, the observations house a group of metal-poor stars with properties of a hotter and heavier disk component and a different origin that the MCM model is not able to generate by pure consideration of a thin disk and dynamical processes such as stellar heating, scattering or radial migration.

### 9.3 RAVE versus SEGUE - a unique comparison

Apart from the model and mock sample testing, the chemo-kinematic correlations obtained from SEGUE have been directly put into relation to those revealed by a compilation of RAVE giant stars. In principle the independent RAVE reference sample is based on the high signal-to-noise giant sample studied in Boeche et al. (2013a). Most of the authors carefully chosen parameter cuts have been adopted. Due to an eased limit in SNR and less restrictive cuts in some of the pipeline quality parameters this work's RAVE giant selection comprises yet more stars which, consistent with the selection of SEGUE G-dwarfs, cover a distance range of up to 3 kpc from the Sun. Not only that RAVE giants have characteristic distances of about 1 kpc, also the distance uncertainty was one of the main drivers to restrict the explored survey volume such that the star's distances would still be reliable with uncertainties mostly around 10% but certainly below a limit of 20% (see Section 4.1.3) for both the RAVE and SEGUE stars. The above adjustment in

selection criteria turned out to be necessary because the original reference sample showed biases against metal-rich stars that could only be detected through the comparison to the independent sample of SEGUE G-dwarfs. Contrary to SEGUE mainly suffering from selection biases due to the complex survey design and targeting strategy, the inclusion of metal-rich RAVE giants in a sample compilation seems to be highly affected by the automatic RAVE pipelines. Those introduce systematic biases against certain types of stars in connection with common sample selection criteria such as cuts in temperature or signal-to-noise. A detailed investigation of the encountered metallicity biases has been described in Chapter 8, together with information on the RAVE stars' parameter set which includes distances and kinematic parameters that, for consistency, have been determined similar to those of the SEGUE G-dwarf.

Against all odds, the two independent spectroscopic surveys show a remarkably good agreement and provide similar insights into the chemo-kinematic Galactic disk properties. Although the comparison of the selected stellar samples with stars of different type is based on parameters from independent pipelines that each suffer from individual issues in the parameter determination. Deviations and systematic shifts due to differences in parameter scales are usually not avoidable and indeed present in case of the RAVE-SEGUE comparison. But, as this thesis could demonstrate, they are manageable as long as they are well studied and understood.

Although the two samples do cover a similar volume, the number density of the targets vary as a function of height. But as expected the chemo-kinematic relations traced by RAVE and SEGUE are in agreement within smaller bins of vertical height,  $z$ , and galactocentric radius,  $R$ . Even within subgroups of orbital families both surveys show a comparable behaviour. Moreover, it is clearly seen that in those  $z$ -bins where one of the surveys lacks statistics, the other beautifully complements it. The best matches in the chemo-kinematic relations traced by both surveys are of course found for the intermediate heights ( $0.5 \text{ kpc} < z < 1.0 \text{ kpc}$ ) where both surveys show a similar number of stars and are only marginally influenced by volume geometry effects. For the lower or higher regions either RAVE or SEGUE dominate and show their particular strength. With this demonstrated it is clear that the comparison works very well and allows a suitable combination of spectroscopic data that explores the near volume of the disk around the solar neighbourhood within 3 kpc from the Sun. Most importantly, both surveys complement each other in an optimal way. In combination RAVE and SEGUE offer the great opportunity to obtain a unique and more complete view on the the Galactic disk and its chemo-kinematic structure.

## 9.4 Closing remarks and future prospects

Over the past decade progress has been made in the field of Galactic science. Not only that the more sophisticated observational datasets (e.g. SEGUE, RAVE, APOGEE, Gaia-ESO etc.) now allow to take a very detailed look at the Galaxy's chemo-dynamical structure, with even more data to come from APOGEE (south), LAMOST or GALAH. Also many new modelling approaches have reserved itself a seat in the spinning carousel of unravelling the history and evolution of the Galaxy, mostly driven by the question whether there are two distinct Galactic disk components, a thin and thick disk, or not. Supported by various observational evidences from high or low resolution (find a short review of the current status quo in Kawata & Chiappini 2016) the current consensus is that there are at least two different types of disks in the Milky Way. An open question however is how to best define those disks, either by geometry (Gilmore & Reid 1983), kinematics (Adibekyan et al. 2012; Bensby et al. 2014), chemistry (Anders et al. 2014; Hayden et al. 2015; Nidever et al. 2014) or age (Fuhrmann 2011). Also their origin, i.e. their most probable formation scenarios are still under debate. Exactly that is the point where

models and simulations enter the game as an inevitably important tool to scientifically exploit Galactic surveys and the impact of their selection effects.

Basically, four types of modelling approaches (for a recent summary see Sanders & Binney 2015; Kawata & Chiappini 2016) are currently on the market, these are (1) fitting observational data with a Galaxy model that is either a mass, stellar population or dynamical model (Sanders & Binney 2015; Robin et al. 2014), (2) employing semi-analytic models which follow pure chemical or chemo-dynamical evolution (Chiappini et al. 1997; Boissier & Prantzos 1999), (3) building hybrid models that combine the advantages of the hierarchical build-up of cosmological simulations with the flexibility of semi-analytic models that better allow to regulate the important small scale physics, such as, feedback, star formation or chemical history (Minchev et al. 2013) which are still problematic in cosmological simulations, or (4) using fully self-consistent cosmological  $N$ -body simulations. Both the third and the fourth approach allow to link current observed properties with the cosmological formation history of the Galaxy (Brook et al. 2012). Momentarily it is important that all these approaches coexist. Each of them has its advantages and shortcomings, but altogether they may help to solve the puzzle by addressing specific issues from their individual point of view.

Hence this thesis fits well into this greater scientific context. This is because the presented work provides a new building stone in the current discussion on the distinctiveness of the Galactic disk components by leaping forward in the field of synthetic stellar mocks that have proven to make a major contribution in constraining models of the Galaxy. Despite the remarkable consistency, already in existence for this work's investigated observations and models, it is clear that in certain aspects the modelling approaches are still inadequate to exploit the full information content of the Galaxy. Not only that the performance of the TRILEGAL model would benefit from additional features such as a radial and vertical metallicity gradient that could close the missing link between chemistry and kinematics. Also the MCM model approach seems to need further improvement. Originally, one of its main goals was to test whether it is possible to create a discontinuity in the chemical abundance plane without the need of invoking a discrete thick disk, but only through the work of radial mixing and mergers. Considering the outcome of this thesis the answer to this is no. Especially for the higher latitudes and in the inner disk regions where, due to the thick disk's shorter scale length, the lack of a heavier thick disk component would leave its signature most effectively the MCM model shows difficulties to keep up with the observations. This suggests two things. Either the model needs a separate thick disk with a chemical signature as proposed by the two infall model (Chiappini 2009). Or the modelling of the inner galaxy (introducing a more complex chemical evolution of the bulge/bar/inner disk region) needs to be revised which could than lead to an increase of old and more metal-poor radial migrators that end up at the solar radius, contributing a population of stars currently missing in the model. So far, the availability of only little observational constraints has complicated the proper modelling of the inner disk regions. In the pre-APOGEE era there has been essentially no observational information beyond 5 kpc. But the prospects are good. Especially, the APOGEE south project will provide more tight constraints on the model in the inner part of the Milky Way. However, to test if this or the addition of a distinct thick disk would lead to a better agreement between the MCM model and this work's SEGUE dataset is beyond the scope of this thesis and subject to further studies. Independently, a more detailed investigation of the smoothing, which is a key ingredient when transforming  $N$ -body mass particles from a simulation into simple stellar populations, could lead to a better understanding of the MCM properties because the smoothing does have a direct impact on the model's stellar density distribution with radius and height.

In the future the most crucial improvement providing constraints to all models and many

observational dataset will certainly be the availability of precise stellar ages. These will help to lift each chemo-dynamical analysis to a higher level. In that context the role of asteroseismology has already been demonstrated to be of great importance to the field of galactic archaeology (Anders et al. 2017; Chiappini et al. 2015a). ESA's Gaia mission, the upcoming ESA's PLATO mission and the K2 mission of Kepler (e.g. Stello et al. 2015), which is going to deliver asteroseismic results for RAVE stars, will complement the precise chemical abundance information from ground-based high-resolution surveys such as APOGEE, Gaia-ESO or GALAH and as such smooth the way to better constrain the formation scenarios of the Galactic disk.



This part of the Appendix contains supplementary information on the RAVE survey's completeness and selection function. A selection function that can be determined in a comparatively easy way in contrast to the SEGUE survey selection function (see Chapter 5) which shows itself to be more complex due to a complicated target selection process and object sampling.

## A.1 The RAVE selection function

RAVE's selection function is solely dependent on the apparent  $I$ -band magnitude and the angular position of the star. As such the probability  $S$  that an object is selected and observed by RAVE can be expressed as

$$S = S(l, b, I, J - K_s) \quad (\text{A.1})$$

where  $l$  and  $b$  are the Galactic coordinates of the object and  $I$  and  $J - K_s$  are its corresponding magnitude and colour. Nevertheless, the inhomogeneous photometry used to create the different input catalogues is a source for possible selection biases. An additional important aspect is also that the RAVE targets are divided into bins in  $I$ -band magnitude in order to avoid problems due to fibre cross-talk. Within the RAVE fibre-fed spectrograph the individual spectra are projected close to each other on the CCD chip. Scattered light from a spectrum can easily affect its adjacent spectrum and vice versa which becomes problematic in case neighbouring fibres are pointed to objects whose brightness differs a lot. Hence only targets from narrow magnitude bins ( $[9, 10]$ ,  $[10, 10.8]$ ,  $[10.8, 11.3]$ ,  $[11.3, 12]$ ) are observed together in an exposure. The binning of the input catalogue directly leads to steps in the overall  $I$ -magnitude distribution of the observed RAVE stars as shown in Figure A.1. To circumvent problems with the inhomogeneity of the RAVE target data the best way to investigate the survey's completeness is by using the full capacity of 2MASS since all RAVE targets possess accurate 2MASS photometry in  $J$ ,  $H$ ,  $K_s$ . Moreover 2MASS contains all additional potential candidates that could have been included in the input catalogue. The overall completeness compared to 2MASS is studied and described extensively in the PhD thesis of Tillmann Piffl (Piffl 2014). Moreover, a recent paper by Wojno et al. (2016) is exclusively dedicated to the RAVE selection function. In this thesis, the major steps and results of the latter study are summarised. It is important to determine the selection function as a

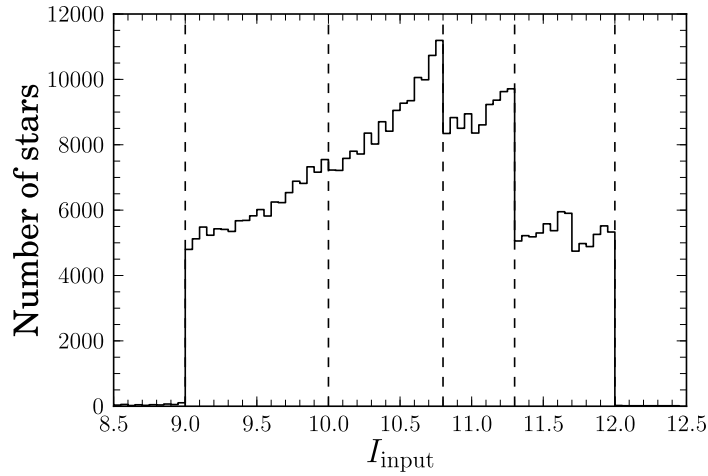


**Figure A.1:** Input  $I$ -band magnitude distribution for the full RAVE catalogue. Based on these input magnitudes all initial RAVE targets were selected. The distribution is based on different source catalogues. The four magnitude bins used for the observations are indicated by the dotted lines.

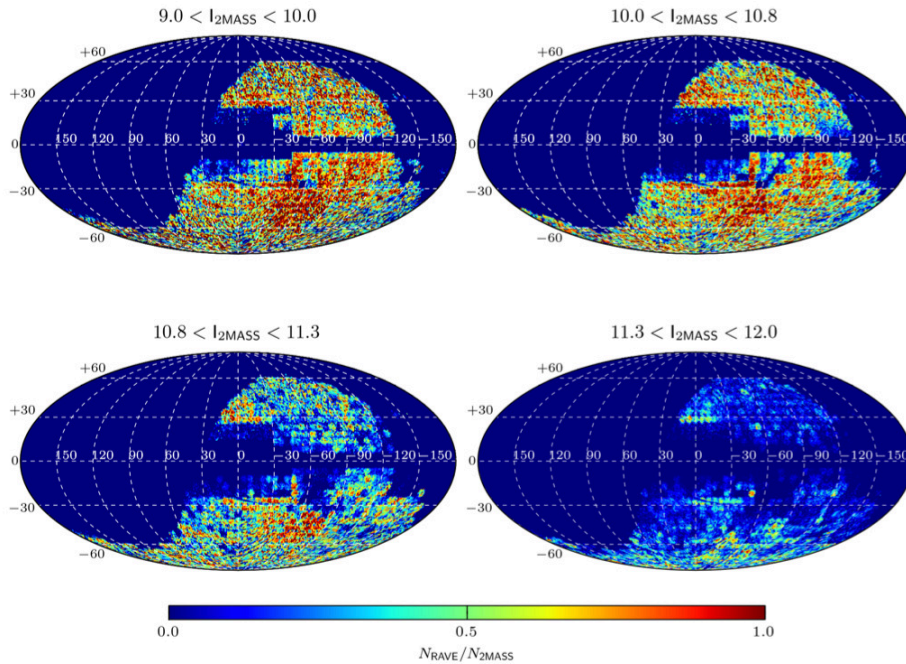


**Figure A.2:** Projection of the RAVE survey's completeness distribution w.r.t 2MASS as a function of angular position in Galactic coordinates and apparent magnitude. Each panel shows one of the four magnitude bins the RAVE input targets were divided in for observations. The completeness is highest in the brights bin (upper left panel) which contains less potential photometric targets and was primarily observed. The figure is the same as Figure 3 in Kordopatis et al. (2013).

function of position on the sky. In case of RAVE this is due to two reasons: (1) RAVE targets are inhomogeneously distributed on the sky because due to the altitude of the observatory some fields have been subject of the observations more often than others and (2) the stellar density varies with distance from the Galactic disk and position in the Galaxy due to structure and dust. In order to compute the completeness of each of the input catalogue magnitude bins the observed area is divided into small pixels. The completeness in an individual sub-area is then the number of stars observed by RAVE,  $N_{\text{RAVE}}$ , divided by the number of 2MASS objects,  $N_{\text{2MASS}}$ , that are located within the pixel area. The selection fraction can be written as

$$S(I_{\min}, I_{\max}) = \frac{N_{\text{RAVE}}(I_{\min}, I_{\max})}{N_{\text{2MASS}}(I_{\min}, I_{\max})} \quad (\text{A.2})$$

where  $I_{\min}$  and  $I_{\max}$  are the upper and lower limits in magnitude in each bin. Figure A.2 illustrates the completeness of the RAVE survey in the four different magnitude bins with respect to 2MASS. As expected the completeness is higher in the brighter than in the fainter bins which is a consequence of the fact that there are less bright objects available for targeting and RAVE preferentially observed bright stars.

In summary, the survey selection function is an expression for the relation between the spectroscopic data sample and the underlying photometric population it is selected from. In its basic form the selection function represents the specific target sampling of the survey as such it reflects e.g. the limited number of spectroscopic fibres or, as in the case of RAVE, the uneven number of observed objects in different magnitude bins.



This part of the Appendix deals with supplementary information on the SEGUE survey and this work's G-dwarf sample. First, Sections B.1 and B.2 focus on the SEGUE Stellar Parameter Pipeline (SSPP) and its improvements for DR9. Then, Section B.3 comments on the SDSS bitmask system and Section B.4 list the SQL code used to download the basic dataset of SEGUE G-type stars from the SDSS CasJobs server that served to define this work's sample of SEGUE G-dwarfs.

## B.1 General adjustments of the SSPP for DR9

In order to generally improve the SSPP for DR9 all SSPP estimators previously used in the DR8 version of the pipeline have been systematically investigated for reliability and robustness. This review (Schlesinger et al. 2012) revealed that some of the methods produce less accurate  $\log g$  estimates than others. Also some techniques do cover only a limited range in metallicity introducing a bias against higher metallicities because they are not able to measure values above solar metallicity. The outcome of this examination and the fact that the comparison with the high-resolution sample showed large deviations for some of the methods led to the exclusion of certain estimators in the DR9 version of the SSPP. This mainly concerns the auto-correlation function (ACF), the Ca II triplet line index **CaIIT** and the neutral network method **ANNSR** which are no longer reported as metallicity estimates. Further, the surface gravity line index methods **MgH**, **CaI2** and **k24** are no longer contributing to the adopted gravity estimates. Regarding the temperature estimates there has been a replacement of the previous photometric temperature estimates with only a single method based on the Infrared Flux Method (IRMF). The latter technique uses the relation between the  $(g - r)$  colour and the temperature of the object accounting for effects of  $[\text{Fe}/\text{H}]$  and  $\log g$  on this relation.

Finally, this leaves a maximum number of nine independent methods for  $T_{\text{eff}}$ , seven estimates for  $\log g$  and nine techniques for the metallicity. More details on the exclusion and testing of particular methods can be found in the Appendix A of Schlesinger et al. (2012) or the SEGUE-2 paper (Rockosi et al. (in prep.)). The following section also lists some more adjusting refinements that have been applied to those estimators remaining in the DR9 version of the pipeline.

## B.2 Refinement of the SSPP estimators in DR9

For some of the remaining methods reported in the DR9 SSPP the DR8 version of the pipeline exhibits artificially peaked and spiky distributions, especially for some of the metallicity estimators. To deliver more realistic and optimal values that result in smoother distributions most of the SSPP methods have been additionally adjusted. The following bullet points list some of the major refinements that have an positive effect on the parameter distributions:

- For methods that are based on  $\chi^2$  minimisation (`k24`, `ki13`, `NGS1`, `NGS2` and `CaI1K1`) the  $\chi^2$  interpolation method is changed from linear to cubic spline to interpolate the flux values in the grid of synthetic spectra.
- To increase the accuracy of the individual estimators a new set of  $(g - r)$  and SNR limits for all methods is introduced.
- The neutral networks for `ANNRSR` and `ANNRR` are trained on a new grid of synthetic spectra and the DR8 parameters.
- Some estimators (`NGS1`, `CaI1K1`) utilise a new grid of synthetic spectra that is based on  $\alpha$ -enhanced Kurucz model atmospheres where the micro-turbulence velocity is a function of surface gravity or fixed at a value of  $1 \text{ km s}^{-1}$  (`NGS2`).
- The grid's range in metallicity is extended to  $[\text{Fe}/\text{H}] = -4.5 \text{ dex}$  and  $[\text{Fe}/\text{H}] = +1.0 \text{ dex}$  for the latter three estimators which improves estimates for stars with low and above solar metallicity.

## B.3 The SDSS bitmask system

In the process of querying this thesis does not make use of the SDSS bitmask system which labels the different categories the SEGUE stars belong to (see SEGUE bitmasks in `segueTargetAll` table in `CASJobs`) and indicates for which target type category an object was originally assigned a fibre for (SEGUE bitmasks in `specObjAll` and `sppParams` tables in `CASJobs`). As such it records why each target was observed spectroscopically and keeps track of the reasons for targeting.

The concept of bitmask in spectroscopic target flags allows e.g. to select a particular stellar type of stars among all SEGUE objects. This selection can be performed in two different ways: (a) if the user wants every object that was assigned a fibre for a specific stellar type in SEGUE-1 e.g all objects that were targeted as G-dwarfs, the target flag column `segue1_target1` in the `specObjAll` or `sppParams` tables needs to be queried using the bit for G-dwarfs, (b) if the user wants every object that meets the criteria of a specific stellar type no matter if the object may also fulfil the criteria of other categories the target flag column `segue1_target1` in the `segueTargetAll` table needs to be queried. In summary, each target in SEGUE-1 and SEGUE-2 is assigned to a spectroscopic fibre because it fulfils the criteria for a particular category. Nevertheless the targets often pass the criteria for multiple categories. Therefore the user has to be careful when working with the various bitmasks that carry the needed information since they vary in what information they provide from table to table in the CAS. While the bitmasks in the `specObjAll` and `sppParams` tables contain information about the criteria a target fulfils at the time of fibre assignment (SEGUE target selection based on DR7 or previous photometry reductions) the bitmasks in `segueTargetAll` reflect the different categories each star belongs to according to the DR9 photometry and astrometry.

## B.4 SQL query to select SEGUE G-dwarfs based on photometry

The following collection of SQL queries summarises how a good quality sample of G-dwarfs can be compiled from the full catalogue of SEGUE stars. The cascade of queries is adopted from the one published on [https://www.sdss3.org/dr9/algorithms/gkdwarf\\_query.php](https://www.sdss3.org/dr9/algorithms/gkdwarf_query.php) but has been individually modified to meet this work's intentions. The major difference is that the original queries select the SEGUE G-dwarfs based on bitmasks while for this thesis the selection of stars has been based on the actual photometry published with DR9.

Listing B.1: SQL queries

```

1 ## Query 1
2 # Using the DR9 photometry (pdf-magnitudes from the table PhotoObjAll),
3 # this first query extracts information for all targets that meet the
4 # colour-magnitude criteria of a G-dwarf, regardless of whether or not
5 # they also fulfill the criteria of other SEGUE categories. The selection
6 # also ensures that the spectroscopic observation will be science quality.
7 # The resulting table will have duplicate spectra (e.g., multiple specobjid
8 # for a single bestobjid).
9
10 SELECT
11 sp.specobjid , sp.bestobjid , sp.plate , sp.mjd , sp.fiberid ,
12 so.bestobjid as sobest , so.plate as splate , so.mjd as somjd ,
13 so.fiberid as sofiberid , px.isprimary as pxisprimary , px.isbest as pxisbest ,
14 sp.seguel_target1 , sp.seguel_target2 , so.seguel_target1 as sosegltarg1 ,
15 so.seguel_target2 as sosegltarg2 , sp.survey , so.survey as sosurvey ,
16 so.programname , sp.plateid , so.plateid as splateid ,
17 sp.targetobjid as spptargetobjid , sta.seguel_target1 ,
18
19 poa.l , poa.b , so.ra , so.dec , sp.snr ,
20 pm.pmra , pm.pmraerr , pm.pmdec , pm.pmdecerr ,
21 sp.elodiervfinal , sp.elodiervfinalerr , sp.fehadop , sp.fehadopunc ,
22 sp.teffadop , sp.teffadopunc , sp.loggadop , sp.loggadopunc ,
23 poa.psfmag_u-poa.extinction_u as u0 , poa.psfmag_g-poa.extinction_g as g0 ,
24 poa.psfmag_r-poa.extinction_r as r0 , poa.psfmag_i-poa.extinction_i as i0 ,
25 poa.psfmag_z-poa.extinction_z as z0 , poa.psfmagerr_u , poa.psfmagerr_g ,
26 poa.psfmagerr_r , poa.psfmagerr_i , poa.psfmagerr_z
27
28 INTO mydb.query1
29
30 FROM SpecObjAll as so
31 JOIN PlateX as px on so.plateid = px.plateid
32 JOIN sppParams as sp on sp.bestobjid = so.bestobjid
33 JOIN segueTargetAll as sta on so.bestobjid = sta.objid
34 JOIN PhotoObjAll as poa on so.bestobjid = poa.objid
35 JOIN ProperMotions as pm on poa.objid = pm.objid
36
37 WHERE so.programname like '%segue%'
38 --The above statement ensures that all targets are pulled from
39 --either the segue or seguefaint programs
40 AND so.survey = 'segue1'
41 --This specifies that all targets must be from the SEGUE-1 survey
42 --as SEGUE-2 does not explicitly target these categories
43

```

```
44 AND (poa.psfmag_g-poa.extinction_g) - (poa.psfmag_r-poa.extinction_r) > 0.48
45 AND (poa.psfmag_g-poa.extinction_g) - (poa.psfmag_r-poa.extinction_r) < 0.55
46 AND (poa.psfmag_r-poa.extinction_r) > 14.0
47 AND (poa.psfmag_r-poa.extinction_r) < 20.2
48
49 --The DR9 photometry must meet the criteria of a G-dwarf
50 AND px.isprimary = 1
51 --Requires the plate to be science quality
52 AND sp.scienceprimary = 1
53 --Requires the observation to be science quality
54 ORDER BY sp.bestobjid
55 --Organizes the resulting sample by bestobjid
56
57 ## Query 2
58 # Using the bestobjid for each photometric target, we then
59 # make a list of all of the unique targets from the table
60 # produced in Query 1.
61
62 SELECT
63     bestobjid , count(bestobjid) as count
64
65 INTO mydb.query2
66 FROM mydb.query1
67
68 GROUP BY bestobjid
69 HAVING count(bestobjid) = 1
70
71 ## Query 3
72 # This query uses the list made in Query 2 to pull out the
73 # data from Query 1 for all unique targets.
74
75 SELECT
76     q1.*
77
78 INTO mydb.query3
79 FROM mydb.query1
80 JOIN mydb.query2 as q2 on q1.bestobjid=q2.bestobjid
81
82 ## Query 4
83 # Duplicate spectra are than considered by making a list of all
84 # bestobjid with more than one specobjid. There is only one row
85 # for each target in the resulting data set.
86
87 SELECT
88
89     bestobjid , count(bestobjid) as count
90
91 INTO mydb.query4
92 FROM mydb.query1
93
94 GROUP BY bestobjid
95 HAVING count(bestobjid) > 1
96
97
```

```

98 ## Query 5
99 # Query 5 than extracts the entire information from the Query 1 table
100 # for each of the duplicate observations. One bestobjid will have multiple
101 # rows of data in this file.
102
103 SELECT
104 q1.*
105
106 INTO mydb.query5
107 FROM mydb.query1 as q1
108
109 JOIN mydb.query4 q4 on q4.bestobjid = q1.bestobjid
110 ORDER BY q1.bestobjid
111
112 ## Query 6
113 # In order to get the best sample of stars from the duplicate spectra,
114 # all observations on bright plates are pulled out (programname is
115 # segue rather than seguefaint). There will still be some duplicates
116 # from geometric overlaps.
117
118 SELECT
119 *
120 FROM mydb.query5
121 INTO mydb.query6
122 WHERE programname = 'segue'
123 ORDER BY bestobjid
124
125
126 ## Query 7
127 # Query 7 goes through the data table from Query 6 and lists the bestobjid
128 # for all targets that now only show up once (e.g., eliminates the
129 # geometric overlap duplicates).
130
131 SELECT
132
133 bestobjid , count(bestobjid)
134
135 INTO mydb.query7
136 FROM mydb.query6
137 GROUP BY bestobjid
138 HAVING count(bestobjid) = 1
139
140
141 ## Query 8
142 # Query 8 creates a table for all of the segue plate observations for
143 # the targets that were obsered multiple times. It removes the targets
144 # which are duplicates due to geometric overlaps.
145
146 SELECT
147 q6.*
148
149 INTO mydb.query8
150 FROM mydb.query6 as q6
151 JOIN mydb.query7 as q7 on q7.bestobjid = q6.bestobjid

```

```
152 |
153 | ## Query 9
154 | # Query 9 pulls out the bestobjid for all geometric overlap duplicate
155 | # spectra. For example, the same line of sight observed on plates
156 | # 2042/2062 was studied by plate 2043/2063. Also, plates 2175/2178
157 | # line up with 2186/2189.
158 |
159 | SELECT
160 | q6.bestobjid , count(bestobjid)
161 | INTO mydb.query9
162 | FROM mydb.query6 as q6
163 |
164 | WHERE q6.plate=2042 OR q6.plate=2043
165 | OR q6.plate=2175 OR q6.plate=2178
166 | OR q6.plate=2062 OR q6.plate=2063
167 | OR q6.plate=2186 OR q6.plate=2189
168 | GROUP BY q6.bestobjid
169 | HAVING count(bestobjid)>1
170 |
171 | ## Query 10
172 | # The final query 10 extract for all of the geometric overlap duplicates
173 | # only the spectroscopic observation FROM the brightest plates
174 | # (2042 and 2175).
175 |
176 | SELECT
177 | q6.*
178 | INTO mydb.query10
179 | FROM mydb.query6 as q6
180 | JOIN mydb.query9 q9 on q9.bestobjid = q6.bestobjid
181 | WHERE q6.soplate=2042 OR q6.soplate=2175
182 |
183 | ## Final step
184 | # Download the resulting tables from Query 3 (data for all stars with
185 | # only one spectroscopic observation), Query 8 (data from the bright
186 | # plate for all duplicates except geometric overlaps), and Query 10
187 | # (bright data for geometric overlap duplicates). These three combined
188 | # make a complete G-dwarf sample, with the best, unique observation of
189 | # each target that meets the SEGUE selection criteria.
```

## Supplement to TRILEGAL

This last part of the Appendix hosts supplementary information on the population synthesis model TRILEGAL. Provided are (1) details on the model’s output parameters in Table C.1, (2) a listing of the collection of SEGUE plates used to simulate the survey’s footprint with TRILEGAL in Table C.2 and (3) specific information on the model’s input parameters that have been particularly chosen for this work’s purposes (Table C.3).

**Table C.1:** TRILEGAL output parameters

<b>Population and physical parameters</b>		<b>Photometry</b>	
Gc	Galactic component: 1: thin disk; 2: thick disk; 3: halo; 4: bulge	<i>ugriz</i>	apparent SDSS magnitudes, <b>not</b> dereddened
log <i>Age</i>	log <sub>10</sub> of age in years		
[M/H]	initial metallicity, referenced to the Sun’s	<b>Kinematic</b>	
<i>m</i> <sub>ini</sub>	initial mass in $M_{\odot}$	vel <i>U</i> , vel <i>V</i> , vel <i>W</i>	galactic space motions
log <i>L</i>	log <sub>10</sub> of luminosity in $L_{\odot}$	<i>V</i> <sub>rad</sub>	radial velocity
log <i>T</i> <sub>e</sub>	log <sub>10</sub> of temperature in K	PMracosd, PMdec	proper motions
log <i>g</i>	log <sub>10</sub> of surface gravity in cgs units		
<i>m</i> – <i>M</i> <sub>0</sub>	absolute distance modulus		
<i>A</i> <sub>V</sub>	extinction in <i>V</i> -band		
<i>m</i> <sub>2</sub> / <i>m</i> <sub>1</sub>	mass ratio for binaries (= 0 for single stars)		
<i>M</i> <sub>bol</sub>	apparent bolometric magnitude		
<i>M</i> <sub>act</sub>	actual mass in $M_{\odot}$		

**Table C.2:** Listing of the variety of targeted SEGUE plates. The program name indicates the plate type. Information about where and why a particular plate is targeted in SEGUE is given in the details column. The total number of each SEGUE plate type is listed in the last column. How many plates have been used to simulate the SEGUE survey footprint with TRILEGAL is indicated in the tables third column.

program name	details	# of plates used as simulation input	# of unique plates
segue	segue-1 bright plate ( $r_0 < 17.8$ ); placed without regard to known substructure	165	165
seguefaint	segue-1 faint plate ( $r_0 > 17.8$ ); placed without regard to know substructure	157	157
segue2	segue-2 plate with no distinction into bright/faint; placed without regard to known substructure	196	202
segtest	bright plate using special target selection for testing purposes	6	10
segtestf	faint plate using special target selection for testing purposes	4	4
segcluster	bright plate placed at the location of a globular or open cluster	12	14
segclusterf	faint plate placed at the location of a globular or open cluster	9	8
segpointed	bright segue-1 plate; placed at the probable location of MW substructure	14	16
segpointedf	faint segue-1 plate; placed at the probable location of MW substructure	14	16
seglowlat	segue-1 bright plate; placed at low Galactic latitude, designed with the low latitude targeting strategy	12	12
seglowlatf	segue-1 faint plate; placed at low Galactic latitude, designed with the low latitude targeting strategy	11	11

**Table C.3:** Detailed specifications of the main parameter input of the model used to simulate the SEGUE field plates with TRILEGAL.

TRILEGAL configuration	
<b>Pointing parameters</b>	
Galactic coordinates (epoch 2000) in degree	l, b
field area	7 deg <sup>2</sup>
<b>Photometric system</b>	
magnitude system	SDSS <i>ugriz</i>
limiting magnitude and resolution	(23.0, 0.1)
<b>IMF and binaries</b>	
IMF	Chabrier lognormal
binary fraction with mass ratio in interval	0.3 in [0.7,1.0]
<b>Extinction</b>	
kind of extinction	exponential disk $e^{- z /h_{z,dust}} e^{-R/h_{R,dust}}$
scale height $h_{z,dust}$	110 pc
scale length $h_{R,dust}$	10 kpc
local extinction density $A_V$ in mag/pc	0.00015
extinction at infinity in mag	0.11
dispersion	0.39
<b>Solar position</b>	
position of the Sun ( $R$ and $z$ in the disk)	(8000, 24.5)[pc]
<b>Thin disk</b>	
profile along $z$	$\text{sech}^2(0.5z/h_{z,d})$
scale height $h_{z,d}$ cf. $h_{z,d} = z_0(1 + t/t_0)^\alpha$	$z_0 = 94.6902$ pc, $t_0 = 5.5$ Gyr, $\alpha = 1.6666$
profile along $R$	exponential disk with $e^{-R/h_{R,d}}$
scale length $h_{R,d}$ , truncation radii [min,max]	2913.36, [0.0, 15000.0] pc
local surface density $\Sigma_{d,\odot}$ in $M_\odot/\text{pc}^2$	55.4082
<b>Thick disk</b>	
profile along $z$	$\text{sech}^2(0.5z/h_{z,td})$
scale height $h_{z,td}$	800 pc
profile along $R$	exponential disk with $e^{-R/h_{R,td}}$
scale length $h_{R,td}$ , truncation radii [min,max]	2394.07, [0.0, 15000.0] pc
local volume density $\Omega_{td,\odot}$ in $M_\odot/\text{pc}^3$	0.0015
<b>Halo</b>	
profile	oblate $r^{1/4}$ spheroid
effective radius $r_h$ on plane (about $r_\odot/3.0$ )	2698.93
oblateness $q_h$	0.5830632
local halo volume density $\Omega_{h,\odot}$ in $M_\odot/\text{pc}^3$	0.000100397
<b>Bulge</b>	
profile	Binney et al. 97
scale length $a_m$ in pc	2500.0
truncation scale length $a_0$ in pc	95.0
y/x axial ratio $\eta$ , z/x axial ratio $\psi$	0.68, 0.3
angle major-axis sun-center-line in deg	14.4
central bulge volume density $\Omega_{b,\odot}$ in $M_\odot/\text{pc}^3$	406.0
bulge cutoff mass	0.6



- Abadi, M. G., Navarro, J. F., Steinmetz, M., & Eke, V. R. 2003, *ApJ*, 591, 499
- Abazajian, K., Adelman-McCarthy, J. K., Agüeros, M. A., et al. 2003, *AJ*, 126, 2081
- Abazajian, K. N., Adelman-McCarthy, J. K., Agüeros, M. A., et al. 2009, *ApJS*, 182, 543
- Adibekyan, V. Z., Figueira, P., Santos, N. C., et al. 2013, *A&A*, 554, A44
- Adibekyan, V. Z., Santos, N. C., Sousa, S. G., & Israelian, G. 2011, *A&A*, 535, L11
- Adibekyan, V. Z., Sousa, S. G., Santos, N. C., et al. 2012, *A&A*, 545, A32
- Ahn, C. P., Alexandroff, R., Allende Prieto, C., et al. 2014, *ApJS*, 211, 17
- Ahn, C. P., Alexandroff, R., Allende Prieto, C., et al. 2012, *ApJS*, 203, 21
- Aihara, H., Allende Prieto, C., An, D., et al. 2011a, *ApJS*, 193, 29
- Aihara, H., Allende Prieto, C., An, D., et al. 2011b, *ApJS*, 195, 26
- Alam, S., Albareti, F. D., Allende Prieto, C., et al. 2015, *ApJS*, 219, 12
- Allende Prieto, C., Beers, T. C., Wilhelm, R., et al. 2006, *ApJ*, 636, 804
- Allende Prieto, C., Majewski, S. R., Schiavon, R., et al. 2008a, *Astronomische Nachrichten*, 329, 1018
- Allende Prieto, C., Sivarani, T., Beers, T. C., et al. 2008b, *AJ*, 136, 2070
- Anders, F. 2013, Diploma Thesis, Chemodynamical constraints on Milky Way models from spectroscopic stellar surveys
- Anders, F., Chiappini, C., Rodrigues, T. S., et al. 2017, *A&A*, 597, A30
- Anders, F., Chiappini, C., Santiago, B. X., et al. 2014, *A&A*, 564, A115
- Antoja, T., Helmi, A., Bienayme, O., et al. 2012, *MNRAS*, 426, L1
- Athanassoula, E. 2005, *MNRAS*, 358, 1477
- Aumer, M., White, S. D. M., Naab, T., & Scannapieco, C. 2013, *MNRAS*, 434, 3142
- Baade, W. 1944, *ApJ*, 100, 137

- Babusiaux, C., Gómez, A., Hill, V., et al. 2010, *A&A*, 519, A77
- Baglin, A., Auvergne, M., Barge, P., et al. 2006, in ESA Special Publication, Vol. 1306, ESA Special Publication, ed. M. Fridlund, A. Baglin, J. Lochard, & L. Conroy, 33
- Bailer-Jones, C. A. L. 2011, *MNRAS*, 411, 435
- Beers, T. C., Carollo, D., Ivezić, Ž., et al. 2012, *ApJ*, 746, 34
- Beers, T. C., Flynn, K., & Gebhardt, K. 1990, *AJ*, 100, 32
- Belokurov, V., Zucker, D. B., Evans, N. W., et al. 2006, *ApJ*, 642, L137
- Bensby, T., Alves-Brito, A., Oey, M. S., Yong, D., & Meléndez, J. 2011, *ApJ*, 735, L46
- Bensby, T., Feltzing, S., & Lundström, I. 2003, *A&A*, 410, 527
- Bensby, T., Feltzing, S., Lundström, I., & Ilyin, I. 2005, *A&A*, 433, 185
- Bensby, T., Feltzing, S., & Oey, M. S. 2014, *A&A*, 562, A71
- Bensby, T., Zenn, A. R., Oey, M. S., & Feltzing, S. 2007, *ApJ*, 663, L13
- Bienayme, O., Robin, A. C., & Creze, M. 1987, *A&A*, 180, 94
- Binney, J. 2012, *MNRAS*, 426, 1328
- Binney, J., Burnett, B., Kordopatis, G., et al. 2014, *MNRAS*, 437, 351
- Binney, J., Gerhard, O. E., Stark, A. A., Bally, J., & Uchida, K. I. 1991, *MNRAS*, 252, 210
- Binney, J. & Tremaine, S. 2008, *Galactic Dynamics: Second Edition* (Princeton University Press)
- Bird, J. C., Kazantzidis, S., & Weinberg, D. H. 2012, *MNRAS*, 420, 913
- Bird, J. C., Kazantzidis, S., Weinberg, D. H., et al. 2013, *ApJ*, 773, 43
- Blitz, L. & Spergel, D. N. 1991, *ApJ*, 379, 631
- Boeche, C., Chiappini, C., Minchev, I., et al. 2013a, *A&A*, 553, A19
- Boeche, C., Siebert, A., Piffl, T., et al. 2013b, *A&A*, 559, A59
- Boeche, C., Siebert, A., Williams, M., et al. 2011, *AJ*, 142, 193
- Boissier, S. & Prantzos, N. 1999, *MNRAS*, 307, 857
- Bond, N. A., Ivezić, Ž., Sesar, B., et al. 2010, *ApJ*, 716, 1
- Bournaud, F., Elmegreen, B. G., & Martig, M. 2009, *ApJ*, 707, L1
- Bovy, J. 2015, *ApJS*, 216, 29
- Bovy, J. & Hogg, D. W. 2010, *ApJ*, 717, 617
- Bovy, J., Rix, H.-W., & Hogg, D. W. 2012a, *ApJ*, 751, 131
- Bovy, J., Rix, H.-W., Hogg, D. W., et al. 2012b, *ApJ*, 755, 115

- 
- Bovy, J., Rix, H.-W., Liu, C., et al. 2012c, *ApJ*, 753, 148
- Breddels, M. A., Smith, M. C., Helmi, A., et al. 2010, *A&A*, 511, A90
- Bressan, A., Marigo, P., Girardi, L., et al. 2012, *MNRAS*, 427, 127
- Brook, C. B., Gibson, B. K., Martel, H., & Kawata, D. 2005, *ApJ*, 630, 298
- Brook, C. B., Kawata, D., Gibson, B. K., & Freeman, K. C. 2004, *ApJ*, 612, 894
- Brook, C. B., Stinson, G. S., Gibson, B. K., et al. 2012, *MNRAS*, 426, 690
- Bullock, J. S. & Johnston, K. V. 2005, *ApJ*, 635, 931
- Burnett, B. & Binney, J. 2010, *MNRAS*, 407, 339
- Burnett, B., Binney, J., Sharma, S., et al. 2011, *A&A*, 532, A113
- Cardelli, J. A., Clayton, G. C., & Mathis, J. S. 1989, *ApJ*, 345, 245
- Carollo, D., Beers, T. C., Chiba, M., et al. 2010, *ApJ*, 712, 692
- Carollo, D., Beers, T. C., Lee, Y. S., et al. 2007, *Nature*, 450, 1020
- Casagrande, L., Schönrich, R., Asplund, M., et al. 2011, *A&A*, 530, A138
- Castelli, F. & Kurucz, R. L. 2003, in IAU Symposium, Vol. 210, Modelling of Stellar Atmospheres, ed. N. Piskunov, W. W. Weiss, & D. F. Gray, 20P—+
- Chabrier, G. 2001, *ApJ*, 554, 1274
- Cheng, J. Y., Rockosi, C. M., Morrison, H. L., et al. 2012, *ApJ*, 746, 149
- Chiappini, C. 2009, in IAU Symposium, Vol. 254, IAU Symposium, ed. J. Andersen, Nordströara, B. m, & J. Bland-Hawthorn, 191–196
- Chiappini, C., Anders, F., Rodrigues, T. S., et al. 2015a, *A&A*, 576, L12
- Chiappini, C., Matteucci, F., & Gratton, R. 1997, *ApJ*, 477, 765
- Chiappini, C., Minchev, I., Anders, F., et al. 2015b, in Astrophysics and Space Science Proceedings, Vol. 39, Asteroseismology of Stellar Populations in the Milky Way, ed. A. Miglio, P. Eggenberger, L. Girardi, & J. Montalbán, 111
- Chiba, M. & Beers, T. C. 2000, *AJ*, 119, 2843
- Combes, F. & Sanders, R. H. 1981, *A&A*, 96, 164
- Cooper, A. P., Cole, S., Frenk, C. S., et al. 2010, *MNRAS*, 406, 744
- de Jong, R. S., Bellido-Tirado, O., Chiappini, C., et al. 2012, in Society of Photo-Optical Instrumentation Engineers (SPIE) Conference Series, Vol. 8446, Society of Photo-Optical Instrumentation Engineers (SPIE) Conference Series, 0
- De Lucia, G. & Helmi, A. 2008, *MNRAS*, 391, 14
- Dehnen, W. 1998, *AJ*, 115, 2384

- Dehnen, W. 2000, *AJ*, 119, 800
- Dehnen, W. & Binney, J. 1998, *MNRAS*, 294, 429
- Dékány, I., Minniti, D., Catelan, M., et al. 2013, *ApJ*, 776, L19
- Dias, W. S. & Lépine, J. R. D. 2005, *ApJ*, 629, 825
- Dierickx, M., Klement, R., Rix, H.-W., & Liu, C. 2010, *ApJ*, 725, L186
- Eisenhauer, F., Genzel, R., Alexander, T., et al. 2005, *ApJ*, 628, 246
- Epchtein, N., de Batz, B., Capoani, L., et al. 1997, *The Messenger*, 87, 27
- Feltzing, S. & Bensby, T. 2008, *Physica Scripta Volume T*, 133, 014031
- Feltzing, S., Bensby, T., & Lundström, I. 2003, *A&A*, 397, L1
- Few, C. G., Courty, S., Gibson, B. K., et al. 2012, *MNRAS*, 424, L11
- Flynn, C., Holmberg, J., Portinari, L., Fuchs, B., & Jahreiß, H. 2006, *MNRAS*, 372, 1149
- Frebel, A., Aoki, W., Christlieb, N., et al. 2005, in *IAU Symposium*, Vol. 228, *From Lithium to Uranium: Elemental Tracers of Early Cosmic Evolution*, ed. V. Hill, P. Francois, & F. Primas, 207–212
- Frebel, A., Collet, R., Eriksson, K., Christlieb, N., & Aoki, W. 2008, *ApJ*, 684, 588
- Freeman, K. & Bland-Hawthorn, J. 2002, *ARA&A*, 40, 487
- Freeman, K., Ness, M., Wylie-de-Boer, E., et al. 2013, *MNRAS*, 428, 3660
- Fuhrmann, K. 1998, *A&A*, 338, 161
- Fuhrmann, K. 2004, *Astronomische Nachrichten*, 325, 3
- Fuhrmann, K. 2008, *MNRAS*, 384, 173
- Fuhrmann, K. 2011, *MNRAS*, 414, 2893
- Gilliland, R. L., Brown, T. M., Christensen-Dalsgaard, J., et al. 2010, *PASP*, 122, 131
- Gilmore, G., Randich, S., Asplund, M., et al. 2012, *The Messenger*, 147, 25
- Gilmore, G. & Reid, N. 1983, *MNRAS*, 202, 1025
- Girardi, L., Barbieri, M., Groenewegen, M. A. T., et al. 2012, *TRILEGAL, a TRIdimensional modeL of thE GALaxy: Status and Future*, ed. A. Miglio, J. Montalbán, & A. Noels, 165
- Girardi, L., Grebel, E. K., Odenkirchen, M., & Chiosi, C. 2004, *A&A*, 422, 205
- Girardi, L., Groenewegen, M. A. T., Hatziminaoglou, E., & da Costa, L. 2005, *A&A*, 436, 895
- Girardi, L., Williams, B. F., Gilbert, K. M., et al. 2010, *ApJ*, 724, 1030
- Gonzalez, O. A. & Gadotti, D. A. 2015, *ArXiv e-prints*
- Governato, F., Brook, C., Mayer, L., et al. 2010, *Nature*, 463, 203

- 
- Governato, F., Mayer, L., Wadsley, J., et al. 2004, *ApJ*, 607, 688
- Gratton, R. G., Carretta, E., Claudi, R., Lucatello, S., & Barbieri, M. 2003, *A&A*, 404, 187
- Gratton, R. G., Carretta, E., Matteucci, F., & Sneden, C. 2000, *A&A*, 358, 671
- Guedes, J., Callegari, S., Madau, P., & Mayer, L. 2011, *ApJ*, 742, 76
- Gunn, J. E., Siegmund, W. A., Mannery, E. J., et al. 2006, *AJ*, 131, 2332
- Hambly, N. C., MacGillivray, H. T., Read, M. A., et al. 2001, *MNRAS*, 326, 1279
- Harris, W. E. 1996, VizieR Online Data Catalog, 7195, 0
- Hayden, M. R., Bovy, J., Holtzman, J. A., et al. 2015, *ApJ*, 808, 132
- Hayden, M. R., Holtzman, J. A., Bovy, J., et al. 2014, *AJ*, 147, 116
- Haywood, M. 2001, *MNRAS*, 325, 1365
- Haywood, M., Di Matteo, P., Lehnert, M. D., Katz, D., & Gómez, A. 2013, *A&A*, 560, A109
- Hernquist, L. 1990, *ApJ*, 356, 359
- Hill, V., Lecureur, A., Gómez, A., et al. 2011, *A&A*, 534, A80
- Høg, E., Fabricius, C., Makarov, V. V., et al. 2000, *A&A*, 355, L27
- Holmberg, J., Nordström, B., & Andersen, J. 2007, *A&A*, 475, 519
- Holmberg, J., Nordström, B., & Andersen, J. 2009, *A&A*, 501, 941
- Howard, C. D., Rich, R. M., Clarkson, W., et al. 2009, *ApJ*, 702, L153
- Ibata, R. A., Gilmore, G., & Irwin, M. J. 1995, *MNRAS*, 277, 781
- Irrgang, A., Wilcox, B., Tucker, E., & Schiefelbein, L. 2013, *A&A*, 549, A137
- Ivezić, Ž., Beers, T. C., & Jurić, M. 2012, *ARA&A*, 50, 251
- Ivezić, Ž., Sesar, B., Jurić, M., et al. 2008, *ApJ*, 684, 287
- Jørgensen, B. R. & Lindegren, L. 2005, *A&A*, 436, 127
- Jurić, M., Ivezić, Ž., Brooks, A., et al. 2008, *ApJ*, 673, 864
- Kawata, D. & Chiappini, C. 2016, ArXiv e-prints
- Kawata, D. & Gibson, B. K. 2003, *MNRAS*, 340, 908
- Kobayashi, C. 2004, *MNRAS*, 347, 740
- Kordopatis, G., Binney, J., Gilmore, G., et al. 2015a, *MNRAS*, 447, 3526
- Kordopatis, G., Gilmore, G., Steinmetz, M., et al. 2013, *AJ*, 146, 134
- Kordopatis, G., Recio-Blanco, A., de Laverny, P., et al. 2011, *A&A*, 535, A106

- Kordopatis, G., Wyse, R. F. G., Gilmore, G., et al. 2015b, *A&A*, 582, A122
- Kunder, A., Koch, A., Rich, R. M., et al. 2012, *AJ*, 143, 57
- Kunder, A., Kordopatis, G., Steinmetz, M., et al. 2017, *AJ*, 153, 75
- Lee, Y. S., Beers, T. C., Allende Prieto, C., et al. 2011a, *AJ*, 141, 90
- Lee, Y. S., Beers, T. C., An, D., et al. 2011b, *ApJ*, 738, 187
- Lee, Y. S., Beers, T. C., Sivarani, T., et al. 2008a, *AJ*, 136, 2022
- Lee, Y. S., Beers, T. C., Sivarani, T., et al. 2008b, *AJ*, 136, 2050
- Liu, C. & van de Ven, G. 2012, *MNRAS*, 425, 2144
- Marigo, P., Girardi, L., Bressan, A., et al. 2008, *A&A*, 482, 883
- Martig, M., Bournaud, F., Croton, D. J., Dekel, A., & Teyssier, R. 2012, *ApJ*, 756, 26
- Martig, M., Bournaud, F., & Teyssier, R. 2009, in IAU Symposium, Vol. 254, IAU Symposium, ed. J. Andersen, Nordströara, B. m, & J. Bland-Hawthorn, 429–434
- Matijević, G., Zwitter, T., Bienaymé, O., et al. 2012, *ApJS*, 200, 14
- Matteucci, F. & Brocato, E. 1990, *ApJ*, 365, 539
- McMillan, P. J. 2011, *MNRAS*, 414, 2446
- Miglio, A., Chiappini, C., Morel, T., et al. 2013a, in European Physical Journal Web of Conferences, Vol. 43, European Physical Journal Web of Conferences, 3004
- Miglio, A., Chiappini, C., Morel, T., et al. 2013b, *MNRAS*, 429, 423
- Minchev, I., Boily, C., Siebert, A., & Bienayme, O. 2010, *MNRAS*, 407, 2122
- Minchev, I., Chiappini, C., & Martig, M. 2013, *A&A*, 558, A9
- Minchev, I., Chiappini, C., & Martig, M. 2014a, ArXiv e-prints
- Minchev, I., Chiappini, C., & Martig, M. 2014b, *A&A*, 572, A92
- Minchev, I., Chiappini, C., Martig, M., et al. 2014c, *ApJ*, 781, L20
- Minchev, I. & Famaey, B. 2010, *ApJ*, 722, 112
- Minchev, I., Famaey, B., Combes, F., et al. 2011, *A&A*, 527, A147
- Minchev, I., Famaey, B., Quillen, A. C., et al. 2012, *A&A*, 548, A127
- Minchev, I., Martig, M., Streich, D., et al. 2015, *ApJ*, 804, L9
- Miyamoto, M. & Nagai, R. 1975, *PASJ*, 27, 533
- Monet, D. G., Levine, S. E., Canzian, B., et al. 2003, *AJ*, 125, 984
- Moultaka, J., Ilovaisky, S. A., Prugniel, P., & Soubiran, C. 2004, *PASP*, 116, 693

- Munari, U., Sordo, R., Castelli, F., & Zwitter, T. 2005, *A&A*, 442, 1127
- Munn, J. A., Monet, D. G., Levine, S. E., et al. 2004, *AJ*, 127, 3034
- Navarro, J. F., Frenk, C. S., & White, S. D. M. 1996, *ApJ*, 462, 563
- Navarro, J. F. & Steinmetz, M. 1997, *ApJ*, 478, 13
- Navarro, J. F. & Steinmetz, M. 2000, *ApJ*, 538, 477
- Nidever, D. L., Bovy, J., Bird, J. C., et al. 2014, *ApJ*, 796, 38
- Nissen, P. E. & Schuster, W. J. 2010, *A&A*, 511, L10
- Nordström, B., Mayor, M., Andersen, J., et al. 2004, *A&A*, 418, 989
- Ojha, D. K. 2001, *MNRAS*, 322, 426
- Otolani, S., Renzini, A., Gilmozzi, R., et al. 1995, *Nature*, 377, 701
- Pasetto, S., Chiosi, C., & Kawata, D. 2012, *A&A*, 545, A14
- Paunzen, E. 2008, Contributions of the Astronomical Observatory Skalnaté Pleso, 38, 435
- Perryman, M. A. C., de Boer, K. S., Gilmore, G., et al. 2001, *A&A*, 369, 339
- Perryman, M. A. C., Lindegren, L., Kovalevsky, J., et al. 1997, *A&A*, 323, L49
- Pier, J. R., Munn, J. A., Hindsley, R. B., et al. 2003, *AJ*, 125, 1559
- Piffl, T. 2014, PhD thesis, Astrophysical Institute Potsdam, An der Sternwarte 16, 14482 Potsdam, Germany
- Piontek, F. & Steinmetz, M. 2011, *MNRAS*, 410, 2625
- Pont, F. & Eyer, L. 2004, *MNRAS*, 351, 487
- Prusti, T. 2012, *Astronomische Nachrichten*, 333, 453
- Raha, N., Sellwood, J. A., James, R. A., & Kahn, F. D. 1991, *Nature*, 352, 411
- Re Fiorentin, P., Bailer-Jones, C. A. L., Lee, Y. S., et al. 2007, *A&A*, 467, 1373
- Recio-Blanco, A., Bijaoui, A., & de Laverny, P. 2006, *MNRAS*, 370, 141
- Reddy, B. E., Lambert, D. L., & Allende Prieto, C. 2006, *MNRAS*, 367, 1329
- Reylé, C., Marshall, D. J., Robin, A. C., & Schultheis, M. 2009, *A&A*, 495, 819
- Rieke, G. H. & Lebofsky, M. J. 1985, *ApJ*, 288, 618
- Rix, H.-W. & Bovy, J. 2013, *A&A Rev.*, 21, 61
- Robin, A. C., Haywood, M., Creze, M., Ojha, D. K., & Bienayme, O. 1996, *A&A*, 305, 125
- Robin, A. C., Luri, X., Reylé, C., et al. 2012, *A&A*, 543, A100
- Robin, A. C., Reylé, C., Derrière, S., & Picaud, S. 2003, *A&A*, 409, 523

- Robin, A. C., Reyl e, C., Fliri, J., et al. 2014, *A&A*, 569, A13
- Rodrigues, T. S., Girardi, L., Miglio, A., et al. 2014, *MNRAS*, 445, 2758
- Roeser, S., Demleitner, M., & Schilbach, E. 2010, *AJ*, 139, 2440
- R oser, S., Schilbach, E., Schwan, H., et al. 2008, *A&A*, 488, 401
- Rossetto, B. M., Santiago, B. X., Girardi, L., et al. 2011, *AJ*, 141, 185
- Ro kar, R., Debattista, V. P., Quinn, T. R., Stinson, G. S., & Wadsley, J. 2008a, *ApJ*, 684, L79
- Ro kar, R., Debattista, V. P., Stinson, G. S., et al. 2008b, *ApJ*, 675, L65
- Ruchti, G. R., Fulbright, J. P., Wyse, R. F. G., et al. 2011, *ApJ*, 737, 9
- Ruphy, S., Robin, A. C., Epchtein, N., et al. 1996, *A&A*, 313, L21
- Saito, R. K., Minniti, D., Dias, B., et al. 2012, *A&A*, 544, A147
- Sales, L. V., Helmi, A., Abadi, M. G., et al. 2009, *MNRAS*, 400, L61
- Sanders, J. L. & Binney, J. 2015, *MNRAS*, 449, 3479
- Santiago, B. X., Brauer, D. E., Anders, F., et al. 2016, *A&A*, 585, A42
- Scalo, J. M. 1986, *Fund. Cosmic Phys.*, 11, 1
- Scannapieco, C., Tissera, P. B., White, S. D. M., & Springel, V. 2005, *MNRAS*, 364, 552
- Scannapieco, C., Tissera, P. B., White, S. D. M., & Springel, V. 2006, *MNRAS*, 371, 1125
- Scannapieco, C., Wadepuhl, M., Parry, O. H., et al. 2012, *MNRAS*, 423, 1726
- Schlegel, D. J., Finkbeiner, D. P., & Davis, M. 1998, *ApJ*, 500, 525
- Schlesinger, K. J., Johnson, J. A., Rockosi, C. M., et al. 2014, *ApJ*, 791, 112
- Schlesinger, K. J., Johnson, J. A., Rockosi, C. M., et al. 2012, *ApJ*, 761, 160
- Sch onrich, R. 2012, *MNRAS*, 427, 274
- Sch onrich, R., Asplund, M., & Casagrande, L. 2011, *MNRAS*, 415, 3807
- Sch onrich, R. & Bergemann, M. 2014, *MNRAS*, 443, 698
- Sch onrich, R. & Binney, J. 2009a, *MNRAS*, 396, 203
- Sch onrich, R. & Binney, J. 2009b, *MNRAS*, 399, 1145
- Sch onrich, R., Binney, J., & Dehnen, W. 2010, *MNRAS*, 403, 1829
- Schultheis, M., Zasowski, G., Allende Prieto, C., et al. 2014, *AJ*, 148, 24
- Sellwood, J. A. & Binney, J. J. 2002, *MNRAS*, 336, 785
- Sharma, S. & Bland-Hawthorn, J. 2013, *ApJ*, 773, 183

- 
- Sharma, S., Bland-Hawthorn, J., Johnston, K. V., & Binney, J. 2011, *ApJ*, 730, 3
- Sharma, S. & Steinmetz, M. 2006, *MNRAS*, 373, 1293
- Shen, J., Rich, R. M., Kormendy, J., et al. 2010, *ApJ*, 720, L72
- Siebert, A., Famaey, B., Binney, J., et al. 2012, *MNRAS*, 425, 2335
- Siebert, A., Williams, M. E. K., Siviero, A., et al. 2011, *AJ*, 141, 187
- Skrutskie, M. F., Cutri, R. M., Stiening, R., et al. 2006, *AJ*, 131, 1163
- Smolinski, J. P., Lee, Y. S., Beers, T. C., et al. 2011, *AJ*, 141, 89
- Sousa, S. G., Santos, N. C., Israelian, G., Mayor, M., & Udry, S. 2011, *A&A*, 533, A141
- Sparke, L. S. & Gallagher, III, J. S. 2007, *Galaxies in the Universe*
- Springel, V. 2012, *Astronomische Nachrichten*, 333, 515
- Springel, V., Frenk, C. S., & White, S. D. M. 2006, *Nature*, 440, 1137
- Steinmetz, M., Zwitter, T., Siebert, A., et al. 2006, *AJ*, 132, 1645
- Stello, D., Huber, D., Sharma, S., et al. 2015, *ApJ*, 809, L3
- Stinson, G. S., Bailin, J., Couchman, H., et al. 2010, *MNRAS*, 408, 812
- Stinson, G. S., Bovy, J., Rix, H.-W., et al. 2013a, *MNRAS*, 436, 625
- Stinson, G. S., Brook, C., Macciò, A. V., et al. 2013b, *MNRAS*, 428, 129
- Stoughton, C., Lupton, R. H., Bernardi, M., et al. 2002, *AJ*, 123, 485
- Takeda, G., Ford, E. B., Sills, A., et al. 2007, *ApJS*, 168, 297
- Tissera, P. B., White, S. D. M., & Scannapieco, C. 2012, *MNRAS*, 420, 255
- Turon, C., Primas, F., Binney, J., et al. 2008, ESA-ESO Working Group on Galactic Populations, Chemistry and Dynamics, Tech. rep.
- Veltz, L., Bienaymé, O., Freeman, K. C., et al. 2008, *A&A*, 480, 753
- Villalobos, Á. & Helmi, A. 2008, *MNRAS*, 391, 1806
- Watson, F. G., Parker, Q. A., Bogatu, G., et al. 2000, in Society of Photo-Optical Instrumentation Engineers (SPIE) Conference Series, Vol. 4008, Society of Photo-Optical Instrumentation Engineers (SPIE) Conference Series, ed. M. Iye & A. F. Moorwood, 123–128
- Widrow, L. M., Pym, B., & Dubinski, J. 2008, *ApJ*, 679, 1239
- Wiersma, R. P. C., Schaye, J., Theuns, T., Dalla Vecchia, C., & Tornatore, L. 2009, *MNRAS*, 399, 574
- Williams, M. E. K., Steinmetz, M., Binney, J., et al. 2013, *MNRAS*, 436, 101
- Williams, M. E. K., Steinmetz, M., Sharma, S., et al. 2011, *ApJ*, 728, 102

- Wilson, M. L., Helmi, A., Morrison, H. L., et al. 2011, *MNRAS*, 413, 2235
- Wojno, J., Kordopatis, G., Piffl, T., et al. 2016, ArXiv e-prints
- Xue, X. X., Rix, H. W., Zhao, G., et al. 2008, *ApJ*, 684, 1143
- Yanny, B., Rockosi, C., Newberg, H. J., et al. 2009, *AJ*, 137, 4377
- York, D. G., Adelman, J., Anderson, Jr., J. E., et al. 2000, *AJ*, 120, 1579
- Zacharias, N., Finch, C., Girard, T., et al. 2010, *AJ*, 139, 2184
- Zacharias, N., Finch, C. T., Girard, T. M., et al. 2013, *AJ*, 145, 44
- Zacharias, N., Urban, S. E., Zacharias, M. I., et al. 2004, *AJ*, 127, 3043
- Zoccali, M. 2015, in *Astronomical Society of the Pacific Conference Series*, Vol. 491, *Astronomical Society of the Pacific Conference Series*, ed. S. Points & A. Kunder, 118
- Zoccali, M., Renzini, A., Ortolani, S., et al. 2003, *A&A*, 399, 931
- Zucker, D. B., de Silva, G., Freeman, K., Bland-Hawthorn, J., & Hermes Team. 2012, in *Astronomical Society of the Pacific Conference Series*, Vol. 458, *Galactic Archaeology: Near-Field Cosmology and the Formation of the Milky Way*, ed. W. Aoki, M. Ishigaki, T. Suda, T. Tsujimoto, & N. Arimoto, 421
- Zwitter, T., Matijević, G., Breddels, M. A., et al. 2010, *A&A*, 522, A54
- Zwitter, T., Siebert, A., Munari, U., et al. 2008, *AJ*, 136, 421

---

## Acknowledgements

---

Foremost, I would like to express my sincere gratitude to my supervisor Matthias Steinmetz for offering me the chance to write my dissertation and do my research at the Leibniz Institute for Astrophysics Potsdam (AIP). The AIP provided an extraordinarily intriguing environment where I could not only pursue my interest for the Milky Way and Galactic Archaeology in particular but where I could also look over the rim of the Local Universe by following recent scientific developments in various other fields of astronomy and astrophysics.

Special thanks I owe to Cristina Chiappini for giving me continuous support, guidance and insightful comments and for taking time whenever I expressed the need for help and advice. Her patience and comprehensive knowledge helped me to successfully conduct my thorough research project.

I also want to thank my colleagues at the AIP and around the world for their support and all of their comments. I am very grateful for the many discussions I had with them. In particular the constant exchange with Friedrich Anders, Ivan Minchev and Roelof de Jong provided me with inspiring ideas for my research.

Finally, I must express my very profound gratitude to my family, boyfriend and best friend for providing me with unfailing support and continuous encouragement throughout my years of study and through the process of researching and writing this thesis. This accomplishment would not have been possible without each single one of them. Thanks to all of you.



---

## Selbstständigkeitserklärung

---

Hiermit erkläre ich, dass ich die vorliegende Doktorarbeit mit dem Titel „Chemo-Kinematic Constraints on Milky Way Models from the Spectroscopic Surveys SEGUE & RAVE“ selbstständig verfasst habe. Alle verwendeten Quellen und Hilfsmittel habe ich angegeben. Alle Stellen, die wörtlich oder sinngemäß anderen Werken entnommen sind, sind als solche gekennzeichnet.

Dorothee E. Brauer  
Potsdam, den 21. November 2016

